AN INVESTIGATION OF PLASMA PRETREATMENTS AND PLASMA POLYMERIZED THIN FILMS FOR TITANIUM/POLYIMIDE ADHESION

Ronald Attilio DiFelice

Dissertation submitted to the Faculty of the
Virginia Polytechnic Institute and State University
in partial fulfillment of the requirements for the degree of

Doctor of Philosophy
in
Chemistry

John G. Dillard, Chair
Gary L. Long
Herve' Marand
Tom C. Ward
James P. Wightman

April, 2001
Blacksburg, Virginia

Keywords: Plasma Polymer, Plasma Treatment, Oxygen Plasma Treatment, Plasma Polymerized Acetylene, Plasma Polymerized Organo-Metallics, XPS, DOE, AFM Scratch Test, Nanoindentation, Ti-6Al-4V, Silicon(111), FM-5 Adhesive

An Investigation of Plasma Pretreatments and Plasma Polymerized Thin Films for Titanium/Polyimide Adhesion

Ronald Attilio DiFelice

(ABSTRACT)

Plasma pretreatments are environmentally benign and energy efficient processes for modifying the surface chemistry of materials. In an effort to improve the strength of the titanium alloy/FM-5 polyimide adhesive joint for aerospace applications, oxygen plasma pretreatments and novel thin plasma polymerized (PP) films were investigated as adhesion promoters. Plasma treatments were carried out using custom-built, low pressure, radio frequency, inductively coupled plasma reactors. Ti-6Al-4V coupons were plasma treated and used to prepare miniature single lap shear (SLS) joints. The effects of plasma pretreatments on surface chemistry were studied using x-ray photoelectron spectroscopy (XPS), Auger electron spectroscopy (AES), Fourier transform infrared analysis (FTIR), and contact angle measurements. Relationships between composition, mechanical properties, and adhesion of PP films on Ti-6Al-4V and silicon wafers were investigated. The nanomechanical properties (modulus, hardness and adhesion) were studied using atomic force microscopy (AFM) nanoindentation and nanoscratch testing.

A design of experiments (DOE) three factorial model was used to optimize the parameters for oxygen plasma treatments. Oxygen plasma pretreatments enhanced joint strength by cleaning the titanium surface and creating an extended oxide layer. Nanoindentation of oxygen plasma treated substrates showed no change in the surface mechanical properties due to the oxygen plasma treatment. This suggested that the improved SLS strength of the oxygen plasma pretreated substrates was due to the cleaning of the substrate and the removal of carbonaceous contaminants, rather than any changes in the morphology of the oxide layer.

PP acetylene films were predominantly carbon, with oxygen as the other main constituent (incorporated mostly as C-O and C=O). For all SLS specimens tested, the adhesion between PP acetylene and FM-5 adhesive was adequate. However, the strength of SLS joints was limited by the adhesion of the PP acetylene to the Ti-6Al-4V substrate. The effects of a large number of plasma parameters, such as substrate pretreatment, carrier gas, input power, flow rate and film thickness were investigated. All samples failed at the PP film/Ti-6Al-4V interface or within the

PP acetylene film, and thicker PP films yielded lower SLS strengths. PP films deposited at lower power exhibited higher hardness and reduced modulus than films deposited at higher power. Overall, thinner films exhibited higher hardness and reduced Young's modulus than thicker films. PP films of higher hardness yielded higher critical loads at debond (thickness normalized) during the nanoscratch test.

Thin films were developed via the vapor plasma polymerization of titanium(IV) isobutoxide (TiiB). XPS results suggested that titanium was incorporated into the film as TiO_2 clusters dispersed in an organic matrix. No evidence for Ti-C was obtained from the XPS spectra. PP films of TiiB were much more compliant than PP acetylene films. This behavior was attributed to decreased fragmentation and lower crosslinking that occurred during PP TiiB film deposition. These PP films did not exhibit sol-gel-like qualities, and because of the way titanium was incorporated into the films, a more appropriate name for these films might be "titanium dioxide-doped plasma polymerized films."

DEDICATION

to

My parents, Anne and Attilio DiFelice

Acknowledgements

Much gratitude is owed to my committee members for their help with this endeavor. I would like to thank Dr. John Dillard, Dr. Gary Long, Dr. Herve' Marand, Dr. Tom Ward, and Dr. Jim Wightman for all that they have taught me through my graduate school years at Virginia Tech. Dr. Gary Long is particularly acknowledged for providing the plasma power source and the laboratory space for this study. I especially thank my advisor, Dr. John Dillard, for his guidance and support; knowing him has improved me as a researcher and as a person.

Many thanks are owed to the Center for Adhesive and Sealant Science (CASS), which provided financial support through the Adhesive and Sealant Council (ASC) Education Foundation. Support from these organizations also allowed me to attend many outstanding conferences, and I have benefited personally and professionally from these experiences. I would also like to thank the Virginia Space Grant Consortium, which provided additional funding for the final two years of this work. PRF, Inc. and the Department of Defense are also acknowledged for providing components of the plasma system. Dr. Dehua Yang and Hysitron, Inc. (Minneapolis, MN) are gratefully acknowledged for their collaboration on the AFM nanomechanical studies.

Special thanks go to Mr. Frank Cromer, whose patience and help with surface analytical instrumentation and data analysis has been invaluable. Jim Coultier in the electronics shop is also acknowledged for his help with a number of plasma reactor-related issues. Thanks to Sherine Obare for her efforts on this project as an undergraduate summer student. Tammy Jo Hiner, Linda Haney, Katy Hatfield, and Kim Mills from the CASS office and Wanda Hensley and Kezia Johnson from the Chemistry Department office are also acknowledged for their administrative help throughout the years.

Thanks to former and current colleagues, who have made my time in Blacksburg most enjoyable. Thanks go to (in no particular order): Maggie Bobbitt Bump, Dave Porter, Amy Eichstadt, Emmett O'Brien, Jianli Wang, Sandra Henderson, Mark Muggli, Dan Brennegan, Marie-Pierre Laborie, Brenda Jackson, William Heard, John Morgan, Sumitra Subrahmanyan, Lei Zheng, Jennifer Hoyt, Steve Hunsucker, Dave Polk, and Lee Williams. I also thank my band mates from GoodTimes and The Joules for giving me a much-needed musical outlet.

I would like to thank all of my family and friends who have supported me unconditionally throughout the years. Especially my mom and dad, my brother (Tony) and sister (Corinne) and their spouses (Stephanie and Brian), niece (Mallory), nephews (Tyler and Ethan), and all of my friends from the Webster class of 1990. Also, I thank Melissa for her support and patience throughout this endeavor. Finally, I'd like to thank my yellow Labrador (Looper) for his perpetual love; he never grows tired of my attention and he never complained once when I came home late from the laboratory.

Table of Contents

Table of Figures

Table of Tables

1.0 Introduction

Alloys of titanium metal are extremely valuable in the aerospace industry, where titanium's lightweight and high strength have been extensively exploited for high performance applications. Increased operational demands in a wide range of environments have pushed current adhesively bonded systems to their performance limitations. The anticipated life of high performance aircraft structures is in excess of 60,000 flying hours, with temperatures during a flight cycle ranging from -50° C to over 180° C. A pressure of 2 psi is anticipated at the projected flying altitude and cruise speed of Mach 2.4. These extreme operating conditions demand materials that possess superior properties over a wide range of temperatures and environments. Accordingly, adhesives have been formulated to offer higher toughness and greater thermo-oxidative stability for long term structural applications at elevated temperatures.[1] There is currently a strong need for research into alternative surface pretreatments that take advantage of such advances in adhesive materials.

Adhesive bonding has several advantages over mechanical fasteners, and these advantages have attracted attention to adhesive bonding as a possible alternative to mechanical fasteners.[2] Recent advances in adherend surface pretreatments have further increased interest in utilizing adhesive joints for aircraft and automotive structures.[2] When considering how an adhesive will perform in a particular application, it is inadequate and unadvisable to predict the adhesive's performance based on the physical properties of the adhesive alone. Instead, the adhesively bonded system (the adherend, the adhesive, and the environment) needs to be evaluated in its entirety to make meaningful interpretations about how the system will actually perform in its service environment. The importance of surface preparation of the adherends cannot be overlooked; surface pretreatments have a significant influence on how a system will perform under stress. Indeed, the adhesion community recognizes that the surface preparation of adherends significantly affects the performance of adhesively bonded components.

Surface pretreatments may increase the surface area of an adherend (by physically roughening the surface), thereby increasing mechanical interlocking between the adhesive and the adherend. Surface pretreatments can also change the surface chemistry of an adherend. One

of the most popular surface preparations for metals involves removing and replacing weak oxide layers with a controlled, more stable oxide layer. Surface pretreatments can also introduce chemical groups onto the adherend's surface that are better suited to interact with the adhesive.

The adhesively bonded system of interest in this study includes titanium alloy (Ti-6Al-4V) and a high temperature polyimide adhesive, designated FM-5. This glass-supported adhesive consists predominantly of the low molecular weight polymer LaRC-PETI-5. This system is of interest because it is being considered for application in the assembly of high-speed aircraft structures. Titanium alloy is widely used in the aerospace industry because of its high strength to weight ratio, good corrosion resistance, and its ability to retain its mechanical properties at elevated temperatures.[3] Extensive research into the development of titanium alloy surface pretreatments that enhance adhesive bonding and promote the retention of bond strength upon environmental exposure has been carried out.[4] Most improvements in titanium joint performance have been achieved through the pretreatment of the metal by mechanical abrasion, solvent cleaning, corona treatment, anodization, or by acid and caustic etching.[5] Unfortunately, these treatments have certain drawbacks that greatly limit their effectiveness. The problems typically associated with mechanical abrasion and solvent treatments, such as lack of uniformity and reproducibility, safety, and waste disposal, are virtually eliminated by plasma pretreatment processes.

The plasma pretreatment of metals is an attractive option for improving adhesion because it combines the features of safety, cleanliness, and cost effectiveness while enhancing performance. Plasma pretreatments using non-polymerizable gases remove carbonaceous contaminants from a surface while simultaneously altering its chemistry in other ways. Plasma polymerization is a unique technique for fabricating thin polymer films from almost any organic or inorganic gas.[6,7,8] Through plasma polymerization, a very thin (<100 nanometers), uniform, highly adherent film with a high cross-link density, low solubility, and unusually high thermal stability can be obtained in a solvent-free process.[9] Utilizing thin plasma polymerized (PP) films as surface primers to improve adhesion has met with great success for certain systems.[10] PP films have been used in a variety of applications as permselective membranes, protective coatings, and electrical and biochemical films.[6, 11] Despite the potential advantages, the plasma pretreatment of titanium alloys for adhesion promotion has been narrowly explored, and the literature on the use of PP films for modifying the surface of common metals is limited.[6]

Questions still exist regarding the mechanism of PP film deposition, the chemistry at the film-substrate interface, and the relationship of surface properties to adhesion.[11] An extensive characterization of the mechanical properties of PP films is absent from the literature. Because these films are extremely thin and notoriously insoluble, characterization is difficult. Especially difficult to attain are mechanical properties of thin PP films. Indirect methods using test geometries that rely on an additional adhesive to measure the force needed to debond a thin film are riddled with problems that ultimately distort the significance of the measurement. Recent advances in AFM and nanoindentation techniques provide a new way for measuring properties such as film hardness, modulus and adhesion to a substrate.

The various plasma pretreatments and PP films studied in this work include oxygen plasma pretreatments, PP acetylene, and PP titanium(IV) isobutoxide (TiiB). The investigation of plasma pretreatments and polymerizations was performed by varying the plasma process parameters that govern plasma polymerizations. The effects of pretreatment, carrier gas, flow rate, power output, pressure, and length of exposure on composition and SLS strengths were investigated. The effects of these parameters on PP film composition, mechanical properties, and adhesive performance are reported and discussed.

Table 1.1 lists the analytical techniques utilized in this study and the information obtained from each technique. Collaboration was established with Hysitron, Inc. (Minneapolis, MN) for the nanoindentation and nanoscratch experiments. Table 1.2 lists the common abbreviations used throughout this work.

1.1 Thesis Statement

The surface modification of Ti-6Al-4V for adhesion via plasma pretreatments and plasma polymerizations yields surfaces with unusual chemical and mechanical properties.

1.2 Tables

Table 1.1: Analytical techniques and the information obtained from each.

Technique	Information Yielded
X-ray photoelectron spectroscopy (XPS)	Elemental analysis of the top 50Å of a surface. Also gives information about the valence state of surface atoms.
Auger electron spectroscopy (AES)	Depth profiling was used to determine film thickness and show changes in film composition as a function of depth.
Fourier transform infrared analysis (FTIR)	Revealed the specific functional groups present in the PP film.
Atomic force microscopy (AFM)/ Nanoindentation	Nanoindentation yielded physical properties (hardness and modulus) of the films and PP film/substrate adhesion was evaluated via a scratch test.
Optical Goniometry	Contact angles and surface energies were determined.

Table 1.2: Common abbreviations used throughout the dissertation (alphabetical).

Abbreviation	Description
Å	Angstroms
AES	Auger electron spectroscopy
AFM	Atomic force microscope
AIM	Atomic interfacial mixing
ANOVA	Analysis of Variance
CAP	Competitive ablation and polymerization
DLC	Diamond-like coatings
DOE	Design of experiments
Er	Reduced modulus
eV	Electron volts
FR	Flow rate
FTIR	Fourier transform-infrared spectroscopy
GC/MS	Gas chromatography/mass spectrometry
GPa	Gigapascals
H	Hardness
h_c	Depth of penetration
HMDS	Hexamethyldisiloxane
IC	Inductively coupled
IP	Input power
kcal	Kilocalories
MPa	Megapascals
mTorr	MilliTorr
nm	Nanometers
PECVD	Plasma enhanced chemical vapor deposition
PP	Plasma polymerized
RF	Radio frequency
RSM	Response surface methodology
sccm	Standard cubic centimeters per second
SEM	Scanning electron microscopy
TEM	Transmission-emission microscopy
TiiB	Titanium(IV) isobutoxide
TiiP	Titanium(IV) isopropoxide
TOF-SIMS	Time of flight secondary ion mass spectrometry
TT	Treatment time
XPS	X-ray photoelectron spectroscopy

1.3 References

[1] C.L. Hendricks; S.G. Hill *Polyimides: Synthesis, Characterization, and Applications*; Plenum Press: New York, NY, Vol. 2, 1984; p. 1103.
[2] H. Clearfield; D.K Shaffer; S.L.Vandoren; and J.S. Ahearn *J. Adhesion*, **1989**, *29*, 81.
[3] J.F. Watts and B.R. Dempster *Surf. Interface Anal* **1992**, *19*, 115.
[4] S.R. Brown *Proc. 27th Natl. SAMPE Symp.* **1982**, 363.
[5] S.L. Kaplan; P.W. Rose *Int. J. Adhes. and Adhes.* **1991**, *11*, 109.
[6] R. d'Agostino *Plasma Deposition, Treatment, and Etching of Polymers*; Academic Press: Boston, MA, 1990; Chapter 1.
[7] *Plasma Polymerization and Plasma Interactions with Polymers*; K. Yasuda, Ed.; Appl. Polym. Symp. No. 46; Wiley & Sons: New York, NY, 1990, Chapter 1.
[8] H.K. Yasuda *Plasma Polymerization*; Academic Press: Orlando, FL, 1985; Chapter 3.
[9] Y.M. Tsai; U.R. Aggarwal; F.J. Boerio; D.B. Zeik; S.J. Clarson; W.J. Van Ooij; A. Sabata *J. Appl. Polym. Sci.: Appl. Polym. Symp.* **1994**, *54*, 3.
[10] Y.M. Tsai; F.J. Boerio; D.K. Kim *J. Adhesion* **1997**, *61*, 247.
[11] W.J. van Ooij; F.J. Boerio; A. Sabata; D.B. Zeik; C.E. Taylor; S.J. Clarson *J. Test. Eval.* **1995**, *23*, 33.

2.0 Literature Review

2.1 Adhesion

Adhesive bonding has several advantages over mechanical fasteners in the construction of certain structures. These advantages include: the elimination of stress concentrations at rivet holes; reduced weight of the joined system; corrosion protection of the joint by sealing it; a smoother, more aerodynamic finish; damping control of vibrations; and the ability to bond complicated parts.[1] These benefits have drawn increased attention to adhesive bonding as an alternative to mechanical fastening.

Structural adhesives are characterized as high modulus, high strength adhesives used between rigid adherends to form a load-bearing joint.[2] Structural adhesives are used in the aerospace industry for joining aluminum, titanium, and composite adherends. Ultimately, a bond that fails cohesively (within the adhesive), rather than adhesively (interfacially), is desired.

Adhesion science is a multidisciplinary field and an area of research that presents many challenges. Currently, there is no universal theory of adhesion, and the actual mechanisms of adhesion operating across various interfaces are still unknown.[3] Uncertainty remains regarding the exact mechanism of adhesion because test methods commonly employed to measure adhesive strength are not well suited to theoretical interpretation. Additionally, the inability to measure interfacial interactions has been a major obstacle to the development of a comprehensive theory.[4] The very nature of adhesion requires that it be defined on both the macroscopic and microscopic level. Bateup[3] suggests the following distinction: Macroscopically, adhesion is that state in which an interface is formed between two bodies such that mechanical work is transferred between the two. Microscopically, adhesion is defined as the state in which an interface is formed between two bodies such that the molecular forces resist separation.

There are four fundamental theories of adhesion: electrostatic theory, diffusion theory, mechanical interlocking theory, and adsorption theory.[2]

2.1.1 Electrostatic Theory

The electrostatic theory relates the forces of adhesion to a capacitor, where the "capacitor" is charged by the contact of the substrate and the adhesive. To break the bond, work must be done to separate the charges. This induces a potential that increases until the substrate and adhesive are separated.[4] Therefore, adhesion is due to the existence of attractive forces across the electric double layer. This theory accounts for adhesion in only a few special cases.

2.1.2 Diffusion Theory

Diffusion theory applies principally to polymer-polymer adhesive systems. It states that adhesion is a result of the diffusion of the chains of one polymer into the chains of another.[5] This mutual diffusion of polymer molecules across an interface has three requirements: the chain segments must possess adequate mobility; the polymers must be mutually soluble; and the polymers must possess similar solubility parameters.[6]

2.1.3 Mechanical Interlocking Theory

The mechanical interlocking theory asserts that adhesion is a result of an adhesive interlocking into the irregularities of a roughened substrate. According to this theory, increased interfacial area of contact improves adhesion.[7] Evidence of this theory is most notably shown by the adhesion of polymers to textiles[8] or metals.[9] Venables[10] reported that mechanical interlocking is critical for good bond strength and long-term durability for metal-polymer bonds, especially in anodized aluminum-polymer systems.

2.1.4 Adsorption Theory

Adsorption theory best explains a variety of adhesion properties, and states that molecular forces arising from primary and secondary interactions are responsible for adhesion.[11]

Furthermore, materials adhere because of the interatomic and intermolecular forces that are established between the substrate and the adhesive.[12] Provided there is good interfacial contact, van der Waals interactions (dipole-dipole interactions and induced dipole-dipole interactions), acid-base interactions, or hydrogen bonding should be sufficient for good adhesion.[4] Since molecular energies across an interface decrease drastically with increasing intermolecular distance, this theory stresses intimate molecular contact. The formation of primary bonds across an interface (covalent, ionic, or metallic), termed chemisorption, is also included under this theory. Primary forces (60 to 1000 KJ/mol) are usually preferred over secondary interactions (0.08 to 40 KJ/mol),[13, 14] but are much more difficult to obtain at an interface.

2.1.5 Polymer - Metal Adhesion

There is strong evidence favoring the adsorption (and chemisorption) mechanism to explain strong metal-polymer adhesion.[15, 16] Bonding enhancement may result from the creation of chemical groups on the stabilized metal surface that produce covalent linkages or acid-base interactions with the adhesive.[15] Chou and Tang[17] investigated the interfacial reactions during the metallization of a polyimide film surface. They concluded that improved adhesion on chromium and titanium surfaces was due to the formation of metal-oxygen-carbon complexes at the metal/polyimide interface, and that a high concentration of oxidized metal at the metal/polyimide interface led to strong adhesion.[18] Likewise, Burkstrand[19] has shown that the formation of metal-oxygen-polymer complexes on oxygen plasma-treated polymer surfaces correlates with the adhesion of metal films. Fowkes[20] emphasized that the formation of strong acid-base interactions at the metal/polymer interface resulted in strong adhesion between metals and polymers. Furthermore, Inagaki *et al*[21] reported that improved adhesion between Kapton® film and evaporated copper metal was due to the formation of coordination bonds between plasma-formed carboxyl groups and oxidized copper. All of these investigations support the adsorption theory of adhesion and emphasize the importance of having specific functionalities at the metal/polymer interface for improved adhesion.

2.2 The Interphase

Interfacial phenomena have a significant influence on all biological and industrial processes and are of fundamental importance to the science of adhesion. Sharpe[22] was the first to define the interphase as "A transition zone between the surface of a substrate and the bulk of a polymer that is solidified against the substrate."[23] An interphase may also be defined as a region of material whose chemical or physical structures have been modified because of contact between two different phases.[24] Unfortunately, the boundaries of the interphase are difficult to define, and the interphase can extend from a few nanometers (nm) to a few thousand nm, depending on the system.[25] While it is more convenient to deal with an interface, which is usually thought of as a mathematical plane with a thickness of zero, this treatment is unrealistic. Surface layers have a definitive thickness, and surface molecules have an influence on neighboring molecules which results in a gradient from the surface to the bulk phase. All transitions from one material to another occur over a finite area, and therefore the word "interphase" is more appropriate for almost every system. Thus, although the definition will vary in the literature, an interphase is a region with a finite volume and a distinct physical gradient in properties.[26]

Figure 2.1 shows a typical system where an adhesive and a substrate meet. The interfacial zone, or interphase, is defined by the location of the boundary lines. The boundaries are positioned to include the entire region where there are non-zero gradients in composition or density.

Most metal surfaces that have been exposed to the atmosphere are covered with some type of oxide layer.[27] Aluminum metal exposed to the atmosphere contains a thin, tough oxide layer which pacifies the surface and prevents continued oxidation. Formation of the oxide layer involves chemisorption of oxygen on the surface, followed by a chemical reaction to form the oxide.[1] This oxide layer is thin and is covered with low molecular weight organic molecules and water adsorbed from the atmosphere. Adsorbed contaminants are problematic and difficult to completely eliminate because as the surface concentration of contaminants decreases, the binding energy of the remaining contaminants increases.[28]

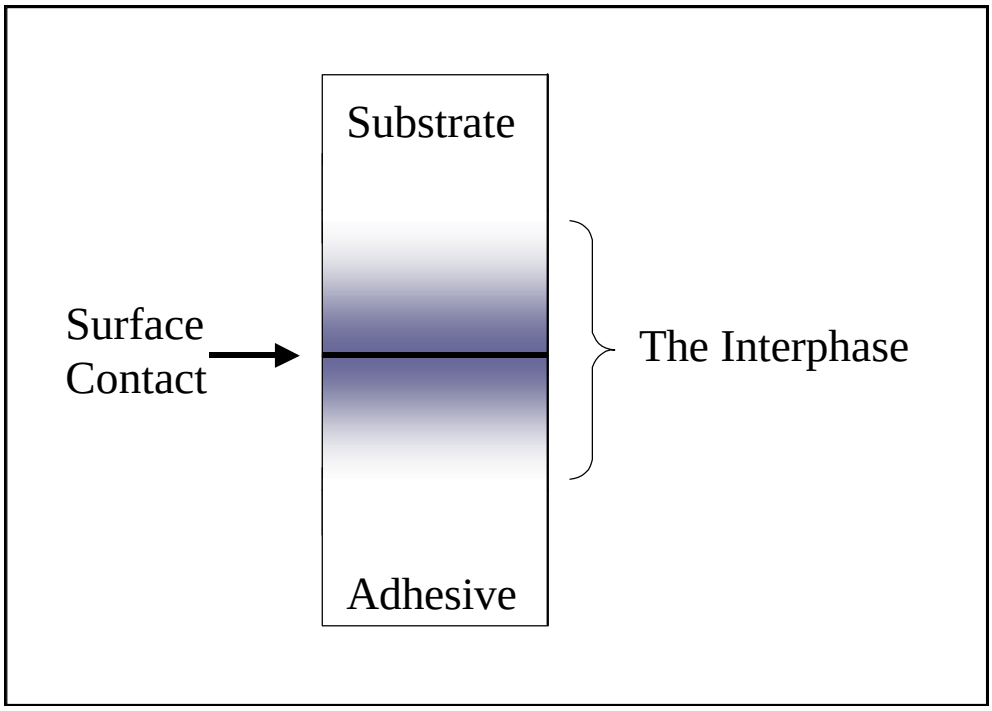

Figure 2.1: The interphase region (adapted from reference 29).

2.3 Surface Pretreatments

The surface pretreatment of metals is often necessary prior to adhesive bonding to replace a preexisting weak oxide layer with a more stable one. The importance of a good surface pretreatment cannot be overemphasized in applications where high performance and durability are critical. There are two basic objectives of surface pretreatments for improving adhesion: to remove loosely bonded surface contamination and to provide intimate contact between the two interacting materials on a molecular scale.[4] Aside from a thorough cleaning, the chemical modification of a metal surface is one of the most powerful ways of enhancing its interaction with a high performance adhesive. An advantage of utilizing plasma processes to pretreat substrates is that typically only the top few microns of the surface are affected. Specifically for titanium alloy, several pretreatments have been studied and utilized in different capacities with varying degrees of success. These pretreatments are discussed in section 2.3.2.

2.3.1 Surface Contaminants

Metal oxide surfaces typically have surface energies greater than 500 mJ/m^2.[30] This is a relatively high surface energy, so a clean surface will rapidly absorb low-energy absorbates, such as hydrocarbons, to lower its surface energy.[31] These omnipresent surface contaminants create a weak boundary layer on the metal oxide and lower the surface energy substantially. This inherently prevents successful wetting of the substrate and limits adhesion. Removing a weak boundary layer via plasma processes is one way of improving adhesion. As little as 0.1 ug/cm^2 of organic contamination on a surface (essentially a monolayer) can interfere with bonding.[32] Organic liquids typically have very low surface energies, and low molecular weight organic contaminants from the atmosphere readily adsorb onto high surface energy solids. Plasma processes can remove surface contaminants and increase the wettability of a substrate,[33] thereby improving adhesion. Plasma treatments can also introduce polar groups onto a surface to increase the surface energy and improve wettability.[34]

2.3.2 Titanium Surface Preparation

The desire to durably bond Ti-6Al-4V for high performance application stimulated the development of high temperature adhesives in the mid-1980s.[35] Dozens of titanium pretreatments have been studied to enhance the adhesion and improve the durability of bonded joints.[36] Critchlow and Brewis provided an excellent review of surface pretreatments for titanium alloys;[36] they identified a total of 35 surface pretreatments and 23 surface analysis methods. The diverse surface pretreatments available for titanium are divided into several broad groups: mechanical (i.e. grit blast); chemical (i.e. acid etch); electrochemical (i.e. chromic acid anodization (CAA)); and others (i.e. etch plus alkoxide primer). Table 2.1 shows the variety of pretreatments available for Ti-6Al-4V to enhance bond durability. A complete listing is provided by Critchlow and Brewis.[36]

Mechanical abrasion of the adherend is commonly used to remove residual contaminants and increase the surface area of the bond region. This is most often achieved by grit blasting the titanium alloy with alumina or silica grit, or by scouring with a Scotch-Brite® pad.[37] These

mechanical abrasion techniques are largely operator sensitive, operator intensive, and present occupational health, safety, and environmental risks. Early studies of bond durability using Ti-6Al-4V substrates showed that surface preparations resulting in minimal surface roughness yielded the poorest results. Significantly micro-roughened titanium alloy exhibited the best bond durability.[38, 39] However, mechanical treatments are not favored for use with thin adherends because they are potentially detrimental to the mechanical integrity of the parent material. Additionally, uniformity and reproducibility are limited.

Table 2.1: Pretreatments available for modifying the Ti-6Al-4V to enhance bond durability.

Treatment	**Class**
Polish and degreasing	Mechanical Treatment
Grit blast	Mechanical Treatment
Plasma spray	Mechanical Treatment
Turco 5578 etch	Chemical
Hydrochloric acid etch	Chemical
Hydrofluoric acid etch	Chemical
Sodium hydroxide etch	Chemical
Nitric-hydrofluoric acid etch	Chemical
Alkaline hydrogen peroxide etch	Chemical
Chromic acid anodization	Electrochemical
Sodium hydroxide anodization	Electrochemical
Sulfuric acid anodization	Electrochemical
Alkaline hydrogen peroxide anodization	Electrochemical
Aluminum alkoxide	Sol/gel
Silicon alkoxide	Sol/gel
Titanium alkoxide	Sol/gel
Phosphate-fluoride conversion coating plus alkoxide primer	Multiple
Grit blast plus alkaline clean	Multiple

Chemical etches generally provide only intermediate levels of durability. Alkaline hydroperoxide etches and TURCO etches (a proprietary alkaline-based etch) are pretreatments that perform relatively well by creating surface macro-roughness and by introducing fresh oxides on the metal.[36] Acid and caustic etching processes are becoming increasingly unacceptable due to environmental, safety, and disposal concerns. [40]

Electrochemical[41, 42] and plasma spray[43] pretreatments provide the best durability results. The most common method for preparing titanium alloy for high performance adhesive bonding

is chromic acid anodization (CAA), a procedure developed by Boeing.[44] The major drawback to this process is the toxic chromate (Cr(VI)) waste, an environmental hazard requiring expensive disposal.[45]

The problems mentioned above are virtually eliminated by plasma pretreatment processes, which produce consistent results in a solvent-free process. By avoiding these deficiencies, the low-pressure plasma pretreatment and plasma deposition of organic films on metals for improved adhesion is an advantageous alternative surface treatment with significant potential. Plasmas using non-polymerizable gases are able to clean substrate surfaces by removing these surface contaminants and etching the surface.[46] Oxygen and helium plasmas are particularly efficient at this process.

2.4 Plasmas

Fundamentally, plasmas are partially ionized gases composed of electrons, ions, photons and various neutral species at many different levels of excitation.[47] Overall, plasmas are electrically neutral. Plasmas can be generated in a variety of ways depending on the application. Plasma generation devices include low-pressure electrical discharges (direct current and alternating current), Penning plasma discharges, microwave-generated plasma devices, radio frequency (RF) capacitive discharges, and RF inductively coupled (IC) plasma devices. High-energy, RF IC plasmas that are produced by exposing a gaseous species at low pressure (<10 Torr) to an induced electric field are utilized in this research.

The major advantages of RF plasma generators are that no internal electrodes are needed and the plasma is easily sustained at a low pressure (< 50 mTorr).[48] Because there are no internal electrodes, no impurities are sputtered off the electrodes and incorporated into the growing film. In this type of generator, plasmas are produced when energy is transferred by an electric field to free electrons within a low-pressure environment. The free electrons collide with molecules and any other surfaces exposed to the plasma.[49] Through inelastic electron collisions with molecules, more electrons, ions, free radicals, and molecules in excited states are generated, and this results in the plasma state.

Figure 2.2 shows how radicals can be formed in a noble gas or oxygen plasma. Cold gas oxygen plasmas contain species such as O^+, O^-, O_2^+, O, and O_3, as well as ionized ozone and

metastably-excited O_2 and free electrons.[40] Each of the energetic fragments is very reactive with other fragments, and any surfaces exposed to the plasma, mostly via free radical chemistry. Plasma pretreatments using non-polymerizable gases remove carbonaceous contaminants from a surface while simultaneously altering substrate chemistry in other ways.[50]

Inductively coupled plasma generators create plasmas when a current flows through a metal coil. A magnetic field is developed around the coil, and as the current is increased, so is the magnetic flux. The increase in the magnetic flux generates a voltage in the coil with a polarity that opposes the change in flux. The ability of a coil to oppose this change is called self-inductance, or simply inductance.[51] Figure 2.3 shows the fields of a close-wound inductive coil, which is the type used in this study.

Helium: $He \rightarrow h\nu + He + He^{+} + e$

Oxygen: $O_2 \rightarrow O_2^{*} + O + O_2^{+} + O^{+} + e^{-}$

Figure 2.2: Helium and oxygen plasma free radical formation.[52]

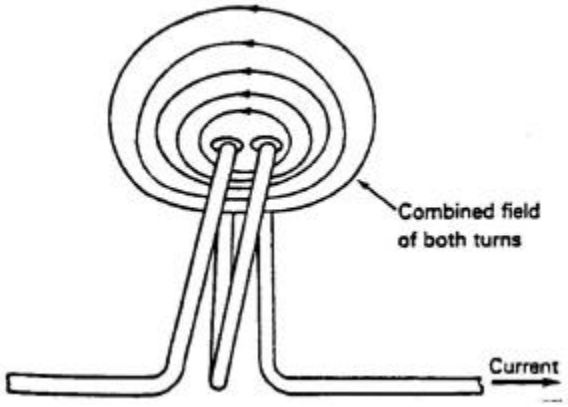

L = inductance (microhenries)
r = radius of the coil (inches)
n = number of turns in the coil
a = length of the coil (inches)

The inductance of a coil varies according to the following equation:

$$L = (r^2)*(n^2)/(9r + 10a)$$

Figure 2.3: The lines of flux for an RF inductively coupled plasma.[51]

Table 2.2 lists typical bond dissociation energies for various organic and inorganic species. In glow discharges, electrons typically have bombardment energies of 20 eV or less (Table 2.3), which is enough energy to break most covalent bonds.[53] Practical plasmas used for surface modification have electron densities of 10^{15} to 10^{16} electrons/meter^3.[54] In low-pressure cold plasmas, electrons do not achieve thermodynamic equilibrium with gas molecules, and thus the temperature of the plasma remains close to ambient. This important feature allows plasma polymerization to be carried out without thermal degradation of reactants or products.[55]

Table 2.2: Typical bond dissociation energies.[64]

Bond	Dissociation Energy (eV)
C-C	3.61
C=C	6.35
C=C (π bond)	2.74
C-H	4.3
C-N	3.17
C=N	9.26
C-O	3.74
C=O	7.78
C-F	5.35
C-Cl	3.52
N-H	4.04
O-H	4.83
O-O	1.52

Table 2.3: Energy available in a glow discharge.[56]

Species	Energy (eV)
Electrons	0 - 20
Ions	0 - 2
Metastables	0 - 20
UV/Visible	3 - 40

2.5 Plasma Polymerizations

The deposition of thin films on solid substrates by the plasma polymerization process has been practiced for over two decades. [47, 55, 57] The plasma polymerization of simple organic

monomers (i.e. hydrocarbons or silanes) produces films that are highly cross-linked, pinhole-free, thermally and chemically stable, and very adherent.[34] Furthermore, plasma polymerized (PP) films can be prepared from monomers that cannot be polymerized by conventional chemical techniques (i.e. methane, ethane, saturated hydrocarbons, organo-metallics). The characteristics of the plasma-formed films (adhesion, mechanical properties, extent of crosslinking, etc.) are dictated by the choice of kinetic formation parameters such as RF power input, plasma pressure, and reaction time.[58] The significant advantages of depositing thin films via plasma polymerization include:[59]

1) The starting material does not have to contain the type of functional groups normally associated with conventional polymerization.
2) PP films are often highly adherent to a variety of substrates.
3) Deposition is achieved without the use of solvents (environmentally benign process).
4) The thickness of PP films can be easily varied from 20 Å to 1 μm.
5) Through careful control of the plasma polymerization parameters, PP films can be tailored to contain specific functional groups.
6) PP films can be deposited directly onto an activated substrate without breaking vacuum.

2.5.1 Plasma Polymerized Film Deposition

Free radicals are formed in plasmas by bond breakage that occurs upon the absorption of energy generated in the plasma. Through inelastic collisions, monomers are fragmented into activated species or into their constituent atoms. The activated fragments are recombined and rearranged by a rapid step growth mechanism, and deposition occurs due to a loss of kinetic energy upon collision of the activated species with the substrates or walls of the reactor. The loss of kinetic energy is due either to a chemical reaction of the species or increased molecular weight.[60] The activated species for film formation come from the gas phase, but the actual film formation proceeds at the substrate surface. Deposited species containing unpaired electrons are highly unstable, and the molecules become highly reactive at the surface of exposed substrates. The repetition of activation/fragmentation and recombination leads to film formation. This

concept is significantly different than the mechanism of conventional polymerization. Additionally, any gases in a reaction vessel (i.e. nitrogen and oxygen) may be activated into their corresponding radicals and may be incorporated into the films by radical recombination reactions.[54] Consequently, polymers formed in plasmas generally have complex, highly crosslinked structures due to the large number of reaction pathways available during plasma excitation.[61] Carrier gases increase the ionization of acetylene molecules and the ion energies but also expose the surface to bombardment by neutrals, ions, and radicals.[62] Carrier gases assist deposition by increasing ionization and ion energies in the plasma and subimplantation at the surface.[63]

The fragmentation of hydrocarbon starting materials in a plasma is best represented by two types of reactions: the elimination of hydrogen and C-C bond scission. Figure 2.4 shows the predominant sources of free radicals for hydrocarbons exposed to a plasma.

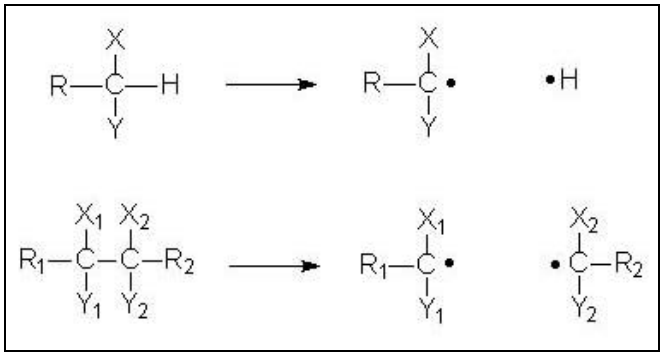

Figure 2.4: Hydrogen elimination and C-C bond scission of hydrocarbons exposed to a plasma.

While most ionizations require energy greater than 10 eV, the dissociation of a molecule requires less energy. For example, the energy required to dissociate a C-C bond is 3.61 eV.[64] In a plasma, the scission of bonds occurs much more frequently than does the formation of ions. Bond scission does not occur as a consequence of the ionization of molecules, but rather it occurs simultaneously with ionization.[64] Bell estimated that the concentration of free radicals in a plasma is usually five to six orders of magnitude higher than that of ions.[65]

In spite of the complexity of plasma polymerization processes, the main set of parameters governing a given process may be optimized and then successfully reproduced.[15] Discharge power, flow rate, frequency of excitation, and working pressure are not independent variables and must all be optimized for a particular polymerization process.

The concentration of residual free radicals produced by a plasma decays rapidly when specimens activated by a plasma are exposed to the atmosphere after treatment. The concentration decreases by half in less than a minute due to oxidation of the surface by the atmosphere and the formation of peroxides.[66] If a plasma treated surface is left under vacuum, residual free radicals are active for considerably longer, and are available to react with any reactive species introduced into the chamber.

Plasma polymerization mechanisms can be distinguished by the type of monomer used in the polymerization process. If the monomer is unsaturated, the plasma may induce polymerization by creating reactive species in the electrical discharge, and the molecular weight then increases by a more conventional step-growth fashion. In the plasma polymerization of saturated carbon compounds, the monomer is fragmented by the plasma into reactive species that recombine and condense on the substrate surface. These polymers, because of the smaller size of the activated species, are very different in structure and stoichiometry than conventionally formed polymers.[67]

It is generally accepted that very little polymerization occurs in the gas phase, where the monomer is fragmented. Instead, energetic species reach the substrate surface and are converted to highly energetic neutral species. The most stable species deposit onto the substrate and form a number of three-dimensional islands that usually have very different chemistry from the precursor. Surface migration of atoms to these islands causes them to grow, and continued growth results in the islands coalescing to form an interconnected network of islands.[68] These films are typically highly crosslinked and conjugated.[69]

Because of the complex processes involved in creating PP films, and because the films are typically very thin and insoluble in most solvents, several researchers have deduced the film chemistry by indirect means. Plasma gas condensates of polymerizable gases can be gathered using a liquid nitrogen cold trap, and intermediate plasma products have been analyzed using FTIR and gas chromatography/mass spectrometry (GC/MS). For example, the plasma fragmentation pattern of methyl methacrylate was studied by Denes et al using GC/MS.[70] Analyzed species trapped directly from the plasma reactor showed 10 distinct fragments from the vapor-phase products and 12 distinct fragments from the liquid-phase products. Analysis of the MS data showed fragmentation products due to de-methylation, de-methoxylation, de-esterification, and de-hydrogenation mechanisms resulting primarily in propyl and propenyl

cations. The quantity of aliphatic components that led to a hydrocarbon-type polymer with significant unsaturation and crosslinking verified that extensive modification of the initial monomer occurred.

Tibbitt et al[71] proposed the structure of PP ethylene using IR absorption spectra and computer analysis. The chains were short and branched, and randomly terminated with frequent crosslinks. The network had no repeating units and contained a number of various functional groups. Trapped free radicals were present, and these caused changes in the film structure upon exposure to the atmosphere.

Polymerization rate must be clearly distinguished from deposition rate because they are often times very different and involve different mechanisms. The deposition rate of a plasma polymer is dependent on more parameters than the polymerization rate. The deposition rate is dependent upon the chemical composition of the substrate, the topography of the substrate, the geometry of the reactor, the reactivity of the monomer, the flow rate, the working gas pressure, the temperature of the substrate, the power, and the frequency of the power source.[72, 73] The substrate temperature is an important parameter to consider when examining deposition rates; the deposition rate decreased with increasing substrate temperature in most studies.[74] Additionally, Lopez and Ratner[75] reported that the chemistry of PP films deposited on substrates at lower temperature more closely resembled the chemistry of the precursor, probably due to reduced fragmentation at reduced temperature. Polymer deposition rate shows a distribution according to substrate position in the reaction chamber because of the heterogeneity of the concentration of active species and monomers in the reaction vessel.

2.5.2 Competitive Ablation and Polymerization

Two types of polymerization processes may occur during plasma processes, plasma-induced polymerization and plasma-state polymerization. Plasma-induced polymerizations occur only with unsaturated monomers and are essentially step-growth polymerizations initiated by the reactive species contained in the plasma. Plasma-state polymerizations are atomic processes that can only occur in a plasma and produce non-polymer-forming byproducts.[30]

When a monomer gas enters the plasma region, it instantly becomes a complex mixture of the original monomer, forming ionized and excited species and fragments, as well as gaseous products that do not participate in the polymerization. When a polymerizable and chemically reactive material is introduced to a plasma, particles can be deposited, ablated, and re-deposited if they collide with a solid surface before they are evacuated. The plasma is constantly in contact with the reactor walls, the solid substrate, and the substrate mount, and polymer-forming intermediates and gas by-products originate from these solids, as well. Within a given monomer–reactor system, the total reactor pressure at constant temperature is a function of only the feed flow rate and the pumping rate. However, once a plasma is initiated, the situation changes dramatically; the pressure becomes a function of the reactions occurring within the plasma. Extending the definition of ablation to include ablation of the solid phase and fragmentation of the gas-phase species, ablation processes contribute to a pressure increase, while plasma polymerization processes contribute to a pressure decrease. In other words, if polymerization processes dominate, a pressure drop is expected when the plasma is ignited; if ablation processes dominate, a pressure increase is expected.

This type of behavior is an example of the Competitive Ablation and Polymerization (CAP) model of plasma polymerization developed by Yasuda and Hsu.[76] An example of this process occurs during the plasma polymerization of carbonyl sulfide and C_2F_4, among others. Deposition rates for these polymerizations increase rapidly, marked by a pressure decrease, until reaching a distinct maximum (in different power regions for different flow rates), and then begin to decrease rapidly. These observations were rationalized as follows: At a low level of energy input, polymerization is dominant, which results in the deposition rate increasing with increasing power. However, above a certain threshold of energy input, ablation processes become significant enough to contribute to the processes of the system. Ablation processes eventually become dominant, and polymer deposition is severely hindered.

Fluorine and oxygen show a significant tendency to induce ablation during plasma processes.[77] Ablation processes occurring during the plasma polymerization of oxygen- or fluorine-containing compounds are generally attributed to the reactive species of these two elements generated during fragmentation.[78] The effect of the ablation process, which continues to increase with increasing power after the deposition plateau, is to decrease the deposition rate. The CAP model is a phenomenological representation of the atomic (fragmentation) type of

deposition that approximates most plasma polymerization processes much better than molecular models based on conventional step-growth polymerization reactions.[79] The CAP model does not apply to all "monomers." Methane in the plasma state, for example, only shows a decrease in pressure due to its low ablation rate.[74]

As an additional illustration of the CAP process, consider the results of an early study by Kay[77] which were later confirmed by Yasuda.[80] Tetrafluoromethane (CF_4) molecules were some of the very few that did not polymerize and deposit thin films on substrates. However, when small amounts of hydrogen were added during plasma polymerization, polymer films were deposited from the plasma. CAP theory explained these results quite well. Taking into account that the F-F bond energy is only 37 kcal/mol, while the energy for H-F is 135 kcal/mol, nearly 100 kcal/mol of stabilization is gained by the reaction of hydrogen with fluorine. Hydrogen, in this instance, behaves as a scavenger of the ablative fluorine species.

Figure 2.5 summarizes the different processes that are competing during plasma polymerization and deposition. Note the many processes in competition that inevitably lead to a very complicated structure being deposited.

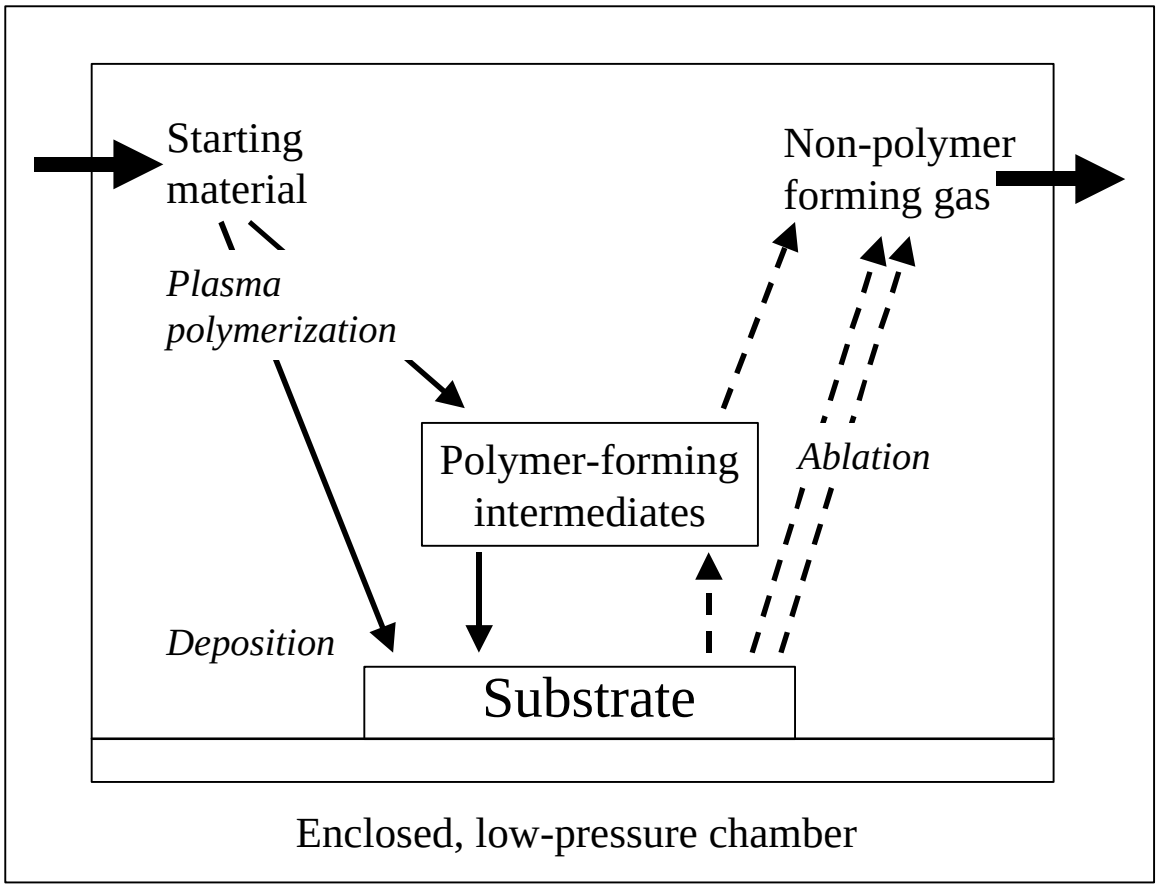

Figure 2.5: Plasma processes occurring during plasma polymerization (adapted from reference 81).

It was mentioned that even when the same monomer is used for plasma polymerization at constant operational conditions (flow rate, discharge power, reaction pressure, etc.), polymers with identical chemical composition are never obtained when a different reactor is used or when substrate position is varied.[54] This is a direct result of the CAP processes that occur. Plasma polymerization processes show intense system dependence, owing to the nature of the polymerization and ablation processes that are occurring simultaneously.

2.5.3 W/FM Parameter

Yasuda demonstrated that to obtain a comparable level of plasma polymerization, an increase in power is needed as the molecular weight is increased.[82, 83] A similar power dependence was noted as the degree of unsaturation of the starting material increased. In

response to these observations, Yasuda[64] introduced a composite parameter (W/FM). W is RF power in Joules/second, F is the monomer flow rate in moles/sec, and M is the molecular weight of the monomer in Kg/mole. This term describes the input energy per unit monomer molecule in J/Kg. It is proportional to the concentration of activated species in the plasma and is very useful in explaining certain plasma polymerization phenomena. Figure 2.6 shows how the polymer deposition rate for most monomers varies with the W/FM parameter.

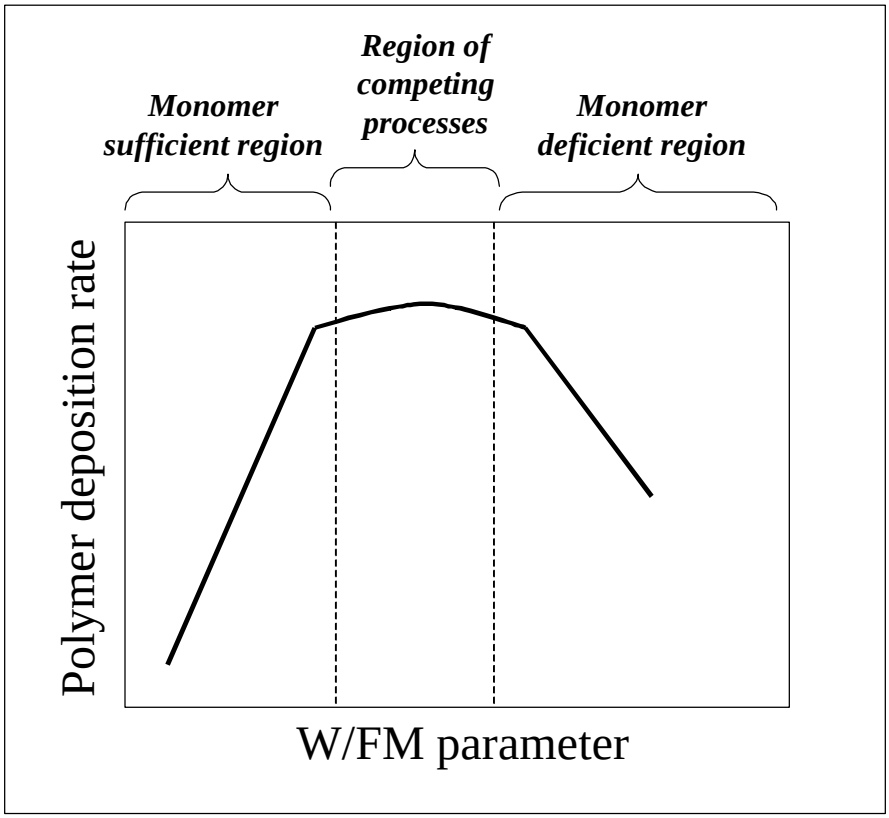

Figure 2.6: The domain of plasma polymer deposition (adapted from reference 86).

Notice in Figure 2.6 that the polymer deposition rate increases at low W/FM values, reaches a maximum, and then decreases at high W/FM values. This trend is well explained by the competitive processes that exist in the reactor at these different power levels. It should be pointed out that in monomer sufficient regions, monomers are subjected to less fragmentation and polymerize with less rearrangement. In the monomer deficient regions, monomer molecules are subjected to heavy fragmentation and plasma polymerization with much greater rearrangement.

W/P yields the energy input per molecule per unit of time, where P is the system pressure. W/F represents the energy input per molecule. In general, a high W/P or W/F results in a higher etching rate while a high W/FM results in an increase in the polymer deposition rate when the W/FM is below some threshold value (the energy deficient region). The deposition rate levels off or decreases when the W/FM exceeds the threshold value in the monomer deficient region.[30, 64]

2.5.4 Atomic Interfacial Mixing and Adhesion

Through competitive ablation and polymerization processes, the activated substrate surface is ablated during deposition while the polymerizable species in the plasma are deposited onto the substrate surface. This concurrent exchange of material allows the activated species of the plasma to form intimate secondary bonds with the bare substrate or its oxide. PP films adhere strongly to substrates because of the highly energetic interactions that occur within a plasma during the process of film deposition. It is not believed that covalent linkages are formed between the carbon atoms of the plasma polymer and the metal. Instead, adhesion is thought to occur as a result of the increased interactions of the atoms caused by the interpenetrating atomic arrangement.[64] The adhesion of these films to various substrates is explained by the concept of Atomic Interfacial Mixing (AIM) proposed by Yasuda et al[84] in 1982.

The AIM principle states that a high degree of inter-diffusion occurs between impinging atoms of the plasma polymer-forming species and the substrate. Atomic interfacial mixing greatly modifies the surface chemistry of the substrate and occurs over more than just a few monolayers.

2.5.5 Monomer Adsorption Effects

There has been some argument regarding non-reacted monomer adsorption onto the substrate surface prior to plasma polymerization. This stems from the experimental reality that the initial monomer flow rate is usually reached by reducing the flow before initiating the

plasma. The two basic types of gas adsorption, physical adsorption (due to van der Waals forces) and chemisorption, have approximate adsorption energies of 0.1 eV and 1 eV, respectively.[74]

Yasuda and Wang[85] suggested that adsorption of non-activated monomer is unlikely, while Biederman and Osada[74] argued that for certain substrates and under certain conditions, a monolayer of monomer can be adsorbed on the substrate even at room temperature. The latter researchers believe that the adsorbed monomers are activated once the plasma is ignited, and the existence of these partially grown reactive sites enhances chemical bonding and film growth. The idea of monomer adsorption occurring on a freshly deposited PP film seems more likely, due to the activated species that remain after deposition. Both of these effects may have important contributions to the overall bond strength of a system using this type of pretreatment process.

2.6 Film Properties

Plasma polymers are distinguished in chemical composition from conventional polymers by the absence of repeating monomer units. The polymer is instead composed of complicated units containing crosslinks and moieties fragmented or rearranged from the original monomers.[86] In many instances, polymer films produced from plasma processes possess superior chemical and physical properties compared to conventionally polymerized material. [80, 87, 88, 89] Unlike conventional polymers, PP films have short segments between cross-links and have very limited long-range molecular mobility. The tighter networks that can be formed from plasma polymerizations are characterized by the absence of rotational mobility of molecules at the surface.[90]

Researchers documented three regions in thin films of PP hexamethyldisiloxane (HMDS): an oxidized surface region (approximately 25 to 75 Å thick) with a composition resembling that of polydialkylsiloxane; a bulk region with a composition close to that of the monomer; and an interfacial region which clearly showed the presence of the substrate oxide layer. At the beginning stages of plasma polymerization, AIM and sputtering of the metal or its oxide modify the composition and structure of the film, which results in region 3 (the interfacial region).[34] Region 1 is quite different from the bulk of the film because of exposure to the atmosphere.[91] As mentioned previously, PP materials usually oxidize rapidly in the atmosphere

because of the high concentrations of free spins remaining in their structures after the plasma treatment.[87, 92, 93] Regions similar to these are expected to exist within PP films deposited as primers in this study.

2.6.1 Film Adhesion

Plasma polymer to metal coupling is most likely due to secondary forces, such as dispersion forces and hydrogen bonding, rather than primary chemical bonds.[74] Adhesion of PP films has been related to the internal stresses in the film. For most films deposited in a vacuum, the polymer is in a state of stress consisting of two components: the thermal stress caused by the differences in thermal expansion of the film and the substrate, and the intrinsic stress caused by the disordered structure of the films.[74] Residual stresses (compressive or tensile) are detrimental to the stability of thin films.[94, 95] The intrinsic stress is specifically a result of the atoms, functional groups, and other fragments being in a configuration that does not correspond to an energetic minimum. In contrast, evaporated films usually posses tensile stresses only (the films want to contract). Overall, a basic understanding of the relaxation kinetics of unstable ultra-thin amorphous carbon films is rather limited.[95]

Although only limited amounts of data are available, Yasuda[60] reported that there are two major trends regarding internal stresses: the slower the deposition of the PP film, the larger is the internal stress; and the overall force acting at the interface of the PP film and the substrate is proportional to the thickness of the film. Films with a minimal thickness for complete surface coverage tend to adhere better to substrates than thick films. Ross[96] reported that 155 Å is required to obtain complete coverage of a metal surface in a capacitively coupled bell jar reactor. The internal stresses within PP films begin to accumulate with film thickness, and this can cause buckling and curling of the film. PP films deposited on a rigid substrate should therefore be less than 1 μm thick to avoid poor mechanical properties and poor adhesion to the substrate.[64]

Finally, tighter networks of the PP films result in higher internal stresses, and poor adhesion and barrier properties of PP films are often due to the deposition of a PP film that is too thick. Yasuda et al[84] found that PP films adhere more strongly to a substrate when W/FM values are high. They determined that film deposition should be conducted at a W/FM value larger than

10^{10} J/kg to achieve good adhesion between PP methane and platinum. Higher crosslink density and a larger extent of AIM are cited as reasons for the better adhesion characteristics of films deposited at higher W/FM values.

2.6.2 Aging and Degradation

X-ray photoelectron spectroscopy (XPS) studies of *in situ* plasma modified polymer surfaces have shown that aging of PP films exposed to the atmosphere occurs in two distinct phases. The initial phase, which occurs very rapidly, involves adsorption of atmospheric contaminants, and in some cases, specific chemical reactions (i.e. oxidation or reduction). The second phase, which occurs much more slowly, involves the reorganization of the plasma treated surface.[97]

Free radicals make up approximately 20 % of the species generated in an RF plasma, and are therefore a major constituent.[74] In many cases, a large number of free radicals remain trapped in the film and cannot recombine rapidly. Monomers with triple bonds and cyclic structures tend to yield polymers with the highest concentration of free radicals.[64] The existing free radicals can react with water vapor and oxygen, or they can recombine. These processes lead to a gradual rearrangement of the plasma polymer network and are sometimes described as aging. PP film changes with time have been documented as increases in dielectric losses by two separate research groups.[98, 99]

Lu et al[95] investigated the chemical stability of amorphous carbon films (100 - 700 Å thick) deposited on Si(100) substrates by radio frequency sputtering. Only subtle changes in the surface topography, microstructure, composition, and nanomechanical properties of the amorphous carbon films were observed after aging in ambient conditions for approximately 2 years. For one particular sample, XPS measurements showed the atomic concentration of carbon, oxygen and nitrogen changed from 89.7 %, 7.4 %, 0.9 %, respectively, to 87.9 %, 8.4 %, and 1.5 %, respectively. The hardness and modulus of the films, as determined by AFM nanoindentation measurements, remained constant within standard deviations. This suggests that changes in the PP films occur fairly quickly after deposition, and that the films are stable after these initial changes.

2.7 PP Films as Adhesion Promoters

Tsai *et al*[100] developed plasma etching and plasma polymerization as cleaning, pretreatment, and adhesion-promoting technologies for steel strips and wires. A tubular reactor was used to deposit thin films on steel substrates using an RF generator. They used XPS, RAIR, AES, and ToF-SIMS techniques to characterize the films. ToF-SIMS was a particularly powerful characterization technique for these films because of its ability to detect aromaticity and crosslinking.[101] They found that PP films of simple hydrocarbons have many potential applications where corrosion protection or the coating of metals is important. The films produced were quite different in structure than those obtained by conventional polymerizations of the same monomers. The PP films had very different properties, including outstanding adhesion and thermal stability. The researchers determined that the concentration of oxygen at the acetylene film/steel substrate interface was lower than for PP ethylene or ethane, indicating a reduction of the oxide had occurred during acetylene deposition. As expected, each of the PP films (ethane, ethylene, and acetylene) contained significant amounts of unsaturation and aromatic functional groups. The PP films of acetylene contained the largest amount of unsaturation. The interfacial bond strength of PP acetylene to natural rubber was stronger than the cohesive strength of the natural rubber, with a 100 % cohesive failure occurring in single lap joints. They also demonstrated that the durability of rubber to steel/acetylene films was very promising; these bonds resisted exposure to steam.[102]

Further investigation into the use of PP primers for rubber-to-metal bonding by Tsai et al[103] also yielded favorable results; PP acetylene films were excellent primers for rubber-to-steel bonding. Thin (750 Å) PP films of acetylene were deposited onto polished steel substrates in an inductively coupled RF reactor, and rubber was used as the "adhesive." Miniature single lap shear joints prepared with PP acetylene out-performed brass control samples, giving 100 % cohesive failure in the rubber. Using a model rubber system consisting of squalene and other natural rubber components, sulfur diffused through the primer to form a layer of sulfide at the primer/substrate interface. Crosslinking, and therefore adhesion, between squalene and the

plasma polymer was due to the reaction between sulfur and the accelerator dicyclohexylbenzothiazole sulfenamide (DCBS) to form perthiomercaptides.

Iriyama et al[104] used PP films of tetraethoxysilane on aluminum granules for corrosion inhibition. They found that these PP films, which were highly crosslinked, had good adhesion to the metal and served as good corrosion resistant coatings. In addition to the corrosion resistant properties of PP films, Taylor *et al*[72] developed PP HMDS films for use as a corrosion inhibiting primer in the adhesive bonding of aluminum. More recently, excellent durability results have been obtained for single lap joints made from aluminum substrates with PP HMDS formed after an initial argon plasma etch.[72] Specimens were loaded in tension at 20 % of their ultimate tensile strength and were then exposed to a cyclically varying corrosive environment until failure occurred. These lap joint specimens usually failed due to corrosion of the substrate; they did not fail due to debonding between the PP film and the adhesive.

Turner et al[105] pretreated aluminum substrates with thin PP films and studied the durability of aluminum/epoxy adhesive joints. Substrates were treated using a plasma etch and coated with a thin PP film of trimethylsilane or HMDS. Wedge testing was conducted in a controlled temperature and humidity chamber at 60° C and 95 % relative humidity. Both direct current and microwave plasma generators were used, and the durability of wedge specimens using this pretreatment process was good compared to phosphoric acid anodized samples.

Arnold et al[106] studied the effects of various pretreatments on Ti-6Al-4V bonded with a thermosetting modified epoxy (AF163-2k). They found that a sol/gel treatment developed by Boeing yielded SLS strengths greater than chromic acid anodized and Turco 5578 (a non-alkaline etch cleaner) treated titanium. Floating roller peel tests showed that sol/gel treatments outperformed other pretreatments in a variety of environmental conditions (room temperature dry, room temperature wet, and hot/dry conditions). These results are important because under certain conditions, PP films of metal alkoxides (i.e. titanium(IV) isopropoxide or titanium(IV) isobutoxide) exhibit sol/gel film characteristics. Sol/gel pretreatments can be tedious processes; in some cases a minimum of 24 hours was needed to promote tackiness before curing the sol/gel.[107] Sol/gel-like films that are produced via the plasma polymerization of a metal alkoxide could yield all of the benefits of a sol/gel thin film from a rapid, efficient plasma polymerization process.

Kagami et al[108] were interested in the electrical properties of PP titanium(IV) isopropoxide. By exposing the substrates directly to the plasma, carbon content in the PP films increased compared to studies by Frenck et al.[109, 110] Kagami et al[108] determined from XPS that the surface of the thin films was composed of $TiC_{1.21}O_{1.72}$, while the bulk composition was $TiC_{0.56}O_{1.55}$. XPS indicated that the organic matrix consisted of mainly $(CH_2)_n$ groups, both at the surface and in the bulk, although a weak peak corresponding to TiC was observed in the bulk. Transmission electron microscopy (TEM) photographs suggested that a continuous network of metal clusters approximately 15 to 25 nm in diameter was present in a polymer matrix. The as-deposited films showed no crystalline structure. Kagami and coworkers found that the presence of excess titanium or oxygen atoms, along with the presence of organic compounds among the lattice, gave rise to unfilled bonds and additional dangling bonds that were a source of electron traps. It is this type of PP organo-metallic film that may be valuable for enhanced adhesive bonding.

For a more exhaustive listing and description of other PP film applications, see excellent reviews by Shi[59, 111] and Biederman[112].

2.8 The System

The adhesively bonded system studied for this thesis consisted of Ti-6Al-4V alloy and a high temperature thermosetting polyimide adhesive (FM-5). The glass-supported adhesive was predominantly the low molecular weight polymer LaRC-PETI-5 (see Figure 2.7). This system is of interest because it is being considered for application in the assembly of high-speed aircraft structures. Ti-6Al-4V is the most widely used of all titanium alloys, since it can be heat-treated to differing strength levels, is weldable, and is relatively easy to machine.[36] Additionally, titanium alloys are attractive materials for aerospace structures because of their high strength to weight ratio and their retention of structural integrity at high temperatures (up to 700° C). FM-5 is radiation resistant and possesses excellent mechanical properties. It has also displayed good chemical resistance to organic solvents and other aircraft fluids, such as jet fuel and hydraulic fluid.[45]

The phenyl acetylene end cap is the active cure site for FM-5, and accordingly, it is of interest to create functional groups on a substrate's surface that will cross-link with the acetylene groups on the adhesive. Thus, a certain degree of unsaturation is desirable in the PP film on the titanium surface. During the curing process, crosslinking of the adhesive occurs with itself, and could also occur with any unsaturated groups within the PP film wetted by the adhesive. The plasma polymerization of acetylene by a mechanism analogous to free radical, chain growth polymerization can result in the incorporation of alkene and alkyne groups into the polymer film.[61, 100, 113] In theory, double and triple bonds of PP acetylene could cross-link with the end caps on the adhesive. If the adhesion between the PP acetylene film and the substrate is adequate, this should lead to improved adhesion and durability.

A better primer may be developed by creating a gradient between the titanium alloy and the adhesive through a PP "sol/gel-like" film. Traditional sol/gel processes of metal alkoxides allow for the low temperature synthesis of high purity ceramic-type materials.[107] The polycondensation of metal alkoxides with H_2O results in three-dimensional mixed metal oxide/hydroxide/alkoxide clusters.[114] PP films from titanium complexes may be able to take advantage of the reactive phenyl acetylene end-groups of FM-5 and form covalent linkages across the interphase as evidenced by Inagaki et al.[115] They used a capacitively coupled (13.56 MHz) bell jar reactor to plasma polymerize sublimated titanium acetylacetonate [$TiO(C_5H_7O_2)_2$] at low pressures for use as CO gas sensor devices. They presented FTIR evidence that indicated the presence of non-complexing C=C and C=O groups within the film. Such unsaturation will allow crosslinking to occur with FM-5, providing strong covalent linkages for better joint performance. Furthermore, if a sufficient amount of unsaturation cannot be generated, PP organo-metallics should enhance adhesive performance by creating a gradient from the titanium alloy to the polyimide adhesive. There is ample evidence that some films of PP titanium(IV) isopropoxide are organic/inorganic hybrids in which metal clusters reside in a polymer matrix.[115]

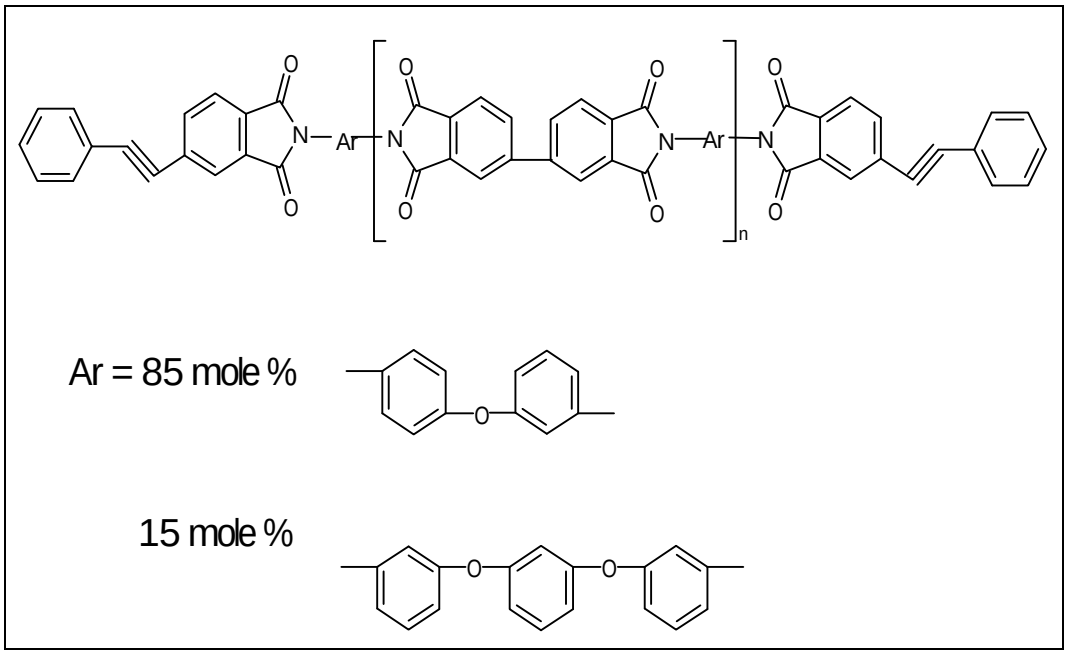

Figure 2.7: The main constituent of FM-5 adhesive, LaRC PETI-5.

2.9 Single Lap Shear Joints

Single lap shear joints were prepared and tested to evaluate adhesion and to compare the effect of substrate pretreatment on joint performance. The true shear strength, which can only be determined if normal (perpendicular) stresses are entirely absent, cannot be easily determined by testing SLS specimens. Many factors affect the apparent shear strength of a specimen, including tensile, peel, and compressive stresses. In fact, the failure of a typical SLS specimen is usually controlled by the peak tensile stresses in the adhesive, not by the average shear stress.[116] The factors that contribute to the tensile stresses include the size and shape of the specimen, the adherend properties, the adhesive properties, the thickness of the adhesive, the area of overlap, and the internal stresses or flaws within the adhesive. Stress concentrations are also present: Goland and Reissner[117] have shown that normal and shear stress concentration factors increase toward the ends of the overlap. Modern finite element analysis has also confirmed this finding.[116] Thus, the strength of a SLS specimen is regarded as the average shear stress that exists when the combined stress concentrations reach a critical level and the joint fails.

Figure 2.8 shows a typical single lap shear (SLS) joint, where *l* is length of overlap and P is representative of the force applied to the joint. Figure 2.9 shows a close-up of the SLS joint and Table 2.4 lists the variables that are important when considering how the joint is stressed.

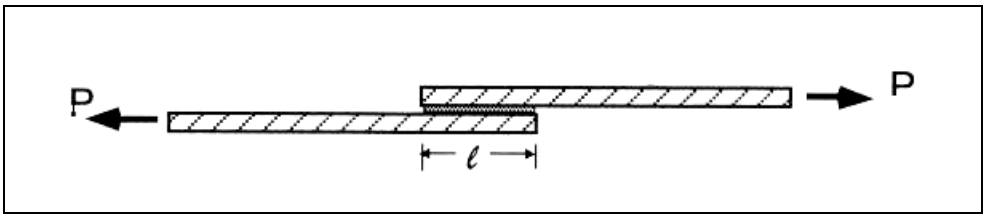

Figure 2.8: Single lap shear joint.

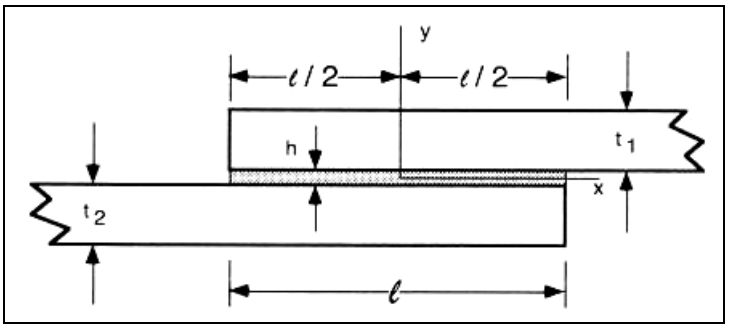

Figure 2.9: The variables of the single lap shear joint.

Table 2.4: Single lap shear joint notation.

Symbol	Description
h	adhesive thickness
t	adherend thickness
E	Young's modulus of adherends
G	Shear modulus of adhesive
l	length of overlap
P	Force per unit width

The SLS specimens prepared and tested in this study were smaller than those recommended by ASTM standard # D 1002-94 because of the space limitations of the plasma reactor. For short SLS specimens, the adherends are usually stronger than the adhesive joint, which tends to drive failure to occur within the adhesive. If the adhesive is somewhat compliant, plastic flow can occur when the stress in the adhesive exceeds the elastic limit. In addition, elastic deformation may occur throughout the adhesive layer at failure.[118] Conclusions about the

fatigue resistance of a system based on the results of short SLS specimens should therefore be avoided.

A final consideration involves the change in volume of the polymer adhesive during the cure cycle. When a crosslinkable polymer is cured, it shrinks volumetrically because of crosslinking. When bonding two adherends with a crosslinkable adhesive, the shrinkage is restrained by the substrates, and this causes internal stresses to arise within the adhesive. The internal stresses affect the adhesive's resistance to an externally applied stress, and may reduce the SLS strength.[119]

2.10 Analytical Techniques

2.10.1 X-ray Photoelectron Spectroscopy

XPS has evolved into a powerful surface analysis technique in the last twenty years and is arguably the most popular surface analysis technique because of the excellent qualitative and quantitative elemental analysis it provides. In 1967, it was established that energy analyzed electrons, photo-emitted during the irradiation of a solid sample by monochromatic x-rays, exhibited sharp peaks corresponding to the binding energy of core-level electrons.[120] These binding energies can be used to identify the chemical constituents of materials to a depth of 50 Å, and can distinguish between oxidation states of the elements analyzed.[121]

When a surface is bombarded with mono-energetic radiation ($h\nu$) of sufficient energy in a vacuum, photons are absorbed by surface atoms and each absorption event results in the prompt emission of an electron.[122] Because energy is conserved, the kinetic energy of the emitted electron plus the energy required to remove it from its orbital must equal the x-ray energy. The kinetic energy of emitted electrons can be measured with an electron spectrometer, the x-ray energy is known, and the binding energy of the electron can be obtained from the following relationship:

$$E_b = hn - KE + j_s \qquad \textbf{Equation 2.1}$$

where E_b is the binding energy of the emitted electron, $h\nu$ is the x-ray energy, KE is the kinetic energy of the ejected electron, and j_s is the work function of the spectrometer.[122]

Each element has a unique atomic structure, and thus binding energies for core electrons are distinct and readily identified using XPS. The oxidation states of an element can also be distinguished because of the different electrostatic environments surrounding electrons bound to different atoms. For example, carbon in a very electronegative environment (i.e. an ester carboxyl group) will eject a 1s electron that appears at a higher binding energy than a carbon in a less electronegative environment (i.e. an aliphatic group). Generally, the electrons of atoms with highly electronegative substituent groups exhibit higher binding energies than the same atoms bound to groups with lower electronegativity.[122]

2.10.2 Auger Electron Spectroscopy

Auger electron spectroscopy (AES) is another widely used high-vacuum analytical technique for discerning the chemical composition of a solid surface. The technique features the ability to detect all elements above helium, rapid data acquisition, and a high sensitivity for analysis of the top 50 Å of a surface.[123] AES can also be used in conjunction with inert gas ion sputtering of a surface to obtain information about the composition of a sample as a function of depth. [124] This is called depth profiling, and it was used extensively in this study.

One way secondary (Auger) electrons are emitted is via the bombardment of a sample by an incident electron beam (2 or 3 kV). The electrons are then collected and analyzed according to their energy by an electron spectrometer. Core electrons are initially ionized by interaction with an incident electron beam, and this vacancy is immediately filled by another electron (i.e., an L_1 to K transition). The energy released from this transition (i.e., E_K - E_{L1}) can be in the form of x-rays, or it can be transferred to another electron (i.e., in the L_2), which is then ejected from the atom as an Auger electron. The measured energy of the ejected electron (E_A) is given by:

$$E_A = E_K - E_{L_1} - E_{L_2} - j_A \qquad \textbf{Equation 2.2}$$

The work function of the spectrometer is given by φ_A. In the example given above, the Auger ejection process would be termed "the KL_1L_2 Auger transition." The Auger electrons appear as

small peaks in the total energy distribution function N(E). Each element has characteristic Auger electron energies that are independent of the incident electron beam energies.[123]

2.10.3 Scanning Electron Microscopy

Scanning electron microscopy (SEM) is a very versatile technique employed for the examination and analysis of the microstructural characteristics of solid objects. SEM is capable of high resolution (values of the order of 10 nm), and its greater depth of focus allows more three-dimensional information to be gathered than optical microscopy.[125] The technique uses a rastered electron beam (typically 2 to 30kV) to strike a solid sample and cause secondary electrons, back-scattered electrons, x-rays and Auger electrons to be emitted. The intensities of the emitted secondary electrons vary with topography and may be detected and displayed using a cathode ray tube screen, producing a detailed image of the surface.[124]

2.10.4 Contact Angle Analysis

Wettability, which is the ability of a liquid to spread over a solid, has large implications for adhesion. Liquids will spread onto solids of higher surface energy because the overall surface energy of the system is minimized when the solid is covered by the lower surface energy liquid.[126] The intimate contact required between a substrate and an adhesive for good adhesion demand that the adhesive wet the substrate well. The wettability and surface energies of substrates are monitored using contact angle measurements. Contact angles, as measured by a goniometer or some other means, are lower for more wettable surfaces, reaching a lower limit of zero degrees for complete wetting. Decreases in contact angle often correlate with an increase in adhesion, and for this reason, wettability has been used as an indicator of adhesion.[127]

The surface free energies of a solid cannot be measured directly, but the surface free energies of low surface energy solids can be indirectly estimated by contact angle measurements. The contact angle (θ_{ls}) of a liquid (*l*) on a solid (*s*) is given by the Young equation:

$$Cosq = \frac{g_{sv} - g_{sl}}{g_{lv}}$$ **Equation 2.3**

where γ_{sv} is the surface free energy of the solid in equilibrium with the saturated vapor of the liquid, γ_{lv} is the surface tension of the liquid in equilibrium with the solid, and γ_{sl} is the solid-liquid interfacial free energy (see Figure 2.10).[128]

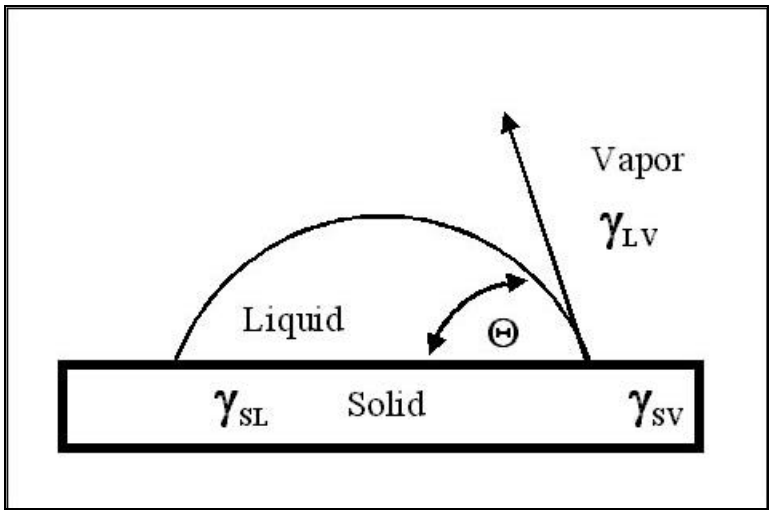

Figure 2.10: Contact angle variables.

Note that surface roughness is neglected in Equation 2.3, so it is important only to compare results from samples of similar roughness. Equation 2.3 holds only provided that:

$$g_{sv} - g_{sl} \leq g_{lv}$$ **Equation 2.4**

The contact angle concept is important not only because it can yield surface energies, but because it gives a definition to the notion of wettability. A non-spreading liquid, for example, means that $\theta_{ls} \neq 0$, while a liquid that wets a solid completely is assigned $\theta_{ls} = 0$. Early experiments showed that every liquid wets every solid to some extent, so that $\theta_{ls} \neq 180$.[129] From the Young equation, Dupre[130] introduced the reversible work of adhesion of liquid and solid, W_A, in the form of the following equation:

$$W_A = g_{sv} + g_{lv} - g_{sl}$$ **Equation 2.5**

This thermodynamic expression simply says that the work of separating liquid and solid phases must be equal to the change in free energy of the system.

2.10.5 Atomic Force Microscopy/Nanoindentation and Nanoscratch Tests

A high-resolution nanomechanical test instrument is capable of performing both indentation and scratch testing. When mounted to an Atomic Force Microscope (AFM), it can also provide *in situ* images. In the indentation mode, the instrument is a load-controlled displacement-sensing device. An indenter tip is driven into a sample using forces varying from 15 - 300 μN, and is then withdrawn by decreasing the applied force. The applied load (P) and depth of penetration (h) into the sample are continuously monitored. A load vs. depth curve can then be generated from the collected data. Figure 2.11 shows a load vs. depth curve in which the load is increased at a constant rate to some peak value (loading), held at that value for a set amount of time, and then decreased to zero (unloading) at the same rate as loading. The sample hardness (H) and reduced elastic modulus (E_r) can then be calculated from the curve. If the loading and unloading curves were identical, this would indicate pure elastic deformation, and no indent would be visible after the test.[131]

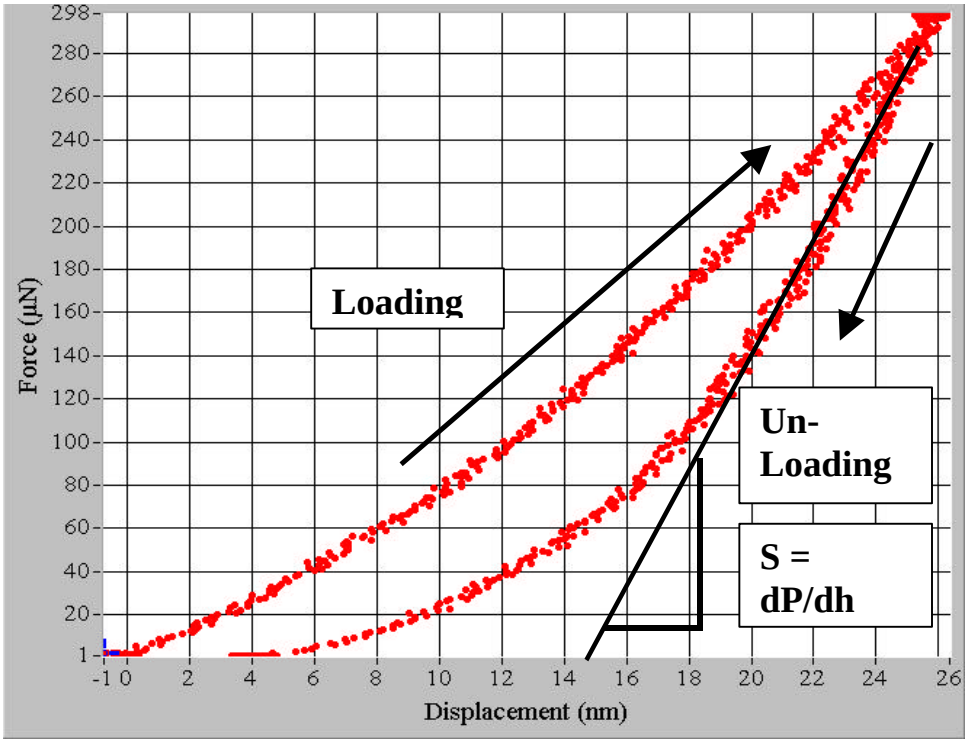

Figure 2.11: An example of a load vs. depth curve of fused silica provided by Hysitron.

The reduced modulus is defined by the following equation:[132]

$$E_r = S\frac{\sqrt{p}}{2\sqrt{A}} \qquad \textbf{Equation 2.6}$$

where S, defined as the unloading stiffness, is the initial derivative of force with respect to depth during the initial unloading $\left(\frac{dP}{dh}\right)$. A is the projected contact area and is determined by indenting a known sample and iteratively fitting the results. The reduced modulus is related to the modulus of elasticity (E) through the following equation:[132]

$$\frac{1}{E_r} = \frac{\left(1-n_1^2\right)}{E_1} + \frac{\left(1-n_2^2\right)}{E_2} \qquad \textbf{Equation 2.7}$$

where the subscript 1 corresponds to the indenter material, the subscript 2 refers to the indented material, and ν is Poisson's ratio. For the diamond indentor tip used, E_1 was 1140 GPa and ν_1 was 0.07. Poisson's ratio varies between 0 and $1/2$ for most materials.

The unloading stiffness (S) is calculated by fitting the unloading curve to the power law relation using the approach taken by Oliver and Pharr:[132]

$$P = A(h-h_f)^m \qquad \textbf{Equation 2.8}$$

where A, h_f, and m are determined by a least squares fitting parameter. The stiffness can be calculated from the derivative of the preceding equation

$$S = \frac{dP}{dh}(h_{\max}) = mA(h_{\max}-h_f)^{m-1} \qquad \textbf{Equation 2.9}$$

The hardness is defined by the ratio of the maximum load to the projected contact area

$$H = \frac{P_{\max}}{A} \qquad \textbf{Equation 2.10}$$

The contact area is determined from a tip calibration function $A(h_c)$ where h_c, the contact depth, is found by using the equation

$$h_c = h_{\max} - e\frac{P_{\max}}{S}. \qquad \textbf{Equation 2.11}$$

This approach is based on a simple empirical method developed by Doerner and Nix.[133] They extrapolated the initial linear portion of the unloading curve to zero load, then used the extrapolated depth with the indenter shape function to determine contact area. Tedious experiments with one particular material, METGLAS® 2826, confirmed that this extrapolated depth gives a better estimate of the contact area than either the depth at peak load or the final depth. This observation was later confirmed with finite element simulations.[134]

To account for edge effects, the deflection of the surface at the contact perimeter is estimated by taking the geometric constant ε as 0.72 for a Berkovich diamond. An image of the deformed surface can also be generated immediately before and after the indentation and scratch when the instrument is mounted to an AFM.

The modulus and hardness of PP films can be accurately measured through AFM by using a diamond tip mounted to a metal foil cantilever as described above.[135] Additionally, the adhesion of a PP film to a substrate can be evaluated by comparing force-displacement curves recorded during a scratch. A characteristic critical load at debond can be obtained by noting the discontinuity that occurs in the force-displacement curve when a film debonds from a surface. This critical load at debond is a reliable empirical measure of the adhesive strength of a thin film to a substrate.[136]

The adhesion of PP films to various substrates was evaluated by comparing force-displacement curves recorded during a scratch. A characteristic critical load at debond was obtained by noting the discontinuity that occurred in the force-displacement curve when the film debonded from a surface. This critical load at debond is a reliable empirical measure of the adhesive strength of the film.[136] Figure 2.12 shows a schematic of film failure during a nanoscratch test. There are compressive stresses in front of the diamond tip, tensile stresses behind the diamond tip, and bending stresses at the rim of the unaffected material/deformed region.[137] Typically, delamination at the interface between a film and the substrate occurs in the region ahead of the indenter, where the compressive stresses are present.[138]

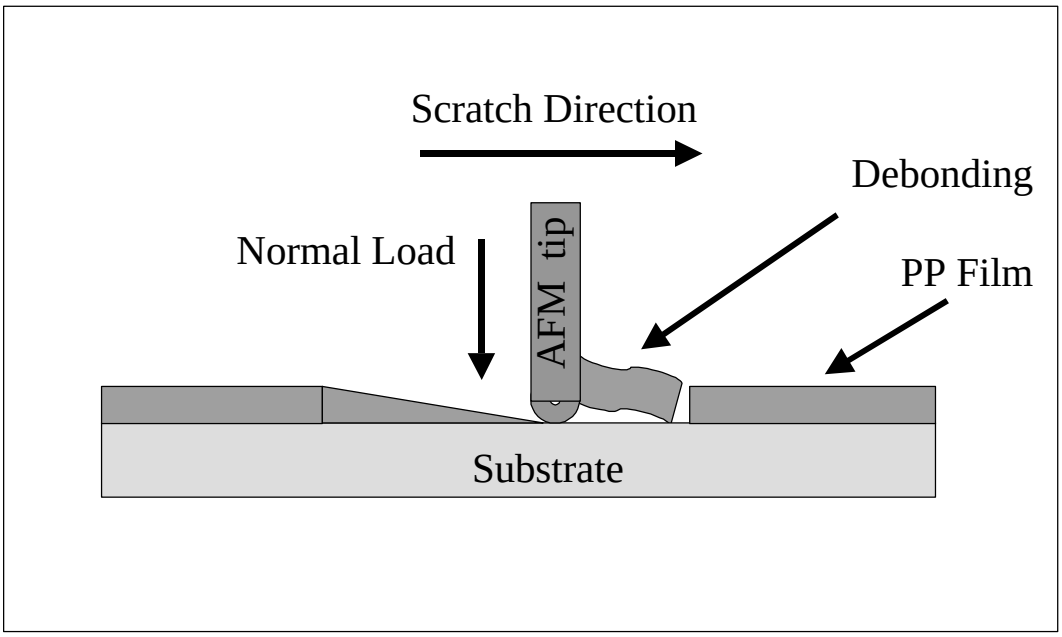

Figure 2.12: Schematic of failure mechanism during scratch tests (adapted from reference 139).

2.11 References

[1] *Handbook of Adhesives, 3rd ed.*; I. Skeist, Ed.; Chapman and Hall: New York, NY, 1990, Chapter 1.
[2] A.J. Kinloch in *Durability of Structural Adhesives*; A. J. Kinloch, Ed.; Applied Science Publishers: London, 1983, Chapter 1.
[3] B.O. Bateup *Int. J. Adhes. and Adhes.* **1981**, *1*, 233.
[4] A.J. Kinloch *J. Mater. Sci.* **1980**, *15*, 2141.
[5] S.S. Voyutski; V.L. Vakula *J. Appl. Polym. Sci.* **1963**, *7*, 475.
[6] S.S. Voyutski *Autohesion and Adhesion of High Polymers*; Wiley and Sons: New York, NY, 1963, Chapter 1.
[7] A.J. Kinloch *Adhesion and Adhesives, Science and Technology*; Chapman and Hall: New York, NY, 1987, Chapter 1.
[8] E.M. Boroff; W.C. Wake *Trans. Institute of the Rubber Industry* **1949**, *25*, 190.
[9] D.E. Packham; K. Bright; B.W. Malpass *J. Appl. Polym. Sci.* **1974**, *18*, 3237.
[10] J.D. Venables *J. Mat. Sci.* **1984**, *19*, 2431.
[11] J.R. Huntsberger In *Treatise on Adhesion and Adhesives*, Vol. 1; R.L. Patrick, Ed.; Marcel Dekker: New York, NY, 1967, p. 119.
[12] A.J. Kinloch *Adhesion and Adhesives, Science and Technology*; Chapman and Hall: New York, NY, 1987, Chapter 3.
[13] L. Pauling *The Nature of the Chemical Bond*; Cornell University Press: Ithaca, NY, 1960.
[14] R.J. Good In *Treatise on Adhesion and Adhesives*, Vol. 1; R. L. Patrick, Ed.; Marcel Dekker: New York, NY, 1967, p. 15.

[15] E.M. Liston; L. Martinu; M.R. Wertheimer In *Plasma Surface Modification of Polymers*, M. Strobel, C. Lyons and K.L. Mittal, Eds; VSP: The Netherlands, 1994, Chapter 1.
[16] J.M. Burkstrand *J. Vac. Sci. Technol.* **1978**, *15*, 223.
[17] N.J. Chou; C.H. Tang *J. Vac. Sci. Technol.* **1984**, A2, 751.
[18] N. Inagaki; S. Tasaka; K. Hibi *J. Adhes. Sci. Technol.* **1994**, *8*, 395.
[19] J.M. Burkstrand *Phys. Rev. B* **1979**, *20*, 4853.
[20] F.M. Fowkes *J. Adhes. Sci. Technol.* **1987,** *1*, 7.
[21] F.K. McTaggart *Plasma Chemistry in Electrical Discharges*; Elsevier Publishing Co.: London, 1967, Chapter 4.
[22] L.H. Sharpe *J. Adhes.* **1972**, *4*, 5.
[23] L.H. Lee *J. Adhes.* **1994**, *46*, 15.
[24] H. Leidheiser Jr.; P.D. Deck *Science* **1988**, *241*, 1176.
[25] C.U. Ko; E. Balcells; T.C. Ward; J.P. Wightman *J. Adhes.* **1989**, *28*, 247.
[26] J.D. Miller; H. Ishinda in *Fundamentals of Adhesion*; L.H. Lee, Ed.; Plenum Press: New York, NY, 1991; Chapter 10.
[27] D.H. Buckley *Surface Effects in Adhesion, Friction, Wear, and Lubrication*; Elsevier Scientific: New York, NY, 1981; Chapter 2.
[28] T.E. Fischer; S.R. Keleman *Surf. Sci.* **1977**, *69*, 1.
[29] I.C. Sanchez in *Physics of Polymer Surfaces and Interface;* I.C. Sanchez, Ed; Butterwoth-Heinemann: Boston, 1992; Chapter 4.
[30] C.M. Reddy, Ph.D. Thesis, University of Missouri-Columbia, December 1998, Chapter 2.
[31] D.M. Mattox *Vacuum Technology and Coating* **2000**, *1*, 28.
[32] D.M. Brewis; D. Briggs *Polymer* **1981**, *22*, 7.
[33] H. Biederman; L. Holland; J. Nedbal *Thin Solid Films* **1977**, *41*, 329.
[34] W.J. van Ooij; F.J. Boerio; A. Sabata; D.B. Zeik; C.E. Taylor; S.J. Clarson *J. Test. Eval.* **1995**, *23*, 33.
[35] H.M. Clearfield; D. K. McNamara; G. D. Davis In *Adhesive Bonding*; L. Lee, Ed.; Plenum Press: New York, NY, 1991, Chapter 8.
[36] G.W. Critchlow; D.M. Brewis *Int. J. Adhes. and Adhes.* **1995**, *15*, 161.
[37] A. Mahoon In *Durability of Structural Adhesives;* A. J. Kinloch, Ed.; Applied Science Publishers: London, 1983; p. 255.
[38] S.R. Brown in *Proc. 27th Natl. SAMPE Symp.*; SAMPE: Azusa, CA, 1982, p. 363.
[39] R.F. Wegman; D.W. Levi in *Proc. 27th Natl. SAMPE Symp.*; SAMPE: Azusa, CA, 1982, p. 442.
[40] S.L. Kaplan; P.W. Rose *Int. J. Adhes. and Adhes.* **1991,** *11*, 109.
[41] J.A. Filbey; J.P. Wightman *J. Adhes.* **1989**, *28*, 1.
[42] J.A. Filbey; J.P. Wightman *J. Adhes.* **1987**, *20*, 283.
[43] H.M. Clearfield; D.K. Shaffer; S.L. Vandoren; J.S. Ahearn *J. Adhes.* **1989**, *29*, 81.
[44] C.W. Jennings *J. Adhes.* **1972,** *4*, 155.
[45] H. Parvatareddy, Ph.D. Thesis, Virginia Tech, November 1997; Chapter 2.
[46] D.F O'kane; K.L. Mittal *J. Vac. Sci. Technol.* **1974**, *11*, 567.
[47] H.K. Yasuda, *Plasma Polymerization*; Academic Press: Orlando, FL, 1985, Chapter 2.
[48] H. Suhr "Applications of Non-equilibrium Plasmas to Organic Chemistry" in *Techniques and Applications of Plasma Chemistry Polymers*; J.R. Hollahan and A.T. Bell, Eds.; Wiley and Sons, New York, NY, 1974.

[49] M.A. Lieberman; A.J. Lichtenberg *Principles of Plasma Discharges and Materials Processing*; John Wiley and Sons, Inc.: New York, NY, 1994, Chapter 12.
[50] Y.M. Tsai; F.J. Boerio *J. Appl. Polym. Sci.* **1998**, *70*, 1283.
[51] *Handbook of Electronics Calculations*, 2nd ed.; M. Kaufman; A.H. Siedman, Eds.; McGraw-Hill: New York, NY, 1978; Chapter 4.
[52] G.A. Tishchenko; M. Bleha; V. Tyrackova; T.E. Sukhanova; S.A. Gulevskaya; K.A. Koshcheenko; L.S. Shataeva *Collect. Czech. Chem. Commun.* **1993**, *58*, 365.
[53] L.D. Nielsen, Ph.D. Thesis, University of Wisconsin-Madison, December 1995, Chapter 2.
[54] A.K. Sharma; H. Yasuda *J. Adhes.* **1982**, *13*, 201.
[55] R. d'Agostino *Plasma Deposition, Treatment, and Etching of Polymers*; Academic Press: Boston, MA, 1990; Chapter 1.
[56] D.T. Clark; A. Dilks; D. Shuttleworth *Polymer Surfaces*; Wiley: London, 1978, Chapter 2.
[57] *Plasma Polymerization and Plasma Interactions with Polymers*; K. Yasuda, Ed.; Applied Polymer Symposium No. 46; John Wiley & Sons: New York, NY, 1990, Chapter 1.
[58] E. Kay; L.L. Levenson, W.J. James; R.A. Auerbach *J. Vac. Sci. Technol.* **1979,** *16*, 359.
[59] F. Shi *Surf. Coat. Technol.* **1996**, *82*, 1.
[60] H.K. Yasuda, *Plasma Polymerization*; Academic Press: Orlando, FL, 1985, Chapter 10.
[61] S. Kaplan; A. Dilks *J. Appl. Polym. Sci.: Appl. Polym. Symp.* **1984**, *38*, 105.
[62] P. Lemoine; R.W. Lamberton; A.A. Ogwu; J.F. Zhao; P. Maguire; j. Mclaughlin *J. Appl. Phys.* **1999**, *86*, 6564.
[63] J.W.A.M. Gielen, Ph.D. thesis, Eindhoven University, 1996.
[64] H.K. Yasuda, *Plasma Polymerization*; Academic Press: Orlando, FL, 1985, Chapter 6.
[65] H. Kobayashi; M. Shen; A.T. Bell *J. Macromol. Sci., Chem.* **1974**, *A8*, 1354.
[66] H. Sabharwal; F. Denes; L. Nielson; R. Young *J. Ag. Food Chem.* **1993**, *41*, 2202.
[67] G. Surendran; W.J. James *J. Appl. Polym. Sci.: Appl. Polym. Symp.* **1984,** *38*, 75.
[68] Z. Sun *J. Non-Cryst. Solids* **2000**, *261*, 211.
[69] N. Morosoff; D.L. Patel *ACS Poly. Prepr.* **1986**, *27*, 82.
[70] F. Denes; A.M. Sarmadi; C.E. Hop; R.A. Young *J. Appl. Polym. Sci.: Appl. Polym. Symp.* **1994**, *54*, 55.
[71] J.M. Tibbitt; M. Shen; A.T. Bell *J. Macromol. Sci. Chem. A* **1976**, *10*, 1623.
[72] C.E. Taylor; F.J. Boerio; D.B. Zeik; S.J. Clarson; S.M. Ward; R.A. Dickie In *Proc. 17th Annual Meeting of the Adhesion Society*; F. Beorio, Ed.; The Adhesion Society: Blacksburg, Va., 1994; p. 139.
[73] H. Biederman; D. Slavinska *Surf. Coat. Technol.* **2000**, 125, 371.
[74] H. Biederman; Y. Osada *Plasma Polymerization Processes*; Elsevier: Amsterdam, 1992, Chapter 1.
[75] G.P Lopez; B.D. Ratner *Langmuir* **1991**, *7*, 766.
[76] H. Yasuda; T. Hsu, *Surf. Sci.* **1978**, *76*, 232.
[77] E. Kay presented at the *IUPAC International Roundtable on Plasma Polymerization and Plasma Treatment*, Limoges, France, 1977.
[78] H. Yasuda presented at the *IUPAC International Round table on Plasma Polymerization and Plasma Treatment*, Limoges, France, 1977.
[79] M. Gazicki; H. Yasuda *J. Appl. Polym. Sci.: Appl. Polym. Symp.* **1984,** *38*, 35.
[80] H. Yasuda *J. Polym. Sci. Macromol. Rev.* **1981**, *16*, 199.
[81] N. Inagaki *Plasma Surface Modification and Plasma Polymerization*; Technomic Publishing Company: Lancaster, PA, 1996, Chapter 2.

[82] H. Yasuda *Thin Film Processes*; J. L. Vossen; W. Kern, Eds.; Academic Press: New York, NY, 1978, p. 361.
[83] H. Yasuda; T. Hirotsu; *J. Polym. Sci., Polym. Chem. Ed.* **1978**, *4*, 93.
[84] H. Yasuda; A.K. Sharma; E.B. Hale; W.J. James *J. Adhes.* **1982**, *13*, 269.
[85] H. Yasuda; C.R. Wang *J. Polym. Sci., Polym. Chem. Ed.* **1985**, *23*, 87.
[86] N. Inagaki *Plasma Surface Modification and Plasma Polymerization*; Technomic Publishing Company: Lancaster, PA, 1996, Chapter 5.
[87] M. Millard in *Techniques and Applications of Plasma Chemistry*, J. R. Hollahan and A. T. Bell, Eds.; Wiley: New York, NY, 1974.
[88] *Plasma Polymerization*; M. Shen and A. T. Bell, Eds.; Am. Chem. Soc. Symp. Ser. 108, Am. Chem. Soc.: Washington, DC, 1979, Chapter 1.
[89] W.O. Freitag; H. Yasuda; K. Sharma *J. Appl. Polym. Sci.: Appl. Polym. Symp.* **1984**, *38*, 185.
[90] H. Yasuda; A.K. Sharma; T. Yasuda *J. Polym. Sci., Polym. Phys. Ed.* **1981**, *19*, 1285.
[91] W. J. van Ooij; R. H. G. Brinkuis *Surf. Interface Anal.* **1988**, *11*, 430.
[92] H. Yasuda; M.O. Bumgarner; H.C. Marsh; N. Morosoff; *J. Polym. Sci. Polym. Chem. Ed.* **1976**, *14*, 195.
[93] H. Yasuda; T. Hsu *J. Polym. Sci. Polym. Chem. Ed.* **1977**, *15*, 81.
[94] D.J. Srolovitz; M.G. Goldiner *JOM (TMS)* **1995**, *47*, 31.
[95] W. Lu; K. Komvopoulos; S.W. Yeh *J. Appl. Phys.* **2001**, *89*, 2422.
[96] D.L. Ross *RCA Reviews* **1978**, *39*, 136.
[97] L.J. Gerenger In *Plasma Surface Modification of Polymers*; M. Strobel; C. Lyons; K.L. Mittal, Eds.; VSP: The Netherlands, 1994, Chapter 2.
[98] M. Gazicki; H. Yasuda *Plasma Chemistry and Plasma Processes*; **1983**, *3*, 279.
[99] L. Martinu; H. Biederman; J Nedbal *Thin Solid Films* **1986**, *11*, 136.
[100] Y.M. Tsai; F.J. Boerio; R. Aggarwal; D.B. Zeik; S.J. Clarson; W.J. van Ooij; A. Sabata *J. Appl. Polym. Sci.: Appl. Polym. Symp.* **1994,** *54*, 3.
[101] W.J. van Ooij; A. Sabata *Surf. Interface Anal.* **1992**, *19*, 101.
[102] Y.M. Tsai; F.J. Boerio; W.J. Van Ooij; D.K. Kim *J. Adhes.* **1997**, *62*, 127.
[103] Y.M. Tsai; F.J. Boerio; D.K. Kim *J. Adhes.* **1997**, *61*, 247.
[104] Y. Iriyama; T. Ihara; M. Kiboku *Thin Solid Films* **1996**, *287*, 169.
[105] R.H. Turner; I. Segall; F.J. Boerio; G.D. Davis *J. Adhes.* **1997**, 62, 1.
[106] J.R. Arnold; C.D. Sanders; D.L. Bellevou; A.A. Martinelli; G.B. Gaskin *SAMPE Journal* **1998**, *34*, 11.
[107] C.R. Wold; M.D. Soucek *J. Coat. Technol.* **1998**, *70*, 43.
[108] Y. Kagami; T. Amauchi; Y. Osada *J. Appl. Phys.* **1990**, *68*, 610.
[109] H.J. Frenck; W. Kulish; M. Kuhr; R. Kassing *Thin Solid Films* **1991**, *201*, 327.
[110] H.J. Frenck; E. Oesterschulze; R. Beckmann; W. Kulish; R. Kassing *Mater. Sci. Eng.* **1991**, *A139*, 394.
[111] F. Shi *J. Mater. Sci. - Rev. Macromol. Chem. Phys.* **1996**, *C36*, 795.
[112] H. Biederman *Vacuum* **1987**, *37*, 367.
[113] D.C. Nonhebel; J.C. Walton *Free Radical Chemistry*; Cambridge University Press: Cambridge, 1974.
[114] P.P. Tzaskomapaulette and A. Naseri *J. Electrochem. Soc.* **1997**, *144*, 1307.
[115] N. Inagaki; S. Tasaka; Y. Nozue *J. Appl. Polym. Sci.* **1992**, *45*, 1041.

[116] G.P Anderson; K.L. DeVries; G. Sharon "Evaluation of Adhesive Test Methods" in Adhesive Joints: Formation, Characteristics, and Testing; K.L. Mittal, Ed.; Plenum Press, New York, NY, 1984.
[117] M. Goland; E. Reissner *J. Appl. Mech.* **1944**, *11*, A17.
[118] ASTM Standard D 4896, 1996, Volume 15.06, p. 404.
[119] J.P. Sargent "The Dimensional Stability of Epoxy Adhesive Joints" in Adhesive Joints: Formation, Characteristics, and Testing; K.L. Mittal, Ed.; Plenum Press, New York, NY, 1984.
[120] K. Siegbahn; C. Nordling; A. Fahlman; K. Hamrin; J. Hedman; G. Johansson; T. Bergmark; S. Karlson; I. Lindgren; B. Lindberg, ESCA, Atomic, Molecular and Solid State Structure Studies by means of Electron Spectroscopy; Almquist and Wiksells Boktryckeri: AB, Uppsula, 1967.
[121] *New Characterization techniques for Polymer Films*; Ho-Ming Tong and Luu T. Nguyen, Eds.; Wiley and Sons: New York, NY, 1990; Chapter 11.
[122] W.M. Riggs and M.J. Parker in *Methods of Surface Analysis*; A.W. Czanderna, Ed.; Elsevier: New York, NY, 1989; Chapter 4.
[123] A. Joshi; L.E. Davis; P.W. Palmberg in *Methods of Surface Analysis*; A.W. Czanderna, Ed.; Elsevier: New York, NY, 1989; Chapter 5.
[124] J.A. Filbey; J.P. Wightman In *Adhesive Bonding*; L. Lee, Ed.; Plenum Press: New York, NY, 1991, Chapter 7.
[125] *Practical Scanning Electron Microscopy* J.I. Goldstein and H. Yakowitz, Eds.; Plenum Press, New York, NY, 1977, Chapter 1.
[126] D.J. Shaw *Introduction to Colloid and Surface Chemistry*; Butterworth-Heinemann: Oxford, 1992, Chapter 6.
[127] E.M. Liston; L. Martinu; M.R. Wertheimer *J. Adhes. Sci. Tech.* **1993**, *7*, 1091.
[128] *Modern Approaches to Wettability: Theory and Applications* M.E. Schrader and G.I. Loeb, Eds.; Plenum Press, New York, NY, 1992, Chapter 1.
[129] W.A. Zisman in *Contact Angle, Wettability, and Adhesion* R.F. Gould, Ed.; American Chemical Society, Washington, DC, 1964, Chapter 1.
[130] A. Dupre *Theorie Mechanique de la Chaleur*; Gauthier-Villars: Paris, 1869, p. 369.
[131] W. Lu; K. Komvopoulos *J. Appl. Phys.* **1999**, *85*, 2642.
[132] W.C. Oliver; G.M. Pharr *J. Mater.Res.* **1992**, *7*, 1564.
[133] M.F. Doerner; W.D. Nix *J. Mater. Res.* **1986**, *1*, 601.
[134] A.K. Bhattacharya; W.D. Nix *Int. J. Solids Structures* **1988**, *24*, 881.
[135] G.M. Pharr; W.C. Oliver *MRS Bulletin* **1992**, *17*, 28.
[136] C.C. Schmitt; J.R. Elings *Digital Instruments Brochure*, 1997.
[137] G. Berg; C. Friedrich; E. Broszeit; C. Berger *Fresenius J. Anal. Chem.* **1997**, *358*, 281.
[138] H.S. Park; D. Kwon *Thin Solid Films* **1997**, *307*, 156.
[139] X. Li; B. Bhushan *Wear* **1998**, *220*, 51.

3.0 Experimental

3.1 Materials

3.1.1 Adhesive

FM-5 is a high performance polyimide adhesive originally developed at the NASA Langley Research Center.[1] FM-5 was supplied as a polymer film supported on a woven fiberglass cloth by Cytec Industries Inc. (Havre de Grace, MD). The supported film was 85 % LaRC-PETI-5 by weight, 4 % N-methyl-2-pyrrolidinone (NMP) by weight, and 11 % fiberglass cloth by weight. The Tg of the cured adhesive was approximately 250°C, as measured by dynamic mechanical analysis (DMA) and differential scanning calorimetry (DSC).[2] The thickness of the adhesive film before bonding was 0.5 mm (0.0197 inches) and 0.125 mm (0.0049 inches) after bonding. The successful application of FM-5 relies on heat and pressure to provide the intimate interfacial contact needed to produce a quality bond, as will be discussed.

3.1.2 Substrates

Titanium alloy (Ti-6Al-4V) was obtained from President Titanium (Boston, MA). Sample dimensions were 9.53 mm (0.375 inch) x 34.93 mm (1.375 inch) x 2.29 mm (0.09 inch). To remove grease and other contaminants from the titanium alloy before plasma treating the substrate, each sample was thoroughly cleaned with acetone using 3M Scotch-Brite® scouring pads. In some cases, the substrates were pretreated by grit blasting with silica. Grit blasting was performed in an Ecoline Gritblaster (Grand Rapids, MI), with washed, dried, and screened pure white sand (Riverton Corporation, Riverton, VA).

For the nanomechanical studies, the Ti-6Al-4V substrates were polished before plasma treatment. Samples were cleaned with acetone and Scotch Brite® pads and then epoxied to polymer blocks for easier handling. Polishing wheels and incrementally smaller grits of alumina

(Struers, Westlake, OH) were used to polish the titanium alloy to a 0.3 micron finish. After polishing, the samples were removed from the blocks by dissolving the epoxy with acetone. The samples were sonicated in acetone for 15 minutes and then given a final acetone rinse before being placed in the plasma reactor.

Type N silicon(111) wafers with a native oxide surface were used for nanomechanical studies. The wafers were obtained from Motorola Inc. (Scottsdale, AZ) and were cleaned with acetone prior to film deposition. The wafers had a thickness of between 0.0197 and 0.0217 cm. Glass slides were also used as substrates for some of the plasma polymerized titanium(IV) isobutoxide work. The glass slides were plain Fisherfinest microscope slides (Fisher Scientific, Pittsburgh, PA) and were cleaned with acetone prior to use.

3.1.3 Gases

The gases used in this study are given in Table 3.1. Flow rates were regulated using two 50 sccm mass flow controllers (Brooks Instruments, Hatfield, PA, model 5850) and a Brooks model 5878 control box. Chamber pressure was measured using a thermocouple gauge (Hastings-Raydist, Hapton, VA).

Table 3.1: Purity and manufacturer of the gases used.

Gas	Purity	Manufacturer	Location
Acetylene	High purity	The BOC Group	Murray Hill, NJ
Argon	Ultra high purity/zero grade	Air Products	Allentown, PA
Helium	Ultra high purity	Holox	Norcross, GA
Nitrogen	Low O_2 grade	The BOC Group	Murray Hill, NJ
Oxygen	4.4 grade	The BOC Group	Murray Hill, NJ

3.1.4 Titanium(IV) Isobutoxide

Titanium(IV) isobutoxide ($Ti[(CH_3)_2CHCH_2O]_4$) (Alfa Aesar, Ward Hill, MA, 99+%) was transferred to a custom-made glass vessel using a glove box in a nitrogen atmosphere. Titanium(IV) isobutoxide (TiiB), which is moisture sensitive, was taken through the freeze-thaw

cycle at least 5 times to remove residual gas. To introduce TiiB into the reaction chamber, argon or some other carrier gas was bubbled through the TiiB. For most experiments, TiiB was heated to 70° C prior to its introduction into the plasma chamber to increase its volatility.

3.2 Sample Nomenclature

To provide descriptive sample names, a system of nomenclature was developed that provides information regarding the type of plasma used, the deposition or treatment time, the input power, the flow rate of the main reactive gas, and the carrier gas used. For example, Ac.120s.200w.f10.Ar denotes a sample that was treated with an acetylene plasma (Ac) for 120 seconds (120s) at 200 Watts (200w), using an acetylene flow rate of 10 sccm (f10), with argon as the carrier gas (Ar). When there was no carrier gas used, the suffix relating to the carrier gas was excluded from the sample name. As another example, O2.10m.200w.f20 denotes samples that were treated with an oxygen plasma (O2) for 10 minutes (10m) at 200 Watts (200w) using a flow rate of 20 sccm (f20). For the nanomechanical studies, it was sometimes necessary to denote the substrate on which the film was deposited, and this was added as a suffix (.Ti for polished Ti-6Al-4V or .Si for silicon wafer). Any other pertinent information that was needed to distinguish the samples was added in parenthesis after the name.

3.3 Plasma Reactors

Plasma treatments were carried out at low pressures (< 50 milliTorr) using custom built, radio frequency (RF), inductively coupled plasma reactors. During the initial stages of this study, many reactor designs were considered and tested. After many experiments, full size Pyrex glass reactors were constructed and a two turn coil (measured inductance of 1.11 micro-henries) gave the most stable plasma with the least amount of reflected power. The reactors were driven by a 27.12 MHz ICP (Plasma Power, Inc.) power source, which operated at 50 ohms and delivered up to 300 watts of power. A variable capacitance-matching network connected the induction coil to the power source and allowed the coil to be tuned to match the source resistance. The power

source had the capability of delivering up to 3 kW of power, but the coil could not be properly tuned above 300 watts, and the reflected power (>300 watts) was unacceptable for maintaining a stable, low temperature plasma. The sample holders were designed to hold seven or fourteen samples (see Figure 3.1). Once treated, the samples were handled with tweezers and gloves to avoid contamination.

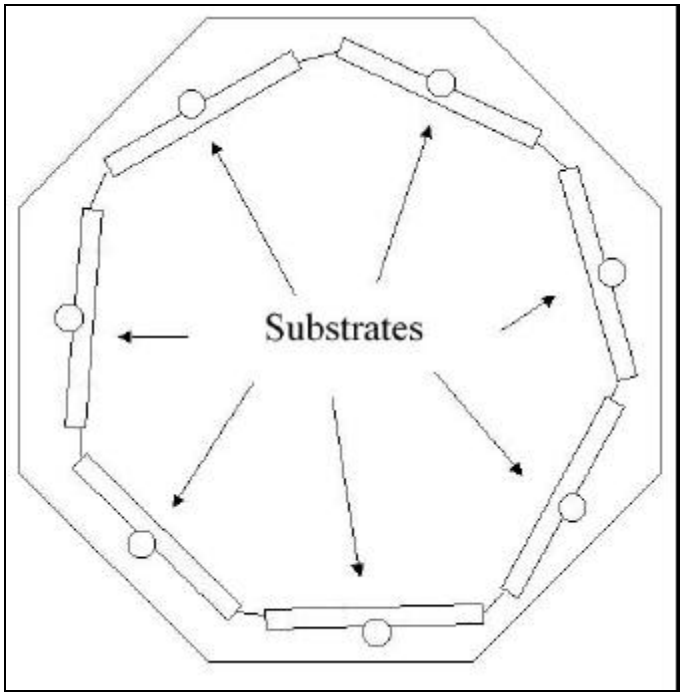

Figure 3.1: Sample holder (top view).

3.3.1 Reactor Chamber 1

Reactor 1 was tubular and stood vertically with a height of approximately 150 cm (59 inches). The width of the reactor was approximately 10.5 cm (4.1 inches), and it narrowed to approximately 5 cm (2 inches) at the ends. A schematic of the reactor is shown in Figure 3.2, and a picture of the reactor is shown in Figure 3.3. The induction coil was located at the bottom of the reactor. The chamber was evacuated to pressures as low as 1 mTorr using a fore pump-backed turbo-molecular pump mounted on the top of the reactor. The samples were located above (downstream) the induction coil and were exposed to the afterglow region of the plasma.

Five inlets to the chamber permitted up to four gases to be metered into the system while simultaneously monitoring the chamber pressure.

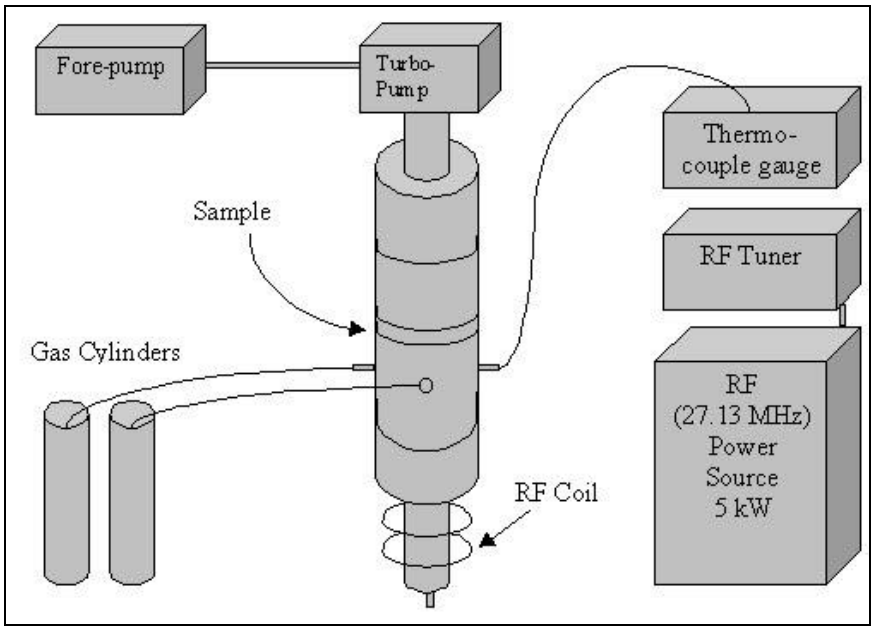

Figure 3.2: Schematic of plasma reactor 1.

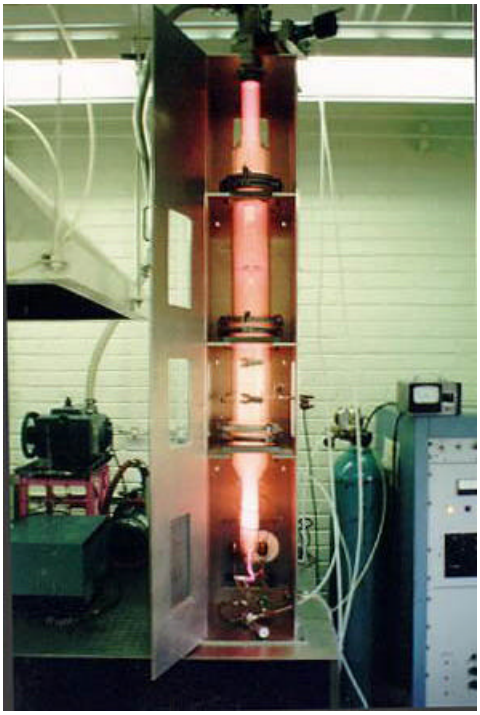

Figure 3.3: Photograph of plasma reactor 1.

3.3.2 Reactor Chamber 2

The second reactor used to prepare all samples in the PP TiiB and nanomechanical studies was smaller than reactor 1, and was positioned horizontally along the bench-top (see Figure 3.4). It was approximately 75 cm (29.5 inches) in length and approximately 10.5 cm (4.1 inches) wide (see Figure 3.5). It narrowed to approximately 5 cm (2 inches) at the ends. In addition to treating samples using the sample holder shown in Figure 3.1, substrates were also placed along the bottom of the reactor to improve the uniformity of the coating. Samples were placed downstream from the coil, and interacted with the afterglow of the plasma. For the nanomechanical studies, the sample and inlet positions relative to the reactor are shown in Figure 3.6.

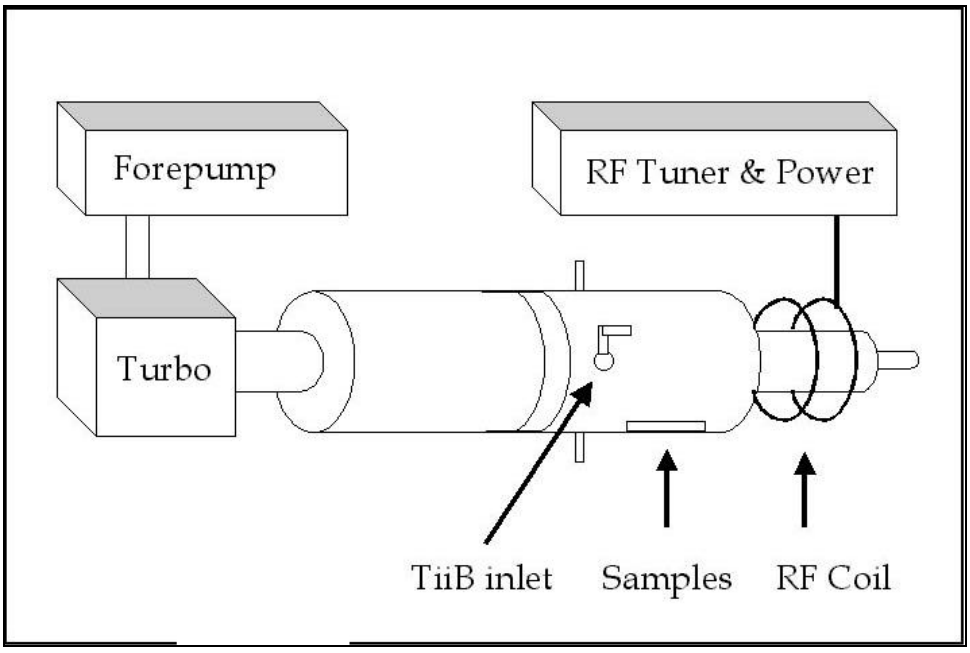

Figure 3.4: Schematic of plasma reactor 2.

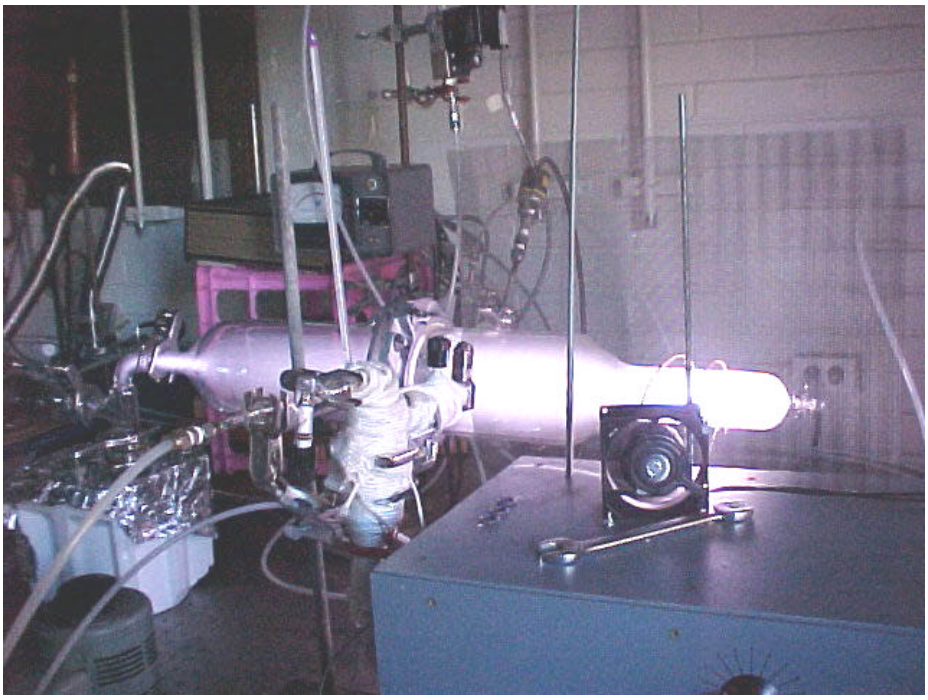

Figure 3.5: Photograph of plasma reactor 2.

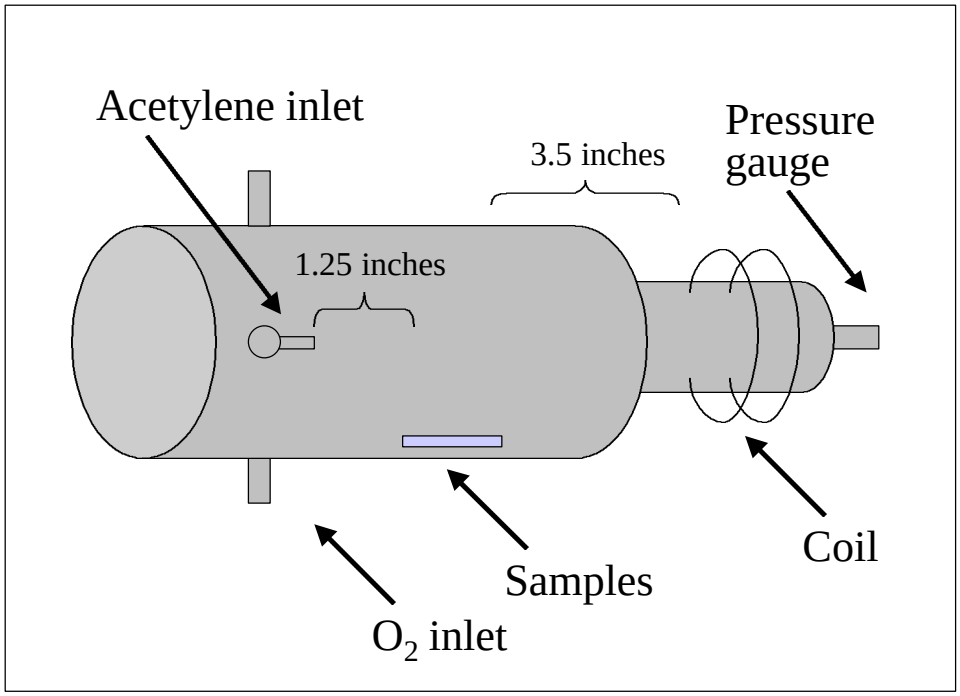

Figure 3.6: Sample position in plasma reactor 2.

3.4 Plasma Treatment

Typically, the substrates were placed in the reactor and the system was pumped down for 10 to 15 minutes to a pressure of less than 20 mTorr. The reaction vessel was then purged with the treatment or carrier gas for 10 minutes. For plasma polymerization processes, the reactive gas was then introduced into the reactor and the pressure was allowed to stabilize for approximately 5 minutes before the plasma was ignited. Once the plasma was initiated at the desired input power, the inductive coil was tuned to match the source impedance to minimize reflected power. Following the plasma treatment, the flow of source gases was terminated and the reaction vessel was purged with high purity oxygen for at least 15 minutes. The purging was done to minimize the effects that different humidity could have on surface reactions once the samples were removed from the reaction vessel. The samples were immediately transferred to a desiccator after treatment and were bonded within 5 days.

3.5 Cure Cycle and Lap-Shear Specimen Fabrication

Once the Ti-6Al-4V substrates were plasma treated, the bonded assembly was constructed and prepared for the curing process. A schematic of the bonded assembly is shown in Figure 3.7. It consisted of the Ti-6Al-4V substrate with its natural or plasma-created oxide, the PP film, and the FM-5 adhesive.

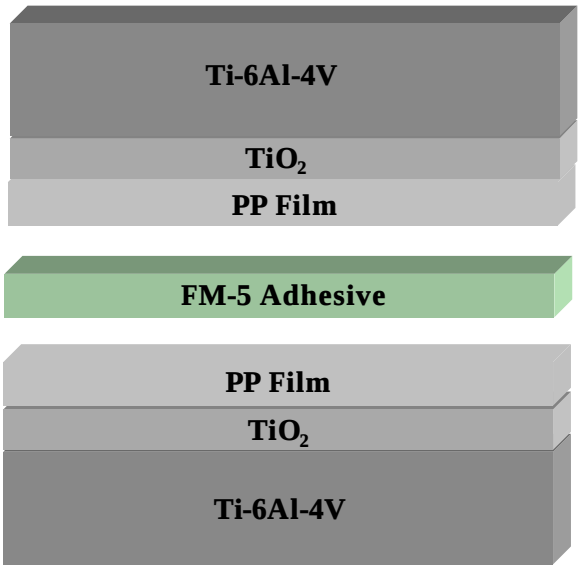

Figure 3.7: Schematic of the bonded assembly (not to scale).

3.5.1 Cure Cycle

Single lap shear specimens were prepared by individually bonding the pretreated Ti-6Al-4V adherends [9.53 mm (0.375 inch) x 34.93 mm (1.375 inch) x 2.29 mm (0.09 inch)]. A bond overlap of 9.52 x 9.52 mm (3/8 inch x 3/8 inch) was used. The samples were bonded with FM-5 using a hot press (Tetrahedron, San Diego, CA) and the following cure cycle: Samples were initially heated to 250° C at a heating rate of 2.2° C/min under contact pressure, held at 252° C for 60 minutes, then heated to 371° C at 2.2° C/min under 0.518 MPa (50 psi) of pressure (see Figure 3.8). The samples were held at 371° C for 60 minutes under 0.518 MPa, then were cooled to room temperature at 10° C/min under contact pressure. N-methyl pyrrolidinone (NMP), which has a boiling point of 202° C, was volatilized during the cure cycle.

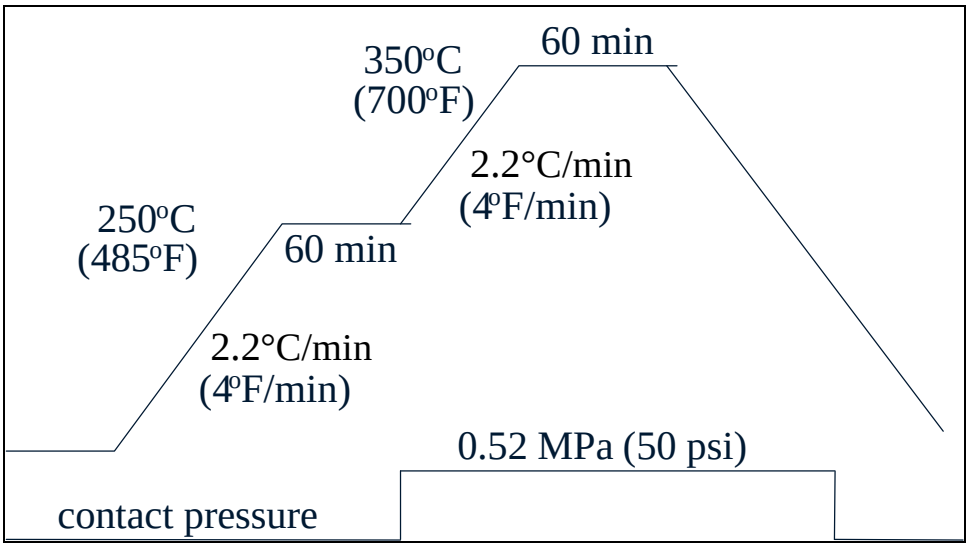

Figure 3.8: Cure cycle for FM-5 adhesive.

3.5.2 Single Lap Shear Testing

A Model 1123 Instron® (5500R) was used to test all lap shear specimens. Testing was performed at room temperature and a pull rate of 1.27 mm/min (0.05 inches/min). An average of three measurements was taken, except where noted.

3.6 Surface Analysis

3.6.1 X-ray Photoelectron Spectroscopy (XPS)

XPS spectra were obtained using a Perkin-Elmer Model 5400 XPS spectrometer with a Mg Kα X-ray source (1253.6 eV), operated at 300 W and 14 kV DC, with an emission current of 25 mA. The spot size was 1.0 x 3.0 mm. Photoelectrons were analyzed in a hemispherical analyzer using a position-sensitive detector. Elemental analysis was carried out using the following photopeaks: C 1s, O 1s, N 1s, Ti 2p, Al 2p, V 2p, Si 2p, Na 1s, Ca 2p, S 2p, Cl 2p, F 1s, Zn $2p_{3/2}$, and Sn 1s. Photoelectron spectral peak areas were scaled to account for an

instrument sensitivity factor and ionization probabilities to yield results which were indicative of surface concentrations in atomic percent. The C-C/C-H carbon peak was calibrated to 285.0 eV, and all assignments were made in reference to this peak (see Table 3.2). A satellite peak arising from $\pi \rightarrow \pi^*$ shake-up transitions of aromatics and unsaturated C=C bonds was observed around 291.6 eV in the C 1s photopeaks of some samples.[3] The assignments used for curve-fitting O 1s photopeaks are given in Table 3. 3

In some cases (where noted), data from two or three spots from the same sample were averaged. A notation of "ND" (not detected) implies that less than 0.5 % of that element was detected. A notation of "trace" implies that less than 1 % of that element was detected. Carbon 1s and oxygen 1s photopeaks were curve-fitted using photopeaks of Gaussian peak shape.[4] Curve fitting was performed to best incorporate probable functionalities into the overall peak. The atomic concentration percentages were also taken into consideration when curve fitting. For example, when analyzing a titanium dioxide surface, if titanium was detected at 6 %, then 12 % of the oxygen detected should be bound to titanium (two oxygen atoms for every one titanium atom in TiO_2). The full widths at half maximum (FWHM) for the curve-fit photopeaks were typically 1.70 eV. However, in some cases, the FWHM was varied by ± 0.15 eV to obtain the best curve-fit.

Table 3.2: XPS peak assignments for curve-fitted C 1s photopeak.[5, 6]

Peak position (eV)	Assignment
284.7	aromatic
284.8	C=C
285.0	C-H/C-C
285.8 - 286.2	C-N
286.3 - 286.7	C-O
287.8 - 288.2	C=O
289.2	O=C-O
291.6	$\pi \rightarrow \pi^*$ shake-up[7]

Table 3. 3: XPS peak assignments for curve-fitted O 1s photopeak. [6, 7]

Peak position (eV)	Assignment
530.2 - 530.8	TiO_2
531.6 - 532.1	O=C
≈ 532.1	SiO_2
533.1 - 533.3	O-C
>533.8	H_2O

3.6.2 Auger Electron Spectroscopy (AES)

AES was performed using a Perkin Elmer PHI 610 Scanning Auger Microprobe. The electron gun beam voltage was 3000 V, the current was 0.05 μA, and the raster size varied from 2 mm^2 to no raster. The sputter rate was typically 25 Å/min, but it varied from 5 to 300Å/min depending on the estimated thickness of the film being measured. The argon ion gun beam voltage was 4000 kV, with a current of 5 μA. The sputter rate was periodically calibrated using the known oxide thickness of a Ta_2O_5 wafer. Three measurements from the same sample were averaged, except where noted. The thickness of a film or oxide layer was determined by measuring the sputter time needed for either the carbon/oxygen or the oxygen/titanium atomic concentrations to intersect. This amount of time, multiplied by the sputter rate, gave the thickness of the layer. For an oxide layer buried beneath a carbon layer, the time between when the carbon/oxygen atomic concentrations intersected and when the oxygen/titanium atomic concentrations intersected was measured.

3.6.3 Scanning Electron Microscopy (SEM)

SEM photomicrographs were obtained using an ISI Model SX-40 scanning electron microscope. Samples were sputter-coated with a thin gold film (≈ 200 Å) to reduce charging effects.

3.6.4 Contact Angle Measurements

Contact angle measurements were made with an optical goniometer (Rame-Hart, Inc., Mountain Lakes, NJ) mounted with a video camera. Measurements were taken at room temperature, and the angles from both sides of the drop were measured and averaged. An average of the angles for at least seven drops was taken. The liquids used were de-ionized, purified H_2O and methylene iodide (99 % pure, Acros Organics, Newark, NJ). The drop volume for the measurements was 5 μl.

When calculating the surface energy of a sample, the harmonic mean method was used (Equations 3.1 and 3.2).[8] The subscripts 1 and 2 refer to the testing liquids (H_2O and CH_2I_2).[9] A description of the symbols and the units is given in Table 3.4. By solving the set of simultaneous equations, the two unknowns (γ_s^d and γ_s^p) can be determined. The total surface energy (γ) of the surface is the sum of the dispersive and polar components ($\gamma_s^d + \gamma_s^p$). The dispersive and polar components of the test liquids were taken from reference 8 and are listed in Table 3.4.

$$(1+\cos\theta_1)\gamma_1 = 4\left(\frac{\gamma_1^d \gamma_s^d}{\gamma_1^d + \gamma_s^d} + \frac{\gamma_1^p \gamma_s^p}{\gamma_1^p + \gamma_s^p}\right) \qquad \textbf{Equation 3.1}$$

$$(1+\cos\theta_2)\gamma_2 = 4\left(\frac{\gamma_2^d \gamma_s^d}{\gamma_2^d + \gamma_s^d} + \frac{\gamma_2^p \gamma_s^p}{\gamma_2^p + \gamma_s^p}\right) \qquad \textbf{Equation 3.2}$$

Table 3.4: Units and description of symbols used to calculate surface energies.

Symbol	Description	Value[8]	Units
θ_1	Contact angle of H_2O	--	degrees
θ_2	Contact angle of CH_2I_2	--	degrees
γ_1	Surface energy of H_2O	72.8	dyne/cm
γ_2	Surface energy of CH_2I_2	50.8	dyne/cm
γ_1^d	Dispersive component of the surface energy of H_2O	22.1	dyne/cm
γ_1^p	Polar component of the surface energy of H_2O	50.7	dyne/cm
γ_2^d	Dispersive component of the surface energy of C_2I_2	44.1	dyne/cm
γ_2^p	Polar component of the surface energy of C_2I_2	6.7	dyne/cm
γ_s^d	Dispersive component of the surface energy of the substrate	--	dyne/cm
γ_s^p	Polar component of the surface energy of the substrate	--	dyne/cm

3.6.5 Fourier Transform Infrared Analysis

Reflectance-absorbance infrared analysis (RAIR) spectra of the PP films on polished Ti-6Al-4V were obtained using a Nicolet Model 710 Fourier transform infrared (FTIR) spectrophotometer equipped with a Spectra-Tech Model FT-80 fixed grazing angle specular reflectance sample apparatus. A KBr beamsplitter and a MCT/A detector were used. Nicolet's Omnic (version 3.1) data acquisition software was used to acquire data and process the results. The signal was optimized at a reflection angle of 80°, so this was the angle used in all cases. Spectra were collected using boxcar apodization at a resolution of 4 cm^{-1}, and 512 scans were averaged for each spectrum collected.

3.6.6 Nanoindentation Tests

Nanoindentation and scratch tests were performed using a Hysitron TriboScope® at Hysitron, Inc. (Minneapolis, MN). The instrument was calibrated by performing an indent in air (no contact with a surface) to ensure that the forces applied were the same as the forces detected. To obtain the relationship between normal displacement and cross sectional area of the indenter tip, fused quartz was used as the calibrating material.

Samples were mounted on an AFM specimen stub and tested using a diamond Berkovich indenter (see Figure 3.9) at room temperature. A trapezoidal loading function was used for the indentation tests (see Figure 3.10). The diamond-tipped cantilever was loaded in 10 seconds, held the maximum load for 3 seconds (to minimize creep), and then unloaded in 10 seconds. The tip was driven into the samples using forces that varied from 15 - 300 μN, and was withdrawn by decreasing the applied force. The applied load (P) and depth of penetration (h) were continuously monitored, and a load vs. depth curve was generated from the collected data (see Figure 2.11 of section 2.10.5). The sample hardness (H) and reduced elastic modulus (E_r) were calculated from the load displacement curve, as described in the Chapter 2. Twelve to fifteen indentation measurements were averaged for each sample. The loads used for indentation were selected to minimize the possible effects of the substrate on the mechanical properties of the thin films. The indentation depth of penetration was maintained at around 25 % of the total film thickness.

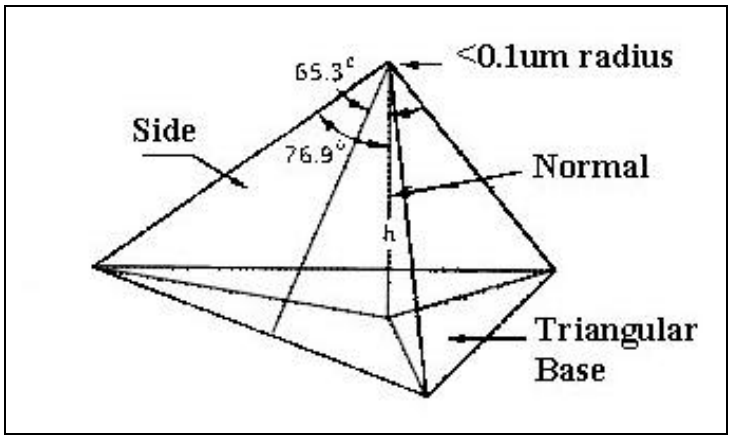

Figure 3.9: Diamond Berkovich indenter.

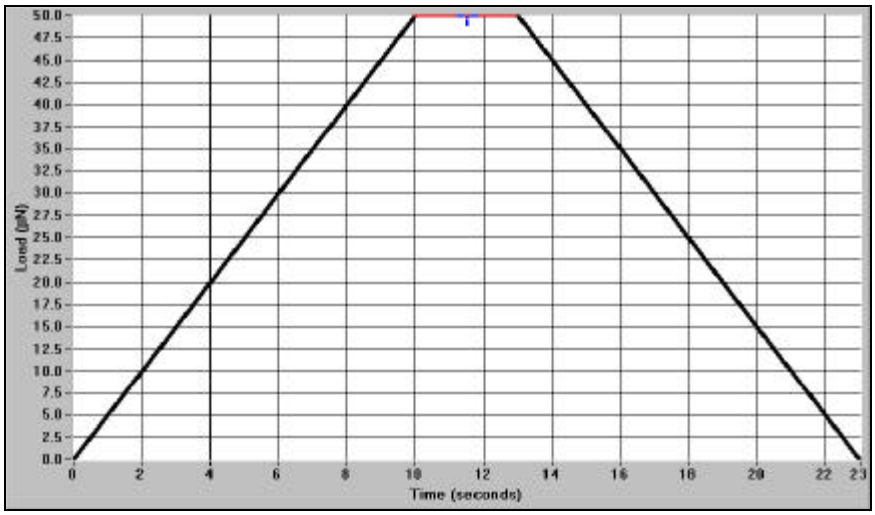

Figure 3.10: Example of load function used during an indentation test**.**

3.6.7 Nanoscratch Tests

The nanoscratch tester was calibrated by performing a scratch in air (no contact with a surface) to ensure that the forces applied were the same as the forces detected. For testing, multiple scratches (3-5) were made on each sample with a conical tip of approximately 700 nm radius. During the actual scratch, the tip was moved ≈ 4 µm in 30 seconds. During this time, the normal load was ramped to the maximum force of 800µN. The adhesion of PP films to various substrates was evaluated by comparing force-displacement curves recorded during a scratch. A typical scratch function for a ramp force scratch is shown in Figure 3.11. A characteristic critical load at debond was obtained by noting the discontinuity that occurred in the force-displacement curve when the film debonded from a surface. This critical load at debond is a reliable empirical measure of the adhesive strength of the film.[10] However, a limitation of the measurement is that the failure mode cannot be obtained from the data, nor is this information easily obtainable by imaging or surface analysis techniques.

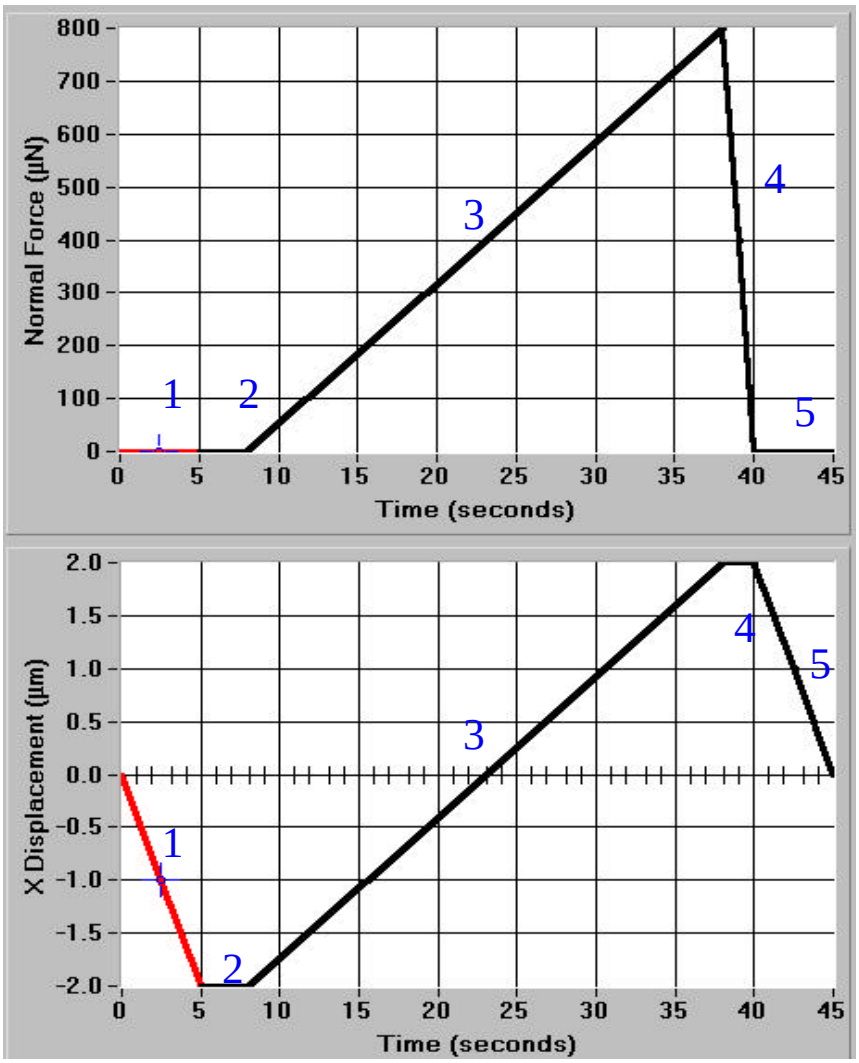

Figure 3.11: Example ramp force scratch test function.

A description of the scratch tests is given in Figure 3.11, where normal force and x-displacement vs. time are shown. The test segment is as follows:

1) The tip moves to –2µm (x-axis) as normal force remains at zero.
2) The tip holds at –2µm (x-axis) for 3 seconds to stabilize.
3) The actual scratch occurs as the tip moves from –2µm to +2µm over 30 seconds along the x-axis. During this time, the normal load is ramped to the maximum force of 800 µN.
4) The tip returns to zero (the origin) along the x-axis. The normal force returns to zero to prevent deformation of the surface.

Figure 3.12 shows a typical scratch test result. The critical debonding event occurs within the area enclosed by the two vertical red lines. Graph **a** of Figure 3.12 shows the normal force vs. time and it reveals how the tip was loaded during the scratch. In the graph of normal displacement vs. time (graph **b**, top right of Figure 3.12), the debond event is obvious as a sharp decrease in slope (see arrow). In the graph of lateral force vs. time (graph **c**, bottom left of Figure 3.12), the critical load at debond is shown as the first spike in the slope (see arrow). Graph **d** of Figure 3.12 shows the lateral displacement vs. time; it simply shows how far across the sample the tip traveled prior to debond. The critical load at debond is calculated from the load at the onset of the event.

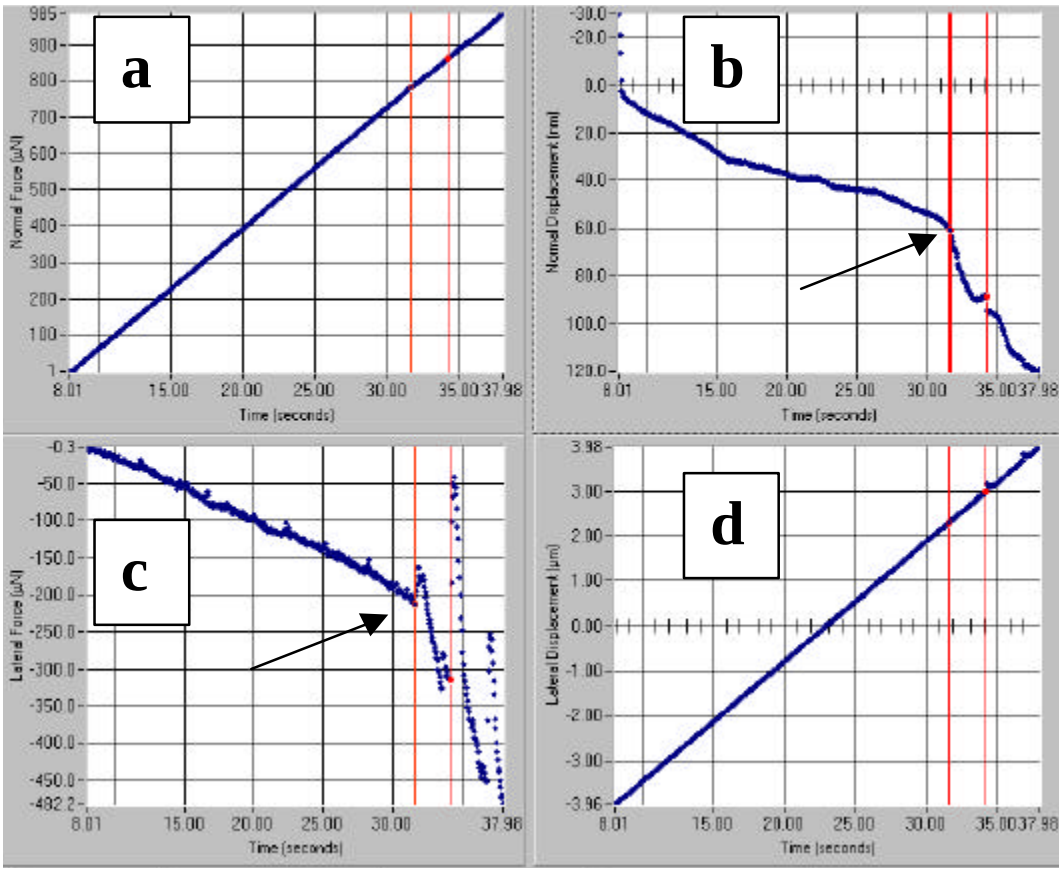

Figure 3.12: Results of an 8µm ramp force scratch test, max force 1000 µN for Ac.130s.10w.f10.Ti: a) normal force vs. time, b) normal displacement vs. time, c) lateral force vs. time, d) lateral displacement vs. time.

3.7 References

[1] J.G. Smith; P.M. Hergenrother, *Polym. Prepr.* **1994,** *35*, 353.
[2] H. Parvatareddy, Ph.D. Thesis, Virginia Tech, Nov. 1997, p. 61.
[3] Y.M. Tsai; F.J. Boerio *J. Appl. Polym. Sci.* **1998**, *70*, 1283.
[4] K.L. Wolfe; K.L. Kimbrough; J.G. Dillard *J. Adhes.* **1995**, *55*, 109.
[5] Y.M. Tsai; F.J. Boerio; W.J. van Ooij; D.K. Kim; T. Rau *Surf. Interface Anal.*, **1995**, *5*, 261.
[6] C.D. Wagner; W.M. Riggs; L.E. Davis; J.F. Moulder; G.E. Muilenburg *Handbook of X-Ray Photoelectron Spectroscopy*; Perkin-Elmer: Eden Prarie, MN, 1979; Appendix 3.
[7] Y.M. Tsai; F.J. Boerio *J. Appl. Polym. Sci.* **1998**, *70*, 1283.
[8] S. Wu *Polymer Interface and Adhesion*; Marcel Dekker: New York, NY, 1982; Chapter 5.
[9] S. Wu *Polymer Interface and Adhesion*; Marcel Dekker: New York, NY, 1982; p. 169.
[10] C.C. Schmitt; J.R. Elings *Digital Instruments Brochure*, 1997.

4.0 Characterization of Materials

4.1 Introduction

The primary substrates used for this study were Ti-6Al-4V, polished Ti-6Al-4V, and silicon(111) wafers. The adhesive used throughout the study was FM-5. A detailed characterization of these materials follows. This information will be helpful when making comparisons and drawing conclusions throughout this investigation.

4.2 XPS Analysis

4.2.1 FM-5 Adhesive

The FM-5 adhesive was taken through the typical curing process described in Chapter 3 and then characterized using XPS. The surface of the adhesive after curing changed only slightly. Data for uncured and cured FM-5 polyimide adhesive are given in Table 4.1. The carbon content increased from 63.9 % before the cure to 68.4 % after the cure, and the silicon content decreased from 9.2 % to 5.5 %. The silicon observed was believed to be in the form of SiO_2 due to the glass scrim cloth that supported the adhesive. However, the binding energy (104.5 eV) was higher than that reported for SiO_2 (103.3 eV),[1] possibly due to charging. The fluorine observed after the cure was unexplainable, but it was reproducible and has been reported by other researchers of FM-5.[2]

The C 1s photopeak of the cured adhesive is shown in Figure 4.1, and it was identical to that of the uncured adhesive. This was expected, because the effect of curing was only to crosslink the acetylenic endcaps of the adhesive, which would not impact the C 1s photopeak very much. The C 1s peak assignments are given in Table 4.2. Cured FM-5 has a characteristic imide carbon peak at a binding energy that is ≈ 3.6 eV higher than the C-H/C-C peak.[3, 4, 5] This peak was useful when determining failure modes because it indicated the presence of adhesive on a failed surface. The XPS atomic concentrations and curve-fit photopeak assignments agree

within ± 5 % with the theoretical composition of FM-5, as calculated using LaRC-PETI-5 stoichiometry. The results were also consistent with the XPS analysis of a similar material, cured LaRC-IA, reported by Holmes.[6]

Figure 4.2 shows the curve-fit O 1s photopeak for cured FM-5, and Table 4.3 lists the peak assignments. The majority of oxygen (45 %) was from SiO_2. Using the oxygen data exclusively suggested that there was 4.7 % silicon in the sample (two oxygen atoms for each silicon atom). This was fairly consistent with the amount of silicon detected (5.3 %), and confirmed that the silicon on the surface of FM-5 was SiO_2. The broadness of the O 1s peak and the component at high binding energy are distinguishing characteristics of the adhesive. The C-O-C photopeak appears at 533.5 eV and 533.8 eV for ULTEM and poly(methyl methacrylate),[3] respectively, but the FM-5 C-O-C photopeak was shifted to an even higher binding energy (534.7 eV) for cured FM-5. The reason for this large shift is unknown, but this feature was reproducible and was useful when determining failure mode.

Table 4.1: XPS analysis of FM-5 polyimide adhesive (an average of 3 measurements).

Sample	% C	% O	% N	% F	% Si	% Sn
As received FM-5 adhesive	63.9±0.4	22.9±0.4	3.6±0.4	ND*	9.2±0.4	trace[$]
Cured FM-5 adhesive	68.4±1.1	20.4±0.9	3.8±0.3	2.1±0.1	5.3±0.4	ND

*A notation of ND means that less than 0.5 % of the element was detected.
[$]A notation of "trace" means that between 0.5 and 1.0 % of the element was detected.

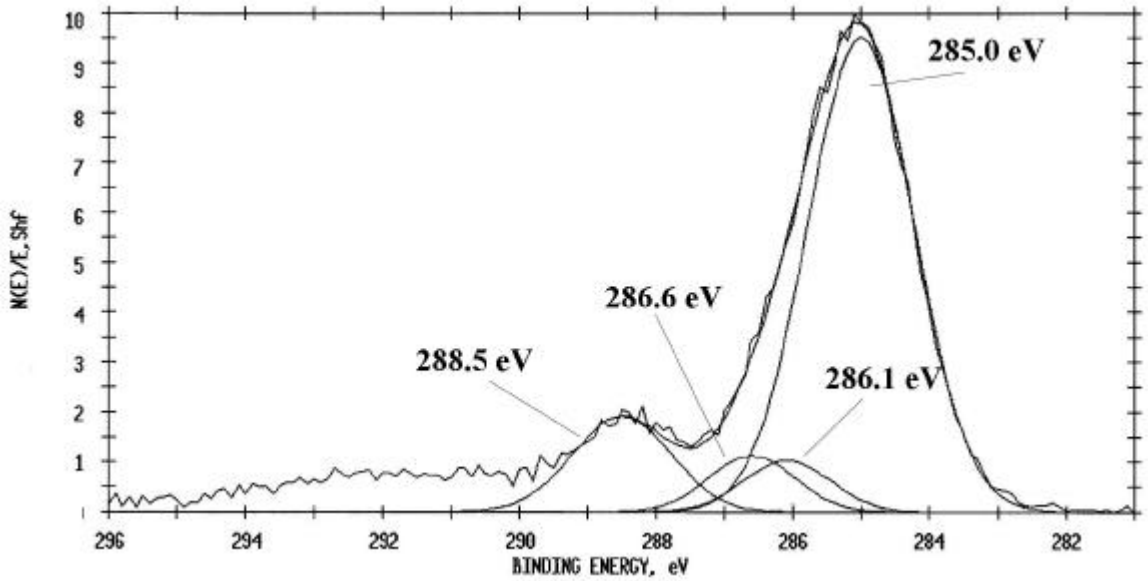

Figure 4.1: Curve-fit C 1s photopeak for cured FM-5 adhesive.

Table 4.2: Peak assignments for the curve-fit C 1s photopeak of cured FM-5 adhesive.[7]

Peak position (eV)	% of total area	Assignment
285.0	73.8	C-H/C-C
286.1	7.1	C-N
286.6	5.8	C-O (C from phenyl)
288.5	13.4	O=C-N (imide)

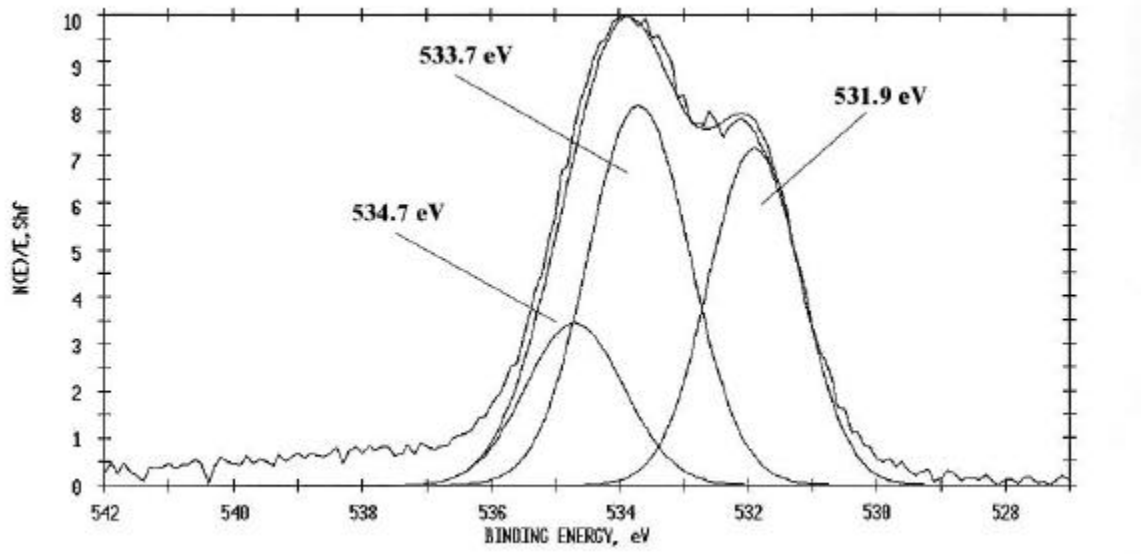

Figure 4.2: Curve-fit O 1s photopeak for cured FM-5 adhesive.

Table 4.3: Peak assignments for the curve-fit O 1s photopeak of cured FM-5 adhesive.[3]

Peak position (eV)	% of total area	Assignment
531.9	36.6	C=O
533.7	44.9	Si-O (Ref. 7)
534.7	18.6	C-O-C

4.2.2 Ti-6Al-4V

Table 4.4 shows XPS results for the differently treated substrates. The surface of as-received titanium alloy was contaminated with grease from the machining of the alloy. After a thorough cleaning with acetone and Scotch Brite© pads, most of carbonaceous contamination was removed, revealing the naturally occurring oxide layer. The carbon content decreased from 97.0 % to 48.2 % after acetone cleaning; the oxygen content increased from 2.7 % to 41.8 %, and the amount of titanium exposed increased from less than 0.5 % to 7.0 %.

Table 4.4: XPS analysis of various Ti-6Al-4V substrates.

Sample	% C	% O	% N	% Ti	% Al	% Si	% Na
As-received Ti-6Al-4V	97.0	2.7	trace	ND	ND	ND	ND
Acetone cleaned Ti-6Al-4V	48.2	41.8	ND	7.0	2.9	ND	ND
Polished Ti-6Al-4V[$] (0.3 micron grit)	45.2	40.3	1.9	7.3	3.3	ND	trace
Grit-blasted Ti-6Al-4V/ acetone cleaned	20.5	55.2	trace	4.2	1.9	17.5	2.4

[$]Ca (0.8 %) and Pb (0.4 %) were also detected.

The curve-fit C 1s photopeak of acetone cleaned Ti-6Al-4V is shown in Figure 4.3, and the peak assignments are listed in Table 4.5. These results are shown because they will be useful when determining failure modes. From the C 1s photopeak, the C-H/C-C contribution dominates (65.4 %). The surface contaminants also exhibited character from C-O, C=O, and O-C=O functional groups. The overall high percentage of carbon (48.2 %) on the substrate's surface

illustrated the extensive adsorption of low molecular weight organic contaminants onto the native oxide layer of Ti-6Al-4V.

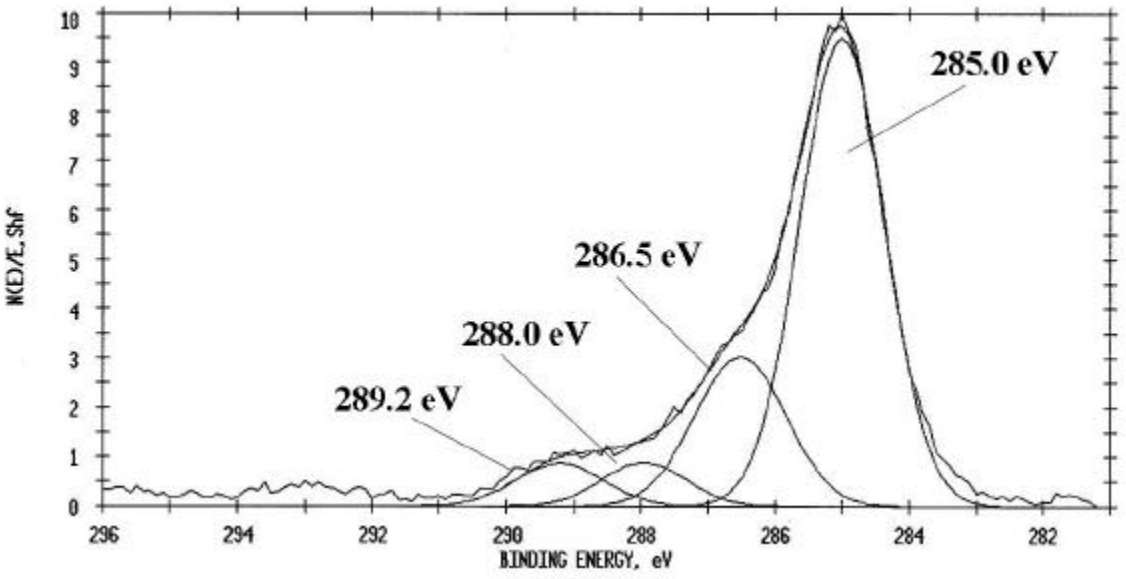

Figure 4.3: Curve-fit C 1s photopeak for acetone cleaned Ti-6Al-4V.

Table 4.5: Curve-fit C 1s photopeak assignments for acetone cleaned Ti-6Al-4V.

Peak position (eV)	% of total area	Assignment
285.0	65.4	C-H/C-C
286.5	22.3	C-O
288.0	6.1	C=O
289.2	6.2	O=C-O

The curve-fit O 1s photopeak for acetone cleaned Ti-6Al-4V is shown in Figure 4.4. It showed a dominant contribution from the photopeak at 530.2 eV, which is the binding energy of Ti-O.[8] The photopeaks at 531.9 and 533.3 eV arose from the C=O and C-O components, respectively, of the carbon contaminants.

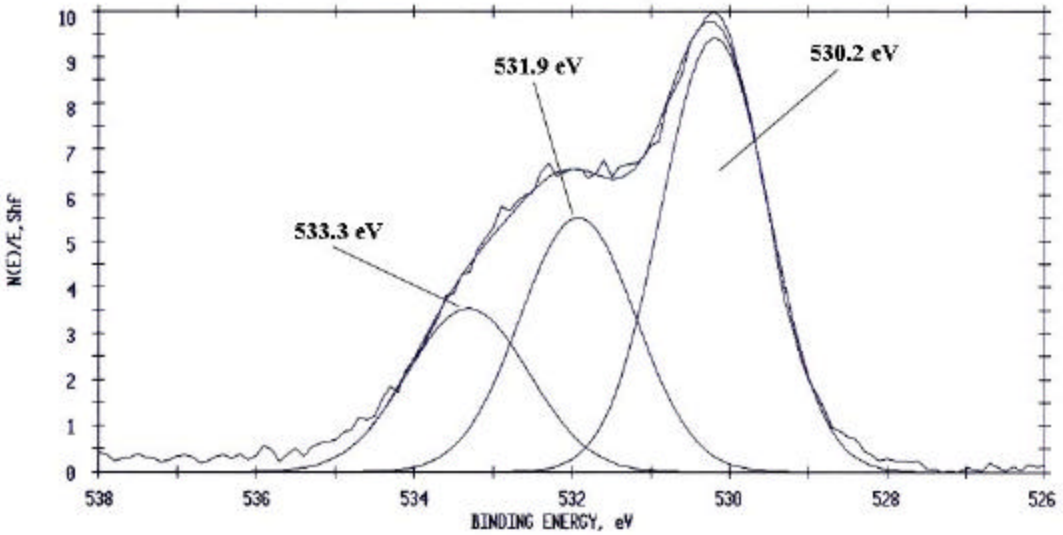

Figure 4.4: Curve-fit O 1s photopeak for acetone cleaned Ti-6Al-4V.

Polishing the Ti-6Al-4V with consecutively smaller grits of alumina caused slight compositional changes in its surface chemistry. The titanium contribution remained the same compared to acetone cleaned Ti-6Al-4V (7.0 vs. 7.3 %), and the carbon content was consistent, as well (48.2 % vs. 45.2 %). The biggest change in surface chemistry was the introduction of small amounts of Na, Ca, and Pb due to the polishing process.

Figure 4.5 is a SEM photomicrograph of acetone cleaned Ti-6Al-4V. At high magnification (5k), the grooves from the machining of the alloy dominate the surface features. Figure 4.6 is a SEM photomicrograph of polished Ti-6Al-4V at the same magnification. After polishing, the roughness was removed and the surface of the substrate was smooth and featureless.

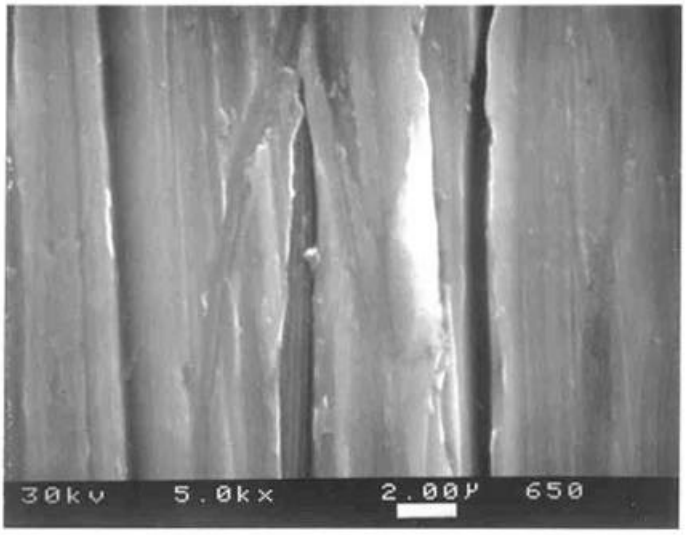

Figure 4.5: SEM photomicrograph of acetone cleaned Ti-6Al-4V.

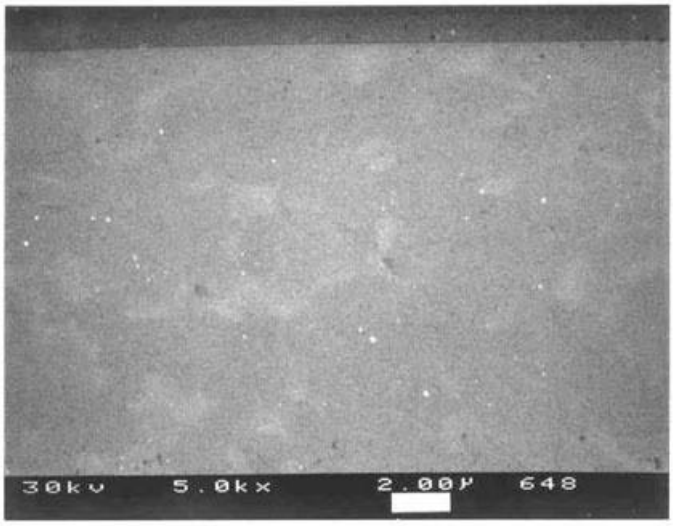

Figure 4.6: SEM photomicrograph of 0.3 μm grit-polished Ti-6Al-4V.

Grit-blasting the Ti-6Al-4V alloy resulted in substantial changes to the surface topography and in the surface chemical composition. The major effect was the decrease in carbon from 48.2 % to 20.5 % compared to the acetone cleaned alloy. The grit blasting also caused significant incorporation of silicon (17.5 %) onto the Ti-6Al-4V surface. This was undoubtedly due to the sand used during the grit blasting procedure, because the silicon was incorporated as SiO_2 (the binding energy of the silicon was 103.9 eV). The O 1s photopeak was

curve-fit (not shown) and approximately 64 % of the photopeak was assigned to Si, which was consistent with the atomic concentrations. Figure 4.7 shows a SEM photomicrograph of the grit-blasted substrate at high magnification. Notice it is substantially rougher than the original Ti-6Al-4V (Figure 4.5), and the grooves from the machining of the alloy have disappeared.

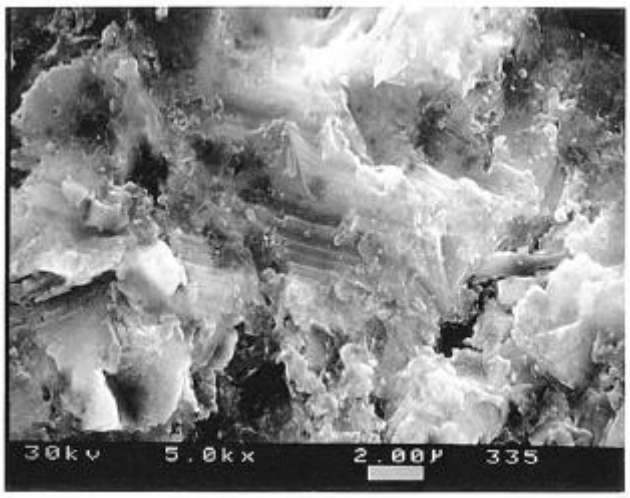

Figure 4.7: SEM photomicrograph of grit blasted Ti-6Al-4V.

4.2.3 Silicon Wafers

Silicon(111) wafers were used for the nanoindentation studies, and Table 4.6 lists the XPS results for an acetone cleaned wafer. The amount of carbon on the acetone cleaned silicon wafer was minimal (≈ 10 %). The silicon/oxygen ratio was not perfectly 1/2 because, as discussed in the next section, the oxide layer on the silicon was very thin (≈ 4 Å). Recall that the sampling depth of XPS is typically 50 Å, so the silicon below the oxide layer was being detected. Figure 4.8 confirms the detection of both SiO_2 (103.3 eV) and silicon metal (99.5 eV).[1]

Table 4.6: XPS analysis for acetone cleaned silicon wafer.

Sample	% C	% O	% N	% Si	% Na
Acetone cleaned silicon wafer	10.4	41.5	ND	47.8	ND

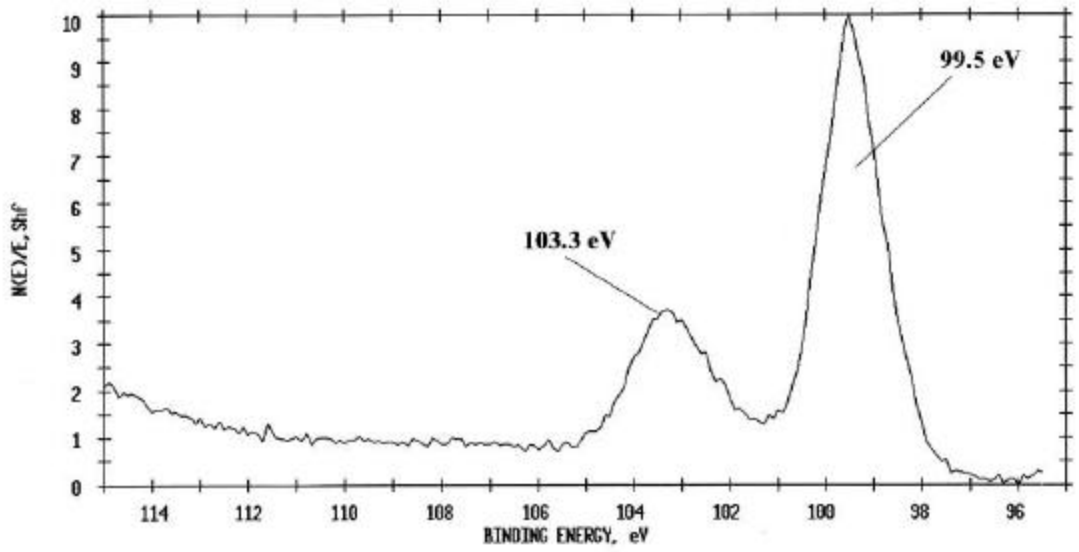

Figure 4.8: Si 2p photopeaks for an acetone cleaned silicon wafer.

4.3 Auger Electron Spectroscopy

The oxide layers on acetone cleaned Ti-6Al-4V, polished Ti-6Al-4V, and silicon were approximately 7, 62, and 4 Å, respectively, as measured by AES. These results emphasize that PP films are probably interacting with the oxides of the substrates, not with the actual metal. Therefore, the properties of the oxide will have a significant effect on the overall adhesive performance of the PP layer.

Table 4.7: AES results for key substrates.

Sample	Oxide thickness (Å)	Std. Dev. (Å)
Acetone cleaned Ti-6Al-4V	6.8	0.4
Polished Ti-6Al-4V	62.1	8.7
Acetone cleaned silicon wafer	3.7	1.6

4.4 Surface Energies

Surface energies were determined for the substrates using the harmonic mean method[9] as described in Chapter 3. Table 4.8 lists the contact angle measurement results. The surface energies varied from 49.7 dynes/cm for grit blasted Ti-6Al-4V to 61.1 dynes/cm for the silicon wafer. Most liquids will spread more on a higher surface energy substrate. Polished Ti-6Al-4V yielded a lower surface energy (50.0 dynes/cm) than acetone cleaned Ti-6Al-4V (59.6 dynes/cm), which indicated that liquids spread to a lesser degree on the polished sample. The surface energy for Ti-6Al-4V was consistent with the literature; Hammermesh and Crane[10] reported a surface energy of 64 dynes/cm for unpolished titanium.

The polar and dispersive components that make up the total surface energy gave additional insight into the surface characteristics of the substrates. For example, from the total surface energy values, it might appear that the surfaces of acetone cleaned Ti-6Al-4V and the silicon wafers were identical. However, the polar component (γ_s^p) of the surface energies were 28.3 and 33.3 dynes/cm for the acetone cleaned substrate and the wafer, respectively. The dispersive components (γ_s^d), which are typically assigned to van der Waals forces,[11] also differed (31.3 and 27.8 dynes/cm). So, although the substrates yielded the same overall surface energy, differences in the surface chemistry were detectable using the harmonic mean method. Namely, the surface of the silicon wafer was more polar than the surface of acetone cleaned Ti-6Al-4V.

Table 4.8: Contact angle and surface energy results for the various substrates.

Substrate	θ_{water} (degrees)	$\theta_{methylene\ iodide}$ (degrees)	γ^d (dynes/cm)	γ^p (dynes/cm)	γ (dynes/cm)
Acetone cleaned Ti-6Al-4V	44.8 ± 2.4	29.9 ± 2.6	31.3 ± 2.7	28.3 ± 2.5	59.6 ± 5.2
Polished Ti-6Al-4V	64.2 ± 2.1	31.2 ± 1.3	32.5 ± 1.6	17.4 ± 0.7	50.0 ± 2.1
Grit-blasted Ti-6Al-4V	69.0 ± 2.3	25.1 ± 1.8	35.4 ± 2.5	14.3 ± 1.0	49.7 ± 3.6
Silicon wafer	38.7 ± 1.6	38.5 ± 1.1	27.8 ± 1.1	33.3 ± 1.4	61.1 ± 2.5

The surface energies of polished Ti-6Al-4V and grit-blasted Ti-6Al-4V were essentially identical (50.0 and 49.7 dynes/cm, respectively). This was surprising, because low surface

energy liquids should appear to spread more on a rougher surface.[12] Typically, liquids penetrate and fill most of the hollows and pores of a rough surface, which results in the formation of a plane that is essentially part solid and part liquid and gives lower contact angles.[13] However, there were differences in the polar and dispersive components; the polished substrate showed a larger contribution from the polar component (17.4 vs. 14.3 dynes/cm) and less from the dispersive component (32.5 vs. 35.4 dynes/cm).

The differences in surface chemistry between the grit blasted and polished substrates could explain the absence of an obvious surface roughness effect. Recall from Section 4.2.2 that grit blasted Ti-6Al-4V showed ≈ 17.5 % silicon, while polished Ti-6Al-4V showed no silicon. Additionally, their carbon and oxygen contents were vastly different. Grit blasted Ti-6Al-4V had 20.5 % C and 55.2 % O, while polished Ti-6Al-4V had 45.2 % C and 40.3 % O. These differences in surface chemistry could have nullified any surface roughness effects.

4.5 Nanoindentation

The hardness and reduced Young's modulus of the acetone cleaned substrates of polished Ti-6Al-4V and silicon wafers were tested using an AFM nanoindenter as described in Chapter 3. The results shown in Table 4.9 are from an average of 12 - 15 indents per sample and showed that there were differences in the hardness and reduced Young's modulus values. Polished Ti-6Al-4V had a hardness of 5.8 GPa and a reduced modulus of 144 GPa, while the silicon wafer yielded a hardness of 10.0 GPa and a reduced modulus of 169 GPa, so the silicon substrate was the harder material.

The hardness for polished Ti-6Al-4V was slightly higher than a literature microhardness value for unpolished Ti-6Al-4V that was determined from a micro hardness tester. In a study by Wu et al,[14] bare Ti-6Al-4V coupon hardness was 3.5 ± 0.4 GPa. Hardness results were obtained using a Type M Shimadzu Micro Hardness Tester. An average of 10 indentation measurements was taken using a load of 2.5 x 10^{-2} kg.[14] The relatively rough (1.6 μm rms) as-received substrates were not polished.

The hardness of the silicon wafer was more consistent with a literature-reported value. Using a Berkovich diamond indenter attached to a Hysitron nanoindenter, Kulkarni and

Bhushan[15] measured the average hardness and reduced Young's modulus of silicon (100). They reported a hardness and reduced modulus of 13.2 and 141 GPa, respectively. The range of loads used for these measurements was 500 to 2000 μN.

Table 4.9: Nanomechanical properties for polished Ti-6Al-4V and silicon(111).

Sample	H (GPa)	Std. Dev. (GPa)	Er (GPa)	Std. Dev. (GPa)
Polished Ti-6Al-4V	5.8	0.6	143.5	9.8
Silicon (111) wafer	10.0	0.3	169.1	2.5

4.6 Single Lap Shear Strength

As control specimens, single lap shear samples of as received Ti-6Al-4V, acetone cleaned Ti-6Al-4V, polished Ti-6Al-4V, and grit blasted Ti-6Al-4V were prepared and tested. Table 4.10 lists the SLS strengths of the specimens tested. As-received Ti-6Al-4V, which was visibly contaminated with grease and oil, exhibited the lowest SLS strength of 1990 ± 300 psi. The failure was interfacial. Acetone cleaned Ti-6Al-4V performed well, giving partially cohesive failure and a SLS strength of 5023 ± 597 psi. Failure was visually estimated at 30 - 50 % cohesive.

To determine any influence of surface roughness on SLS strength, acetone cleaned Ti-6Al-4V, polished Ti-6Al-4V, and grit blasted Ti-6Al-4V were compared. The polished substrates gave interfacial failure and the lowest SLS strength average of 2920 ±1205. The lower SLS strength was probably a result of the decreased amount of mechanical interlocking possible because of the smooth surface. Residual polishing components on the surface of the polished Ti-6Al-4V could have also played a role.

Grit-blasting the surface increased the roughness of the substrate, but this did not translate into any SLS benefits for the system. Over-roughening of a surface can sometimes be detrimental because trapped air and surface contaminants can remain at the bottom of troughs and pores and impede bonding.[16] Additionally, the incorporation of silicon onto the grit-blasted surface could have negated any benefits from the mechanical roughening. The average SLS strength was 5095 ± 210 and the failure mode was visually estimated at 30 to 40 % cohesive. The slight differences in the surface chemistry of the three samples (see Section 4.2.2) inhibited

the correlation of wettability and adhesion to surface roughness alone, but this comparison gave a rough estimate of surface roughness effects.

Table 4.10: SLS strengths for the various substrates.

Sample	SLS strength (MPa)	SLS strength (psi)
As-received Ti-6Al-4V	13.7 ± 2.07	1990 ± 300
Acetone cleaned Ti-6Al-4V*	34.6 ± 4.12	5023 ± 597
Polished Ti-6Al-4V	20.1 ± 8.31	2920 ± 1205
Grit blasted Ti-6Al-4V	35.1 ± 1.45	5095 ± 210

*Average of 11 measurements

4.7 Detailed Analysis of Failure Mode

The failure mode of failed SLS joints could be quickly determined by a visual evaluation of the failed samples. When cohesive failure occurred (failure within the adhesive), glass scrim cloth from torn FM-5 was visible. When adhesive (interfacial) failure occurred, the adhesive remained completely intact on one side of the failed specimen, and metal was exposed on the other side. Unfortunately, such a quick visual analysis was inadequate for clarifying exactly where failure occurred. Because the PP films used as pretreatments were so thin, it was impossible to visually evaluate if failure occurred within the PP film, at one of its interfaces, within the top layer of the adhesive, or within the titanium oxide layer. To answer these questions, XPS analysis of the failed surfaces provided valuable insight.

Table 4.11 contains the experimental parameters for a sample that was pretreated with an oxygen plasma and then coated with plasma polymerized acetylene. The average SLS strength of specimens prepared with these substrates was 9.31 ± 0.90 MPa (1350 ± 130 psi). The XPS wide scan is shown in Figure 4.9 and it revealed that only carbon, oxygen, and nitrogen were present on the surface of the sample. Table 4.12 shows that the PP film composition was 83.3 % carbon, 10.1 % oxygen, and 6.6 % nitrogen. The absence of any titanium confirmed that the substrate was fully covered by the PP film.

Table 4.11: Details of the preparation of Ac.120s.200w.f10.Ar.

Pretreatment		Treatment	
Pressure before:	0 microns	Pressure before:	0 microns
Gas:	oxygen	Carrier gas:	argon
Flow rate:	20 sccm	Flow rate:	20 sccm
Pressure with flow:	3 microns	Pressure with flow:	0 microns
Pressure during activation	2 microns	Monomer gas:	acetylene
Power:	200 watts	Flow rate:	10 sccm
Time:	10 minutes	Pressure with both:	5 microns
		Pressure during activation:	0 microns
		Power:	200 watts
		Time:	2 minutes

Table 4.12: XPS results for non-bonded and failed Ac.120s.200w.f10.Ar samples.

Sample	% C	% O	% N	% Ti	% Si	% Al
Ac.120s.200w.f10.Ar non-bonded	83.3	10.1	6.6	ND	ND	ND
Ac.120s.200w.f10.Ar titanium side	47.6	33.8	3.3	7.2	6.8	1.3
Ac.120s.200w.f10.Ar adhesive side	79.8	12.6	5.5	ND	2.1	ND

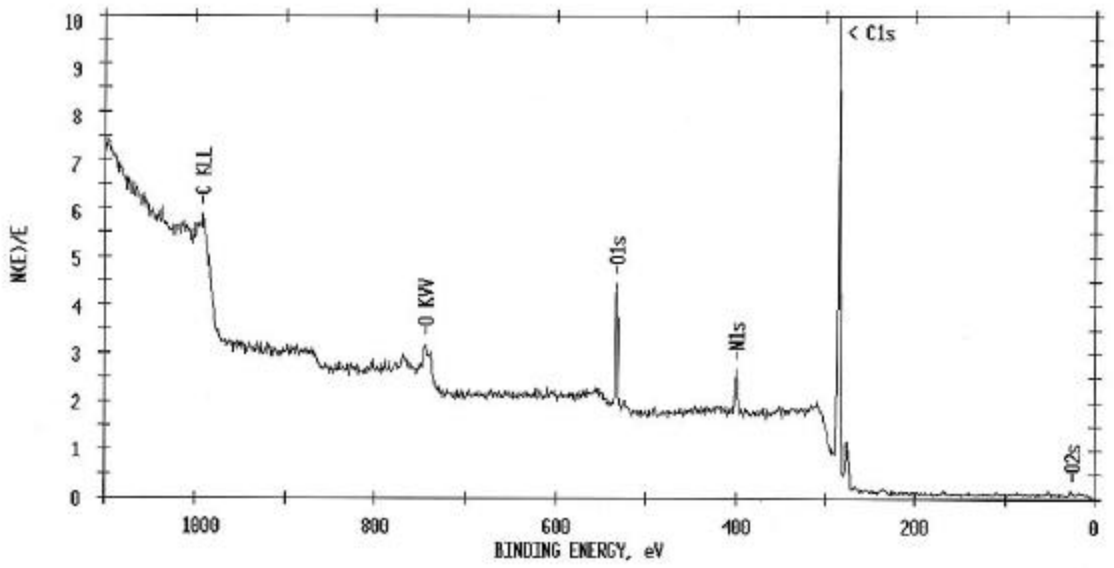

Figure 4.9: XPS wide scan for non-bonded Ac.120s.200w.f10.Ar.

The XPS results from the analysis of the failed surfaces of Ac.120s.200w.f10.Ar are also shown in Table 4.12. The carbon and oxygen content on the two failed surfaces was vastly different; 48 % C, 34 % O on the titanium side and 80 % C, 13 % O on the adhesive side.

Titanium was detected on the titanium failure surface (7 %), but not on the adhesive side. This was a major indication that failure probably occurred between the Ti-6Al-4V and the PP film.

Figure 4.10, Figure 4.11, and Figure 4.12 show the C 1s curve-fit photopeaks for non-bonded Ac.120s.200w.f10.Ar, the titanium failure surface of Ac.120s.200w.f10.Ar, and the adhesive failure side of Ac.120s.200w.f10.Ar, respectively. Notice the similarities of the curves. All three carbon peaks were resolved into identical components of similar area, indicating that the same type of carbon was present on all three surfaces. The C 1s photopeak for non-bonded Ac.120s.200w.f10.Ar and the C 1s photopeak for the adhesive failure side were identical. The C 1s photopeak assignments for non-bonded Ac.120s.200w.f10.Ar and the failed surfaces are given in Table 4.13.

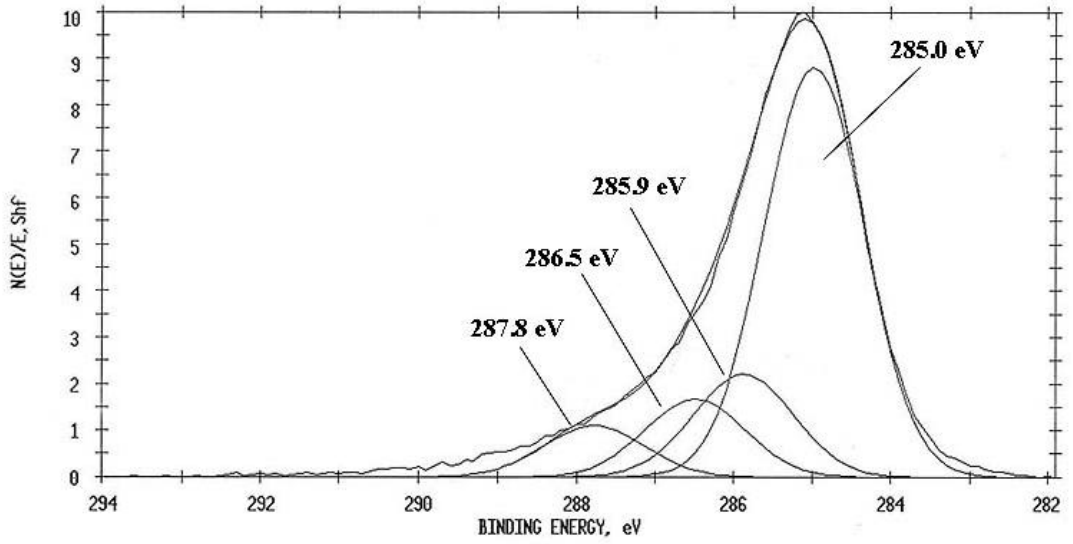

Figure 4.10: Curve-fit C 1s photopeak for non-bonded Ac.120s.200w.f10.Ar.

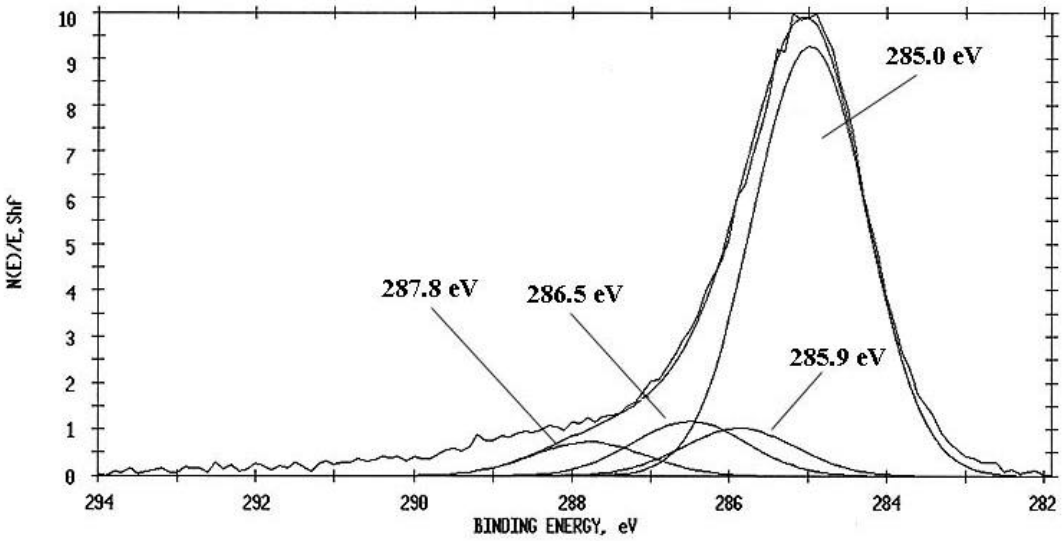

Figure 4.11: Curve-fit C 1s photopeak of the titanium failure side for Ac.120s.200w.f10.Ar.

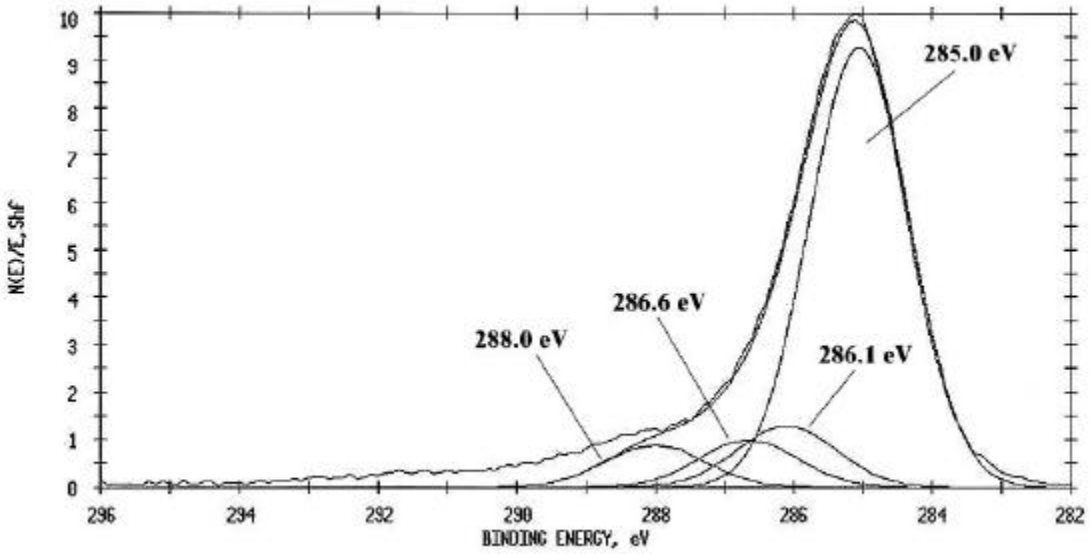

Figure 4.12: Curve-fit C 1s photopeak of the adhesive failure side for Ac.120s.200w.f10.Ar.

Table 4.13: Curve-fit C 1s assignments for non-bonded and failed Ac.120s.200w.f10.Ar.

Sample Ac.120s.200w.f10.Ar	% C-H/C-C	% C-N<	% C-O	% C=O
non-bonded	77.8	9.7	7.3	5.2
titanium side	76.0	8.4	9.6	6.0
adhesive side	74.8	9.8	8.4	7.0

The XPS oxygen peaks of the failed surfaces were also instructive. The O 1s photopeak of the non-bonded specimen (Figure 4.13) was very similar to the O 1s photopeak of the adhesive side of failure (Figure 4.15). Both O 1s curve-fit peaks were resolved into their C=O (≈ 531.7 eV) and C-O (≈ 532.9 eV) components at similar binding energies. This suggested that PP acetylene was present on the adhesive side of failure after debonding.

The oxygen peak of the titanium side of failure (Figure 4.14) closely resembled the oxygen peak of acetone cleaned titanium (Figure 4.4). They both showed large contributions from the titanium-oxygen bond (≈ 530.2 eV). The photopeak assigned at 532.1 eV of Figure 4.14 was due to SiO_2, while the peaks at 531.3 eV and 533.5 eV were assigned to C=O and C-O, respectively. The 531.3 eV photopeak also contained some contribution from Al_2O_3, which typically appears at 531.7 eV.[7] The O 1s curve-fit peak suggested that, while there may be a very thin amount of PP acetylene on the titanium side of failure, the amount of PP acetylene is thinner than the 50 Å sampling depth of the XPS. This information, coupled with the atomic concentration data, suggested that failure occurred at the Ti-6Al-4V/PP film interface. Figure 4.16 is a schematic of the proposed fracture path.

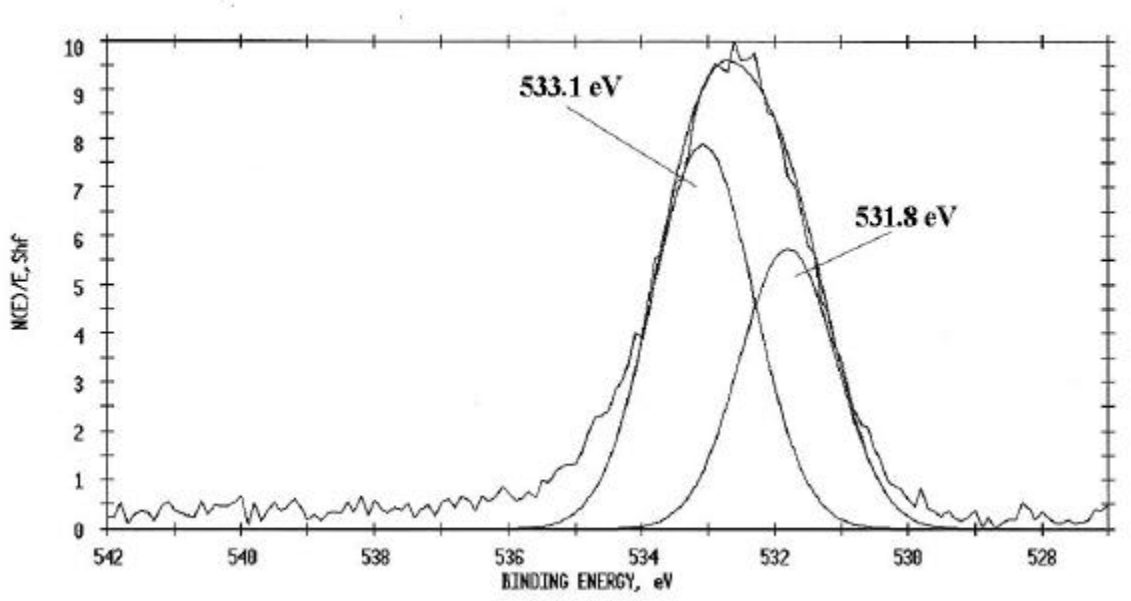

Figure 4.13: Curve-fit O 1s photopeak for non-bonded Ac.120s.200w.f10.Ar.

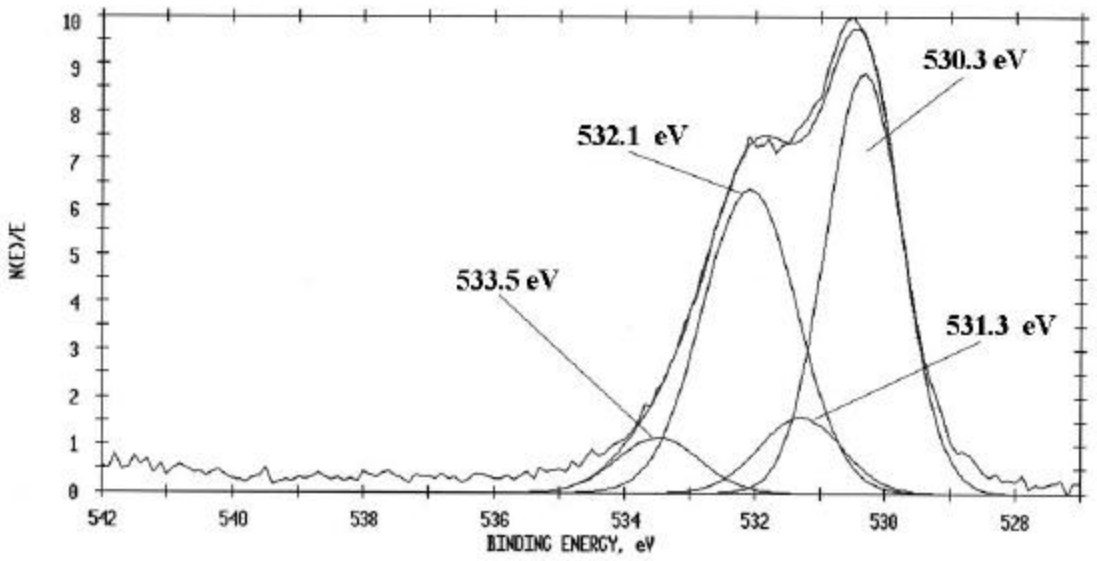

Figure 4.14: Curve-fit O 1s photopeak of the titanium side of failure for Ac.120s.200w.f10.Ar.

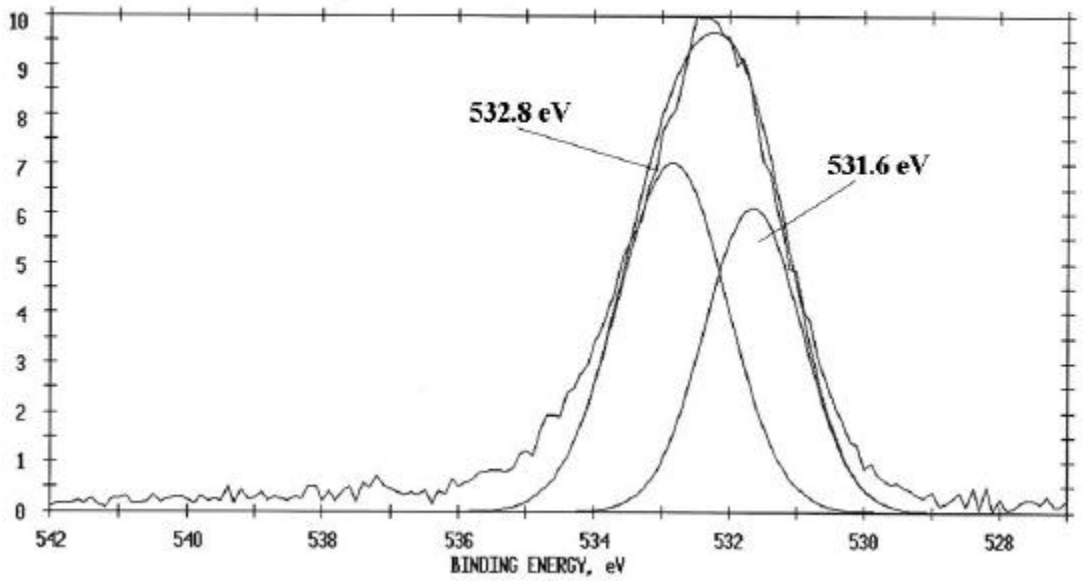

Figure 4.15: Curve-fit O 1s photopeak of the adhesive side of failure for Ac.120s.200w.f10.Ar.

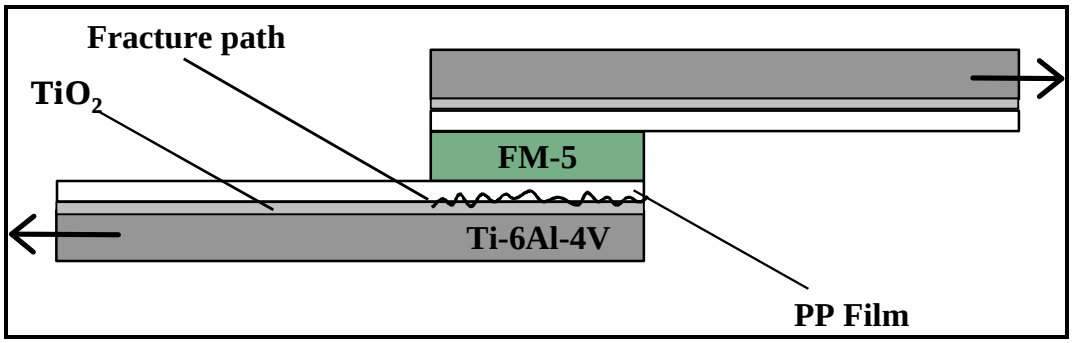

Figure 4.16: Proposed failure mode for Ac.120s.200w.f10.Ar.

The above statements illustrate how the failure mode was determined for each set of failed SLS samples. All of the samples utilizing PP acetylene films as a titanium surface treatment failed at the PP film/Ti-6Al-4V interface or within the PP film. Inagaki and Yasuda[17] reported a similar result from a study of thin films of PP acetylene. They deposited PP films onto various substrates and prepared and tested SLS specimens using an epoxy adhesive. The substrates of the heterogeneous lap joints included polyethylene, poly(tetrafluoroethylene), aluminum, and stainless steel. The PP film thickness on each substrate was 2060 Å, and in every case, failure occurred within the PP film. Single lap shear values varied from 253 to 686 psi, depending on the substrates.

Figure 4.17 shows some of the typical failure modes encountered during this study. Both sides of the failed SLS joints are shown. For the failed acetone cleaned specimen, the scrim cloth was visible and the cohesive failure was visually determined to be ≈ 30 %. The fracture path for this particular sample was interfacial on the two edges and cohesive in the middle of the bond. For the polished Ti-6Al-4V substrates, which showed poor SLS strength, failure was completely interfacial. The grit blasted specimens exhibited partially cohesive failure, but to a lesser degree than the acetone cleaned SLS joints. The failure was visually estimated at 20 - 25 % for the grit blasted samples. Sample Ac.120s.200w.f10.Ar, the featured specimen discussed above, exhibited failure between the metal and the PP film, as seen in the figure. The failure of Ac.120s.200w.f10.Ar was typical of most of the specimens that were primed with a PP film.

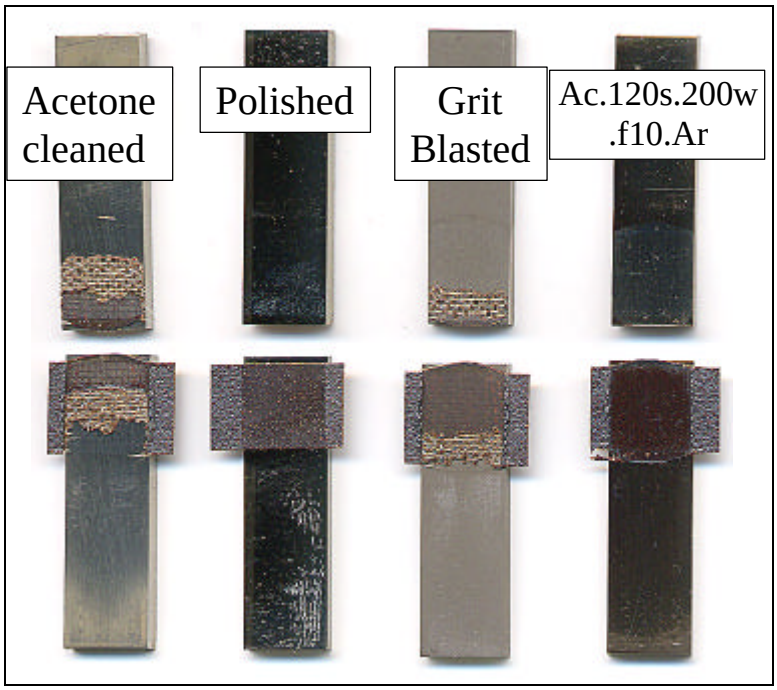

Figure 4.17: Various failure modes.

4.8 Conclusions

The important substrates and the adhesive used for this study were characterized using XPS, AES, contact angle measurements, and AFM nanoindentation tests. XPS results for the Ti-6Al-4V substrate showed that an acetone cleaning was essential to remove grease and other contaminants from the as-received alloy. The surface of acetone cleaned Ti-6Al-4V consisted of carbon (48.2 %), oxygen (41.8 %), titanium (7.0 %), and aluminum (2.9 %). The thickness of the oxide layer was ≈ 6.8 Å, as determined by AES. Polishing the Ti-6Al-4V removed most of the surface roughness that was present due to the machining of the metal. The surface composition of the polished Ti-6Al-4V was altered slightly by the polishing process, namely by the introduction of small amounts of Na, Ca, and Pb. The greatest effect was on the oxide thickness, which grew to ≈ 62 Å. Grit blasting the substrate significantly increased the surface roughness, but it also changed the surface chemistry by introducing a large percentage of SiO_2 (≈ 18 %), decreasing the carbon content to ≈ 21 %, and increasing the oxygen content to ≈ 55 %. The surface of acetone cleaned silicon was predominantly silicon (≈ 48 %) and oxygen (≈ 42 %),

with a much smaller amount of carbonaceous contaminants (≈ 10 %). The oxide layer thickness of acetone cleaned silicon was ≈ 3.7 Å.

Contact angle measurements and surface energy calculations using the harmonic mean method revealed that the silicon wafer had the largest overall surface energy (61.1 dynes/cm), followed by acetone cleaned Ti-6Al-4V (59.6 dynes/cm), polished Ti-6Al-4V (50.0 dynes/cm), and grit blasted Ti-6Al-4V (49.7 dynes/cm). Silicon had the largest polar surface energy component (33.3 dynes/cm) and the smallest dispersive surface energy component. Conversely, grit blasted Ti-6Al-4V had the smallest polar component (14.3 dynes/cm) and the largest dispersive component (35.4 dynes/cm). There were no obvious surface roughness effects on the surface energies.

AFM nanoindentation measurements made on polished Ti-6Al-4V and silicon showed that the silicon wafer was the harder material. Polished Ti-6Al-4V had a hardness of 5.8 GPa and a reduced modulus of 144 GPa, while the silicon wafer had a hardness of 10.0 GPa and a reduced modulus of 169 GPa.

The SLS strengths of control specimens were determined, and a detailed analysis of failure mode was discussed. Acetone cleaned and grit-blasted Ti-6Al-4V exhibited good SLS strength (5023 psi and 5095 psi, respectively), outperforming as-received Ti-6Al-4V (1990 psi), and polished Ti-6Al-4V (2920 psi). The failure mode of representative samples that were PP acetylene-primed (Ac.120s.200w.f10.Ar, 1350 psi) was determined through XPS analysis of the two sides of failure. Failure occurred at the PP film/substrate interface, or within the PP film very close to the substrate. This was in contrast to the behavior of SLS specimens prepared from acetone cleaned Ti-6Al-4V substrates, which exhibited mixed mode failure; failure was visually estimated at 30 % cohesive and 70 % interfacial. Grit blasted substrates also failed partially cohesively, but to a lesser extent (≈ 25 %). SLS specimens prepared from as-received Ti-6Al-4V and polished Ti-6Al-4V failed interfacially.

4.9 References

[1] C.D. Wagner; W.M. Riggs; L.E. Davis; J.F. Moulder; G.E. Muilenburg *Handbook of X-Ray Photoelectron Spectroscopy*; Perkin-Elmer: Eden Prarie, MN, 1979; p. 52.
[2] R.K. Giunta, Ph.D. Thesis, Virginia Tech, October 1999, Chapter 6.
[3] G. Beamson; D. Briggs *High Resolution XPS of Organic Polymers*; Wiley and Sons: New York, NY, 1992, p. 118.
[4] Y. Nakamura; Y. Suzuki; Y. Watanabe *Thin Solid Films* **1995**, *290*, 367.
[5] C. Girardeaux; E. Druet; P. Demoncy; M. Delamar *J. Electron Spectrosc. Relat. Phenom.* **1995**, *74*, 57.
[6] B.L. Holmes, Masters Thesis, Virginia Tech, 1994, Chapter 4.
[7] C.D. Wagner; W.M. Riggs; L.E. Davis; J.F. Moulder; G.E. Muilenburg *Handbook of X-Ray Photoelectron Spectroscopy*; Perkin-Elmer: Eden Prarie, MN, 1979; Appendix 1.
[8] C.D. Wagner; D.A. Zatko; R.H. Raymond *Anal. Chem.* **1980**, *52*, 1445.
[9] S. Wu *Polymer Interface and Adhesion*; Marcel Dekker, Inc.: New York, NY, 1982; Chapter 5.
[10] C.L. Hammermesh; L.W. Crane *J. Appl. Polym. Sci.* **1978**, *22*, 2395.
[11] D.J. Shaw *Colloid and Surface Chemistry*; Butterworth-Heinemann: Jordan Hill, Oxford, 1994; Chapter 4.
[12] W.A. Zisman In *Contact Angle, Wettability, and Adhesion*; R.F. Gould, Ed.; ACS: Washington, DC, 1964, Chapter 1.
[13] D.J. Shaw *Colloid and Surface Chemistry*; Butterworth-Heinemann: Jordan Hill, Oxford, 1994; Chapter 6.
[14] L. Wu; B.C. Holloway; D.P. Beesabathina; C. Kalil; D.M. Manos *Surf. Coat. Technol.* **2000**, *130*, 207.
[15] A.V. Kulkarni; B. Bhushan *J. Mater. Res.* **1997**, *12*, 2707.
[16] G.D. Davis *Surf. Interface Anal.* **1991**, *17*, 439.
[17] N. Inagaki; H. Yasuda *J. Appl. Polym. Sci.* **1981**, *26*, 3333.

5.0 Oxygen Plasma Treatments

5.1 Introduction

Plasmas are capable of removing molecular layers from polymer surfaces and are effective at removing organic contamination from inorganic surfaces. Plasma treatments of metals with non-polymerizable gases typically result in hyper-clean surfaces that yield stronger bonds than traditionally cleaned surfaces.[1] The free radicals created by low pressure gas plasmas are responsible for most of the surface changes. The removal of carbonaceous contaminants is the major reason for improved bonding to plasma treated surfaces.[2] Plasma etching is an important pretreatment alternative to traditional solution cleaning, and is effective at removing weak boundary layers.

Kruger et al[3] studied plasma cleaning processes and their effects on steel. An oxygen plasma treatment removed carbonaceous contaminants and created a well-defined Fe_2O_3 surface. They noticed a dependence of SLS strength on the cleanliness of the steel, as determined by the XPS C 1s/Fe 2p ratio. Polyurethane was the adhesive, and SLS strength decreased linearly from a high of 30 MPa to a low of 7 MPa when the C 1s/Fe 2p ratio was varied from 3 to 13. Low-pressure oxygen and hydrogen plasma treated steel gave the cleanest surfaces and yielded the best SLS strengths (≈ 30 MPa).

During the initial stages of this investigation, a suitable plasma pretreatment that could further clean the substrates prior to deposition was sought. Oxygen plasma pretreatments outperformed argon, nitrogen, helium, and ammonia pretreatments in terms of their ability to thoroughly clean a substrate and enhance the SLS strength. In an oxygen discharge, there are three main charge carriers: the electrons, the O^+ ion and the O^- ion. There are also several minority species, such as O_2^+, O_2^-, O_3^-, metastables and other various free radicals.[1] O_2 plasma etches ultimately yield CO, CO_2, and H_2O as the low molecular weight byproducts of cleaning.[2]

Early experiments showed that oxygen plasma treatment removed excess carbonaceous contaminants from the surface of Ti-6Al-4V while introducing a stable, more uniform oxide layer. The XPS results from Chapter 4 revealed that a typical Ti-6Al-4V sample that was

thoroughly cleaned with acetone and a Scotch Brite® scouring pad showed a surface composition of ≈ 48 % carbon and ≈ 7 % titanium. After a typical oxygen plasma pretreatment, the carbon content decreased to ≈ 28 % and the amount of exposed titanium increased to ≈ 15 %. Additionally, average SLS strength typically increased by over 3.45 MPa (500 psi).

The optimization of SLS strength was desired for the Ti-6Al-4V/FM-5 system, and oxygen plasma pretreatment processes looked promising. However, optimizing the oxygen plasma pretreatment process was daunting because of the large number of plasma parameters that influence the final chemistry, morphology, and mechanical properties of the substrate. The traditional approach of only changing one variable at a time would have been very time consuming, and the results would have neglected any interactions between the variables. A designed experimental approach was adopted to obtain the most meaningful results from the fewest number of experiments. The process of properly designing an experiment is well documented.[4, 5, 6]

Although the design of experiments (DOE) approach requires much more pre-experimental planning, it greatly enhances the validity and usefulness of the developed model because it assesses the effects of input variables and the interactions between them. The advantages of using statistical design of experiments include: 1) experimental error is used as a basis of evaluation, 2) the interaction between variables is accounted for and measured, 3) the number of measurements is minimized to achieve preset goals, 4) several optimization criteria are handled simultaneously, and 5) there is high confidence that the conclusions will be valid over the experimental region.

Following procedures outlined in the literature and utilizing an experimental design program called Design Expert Plus®, a 2-level factorial design (2^3) was developed for the oxygen plasma treatment of titanium alloy. The main objective of the DOE was to optimize the SLS strength of the Ti-6Al-4V/FM-5 system with respect to treatment time, power input, and oxygen flow rate.

5.2 Experimental

The DOE approach dictates that the best results are obtained when a full-factorial test matrix is developed and all possible combinations of variables are tested. A three factorial design with 2 levels set for each variable requires 8 experiments. The factors and levels are shown in Table 5.1. The treatment time, input power, and flow rate were assigned the symbols A, B, and C, respectively. The code -1 refers to the low level tested and +1 refers to the high level tested. The levels of the factors were selected based on reasonable parameters for an industrial plasma process. The limits of the custom-built plasma reactor processing system were also considered. The three variables of power input, treatment time, and flow rate were assigned limits of 50 to 300 watts, 1 to 30 minutes, and 20 to 50 sccm, respectively. The samples were cleaned with acetone and Scotch Brite® pads before plasma treatment. After plasma treatment, the reaction chamber was purged with oxygen for 15 minutes before the samples were exposed to the atmosphere and placed in a desiccator for analysis or bonding.

Table 5.1: DOE experimental factors and levels.

Factors	Symbol	Low (-1)	High (+1)
Treatment time (minutes)	A	1	30
Input power (Watts)	B	50	300
Flow rate (sccm)	C	20	50

Table 5.2 contains the test matrix for the eight experiments. In the table, TT represents treatment time, IP represents input power, and FR represents flow rate. The order of the runs was randomly set by the experimental design program. This randomization minimized the chance that extraneous variable effects were confused with the effects of the designed and controlled variables. Failure to randomize can lead to unknown errors in conclusions.

Table 5.2: The three factor - 2 level experimental design for oxygen plasma pretreatments.

Run	(A) Treatment time (minutes)	TT level	(B) Input power (watts)	IP level	(C) Flow rate (sccm)	FR level
1	1	-1	300	+1	20	-1
2	30	+1	300	+1	20	-1
3	1	-1	300	+1	50	+1
4	1	-1	50	-1	50	+1
5	30	+1	50	-1	20	-1
6	1	-1	50	-1	20	-1
7	30	+1	50	-1	50	+1
8	30	+1	300	+1	50	+1

Graphical and statistical analysis were performed on the results of the experiments listed in Table 5.2. A predictive equation for the response (the SLS strength) was derived using the average effects of each factor and 3-dimensional surface contour plots were generated using Response Surface Methodology (RSM). RSM is useful for mapping a response surface over a particular region of interest, for optimizing that response, and for the quick selection of efficient operating conditions to achieve desired responses.

There were 7 degrees of freedom between the eight treatment combinations in the 2^3 design. There were three degrees of freedom for the main effects, plus 4 degrees of freedom for interactions (AB, AC, BC, and ABC). Interaction plots were developed to determine if there were any strong interactions between factors. Two factors, A and B, are said to interact if the difference in mean responses for the 2 levels of one factor is not constant across levels of a second factor. The ABC interaction is defined as the average difference between the AB interaction for the 2 different levels of C.

5.3 Experimental Design Results

The treatment conditions along with the oxide thickness after pretreatment (AES) and the XPS atomic concentrations of the substrates following pretreatment are shown in Table 5.3. Not shown in the table are the atomic concentrations of aluminum for each substrate, which varied from ≈ 3 - 4 %. The results are arranged in the order the experiments were conducted, and Run 6

is highlighted because it gave the best overall SLS strength. The SLS strengths reported in the table are the average of three measurements. The three measurements were not considered to be true replicates because they were treated in the same reactor during the same experiment. Therefore, they were not treated as replicates in the model.

The oxide thickness varied from 60 to 110 Å after oxygen plasma treatment, which was a large increase from the approximately 7 Å thick oxide layer that was present on acetone cleaned Ti-6Al-4V (see Figure 5.1). This growth in the oxide layer was expected, as it has been reported in the literature. In a study of plasma treatments for the corrosion protection of steel, Grundmeier et al[7] observed a thickening of the iron oxide layer after O_2 plasma treatment. The oxide layer grew to over 60 Å from an initial thickness 30 Å. FT-IRRA (IR under grazing incidence) spectra showed a loss of amorphous organic contaminants and the formation of iron oxy-hydroxide (amorphous FeOOH) and iron oxide (alpha-Fe_2O_3). It was assumed that the thickness of the additional oxide produced resulted from the high field mechanism of oxide growth initiated by the adsorption of oxide ions and hydroxides on top of the iron oxide. This type of growth was also observed for the plasma oxidation of lead by Fromhold.[8]

Table 5.3: Factors and responses considered for oxygen plasma treatments.

	Factor	Factor	Factor	Response	Response	Response	Response	Response
Run	Treatment time	Input power	Flow rate	SLS Strength	Oxide Thickness	Carbon Conc.	Oxygen Conc.	Titanium Conc.
Unit	minutes	watts	sccm	psi	Å	atomic %	atomic %	atomic %
1	1	300	20	5366 ± 885	58.3 ± 7.5	27.8	51.0	16.5
2	30	300	20	3508 ± 323	106 ± 15.6	23.7	53.6	15.1
3	1	300	50	4343 ± 668	61.1 ± 2.0	29.9	50.3	15.5
4	1	50	50	5044 ± 483	59.9 ± 5.9	25.5	52.9	17.0
5	30	50	20	5135 ± 430	68.6 ± 5.7	26.8	52.6	16.4
6	1	50	20	5682 ± 503	66.5 ± 13.0	26.6	51.9	17.2
7	30	50	50	5093 ± 401	106 ± 6.1	25.9	52.8	16.7
8	30	300	50	5461 ± 583	88.9 ± 14.5	27.5	52.2	16.1

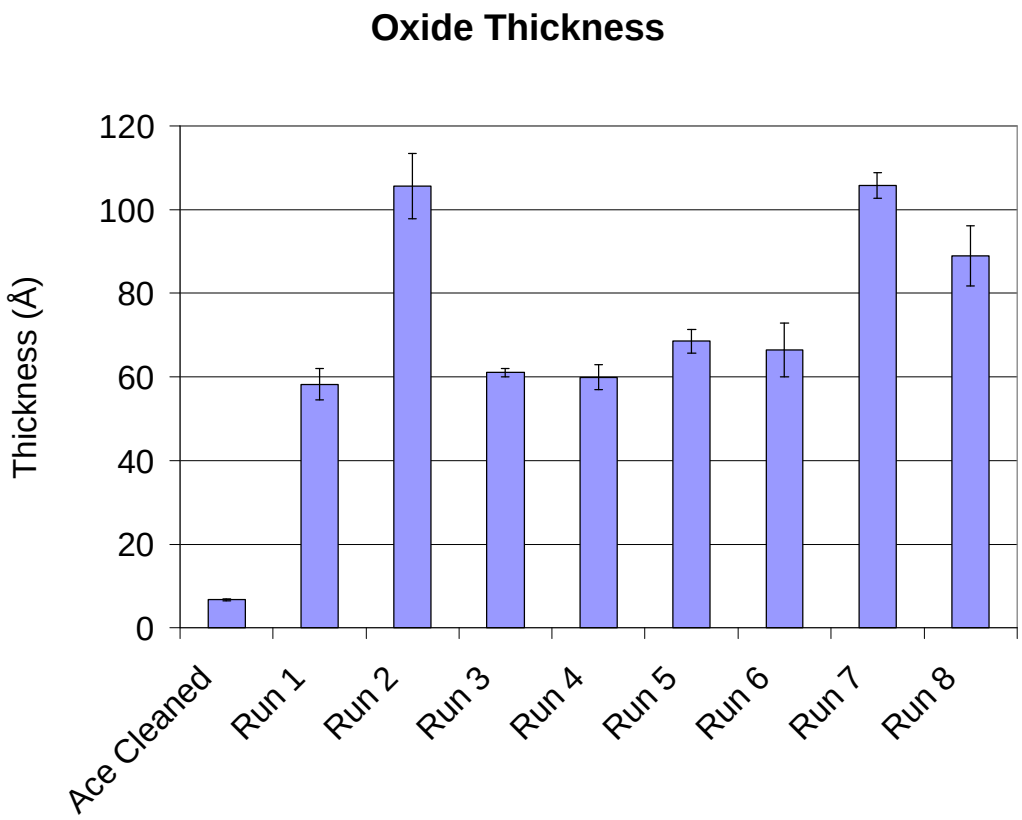

Figure 5.1: Oxide thicknesses of the oxygen plasma treated substrates.

Recall from Chapter 4 that the surface of acetone cleaned Ti-6Al-4V was ≈ 48 % carbon, 42 % oxygen, 7 % Ti, and 3 % Al. The oxygen plasma treatment decreased the carbon content on the surface of Ti-6Al-4V to below 30 %, increased the oxygen content to over 50 %, and increased the titanium content to over 15 %. Among the oxygen plasma treated samples, however, the surface compositions remained relatively constant, indicating that most of the cleaning occurred within the first 1 minute of plasma exposure (see Figure 5.2). Oxygen plasma treatments induced significant changes in the surface chemistry, and in some cases, these changes resulted in an increase in SLS strength of the bonded system from the acetone cleaned value of 5023 ± 597 psi reported in Chapter 4.

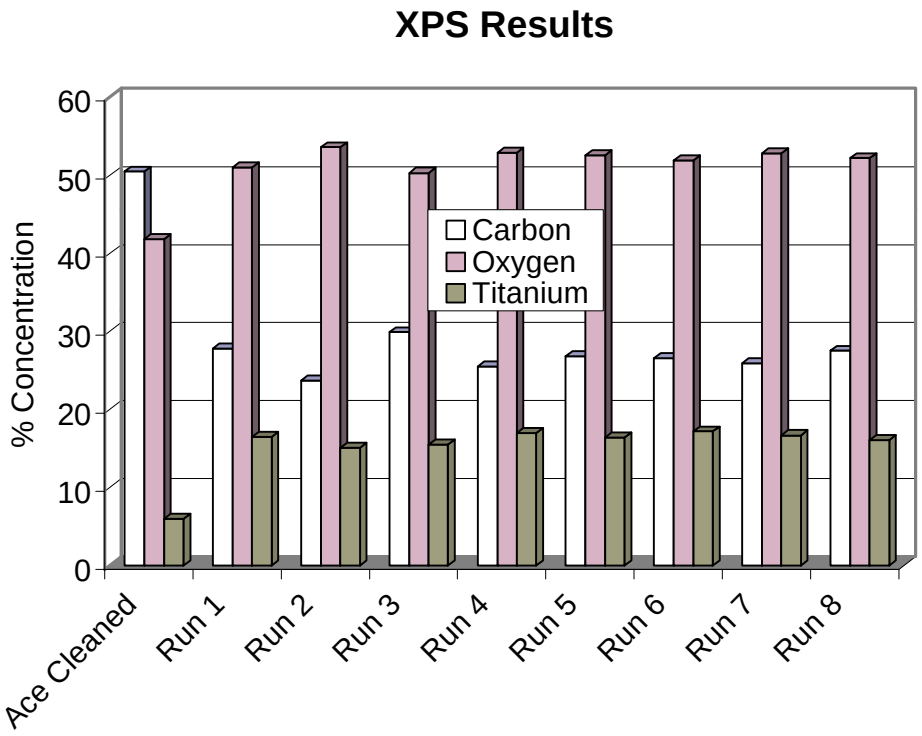

Figure 5.2: XPS analysis of the oxygen plasma treated substrates.

5.3.1 Assessment of the Model

Unfortunately, the standard deviations were large for the SLS strength measurements, and no true replicates were performed to confirm the results. Therefore, caution should be used when assessing the model and evaluating the results. This DOE served as a preliminary look into what variables are important for oxygen plasma pretreatments. The model was also useful for ascertaining how the variables interacted and what interactions were most important.

Several features of the DOE results can be analyzed to assess the validity of the model. An analysis of variance (ANOVA) allows one to decide whether the differences among sample means are large enough to imply that the population means are different.[9] The ANOVA table showed the Model Probability>F to be 0.0855. This term, commonly called the p-value, is the probability that the trends associated with the data were completely random. So, for this set of data, there was approximately a 9 % chance that the SLS changes were not a result of the changes in the variables. Therefore, the null hypothesis, which assumes that the variables had no

effects or interactions, was disproved. Typically, a p-value of less than 0.10 indicates that there were variable effects, while values larger than 0.10 suggest that the variables had no significance.[10]

The post-ANOVA t-test p-values were inspected and are listed in Table 5.4. Values of 0.10 or lower indicate significance and that the experimental error was low enough so that real effects could be seen.[10]

Table 5.4: ANOVA t-test results.

Factor	[t]
A	0.1223
B	0.0671
C	0.4893
AC	0.0429
BC	0.0945
ABC	0.0643

The half normal % probability is plotted against the effect in Figure 5.3. The half normal % probability is the cumulative probability of getting a result at or below any given level. The half normal % probability ignores the sign of the effect. Thus, large absolute values show up as outliers in the upper right hand section of the graph and are easily identified as important effects. The differential effect from the high setting to the low setting of each factor (the x-axis of Figure 5.3) was determined by taking the average response of an effect at its high setting and subtracting the average response of the effect at its low setting. Factors to the right of the guideline in Figure 5.3 represent factors that have a significant effect on the response. Factors C and AB have an insignificant effect on the response, while factor AC has the largest impact on the response. Therefore, factors C and AB were not significant and therefore should not be included in the model. Factor C was the flow rate, which determined the concentration of O_2 in the system. The flow rate may not have a significant effect because at these two flow rates, the rate determining factor might be the input power instead of the supply of oxygen into the system. This would also explain the fact that the flow rate/input power interaction (BC) is significant (Figure 5.3). Although C was determined to be a non-factor, it was kept in the model to maintain proper hierarchy (all main effects present in the interactions should be included in the model).

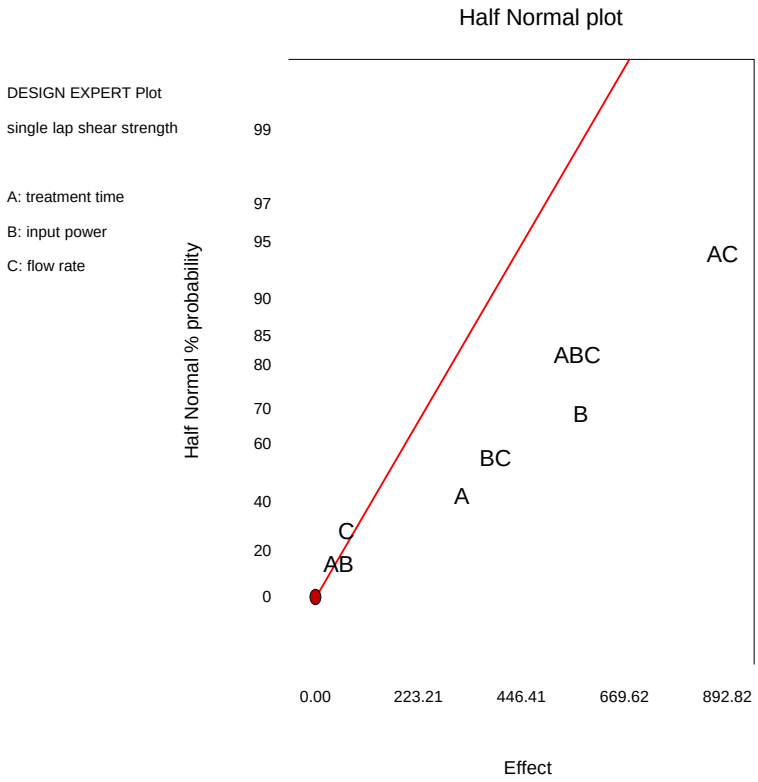

Figure 5.3: Half normal plot for DOE.

A check of the normality assumption was made by constructing a normal probability plot of the residuals. Figure 5.4 shows the normal probability plot of the residuals. Residuals are the difference between the observed value and the fitted value for a response. A studentized residual is simply a residual divided by its associated standard error. They typically reflect noise in the observed data. If the ANOVA is to be validated, the points should fall approximately on a straight line, as shown in Figure 5.4.[11] If the errors were not normally distributed, then there would be a pattern in the plot and a transformation of the response might be needed for the assumptions of the ANOVA methods to be met. Probability plotting is basically a technique for determining whether sample data conform to a hypothesized distribution. The construction of a probability plot is described elsewhere.[12]

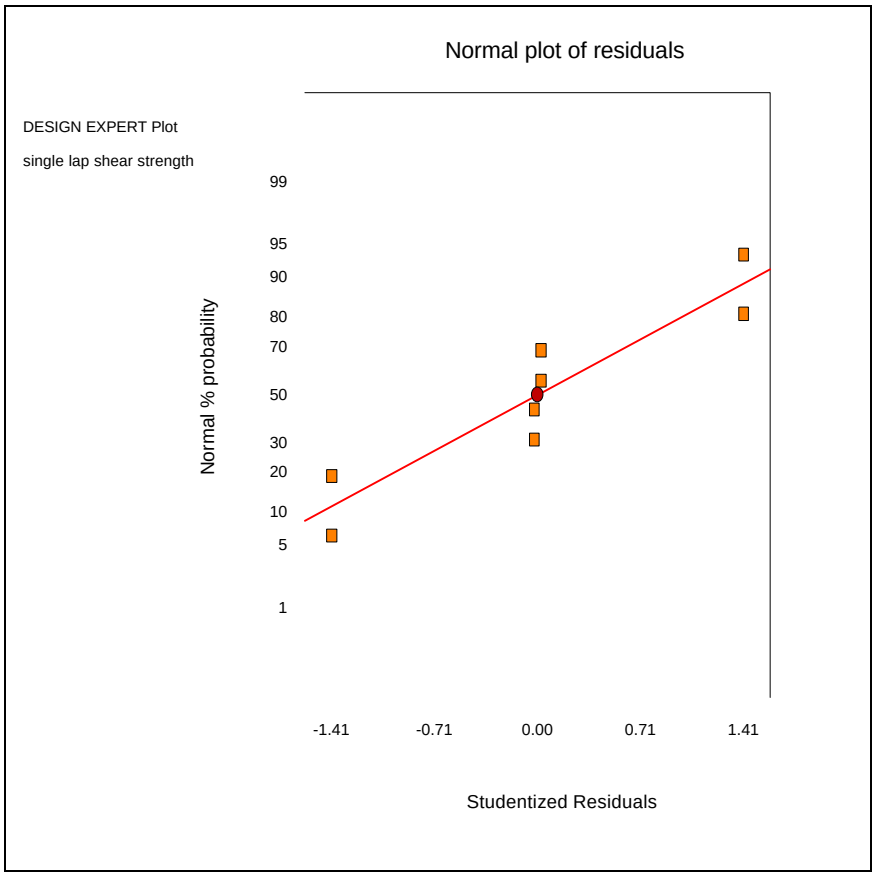

Figure 5.4: Normal probability plot of residuals.

Figure 5.5 shows the plot of studentized residuals vs. predicted response. The ANOVA method assumes that the errors are independent of the magnitude of the data, therefore the data points of this plot should be randomly and evenly distributed about the zero line, as shown in Figure 5.5. If the variance expanded with larger predicted values, then a transformation of the response might be needed. Since this was not seen, the assumption of constant variance regardless of the size of the response was verified.

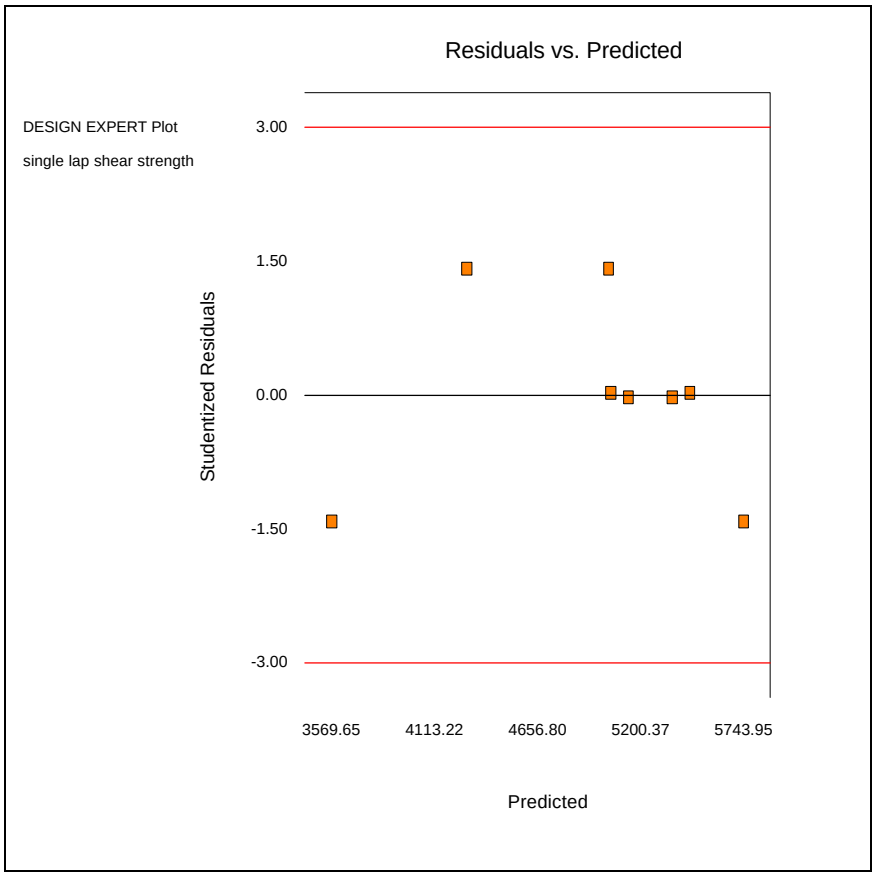

Figure 5.5: Residuals vs. predicted.

5.3.2 Determining the Equation

The average response (SLS_{ave}) was taken by adding all of the SLS strengths shown in Table 5.3 and dividing by the number of experiments. The value of the differential effect from the high to low setting for each factor was then determined. For example, the differential effect of factor A was found by averaging the response of A at the high setting and subtracting the average response of A at the low setting (see Equation 5.1).

Equation 5.1

$$DA = (A_{+})_{ave} - (A_{-})_{ave}$$
$$= [(3508 + 5093 + 5135 + 5461)/4] - [(4343 + 5044 + 5366 + 5682)/4]$$
$$= 309.5$$

where ΔA is the differential factor for A, $(A_{+})_{ave}$ is the average response of A at its high setting, and $(A_{-})_{ave}$ is the average response of A at its low setting. The differential effects for factor interactions can also be found by essentially the same procedure. To determine whether an interaction is at its high or low setting, the levels of the individual factor (shown in Table 5.2) must be multiplied. For example, to determine the setting of the AB interaction for Run 1, multiply (-1) and (+1). The result is (-1), so Run 1 is a low setting for the AB interaction.

The differential factors were then used to formulate the predictive equation. SLS_{pred} represents the predicted response in Equation 5.2. Because factors C and AB were determined to be insignificant, they were not included in the equation.

Equation 5.2

$$SLS_{pred} = SLS_{ave} + (DA/2)A + (DB/2)B + (DAC/2)AC + (DBC)BC + (DABC/2)ABC$$

Where A is the coded treatment time (-1, +1), B is the coded input power (-1, +1), C is the coded flow rate (-1, +1), and the multiplication of two main factors represents the interaction between two main factors. The final coded equation is given in Equation 5.3.

Equation 5.3

$$SLS\ Strength = 4954.06 - 154.86(A) - 284.59(B) + 446.41(AC) + 201.21(BC) + 297.26(ABC)$$

The final equation in terms of actual factors is given in Equation 5.4. Design Expert Plus© calculated the factor coefficients using least squares estimates.

Equation 5.4

$$SLS\ Strength = 6133.29 - 12.64(TT) + 0.16(IP) + 0.14(TT)(FR) - 0.62(IP)(FR) + 0.011(TT)(IP)(FR)$$

5.3.3 Interactions

One of the major advantages of DOE analysis is the ability to assign the response to interactions between two main factors. An interaction is said to occur when the combined change

of changing two factors produces an effect different from that of the sum of effects expected by changing either factor alone. An interaction graph is constructed by plotting the average response for each level of factor B as a function of factor A. When strong interactions exist between factors, the interaction diagrams show intersecting lines or lines that verge towards each other. When no interactions exist, the lines are typically parallel.

Figure 5.6 shows the interaction plot of factors A and B (treatment time and input power). The lines are almost perfectly parallel, which is a sign that the factors do not interact. This confirms that AB interactions were insignificant and should not have been included in the model. The AB interaction plot was in contrast to the appearance of the AC interaction graph shown in Figure 5.7. The AC interactions are predicted to be strong, as depicted by the intersecting lines. Figure 5.8 shows the BC interaction diagram. Again, the lines intersect, indicating that there are strong interactions between the factors B and C.

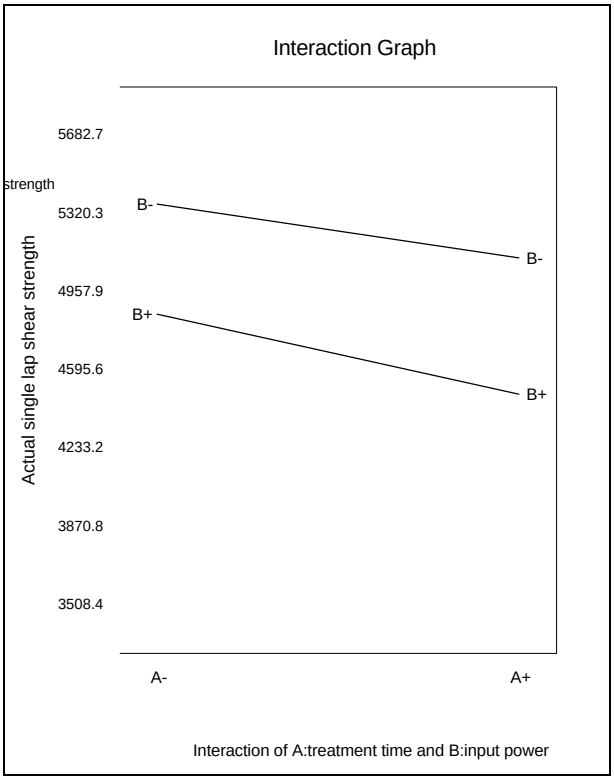

Figure 5.6: Interaction graph of factors A and B.

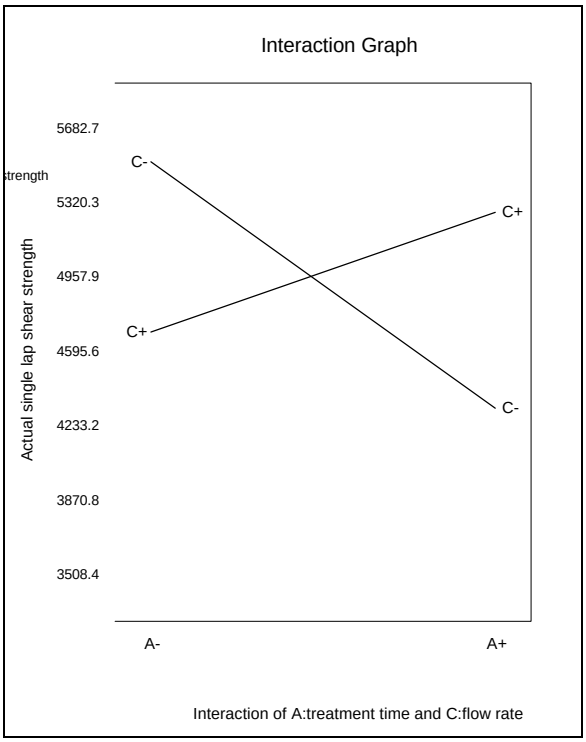

Figure 5.7: Interaction graph of factors A and C.

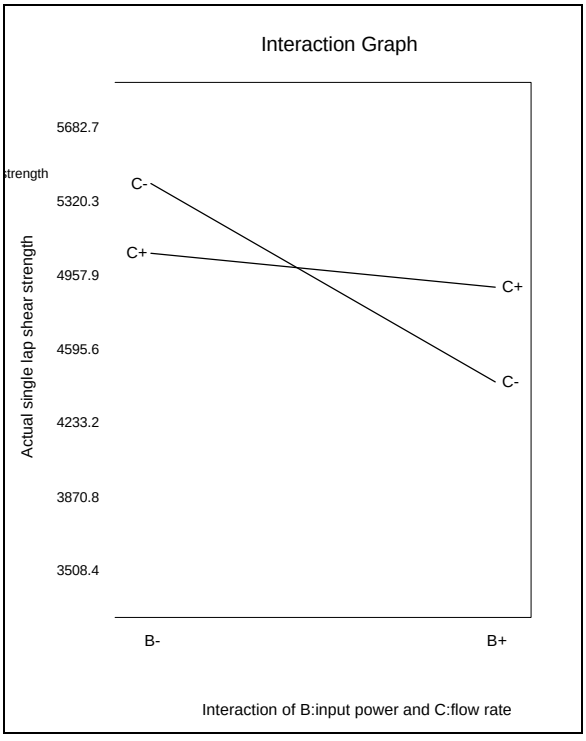

Figure 5.8: Interaction graph of factors B and C.

5.3.4 RSM Results

Figure 5.9 and Figure 5.10 show the three-dimensional contour plots for oxygen flow rates of 20 sccm and 50 sccm, respectively. SLS strength was the response of interest, and the areas of the surface plot with the highest SLS strength are clearly shown. At the low flow rate, SLS strength was optimized using short treatment times and low input power. As treatment time was increased, the SLS strength decreased. The model predicts that long treatment times and high input power yield the lowest SLS strength for this flow rate.

At high flow rates (Figure 5.10), SLS strength was optimized using long treatment times and high input power. In contrast to the behavior at 20 sccm, increasing the treatment time led to an increase in the SLS strength. The model predicts that SLS strength is at a minimum when the input power is high and the treatment time is low.

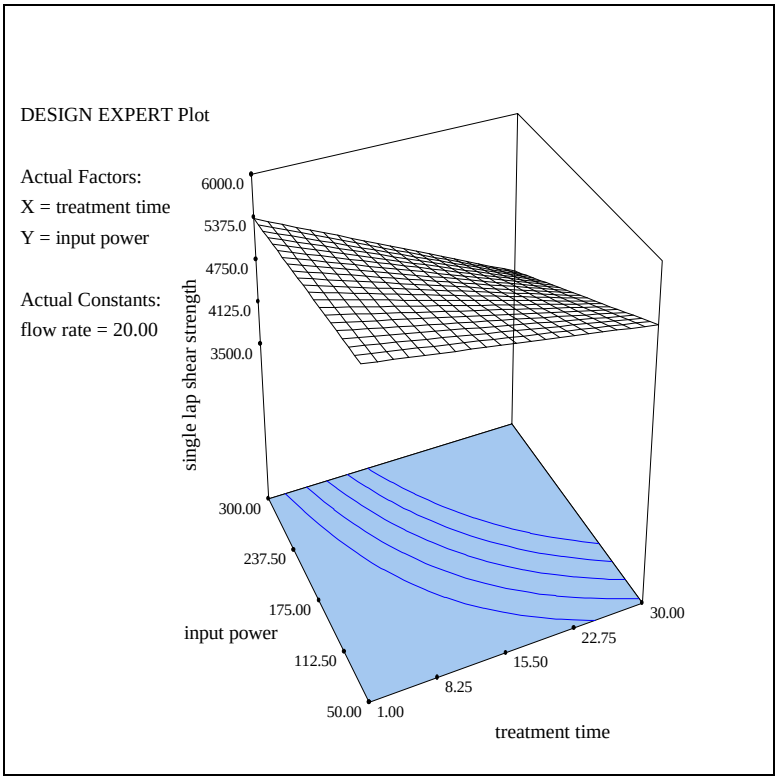

Figure 5.9: RSM contour plot at a flow rate of 20 sccm.

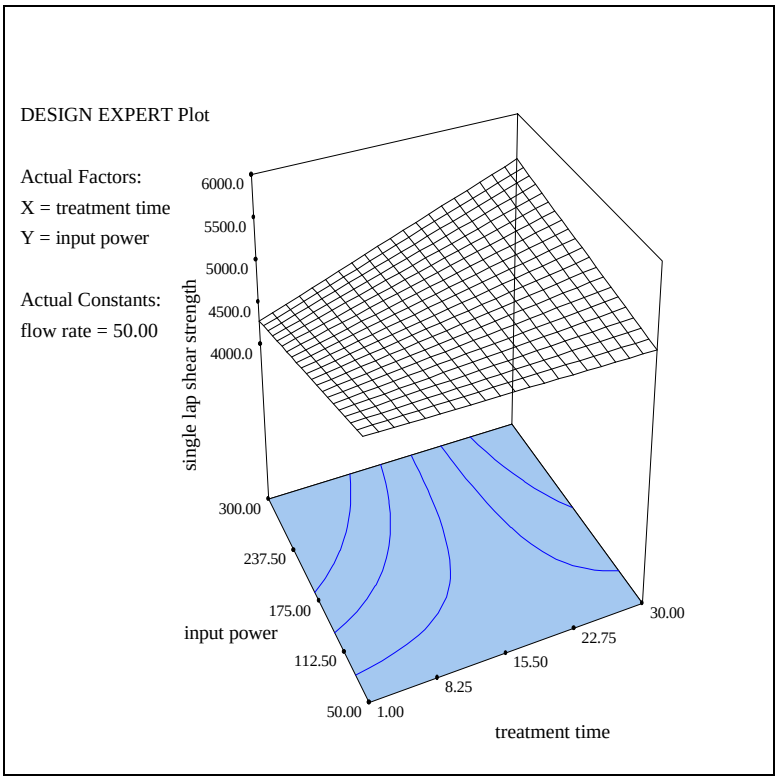

Figure 5.10: RSM contour plot at a flow rate of 50 sccm.

Overall, the samples pretreated with an oxygen plasma for 1 minute at 50 Watts with a flow rate of 20 sccm (short treatment time and low input power) yielded the best SLS strength (5680 ± 500 psi). In all cases, failure was visually estimated to be between 35 % and 45 % cohesive. A detailed analysis of the failure mode is given later in this chapter.

The DOE software can suggest experimental routes to optimizing a specified response. Constraints of the experiments are selected, and a desirability function is created which will be zero outside of the constraints and 1 when the goal is met within the constraints. The program seeks to maximize this function by statistical methods discussed in reference 13. Setting the boundaries to the experimental limits of the factors tested, the desirability function was maximized for a treatment time of 2.02 minutes, a power input of 135 watts, and a flow rate of 29.2 sccm. This experiment was performed, and the average SLS strength was 5637 ± 207 psi, which was a higher SLS strength than most of the experiments performed and essentially identical to the previous maximum (5680 ± 500 psi). This was a good validation of the model and confirmed that a good fit with the experimental data was made.

5.4 Failure Mode

Sample O2.10m.200w.f20 was treated with an oxygen plasma for 10 minutes using an input power of 200 watts and a flow rate of 20 sccm. It had an average SLS strength of 3879 ± 190 psi. The non-bonded oxygen plasma treated surface was composed of 27.6 % C, 50.7 % oxygen, 16.2 % titanium, 3.7 % Al, with traces of calcium and sulfur. The XPS wide scan of O2.10m.200w.f20 is shown in Figure 5.11. The trace amount of calcium is presumed to be from the glass of the reactor walls. The trace amounts of sulfur were of unknown origin, but were reproducible.

The C 1s curve-fit photopeak of the non-bonded surface is shown in Figure 5.12. Contributions from hydrocarbons (285.0 eV), ether groups (286.5 eV), carbonyls (287.9 eV), and carboxylates (289.3 eV) were apparent and were probably due to carbonaceous contaminants that adsorbed once the sample was exposed to the atmosphere. This C 1s photopeak was typical of all of the oxygen plasma treated surfaces.

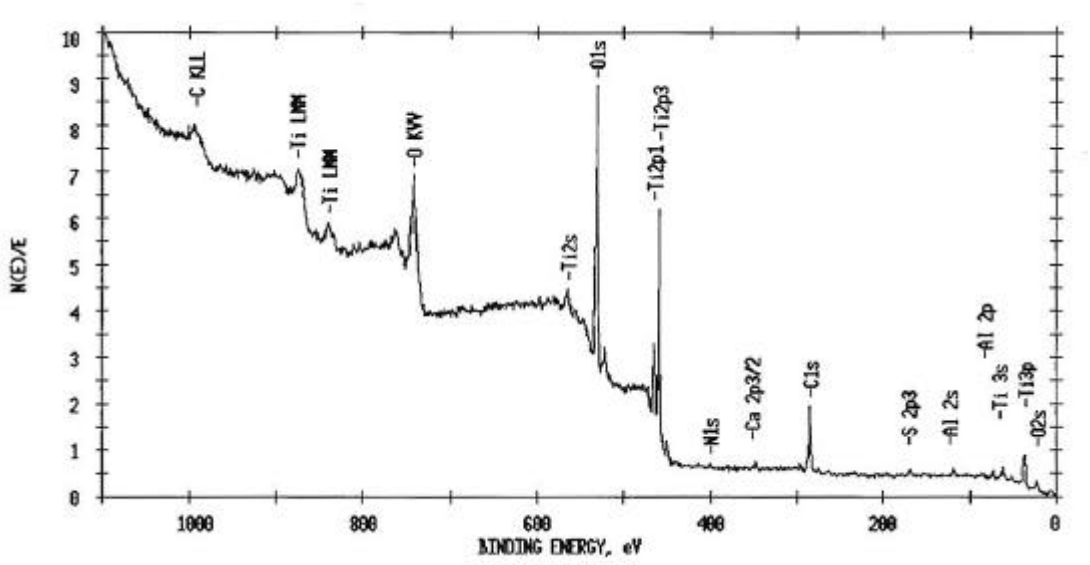

Figure 5.11: XPS wide-scan of O2.10m.200w.f20.

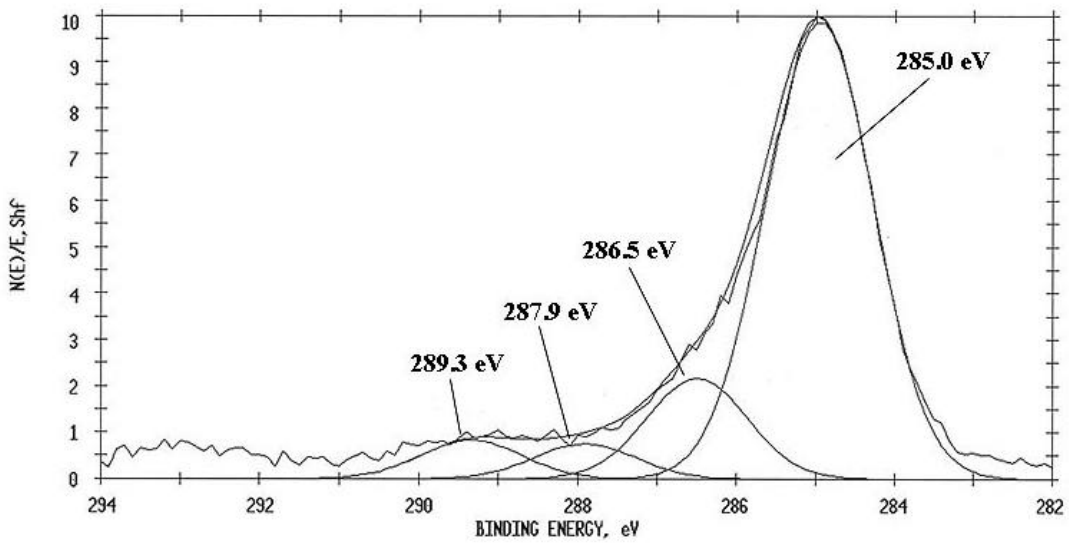

Figure 5.12: Curve-fit C 1s photopeak for non-bonded O2.10m.200w.f20.

The O 1s curve fit for oxygen plasma treated Ti-6Al-4V is shown in Figure 5.13. The photopeak at 530.2 eV, which is typical of TiO_2,[14] dominated the curve-fit spectrum (≈ 64 % of the O 1s photopeak). From the curve-fit O 1s peak alone, a titanium concentration of 16.3 % was predicted [(64 % x 50.7 %)/2]. The measured titanium concentration was 16.2 %, so the presence of TiO_2 was confirmed. The photopeaks at 531.6 eV and 532.7 eV were assigned to the C=O and C-O contributions, respectively, of the organic contaminants on the surface. The photopeak at 531.6 eV also contained a contribution from Al_2O_3. This O 1s photopeak was typical of every oxygen plasma treated surface.

The Ti 2p photopeaks of titanium were well defined for oxygen plasma treated Ti-6Al-4V and are shown in Figure 5.14. The lower binding energy peak (458.7 eV) was due to Ti $2p_{3/2}$ electrons and the higher binding energy peak (464.5 eV) was due to Ti $2p_{1/2}$ electrons. The separation of 5.8 eV (464.5 - 458.7 eV) for the 2p photopeaks is a distinguishing feature of TiO_2,[15] and this was a confirmation of the form of titanium on the oxygen plasma treated surfaces. Again, this spectrum was typical of an oxygen plasma cleaned Ti-6Al-4V substrate.

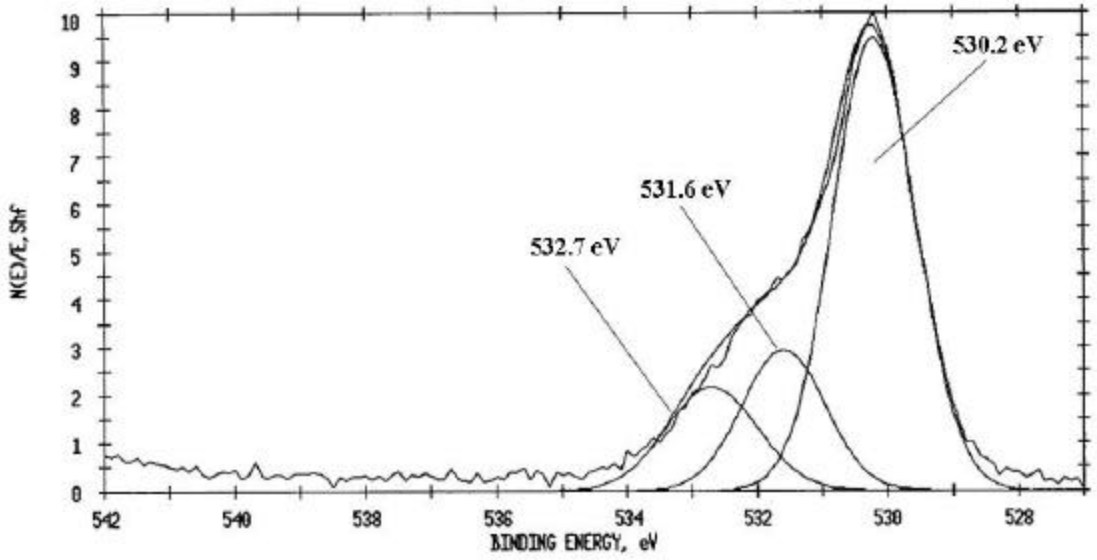

Figure 5.13: Curve-fit O 1s photopeak for non-bonded O2.10m.200w.f20.

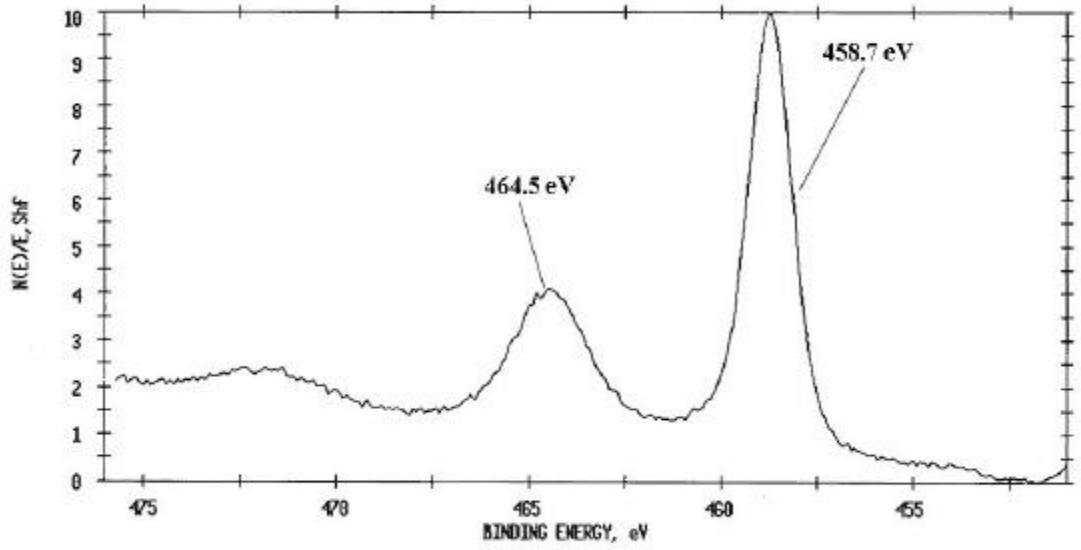

Figure 5.14: Ti $2p_{3/2}$ (458.7 eV) and $2p_{1/2}$ (464.5 eV) for non-bonded O2.10m.200w.f20.

The failure mode for O2.10m.200w.f20 specimens was determined by visually inspecting the failed specimens and by examining the XPS data and the C 1s curve-fit photopeaks of the failed surfaces. The curve-fit C 1s photopeaks of the failed surfaces are shown in Figure 5.15 and Figure 5.16. Although the samples failed partially cohesively, the XPS results analyzed here

were from the portion of the failure surface that was visually interfacial. Table 5.5 is a summary of the XPS results. Note that on the titanium alloy failure side, approximately 9 % titanium was detected, yet the carbon content was still relatively high (≈ 76 %). The C 1s photopeaks for both failure surfaces were essentially identical and showed characteristics of the adhesive. Specifically, both showed the imide photopeak at ≈ 288.6 eV, which was a distinguishing characteristic of the adhesive. The XPS results indicate that the failure occurred within the FM-5 adhesive, close to the titanium oxide surface. Failure was mixed mode, so the crack propagated in and out of the adhesive along the oxide layer, and also partially propagated through the adhesive. Figure 5.17 shows a schematic of the proposed failure mode for O2.10m.200w.f20, which was representative of all of the oxygen plasma treated samples.

Table 5.5: XPS results for non-bonded and failed O2.10m.200w.f20 samples.

Sample	% C	% O	% N	% Ti	% Al	% Si	% Ca
Non-bonded O2.10m.200w.f20	27.6	50.7	trace	16.2	3.7	ND	Trace
Titanium side of O2.10m.200w.f20	75.8	11.2	4.8	8.9	ND	ND	ND
Adhesive side of O2.10m.200w.f20	87.8	5.0	5.8	ND	ND	1.2	ND

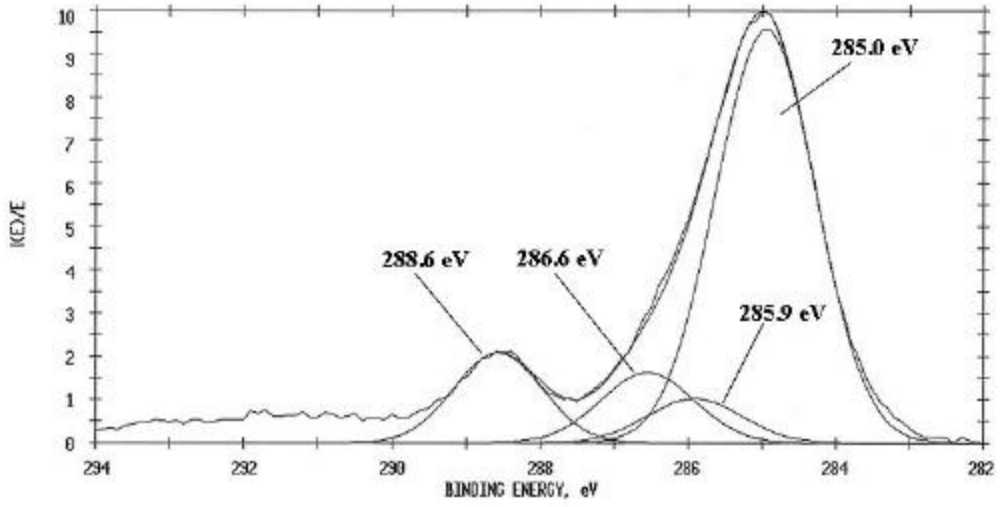

Figure 5.15: C 1s curve-fit for the Ti failure side for O2.10m.200w.f20.

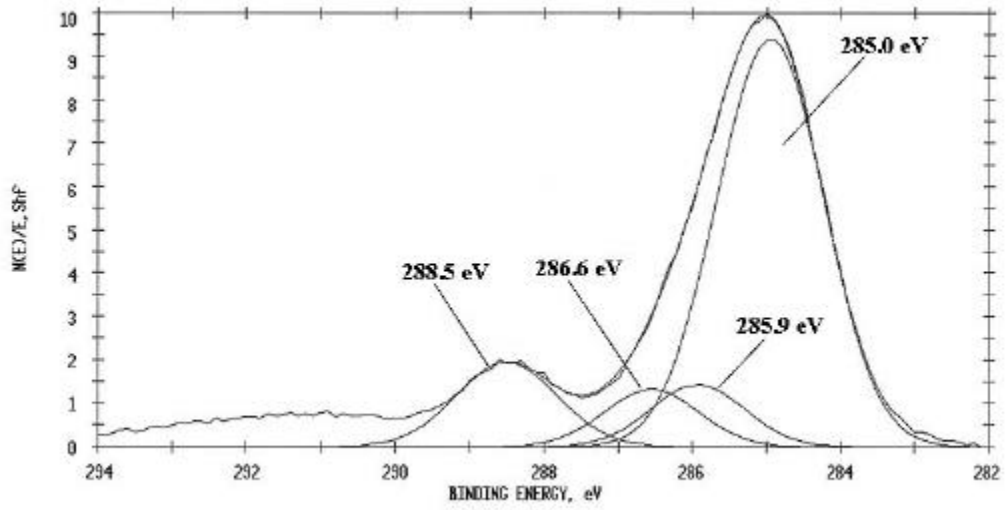

Figure 5.16: C 1s curve-fit for the adhesive failure side for O2.10m.200w.f20.

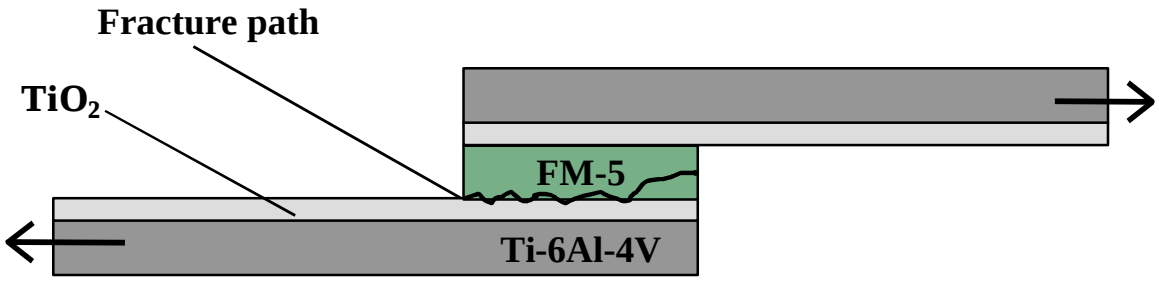

Figure 5.17: Proposed failure mode for O2.10m.200w.f20.

5.5 Surface Energies

Sample set O2.10m.200w.f20 was treated for 10 minutes using an input power of 200 watts and a flow rate of 20 sccm. Sample O2.120s.200w.f20 was treated for 2 minutes using an input power of 200 watts and a flow rate of 20 sccm. Although treated for different times, the surface chemistries of the two sample sets can be considered essentially the same, as demonstrated in Section 5.3. The oxide thicknesses and the XPS results are listed in Table 5.6. The oxide thickness of O2.120s.200w.f20 was only measured once, and the measurement was taken over 24 hours after the plasma treatment. There was very little change in the surface composition of O2.120s.200w.f20 due to the different atmosphere-exposure times (1 hour vs. 24

hours). Also, the oxide thickness and surface chemistry of the two samples were identical despite the different plasma treatment times, which further confirmed the results from Section 5.3. The C 1s photopeaks for these samples were identical to the C 1s photopeak shown in Figure 5.12.

Table 5.6: AES and XPS results for oxygen plasma treated samples.

Substrate	Thickness (Å)	% C	% O	% Ti	% Ca	% Al
O2.120s.200w.f20 (1 hour after treatment)	76.0 ± 23.8	25.5	54.6	14.3	2.1	3.5
O2.120s.200w.f20 (24 hours after treatment)	76.0 ± 23.8	26.5	53.9	14.3	2.1	3.2
O2.10m.200w.f20 (≈ 72 hours after treatment)	74.6 ± 11.9	26.0	54.2	15.0	1.7	3.1

The surface energies were calculated as outlined in Chapter 3, and the results are shown in Table 5.7. Within standard deviations, the overall surface energies of the samples were essentially identical, and they closely correlated with the surface energy of acetone cleaned Ti-6Al-4V (59.6 dynes/cm). The measurements were taken at three different time intervals after plasma treatment, and a decrease in surface energy with time was observed. After 1 hour, the surface energy was 67.4 dynes/cm, and the polar component (36.3 dynes/cm) was significantly larger than the polar component of acetone cleaned Ti-6Al-4V (28.3 dynes/cm). The overall surface energy decreased to 62.2 dynes/cm after 24 hours, but was essentially unchanged when considering the standard deviations. The surface energy decreased to 60.7 dynes/cm after 72 hours, but again, the change was insignificant when considering the standard deviations. Despite the large standard deviations, the decrease of surface energy with time is reasonable and is probably real, based on results reported in the literature.[7]

Grundmeier et al[7] made contact angle measurements on oxygen plasma treated iron oxide surfaces using water, and a time-dependence was reported. They found that initially, an oxygen plasma cleaning of steel led to a higher surface energy. Up to 20 minutes after the oxygen plasma cleaning, the contact angle of water was 12 to 14 degrees. After 30 minutes, a sharp increase in the contact angle was observed. The contact angle reached a value of almost 70 degrees after about 100 minutes due to the absorption of hydrophobic contaminants.

Table 5.7: Surface energies for oxygen plasma treated Ti-6Al-4V.

Substrate	γ^d (dynes/cm)	γ^p (dynes/cm)	γ (dynes/cm)
Acetone cleaned Ti-6Al-4V	31.3 ± 2.7	28.3 ± 2.5	59.6 ± 5.2
O2.120s.200w.f20 (1 hour after treatment)	31.2 ± 2.8	36.3 ± 3.2	67.4 ± 6.0
O2.120s.200w.f20 (24 hours after treatment)	31.2 ± 3.6	31.0 ± 3.5	62.2 ± 7.1
O2.10m.200w.f20 (≈ 72 hours after treatment)	29.1 ± 2.4	31.6 ± 2.6	60.7 ± 4.9

5.6 Nanoindentation

Polished Ti-6Al-4V and silicon wafers (samples O2.121s.135w.f29) were treated with an oxygen plasma to determine how the morphological changes induced by the plasma treatment affect the hardness and modulus values of the samples. The reaction chamber was purged for 15 minutes prior to plasma initiation. The oxygen flow rate was 29 sccm, the input power was 135 watts, and the treatment time was 121 seconds. These parameters were selected based on the results from the oxygen plasma treatment study reported Section 5.3.4. The chamber pressure increased to from 30 mTorr to 38 mTorr during the oxygen plasma treatment, which was a confirmation of the ablative effects of the plasma. The chamber was purged for 15 minutes with O_2 following the treatment.

The XPS results for the samples, which are an average of two measurements, are shown in Table 5.8. The oxygen plasma treatment reduced the amount of carbonaceous contaminants on the substrate surfaces and exposed more of the substrate. The carbon content changed from 45.2 % for polished Ti-6Al-4V to 22.7 % for O2.121s.135w.f29.Ti and the Ti content increased from 7.3 % to 10.9 %, respectively. The oxygen content also increased after plasma treatment of the polished Ti-6Al-4V, increasing from 40.3 % to 55.8 %. The sodium detected on O2.121s.135w.f29.Ti was attributed to sodium from the Pyrex glass reactor. Oxygen plasmas are relatively aggressive plasmas, and they can etch away the glass surface of the reactor, which results in active sodium species that can react with the substrate.

For the silicon wafer substrate, The oxygen plasma treatment had little effect on the carbon concentration (10.4 % vs. 10.9 %). The treatment increased the oxygen content on the

silicon wafer's surface from 41.5 % prior to plasma treatment to 49.6 % after the pretreatment. The amount of silicon actually decreased after plasma treatment, from 47.8 % to 39.5 %. This was a direct result of the increased oxide thickness that the oxygen plasma induced, as shown by the AES results (Table 5.9).

Table 5.8: XPS Atomic concentration for pre and post oxygen plasma treated samples.

Sample	% C	% O	% Ti	% Si	% Na
Polished Ti-6Al-4V*	45.2	40.3	7.3	ND	trace
O2.121s.135w.f29.Ti [$]	22.7	55.8	10.9	ND	5.9
Silicon wafer	10.4	41.5	ND	47.8	ND
O2.121s.135w.f29.Si	10.9	49.6	ND	39.5	ND

[*]N (1.9 %) and Al (3.3 %) were also detected on polished Ti-6Al-4V.
[$]Al (2.7 %), Ca (1.6 %), and Zn (trace) were also detected on O2.121s.135w.f29.Ti.

Table 5.9: Oxide layer thickness (AES) for pre and post oxygen plasma treated samples.

Sample	Oxide thickness (Å)	Std. Dev. (Å)
Polished Ti-6Al-4V	62.1	8.7
O2.121s.135s.f29.Ti	79.4	9.0
Silicon wafer	3.7	1.6
O2.121s.135w.f29.Si	6.1	1.2

AES results showed that the oxide thickness on polished Ti-6Al-4V was 62.1 ± 8.7 Å and increased to 79.4 ± 9.0 Å after oxygen plasma treatment. The oxide layer thickness of the silicon wafer prior to oxygen plasma treatment was 3.7 ± 1.6 Å and increased to 6.1 ± 1.2 Å due to the treatment. The increases in thickness are significant (≈ 28 % for polished Ti-6Al-4V and ≈ 65 % for the silicon wafer), but even more significant may be a change in morphology of the oxide layer induced by the plasma treatment. Oxygen plasma treatments have the ability to replace a weakly bound oxide layer with a more stable one. The hardness and modulus values are reported in Table 5.10. Because the oxide thicknesses of the two substrates were so thin, the indentations penetrated through the oxide layer in every case, as shown by h_c. Therefore, the hardness and modulus values reported are more representative of the bulk of the substrates rather than their oxides.

There was no change in the hardness and reduced Young's modulus for polished Ti-6Al-4V (5.8 GPa) compared to oxygen plasma treated Ti-6Al-4V (5.8 GPa). Likewise, there was

essentially no change in the hardness and reduced Young's modulus of the silicon wafer (10.0 GPa) compared to oxygen plasma treated silicon (10.2 GPa). This leads to the conclusion that, while the oxygen plasma treatment may etch away the initial oxide layer and deposit a fresh new one, the mechanical properties of the freshly deposited oxide layer are essentially the same as the previous oxide layer. Furthermore, it seems that the increase in SLS strength is due to the removal of the weak boundary layer of carbon contaminants, rather than any change in the hardness or reduced Young's modulus of the oxide layer.

Table 5.10: Nanoindentation results for oxygen plasma treated samples O2.121s.135w.f29.

Sample	H (GPa)	Er (GPa)	h_c (nm)
Polished Ti-6Al-4V	5.8 ± 0.6	143.5 ± 9.8	28.4 ± 2.4
O2.121s.135w.f29.Ti	5.8 ± 0.5	142.0 ± 12.2	28.4 ± 2.2
Silicon wafer	10.0 ± 0.3	169.1 ± 2.5	19.2 ± 0.5
O2.121s.135w.f29.Si	10.2 ± 0.6	172.4 ± 5.5	18.0 ± 0.9

Figure 5.18 and Figure 5.19 show the AFM photomicrographs of indented oxygen plasma treated polished Ti-6Al-4V and silicon. The indents were well resolved and showed a sharp entry into the materials. The figures also show that the polished Ti-6Al-4V substrate was rougher than the silicon wafer, as discussed in Chapter 4. The indent into the silicon wafer was smaller than the Ti-6Al-4V indent because it was the harder material and the indenter was not able to penetrate as deeply.

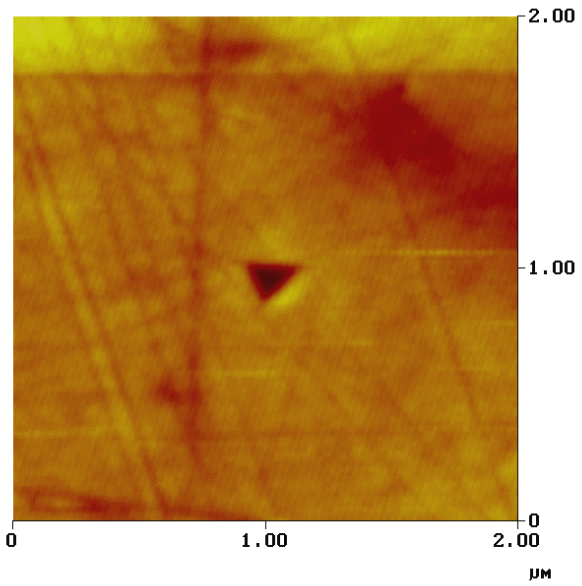

Figure 5.18: In situ topographic image of indentation in O2.121s.135w.f29.Ti under 300 µN load.

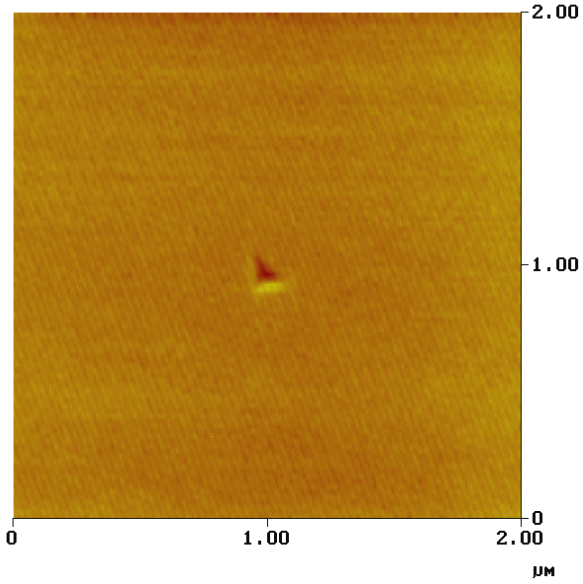

Figure 5.19: In situ topographic image of indentation in O2.121s.135w.f29.Si under 300 µN load.

5.7 Conclusions

Initial experiments treating Ti-6Al-4V samples with oxygen plasmas revealed that this procedure cleaned carbonaceous contaminants from the substrates, exposed more of the metal alloy, and created an extended oxide layer on the titanium surface. Oxygen plasma pretreatments of titanium alloy enhanced the single lap shear strength, compared to results for acetone cleaned titanium alloy. This effect was mainly due to removal of residual carbon and the introduction of a thicker oxide layer. In some instances, this pretreatment improved SLS strengths by over 6.2 MPa (600 psi).

Utilizing an experimental design program called Design Expert Plus 5.0®, a three factorial model was developed to optimize the single lap shear strength for oxygen-plasma treated Ti-6Al-4V bonded with FM-5. Small titanium alloy coupons were plasma treated and used to prepare miniature SLS joints. In all cases, the one-step oxygen plasma pretreatments resulted in a cleaner surface that showed a much reduced percentage of carbon, an increased percentage of oxide, an increased percentage of titanium, and an extended oxide layer.

The DOE model was validated by an analysis of variance. Interaction graphs showed that interactions between the treatment time and flow rate, and interactions between flow rate and input power were significant, so the effects of these parameters should not be considered individually. The flow rate and the treatment time/input power interaction were non-factors. The model developed suggested that at low flow rates, SLS strength was optimized using low input power and short treatment times. At high flow rates, the SLS strength was optimized by using high input power and high treatment times. Using the DOE optimization procedure, the best results were generated from samples pretreated with an oxygen plasma for 1 minute at 50 Watts (20 sccm). These samples yielded a SLS strength of 58.8 ± 5.2 MPa (5680 ± 500 psi), which was a nice confirmation of the model. However, the p-value (0.0855) of the model and the fact that it was an unreplicated factorial design suggest that caution should be used when interpreting these results.

Visual analysis and XPS results confirmed that the failure mode was partially cohesive. Typical oxygen plasma treated specimens showed approximately 30 % cohesive failure. For the portion of the failure mode that was interfacial, it was determined that the crack propagated along the adhesive/TiO_2 interface.

Contact angle measurements of selected oxygen plasma treated samples showed that the surface energies of freshly treated specimens (67.4 dynes/cm) were higher than acetone cleaned substrates (59.6 dynes/cm). This was predominantly due to an increase in the polar component of the surface energy. However, this difference disappeared upon exposing the samples to the room temperature atmosphere for over 24 hours. The surface energy eventually approached that of acetone cleaned Ti-6Al-4V after 3 days, with the polar component decreasing accordingly.

AFM nanoindentation of oxygen plasma treated substrates showed essentially no change in the surface mechanical properties due to the oxygen plasma treatment. The hardness values of the titanium alloy and silicon wafer substrates were 5.8 and ≈ 10.1 GPa, respectively. No change of hardness with plasma treatment suggested that the improved SLS strength of the oxygen plasma pretreated substrates was due to the cleaning of the substrate and the removal of carbonaceous contaminants, rather than any changes in the morphology of the oxide layer.

5.8 References

[1] H. Kersten; E. Stoffels; W.W. Stoffels; M. Otte; C. Csambal; H. Deutsch; R. Hippler *J. Appl. Phys.* **2000**, *87*, 3637.
[2] E.M. Liston Paper presented at First International Conference, Namur, Belgium, September 1991; Section IV, 429.
[3] P. Kruger; R. Knes; J. Friedrich *Surf. Coat. Technol.* **1999**, *112*, 240.
[4] S.R. Schmidt; R.G. Launsby *Understanding Industrial Designed Experiments*; Air Academy Press: Colorado Springs, Colorado, 1994.
[5] B.S. Yandell *Practical Data Analysis for Designed Experiments*; Chapman and Hall: New York, NY, 1997.
[6] R.H. Meyers; D.C. Montgomery *Response Surface Methodology: Process and Product Optimization Using Designed Experiments*; Wiley: New York, NY, 1995.
[7] G. Grundmeier; M. Stratmann *Mater. Corros.* **1998**, *49*, 150.
[8] A.T. Fromhold *Thin Solid Films* **1982**, *95*, 297.
[9] R.L. Ott *An Introduction to Statistical Methods and Data Analysis, Fourth edition*; Duxbury Press: Belmont, CA, 1993, Chapter 13.
[10] Design-Expert 5.0 Reference Manual, pg. 24.
[11] Design-Expert 5.0 Reference Manual, pg. 10.
[12] D.C. Montgomery *Design and Analysis of Experiments, 5th Edition*; Wiley and Sons: New York, NY, 2001, Chapter 2.
[13] Design Expert 5.0 Reference Manual.
[14] C.D. Wagner; D.A. Zatko; R.H. Raymond *Anal. Chem.* **1980**, *52*, 1445.
[15] C.D. Wagner; W.M. Riggs; L.E. Davis; J.F. Moulder; G.E. Muilenburg *Handbook of X-Ray Photoelectron Spectroscopy*; Perkin-Elmer: Eden Prairie, MN, 1979, p. 79.

6.0 Plasma Polymerized Acetylene

6.1 Introduction

An investigation of PP acetylene films as an adhesion-promoting pretreatment was undertaken because of the lack of an adequate pretreatment for Ti-6Al-4V for high performance applications. There is evidence that such PP films of acetylene are effective primers for bonding to metal.[1, 2, 3] The interactions between a PP film and a metal substrate are thought to consist of secondary forces such as van der Waals forces and hydrogen bonding, and in many instances, PP films are highly adherent to the substrate.[4] The plasma polymerization of acetylene by a mechanism analogous to free radical, chain growth polymerization can result in the incorporation of alkene and alkyne groups into the polymer film. [1, 5, 6] In theory, double and triple bonds of PP acetylene could cross-link with the end cap groups on the adhesive. If the adhesion between the PP acetylene film and the substrate is adequate, this should lead to improved adhesion and durability.

The PP films investigated in this study were anticipated to resemble PP films of acetylene deposited onto various substrates by inductively coupled RF reactors reported by other researchers.[3, 7] The films were expected to be highly branched and carbon-based, and to contain mostly hydrocarbon groups, with additional mono- and di-substituted acetylene groups, aromatic groups, and ether and carbonyl groups due to oxidation reactions with air.

The effects of varying substrate pretreatment, carrier gas, input power, flow rate, treatment time (film thickness), and monomer inlet are discussed in this chapter, among other topics. The chemical and physical properties of the PP films of acetylene will be discussed and related to SLS strength. Because failure of SLS specimens consistently occurred at the PP film/substrate interface, nanoindentation and nanoscratch testing was performed to assess the nanomechanical and adhesion properties of PP films deposited on two substrates at different input power. The nanomechanical properties were also related to PP film chemistry and SLS strength.

6.2 Experimental

The reaction vessel was evacuated and purged with the initial treatment gas for approximately 10 minutes before any treatment was initiated. Once a treatment began, samples remained under vacuum until all phases of the plasma process were complete. Except where noted, the carrier gas, as well as the monomer gas, were introduced above (after) the induction coil and treated samples were purged with the carrier gas for at least 10 minutes before being removed from the reactor chamber and placed in a desiccator. Sample placement for all treatments, except where noted, was downstream of the induction coil, approximately 22.9 cm (9 inches) from the end of the induction coil. The samples were therefore exposed to the afterglow region of the plasma.

The Ti-6Al-4V substrates were visibly coated after deposition of PP acetylene. Typically, the PP acetylene films were dull gold in color. The films were solvent resistant, as no visible change in the PP films were seen after 30 days in various solvents. The solvents tested were reagent grade acetone, methanol, ethyl ether, N-methyl-2-pyrrolidinone, n-hexane, chloroform, and methyl ethyl ketone. This was evidence that the films were highly crosslinked or branched, which is typical of plasma polymerized films.

The failure mode of the SLS specimens was identical for all the samples discussed in this chapter, except where noted. XPS analysis of the two sides of the failed SLS joints indicated that failure occurred at the PP film/Ti-6Al-4V interface. The determination of failure mode was discussed in Chapter 4. XPS curve-fit photopeak assignments have been justified and referenced in Chapter 3.

6.3 Pretreatment Variation

In the study of oxygen plasma pretreatments discussed in Chapter 5, the best SLS results were generated from samples pretreated with an oxygen plasma for 1 minute at 50 Watts (20 sccm). There was very little dependence of the surface composition and oxide thickness of the substrates on oxygen plasma pretreatment variables. Recall that oxygen flow rates, treatment time, and input power were varied. Even brief oxygen plasma pretreatments at low input power

were efficient at cleaning the substrate's surface and extending the oxide layer. To investigate if oxygen pretreatments of different duration had any impact on film formation of PP acetylene or on the ultimate SLS strength, samples Ac.120s.200w.f10.Ar (20 min. O_2) and Ac.120s.200w.f10.Ar (10 min. O_2) were compared.

Both samples were pretreated with an oxygen plasma (20 sccm, 200 W), and then exposed to an argon/acetylene plasma (20 sccm/10 sccm, 200W, 2 minutes). Ac.120s.200w.f10.Ar (20 min. O_2) were exposed to a 20 minute O_2 pretreatment, while Ac.120s.200w.f10.Ar (10 min. O_2) samples were exposed to a 10 minute O_2 pretreatment. The PP film thicknesses for Ac.120s.200w.f10.Ar (20 min. O_2) and Ac.120s.200w.f10.Ar (10 min. O_2) were 400 ± 15Å and 397 ± 48Å, respectively, and their SLS strengths were 7.65 ± 0.21 (1110 ± 30) and 9.31 ± 0.90 MPa (1350 ± 130 psi), respectively. Prolonging the oxygen plasma pretreatment had no effect the film thickness, as evidenced by the identical PP film thicknesses. Prolonging the oxygen plasma pretreatment resulted in only a slight increase in SLS strength. The compositions of the PP acetylene films varied slightly for the two treatments (see Table 6.1). Sample Ac.120s.200w.f10.Ar (10 min. O_2) contained a significant amount of nitrogen (≈ 7 %), while sample Ac.120s.200w.f10.Ar (20 min. O_2) contained no nitrogen. A C-N< peak was assigned in the C 1s curve-fit photopeak at 285.9 eV for sample Ac.120s.200w.f10.Ar (10 min. O_2) (Figure 6.1), and this accounted for the only differences in the C 1s peaks. The O 1s curve-fit photopeak for Ac.120s.200w.f10.Ar (10 min. O_2) is shown in Figure 6.2 and consisted of photopeaks due to C=O (531.8 eV) and C-O (533.1 eV) linkages. The O 1s photopeak for Ac.120s.200w.f10.Ar (20 min. O_2) (not shown) was identical to that of Ac.120s.200w.f10.Ar (10 min. O_2).

The differences in the nitrogen content for the two samples could not be readily explained, but the difference did not translate into much of a difference in SLS strength. The only difference in the deposition process was that the pressure in the reaction chamber during deposition was < 1 mTorr for Ac.120s.200w.f10.Ar (10 min. O_2) and 8.5 mTorr for Ac.120s.200w.f10.Ar (20 min. O_2).

Table 6.1: XPS results for Ac.120s.200w.f10.Ar (20 min. O_2) and Ac.120s.200w.f10.Ar (10 min. O_2).

Sample	Thickness (Å)	% C	% O	% N	% Ti	SLS (MPa)	SLS (psi)
Ac.120s.200w.f10.Ar (20 min. O_2)	400 ± 15	91.0	9.0	ND	ND	7.65 ± 0.21	1110 ± 30
Ac.120s.200w.f10.Ar (10 min. O_2)	397 ± 48	83.3	10.1	6.6	ND	9.31 ± 0.90	1350 ± 130

AES of the two samples revealed that the underlying oxide layer was slightly affected by the length of oxygen plasma exposure. Figure 6.3 and Figure 6.4 show the Auger depth profiles for these two samples. The sample exposed to the oxygen pretreatment for a longer time developed a slightly thicker oxide layer; the oxide layer was 62 and 91 Å for samples Ac.120s.200w.f10.Ar (10 min. O_2) and Ac.120s.200w.f10.Ar (20 min. O_2), respectively. Oxide thickness, however, did not have any significant influence on SLS strength. The oxide layer thicknesses corresponded well with AES data for samples exposed only to an oxygen plasma, as discussed in Chapter 5. This suggested that there was minimal ablation of the oxide layer during deposition of the PP film.

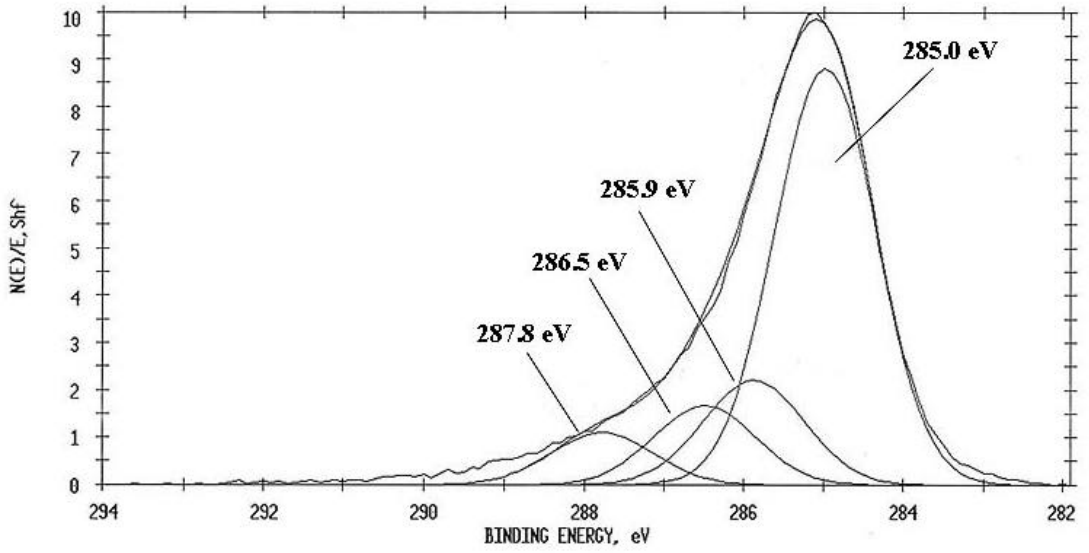

Figure 6.1: Curve-fit C 1s photopeak for Ac.120s.200w.f10.Ar (10 min. O_2).

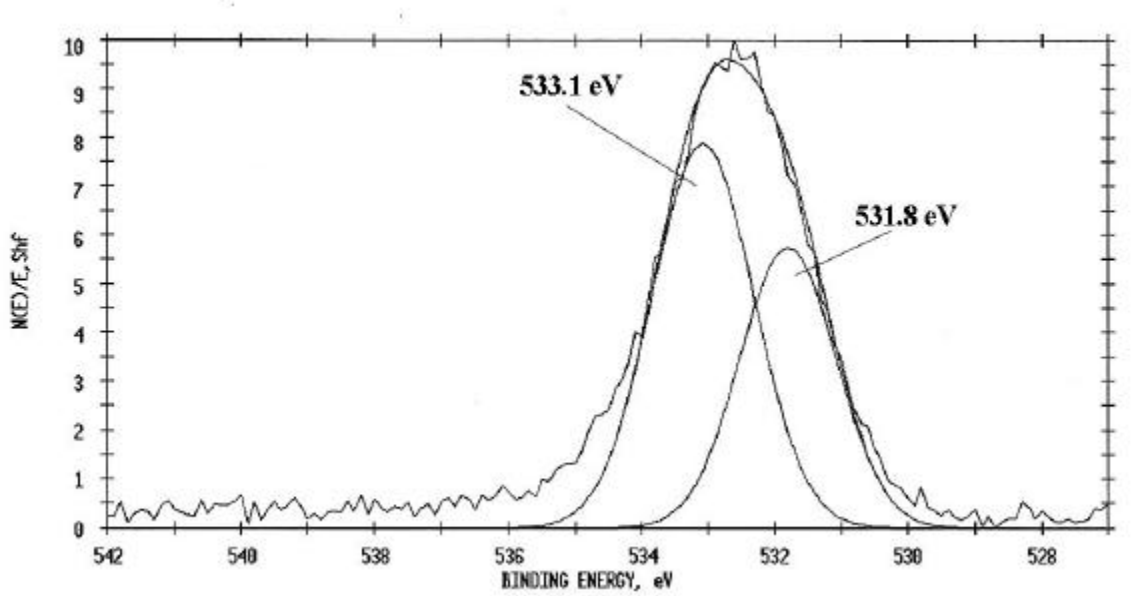

Figure 6.2: Curve-fit O 1s photopeak for Ac.120s.200w.f10.Ar (20 min. O_2).

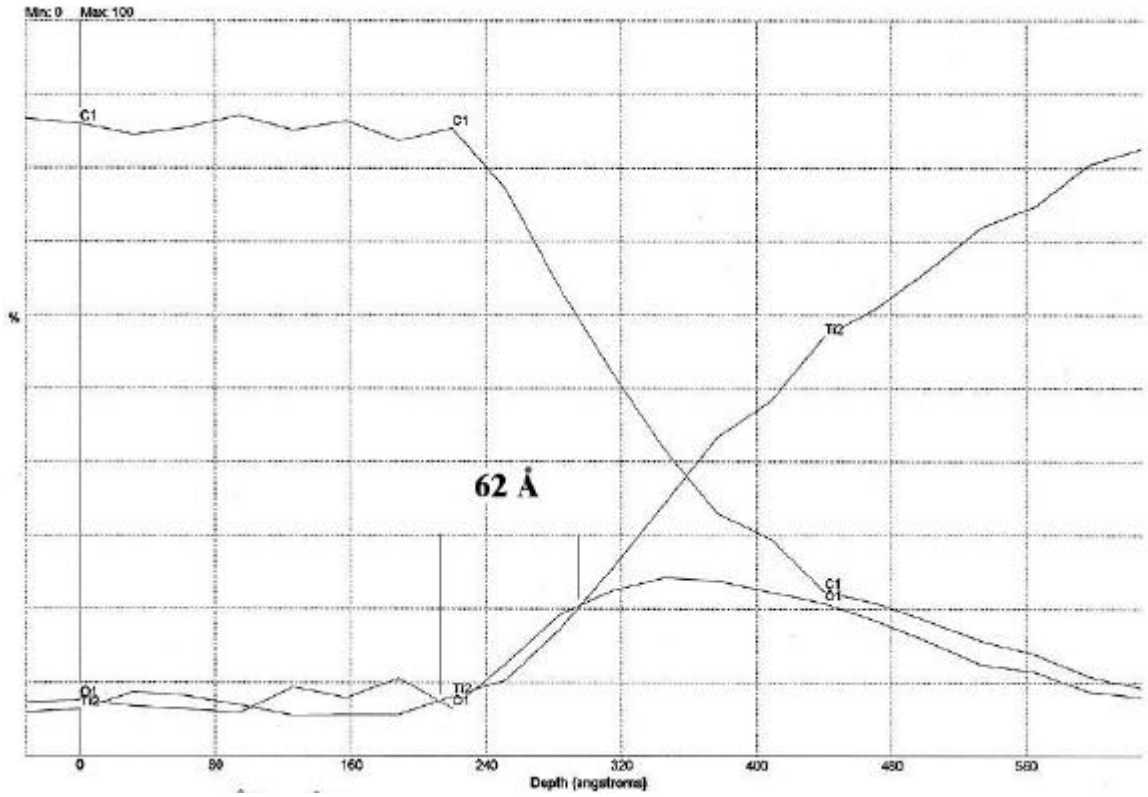

Figure 6.3: AES of sample Ac.120s.200w.f10.Ar (10 min. O_2).

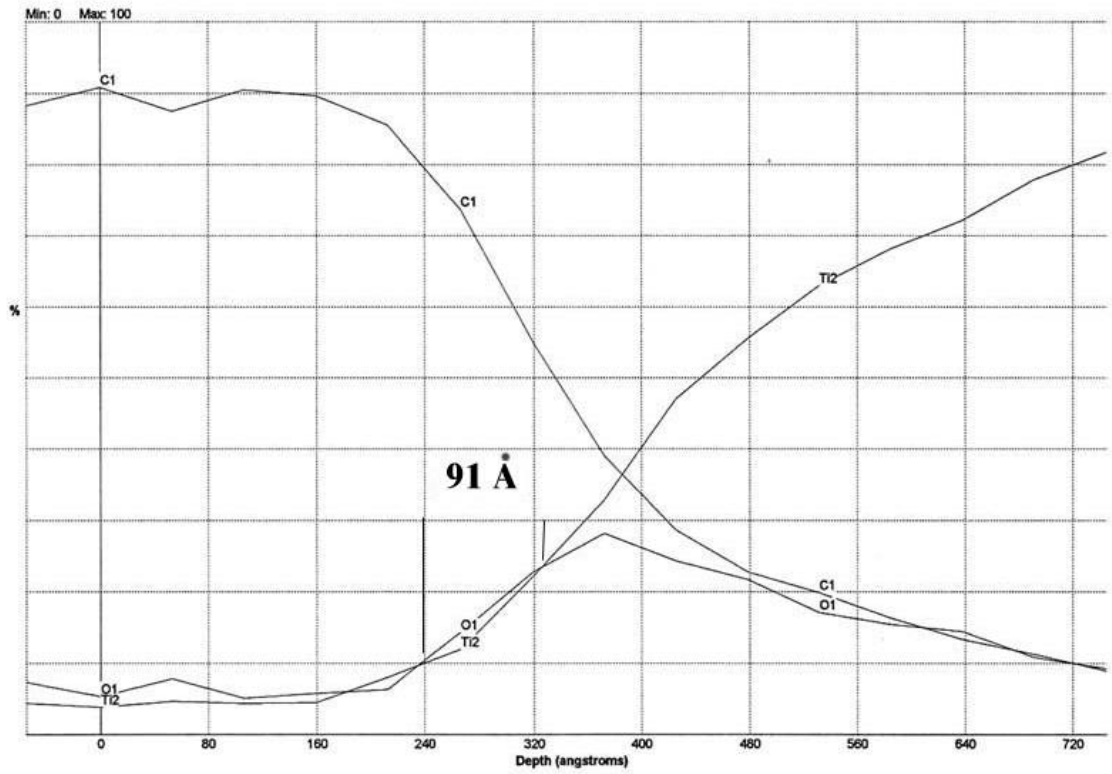

Figure 6.4: AES of sample Ac.120s.200w.f10.Ar (20 min. O_2).

6.4 Variation of Acetylene Introduction Locale

The effect of the location of acetylene introduction (either in front of or after the RF coil) was investigated by comparing samples Ac.120s.200w.f10 (before coil) and Ac.120s.200w.f10 (after coil). Both samples were pretreated with an oxygen plasma (20 sccm, 200W, 10 minutes), and then treated with an acetylene plasma (no carrier gas, 10 sccm, 200 W, 2 minutes). As suggested by their sample names, acetylene was introduced before the RF coil for Ac.120s.200w.f10 (before coil) and after the coil for Ac.120s.200w.f10 (after coil). The XPS determined composition of the PP acetylene films was independent of where the acetylene was introduced. Table 6.2 shows the XPS results from the analysis of the non-bonded samples. The surface compositions of the films were equivalent and both PP films contained approximately 91 % carbon and 8 % oxygen. The curve-fit C 1s photopeaks confirm the similarity of the films; the C 1s peak for Ac.120s.200w.f10 (before coil) was identical to that of Ac.120s.200w.f10 (after coil), which is shown in Figure 6.5. The curve-fit C 1s photopeak mostly reflects the contribution

of C-C/C-H groups (285.0 eV), but C-O (286.5eV) and C=O (287.8 eV) groups were also fit. The O 1s photopeaks (not shown) for the samples were identical and showed contributions from C=O and C-O linkages.

Samples Ac.120s.200w.f10 (before coil) and Ac.120s.200w.f10 (after coil) had PP film thickness of 133 ± 25 Å and 583 ± 13 Å, respectively, and SLS strengths of 9.45 ± 0.76 MPa (1370 ± 110 psi) and 8.55 ± 0.97 MPa (1240 ± 140 psi), respectively. The variation in where the acetylene was introduced had no effect on the surface composition of the samples or the SLS strengths for these systems. The differences in thickness, however, can be attributed to Ac.120s.200w.f10 (after coil) being much closer to the acetylene inlet. The plasma-activated acetylene had to travel a much larger distance to deposit on Ac.120s.200w.f10 (before coil). Yasuda and Hirotsu[8] saw a similar trend in the deposition rate of PP ethylene. In their study, a flow rate of 9.8 sccm was used (no carrier gas), and the monomer was introduced before and after the coil of a tubular reactor. The deposition rate for the monomer introduced before the coil was substantially lower than the deposition rate for the monomer introduced after the coil.

Table 6.2: XPS results for Ac.120s.200w.f10 (before coil) and Ac.120s.200w.f10 (after coil).

Sample	Thickness (Å)	% C	% O	% N	% Ti	SLS (MPa)	SLS (psi)
Ac.120s.200w.f10 (before coil)	133 ± 25	90.4	8.2	1.3	ND	9.45 ± 0.76	1370 ± 110
Ac.120s.200w.f10 (after coil)	583 ± 13	91.8	8.0	Trace	ND	8.55 ± 0.97	1240 ± 140

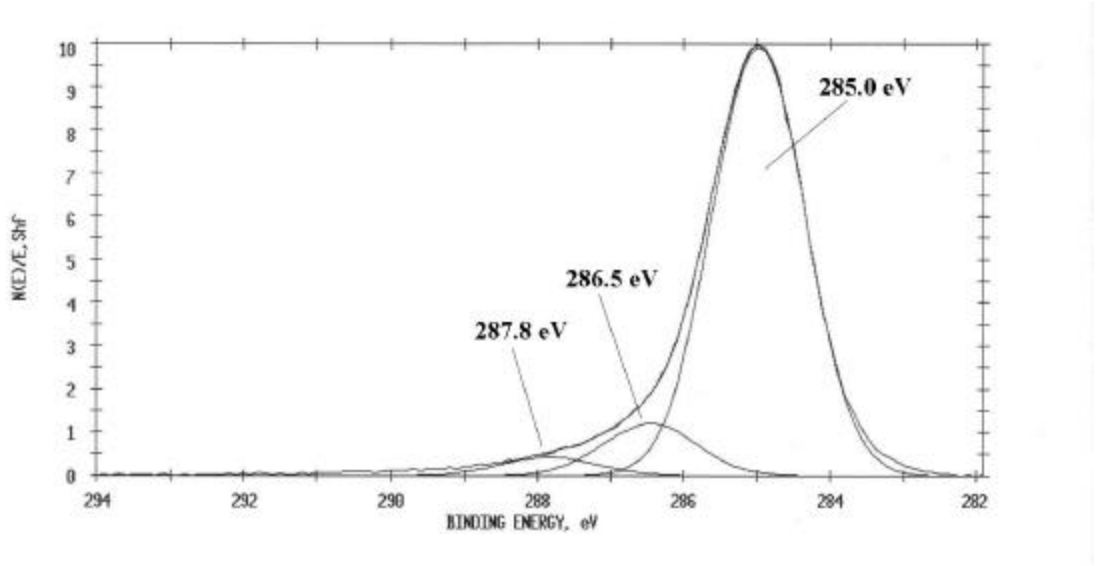

Figure 6.5: Curve-fit C 1s photopeak for Ac.120s.200w.f10 (after coil).

6.5 Argon Carrier Gas Experiments

6.5.1 Power Variation (Ar)

The effect that plasma power input had on SLS strength was investigated by comparing samples Ac.120s.200w.f10.Ar and Ac.120s.100w.f10.Ar. The samples were pretreated with an oxygen plasma (20 sccm, 200W, 10 minutes), then treated with an argon/acetylene plasma (20 sccm/10 sccm). An input power of 200 watts was used for sample Ac.120s.200w.f10.Ar, while an input power of 100 watts was used in the treatment of sample Ac.120s.100w.f10.Ar. The SLS strengths for Ac.120s.200w.f10.Ar and Ac.120s.100w.f10.Ar were 9.31 ± 0.90 MPa (1349 ± 130 psi) and 11.4 ± 0.15 MPa (1656 ± 22 psi), respectively, and the thicknesses of the PP acetylene films were 397 ± 48Å and 127 ± 30Å, respectively. Increasing the input power had the effect of increasing the deposition rate of the PP acetylene threefold; the deposition rate was 3.3 Å/sec at 200W and 1.1 Å/sec at 100W. The surface composition of the two samples remained very similar (see Table 6.3). In fact, the curve resolved carbon peaks (Ac.120s.200w.f10.Ar is shown in Figure 6.1) were essentially identical for the two different treatments, indicating that the surface chemistry of the PP films was not changed by varying the power input. The only

difference in the C 1s photopeaks was due to the incorporation of nitrogen into the curve-fit of Ac.120s.200w.f10.Ar.

Table 6.3: XPS results for Ac.120s.200w.f10.Ar, Ac.120s.100w.f10.Ar, and Ac.39s.200w.f10.Ar.

Sample	Thickness (Å)	% C	% O	% N	% Ti	SLS (MPa)	SLS (psi)
Ac.120s.200w.f10.Ar	397 ± 48	83.3	10.1	6.6	ND	9.31 ± 0.90	1349 ± 130
Ac.120s.100w.f10.Ar	127 ± 30	89.8	10.2	ND	ND	11.4 ± 0.15	1656 ± 22
Ac.39s.200w.f10.Ar	65 ± 14	86.2	13.0	Trace	ND	14.9 ± 1.24	2160 ± 180

The SLS strength was larger for Ac.120s.100w.f10.Ar, which was treated at low input power. The question arises, is this an input power effect or a thickness effect? More samples were prepared to investigate the cause of the differences in SLS strength by decreasing the deposition time for the 200 W PP acetylene. Ac.39s.200w.f10.Ar samples were prepared using identical experimental parameters as used to prepare Ac.120s.200w.f10.Ar, except that the deposition time was reduced to 39 seconds (vs. 2 minutes). The composition of the PP film was very similar to that of Ac.120s.100w.f10.Ar (see Table 6.3), and their C 1s photopeaks were identical (not shown). The thickness of the PP acetylene film for sample Ac.39s.100w.f10.Ar was 65 ± 14 Å, and the SLS strength was 14.9 ± 1.24 MPa (2160 ± 180 psi). This indicated that the SLS strength differences between Ac.120s.200w.f10.Ar and Ac.120s.100w.f10.Ar were probably not due to the power variation, but rather due to a thickness variation. It seems that thinner PP acetylene films yield greater SLS strengths. Results in the next section support this finding.

6.5.2 Thickness Variation (Ar)

The effect of the thickness of the deposited PP acetylene film on SLS strength was investigated by comparing sample Ac.120s.200w.f20.Ar, which was treated for 2 minutes, with sample Ac.30s.200w.f20.Ar, which was treated for 30 seconds. Both samples were pretreated with an oxygen plasma (20 sccm, 200 W, 10 minutes), and then treated with an argon/acetylene plasma (20 sccm/20 sccm, 200W). Ac.120s.200w.f20.Ar had a thickness of 750 ± 48 Å and a

SLS strength of 710 ± 140 psi, while Ac.30s.200w.f20.Ar had a thickness of 62 ± 11 Å and an SLS strength of 2190 ± 350. As has been reported for other systems,[4] the thicker PP film showed a lower SLS strength.

In a study by Dynes and Kaelble,[9] PP styrene and epichlorohydrin were deposited onto aluminum substrates (Al 2024-T3) that had been pretreated with the standard Forest Products Laboratory (FPL) etch. A radio frequency IC plasma reactor was used to deposit films at low pressure, and an epoxy-phenolic adhesive was used to prepare the SLS specimens. They found that the SLS strength decreased as the PP film thickness increased from 100 to 1600 Å (as measured by ellipsometry). For SLS specimens prepared without a PP primer coating, the SLS strength was ≈ 20.7 MPa (3000 psi) and failure occurred almost exclusively within the epoxy adhesive. As the thickness of the PP styrene or epichlorohydrin primer film was increased to 1500 Å, the SLS strength dropped to ≈ 1600 psi and failure was interfacial. They were unable to determine whether failure occurred at the PP film/substrate interface or at the PP film/epoxy interface, but the cohesive element of the failure definitely vanished. Additionally, these researchers saw a change in the surface properties of the PP films with thickness, as determined by contact angle measurements. Specifically, the surface energy of PP polystyrene decreased with film thickness because of a decrease in the dispersive component.

The XPS analysis showed variations in the surface compositions of the films due to differences in thickness (see Table 6.4). Ac.120s.200w.f20.Ar surfaces contained carbon (92.2 %) and oxygen (7.8 %) only, while Ac.30s.200w.f20.Ar contained carbon (84.0 %), oxygen (14.7 %), and nitrogen (1.3 %). The C 1s curve-fit for Ac.120s.200w.f20.Ar (Figure 6.6) differs from the C 1s photopeak of Ac.30s.200w.f20.Ar (Figure 6.7). The C 1s photopeak of Ac.30s.200w.f20.Ar had a larger component from C-O and C=O groups (286.6 and 288.1 eV), and an added resolved peak due to C-N nitrogen (286.0 eV). Also, the C 1s photopeak had a broadness due to a peak or peaks not assigned at binding energies below 285.0 eV. This broadness at low binding energy is indicative of aromaticity and/or the presence of alkene groups,[10] which have been reported by other researchers of PP acetylene.[2]

The phenomenon discussed above has been reported by other researchers and detailed through infrared analysis.[7] It is caused by the fact that certain functional groups are only able to form later in the deposition process through the recombination of free radicals already deposited.

Table 6.4: XPS results for Ac.120s.200w.f20.Ar and Ac.30s.200w.f20.Ar.

Sample	Thickness (Å)	% C	% O	% N	% Ti	SLS (MPa)	SLS (psi)
Ac.120s.200w.f20.Ar	750 ± 48	92.2	7.8	ND	ND	4.90 ± 0.97	710 ± 140
Ac.30s.200w.f20.Ar	62 ± 11	84.0	14.7	1.3	ND	15.1 ± 2.41	2190 ± 350

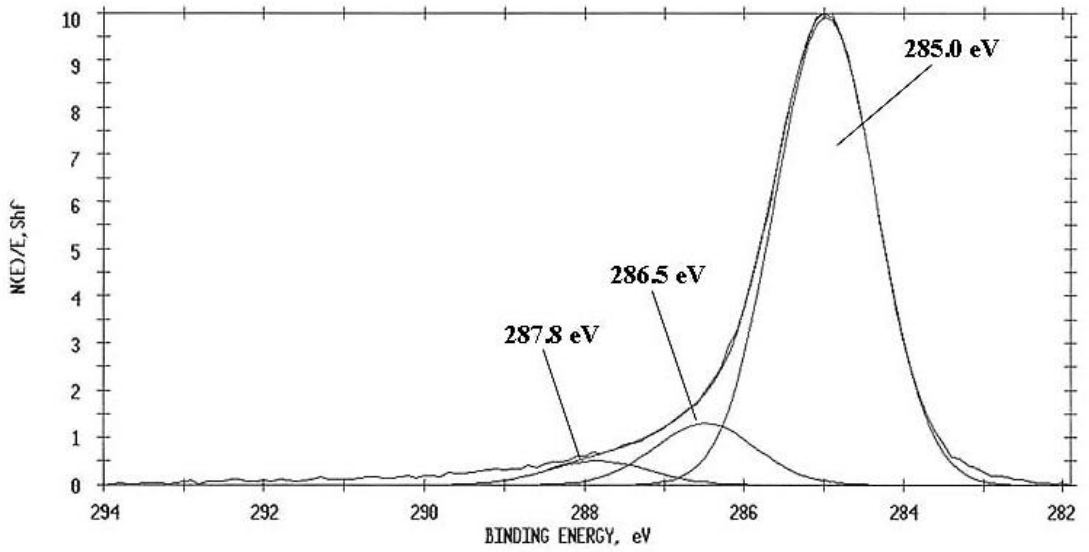

Figure 6.6: Curve-fit C 1s photopeak for Ac.120s.200w.f20.Ar.

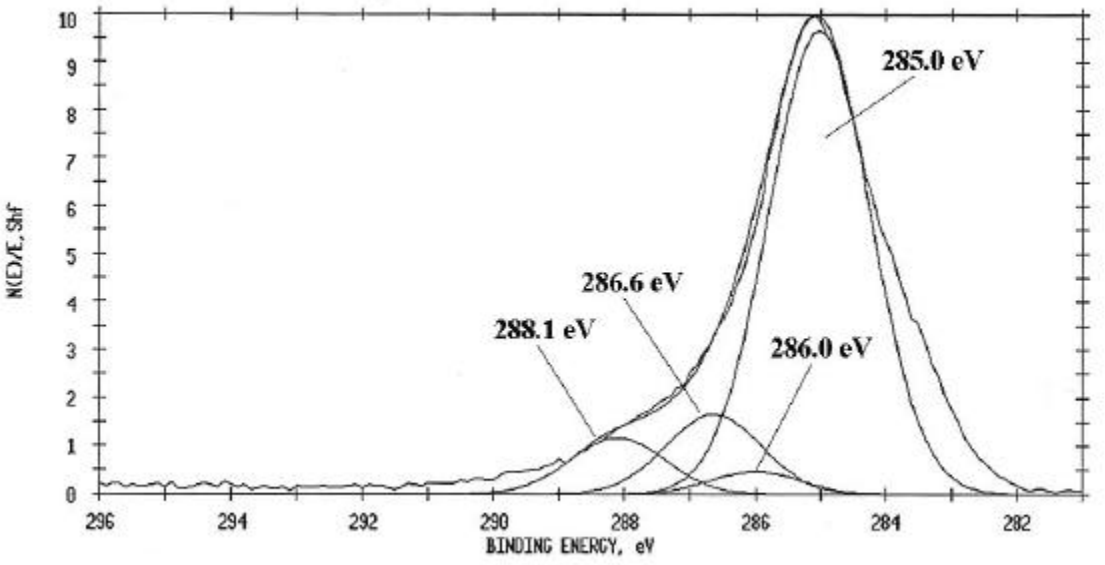

Figure 6.7: Curve-fit C 1s photopeak for Ac.30s.200w.f20.Ar.

6.5.3 Flow Rate Variation (Ar)

The effect of acetylene flow rate on SLS strength was investigated by comparing samples Ac.120s.200w.f20.Ar and Ac.120s.200w.f10.Ar. The samples were pretreated with an oxygen plasma (20 sccm, 200W, 10 minutes), then treated with an argon/acetylene plasma (20 sccm argon, 200W, 2 minutes). Ac.120s.200w.f20.Ar and Ac.120s.200w.f10.Ar had acetylene flow rates of 20 sccm and 10 sccm, respectively. As expected,[11] the higher flow rate yielded a thicker PP film, which had the result of weakening the SLS strength. Ac.120s.200w.f20.Ar had a PP acetylene thickness of 749 ± 48 Å and a SLS strength of 4.90 ± 0.97 MPa (710 ± 140 psi), while Ac.120s.200w.f10.Ar had a PP acetylene thickness of 397 ± 48 Å and a SLS strength of 9.31 ± 0.90 MPa (1350 ± 130 psi). The increase in SLS strength was suspected to be a thickness effect, because the compositions of the PP acetylene from the two processes were very similar, and the thickness was previously shown to significantly affect SLS strength.

The differences in nitrogen cannot be readily explained. It was assumed that sample Ac.120s.200w.f10.Ar reacted with atmospheric nitrogen after the process to a greater extent than Ac.120s.200w.f20.Ar, giving it higher nitrogen content (Table 6.5). This added a slight shoulder to the C 1s photopeak of Ac.120s.200w.f10.Ar compared to Ac.120s.200w.f20.Ar (Figure 6.8 and Figure 6.9). The XPS O 1s peaks (not shown) were identical and showed contributions from carbonyl and ether groups only. These results indicated that for this system, flow rate has a negligible effect on both composition of the PP film and on the SLS strength.

Table 6.5: XPS results for Ac.120s.200w.f20.Ar and Ac.120s.200w.f10.Ar.

Sample	Thickness (Å)	% C	% O	% N	% Ti	SLS (MPa)	SLS (psi)
Ac.120s.200w.f20.Ar	749 ± 48	92.2	7.8	ND	ND	4.90 ± 0.97	710 ± 140
Ac.120s.200w.f10.Ar	397 ± 48	83.3	10.1	6.6	ND	9.31 ± 0.90	1350 ± 130

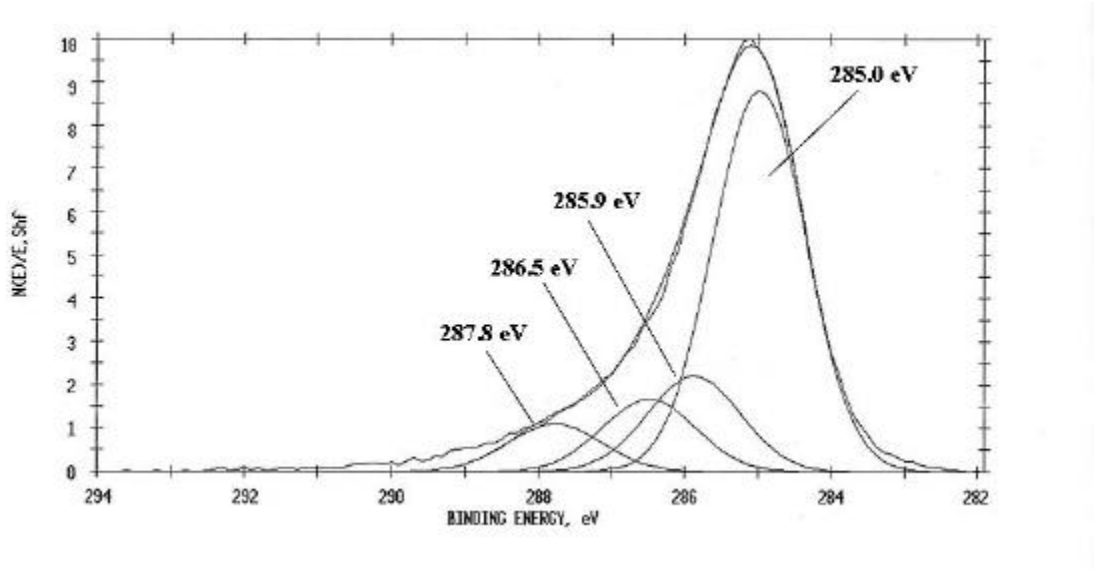

Figure 6.8: Curve-fit C 1s photopeak for Ac.120s.200w.f10.Ar.

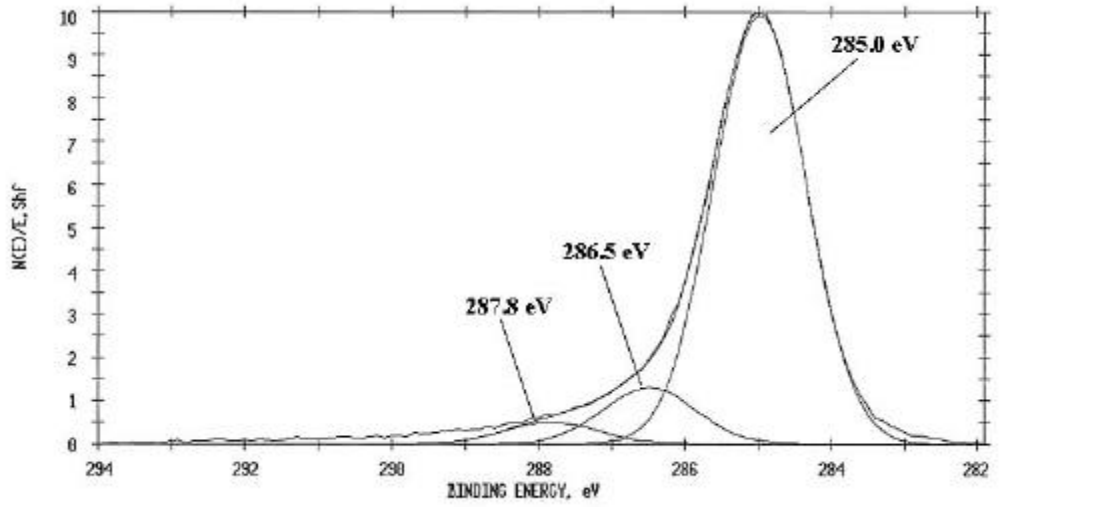

Figure 6.9: Curve-fit C 1s photopeak for Ac.120s.200w.f20.Ar.

6.6 Helium Carrier Gas Experiments

6.6.1 Power Variation (He)

PP films of acetylene deposited using helium as the carrier gas were investigated. Samples Ac.120s.200w.f10.He and Ac.120s.100w.f10.He were compared to evaluate the effect of power input on plasma polymerization and SLS bond strength. For both experiments, the samples were pretreated with a helium plasma (20 sccm, 200 W, 5 minutes), and then exposed to an acetylene/helium plasma (10 sccm/20 sccm, 2 minutes). Sample Ac.120s.200w.f10.He was treated at 200 watts, while sample Ac.120s.100w.f10.He was treated at 100 watts. The deposition rate at 200 watts was higher than the deposition rate at 100 watts. The effect of power input on the composition and thickness of the PP films is shown in Table 6.6. The compositions of the two films were very similar, and their C 1s and O 1s photopeaks were essentially the same. The atomic concentrations of Ac.120s.200w.f10.He and Ac.120s.100w.f10.He were 71 % C, 10 % O, 18 % N, and 72 % C, 13 % O, 16 % N, respectively. Their C 1s photopeaks (not shown) contained contributions from C-H/C-C, C-N, C-O, and C=O groups. The O 1s photopeaks (not shown) showed contributions from C=O and C-O. Despite the similarities in composition, however, their SLS strengths indicate that higher power input resulted in a stronger bond, probably due to increased atomic interfacial mixing.[4] The SLS strength of Ac.120s.200w.f10.He was 12.1 ± 2.07 MPa (1760 ± 300 psi), while Ac.120s.100w.f10.He was 7.58 ± 0.83 MPa (1100 ± 120 psi). Ac.120s.200w.f10.He had a thickness of 293 ± 15 Å, while Ac.120s.100w.f10.He had a thickness of 234 ± 37 Å. Because the thicknesses and surface compositions were so similar, the differences in SLS were most likely a result of the varied input power, with the PP film deposited at lower input power giving poorer adhesion because of decreased atomic interfacial mixing.

Table 6.6: XPS results for Ac.120s.200w.f10.He and Ac.120s.100w.f10.He.

Sample	Thickness (Å)	% C	% O	% N	% Ti	SLS (MPa)	SLS (psi)
Ac.120s.200w.f10.He	293 ± 15	71.3	10.4	18.3	ND	12.1 ± 2.07	1760 ± 300
Ac.120s.100w.f10.He	234 ± 37	71.6	12.5	15.9	ND	7.58 ± 0.83	1100 ± 120

The failure mode of Ac.120s.200w.f10.He was rare in that no titanium was detected on the metal failure side (see Table 6.7), indicating that a thin PP film remained on the surface. The C 1s photopeak from the metal failure side was slightly different from the C 1s photopeak on the adhesive failure side (Figure 6.10 and Figure 6.11). The shoulder on the C 1s photopeak for the adhesive side of failure indicated a small amount of imide carbon, which is characteristic of the cured adhesive. However, the oxygen photopeak (Figure 6.12) from the adhesive failure side was not consistent with the oxygen peak of cured FM-5 (see Chapter 4). This indicated that failure took place within the PP film near the adhesive, but not at the adhesive/PP acetylene interface. Furthermore, the O 1s photopeak from the Ti-6Al-4V failure side (Figure 6.13) was identical to that of the O 1s peak from the adhesive failure side (Figure 6.12), which indicated cohesive failure within the PP film.

The silicon (binding energy of 102.0 eV) detected on the titanium failure side was presumed to be from un-reacted amino propyl silane that migrated to the Ti-6Al-4V surface from the adhesive during annealing. Amino propyl silane is a coupling agent in FM-5.

Table 6.7: XPS results for failed Ac.120s.200w.f10.He and Ac.120s.100w.f10.He.

Sample	% C	% O	% N	% Ti	% Si
Ac.120s.200w.f10.He Ti side	85.3	9.2	4.0	ND	1.5
Ac.120s.200w.f10.He adhesive side	78.0	12.0	8.9	ND	1.1
Ac.120s.100w.f10.He Ti side	70.0	19.8	4.7	3.4	2.2
Ac.120s.100w.f10.He adhesive side	82.3	10.1	6.9	Trace	2.6

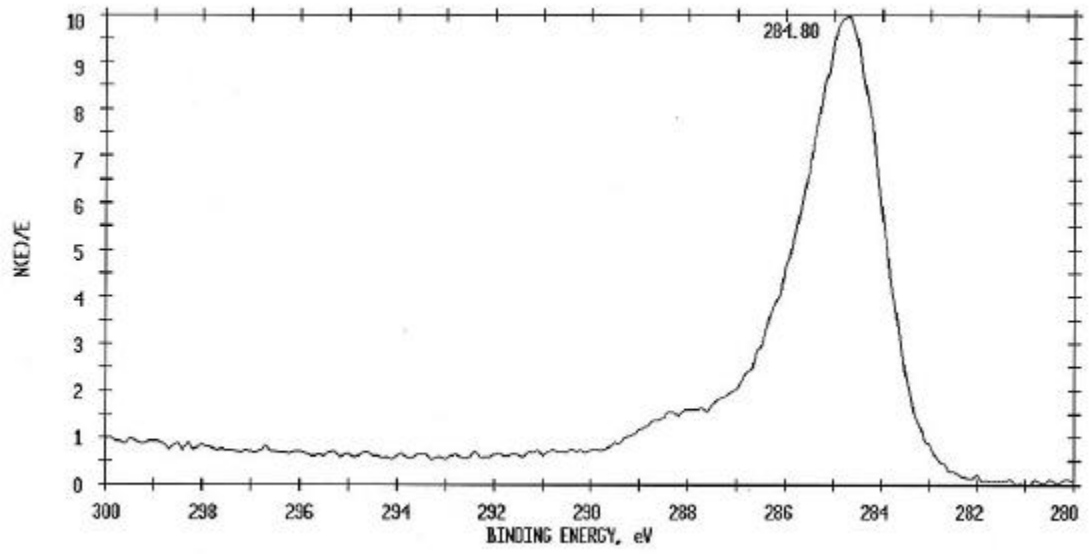

Figure 6.10: C 1s photopeak for Ac.120s.200w.f10.He, adhesive failure side (unshifted).

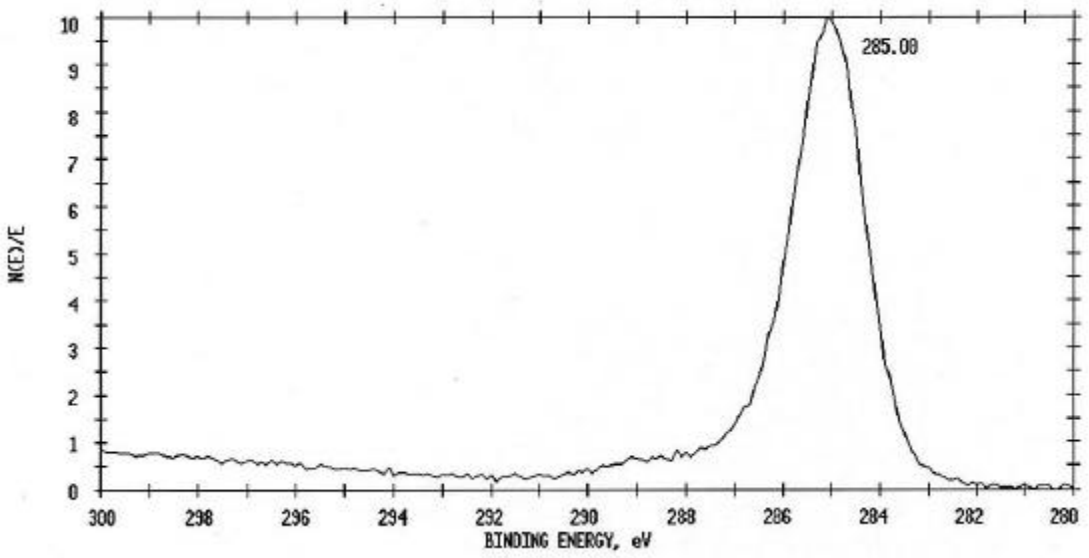

Figure 6.11: C 1s photopeak for Ac.120s.200w.f10.He, Ti-6Al-4V failure side.

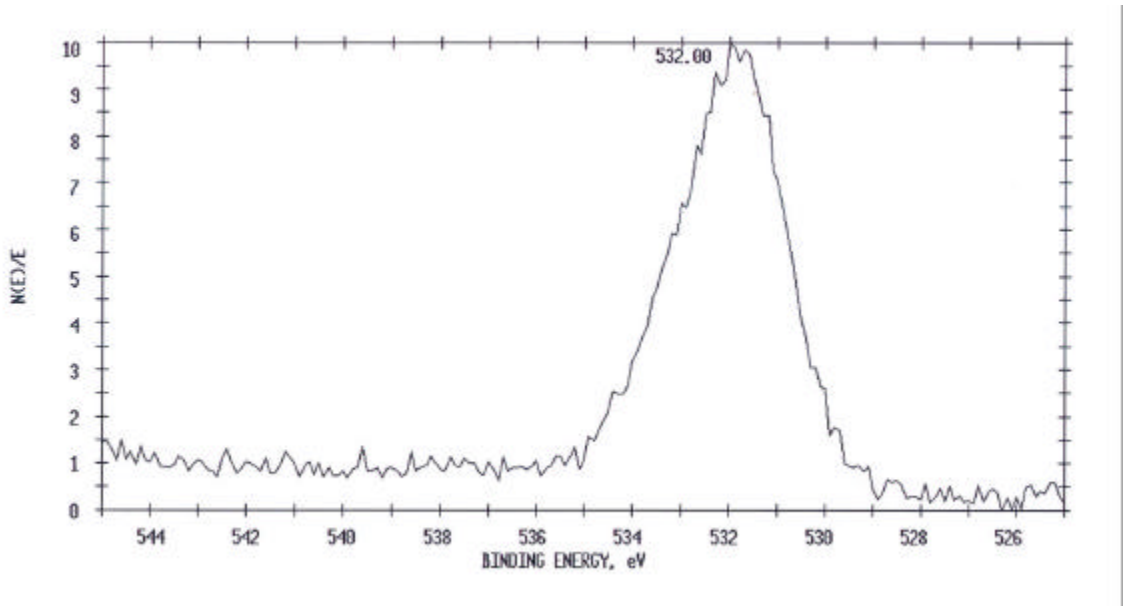

Figure 6.12: O 1s photopeak for Ac.120s.200w.f10.He, adhesive failure side (unshifted).

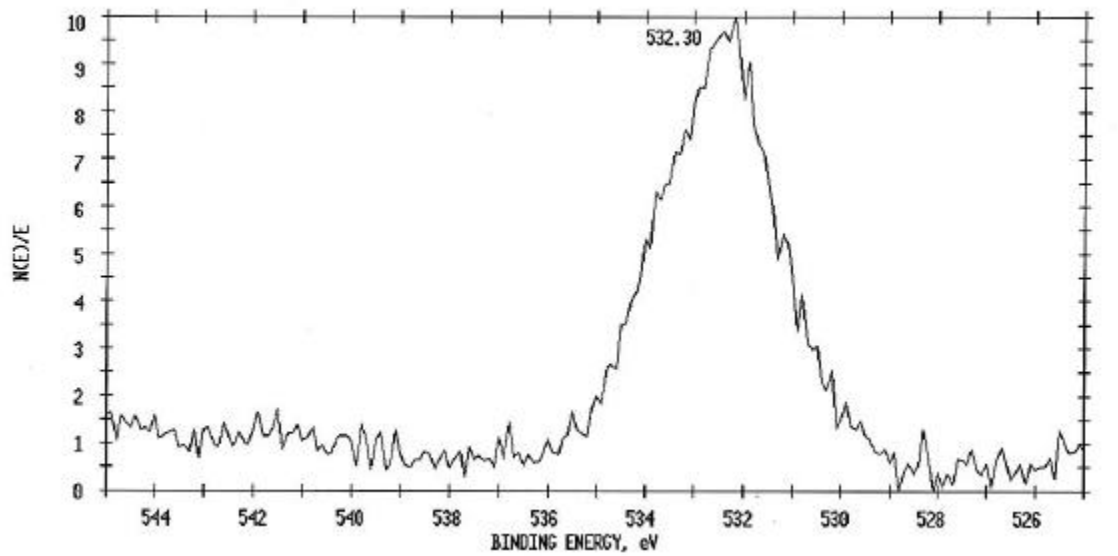

Figure 6.13: O 1s photopeak for Ac.120s.200w.f10.He, Ti-6Al-4V failure side.

A review of the XPS data for sample Ac.120s.100w.f10.He (Table 6.7) indicated that failure occurred at the PP film/Ti-6Al-4V interface. The C 1s photopeaks (not shown) from the two failure sides were identical, and the oxygen peak from the titanium failure side resembled that of acetone cleaned Ti-6Al-4V. The differing modes of failure for the samples seem to be a result of the difference in power input during the plasma polymerization process. Helium

produces a very strong ablative plasma,[6] and at high power input, this effect is accentuated. During the plasma deposition process at 200 W, it is reasonable that more titanium oxide was ablated and combined with the PP acetylene as it deposited. This greater interaction (due to AIM) induced failure within the PP films near the adhesive, rather than at the PP film/Ti-6Al-4V interface, and this produced a higher SLS strength. At the lower power input (100 W), less ablation occurred during deposition and the PP acetylene interacted with titanium to a lesser extent. These weaker interactions at the metal/PP acetylene interface account for the failure mode of Ac.120s.100w.f10.He and its lower average SLS strength.

6.6.2 Thickness Variation (He)

Samples Ac.120s.200w.f10.He and Ac.30s.200w.f10.He were compared to determine the effects of film thickness on SLS strength. The samples were pretreated with a helium plasma (20 sccm, 200W, 10 minutes), then treated with a helium/acetylene plasma (20 sccm/10 sccm, 200W). Ac.120s.200w.f10.He was treated for 2 minutes, while Ac.30s.200w.f10.He was treated for only 30 seconds. AES analysis revealed that the film thicknesses of Ac.120s.200w.f10.He and Ac.30s.200w.f10.He were 293 ± 15 Å and 239 ± 4 Å, respectively. This small difference in thickness can be explained in one of two ways: 1) the pressure difference during the depositions was a factor. The pressure during deposition for sample Ac.120s.200w.f10.He was 10 mTorr, while the pressure during the deposition of sample Ac.30s.200w.f10.He was 3.5 mTorr. Higher pressures during deposition typically result in a longer residence time of plasma species,[12] and this could result in a larger amount of ablation (due to the helium) and a lower deposition rate. 2) Film deposition could be following a non-linear deposition rate. The PP film may deposit quickly to a certain threshold before the ablative rate begins to approach and become equivalent to the deposition rate.

Table 6.8 compares the thickness, surface compositions, and SLS strength for the two sample sets. Ac.120s.200w.f10.He contained a large amount of nitrogen (18 %) compared to Ac.30s.200w.f10.He (2 %), and less carbon (71 % vs. 90 %, respectively). Samples that were exposed for 2 minutes could have contained a larger amount of free radicals after treatment because of the ablative effects of the helium. Because helium in a non-plasma state is non-

reactive, the 15-minute purge after deposition may not have quenched the surface free radicals. Subsequent reaction with atmospheric nitrogen could account for the surface compositional differences.

Table 6.8: XPS results for Ac.120s.200w.f10.He and Ac.30s.200w.f10.He.

Sample	Thickness (Å)	% C	% O	% N	% Ti	SLS (MPa)	SLS (psi)
Ac.120s.200w.f10.He	293 ± 15	71.3	10.4	18.3	ND	12.1 ± 2.07	1760 ± 300
Ac.30s.200w.f10.He	239 ± 4	90.4	7.7	1.9	ND	13.4 ± 1.65	1940 ± 240

The failure modes for the two samples were slightly different, as evidenced from the data in Table 6.9. Ac.120s.200w.f10.He samples failed within the PP acetylene layer near the adhesive, as discussed in Section 6.6.1. Ac.30s.200w.f10.He samples, however, failed at the PP acetylene/TiO_2 interface (8 % titanium detected on the metal failure side). SLS results yielded bond strengths of 12.1 ± 2.07 MPa (1760 ± 300 psi) and 13.4 ± 1.65 (1940 ± 240 psi) for Ac.120s.200w.f10.He and Ac.30s.200w.f10.He, respectively. These essentially identical results showed that the slight thickness variations induced by changing deposition time had very little effect on the overall bond strength. Additionally, the different modes of failure did not result in any significant difference in the SLS strength. The silicon (binding energy of 102.0 eV) detected on the titanium failure side was presumed to be from un-reacted amino propyl silane that migrated to the Ti-6Al-4V surface from the adhesive during annealing.

Table 6.9: XPS results for failed Ac.120s.200w.f10.He and Ac.30s.200w.f10.He.

Sample	% C	% O	% N	% Ti	% Si	% Al
Ac.120s.200w.f10.He Ti side	85.3	9.2	4.0	ND	1.5	ND
Ac.120s.200w.f10.He adhesive side	78.0	12.0	8.9	ND	1.1	ND
Ac.30s.200w.f10.He Ti side	50.3	33.1	3.1	8.3	3.4	1.8
Ac.30s.200w.f10.He adhesive side	80.5	14.1	3.9	ND	1.5	ND

6.6.3 Flow Rate Variation (He)

The effects of flow rate were investigated by comparing samples Ac.30s.200w.f20.He with Ac.30s.200w.f10.He. The samples were pretreated with a helium plasma (20 sccm, 200W, 5

minutes), then treated with a helium/acetylene plasma (20 sccm helium, 200W, 2 minutes). Ac.30s.200w.f20.He and Ac.30s.200w.f10.He had acetylene flow rates of 20 sccm and 10 sccm, respectively. The SLS for samples Ac.30s.200w.f20.He and Ac.30s.200w.f10.He were 9.65 ± 1.72 MPa (1400 ± 250 psi) and 13.4 ± 1.65 MPa (1940 ± 240 psi), respectively, and the thicknesses of the PP films were 119 ± 15 Å and 239 ± 4 Å, respectively. Interestingly, the lower flow rate yielded a thicker film in the same amount of time. From the XPS data, the composition of the two films is almost identical (Table 6.10). The curve resolved C 1s and O 1s peaks (not shown) confirmed this finding. The C 1s photopeaks showed contributions from C-H/C-C, C-N, C-O, and C=O groups, while the O 1s photopeaks showed C=O and C-O contributions. The XPS-determined failure mode for both samples was at the PP acetylene/TiO_2 interface.

Table 6.10: XPS results for Ac.30s.200w.f20.He and Ac.30s.200w.f10.He.

Sample	Thickness (Å)	% C	% O	% N	% Ti	SLS (MPa)	SLS (psi)
Ac.30s.200w.f20.He	119 ± 15	90.5	9.0	0.5	ND	9.65 ± 1.72	1400 ± 250
Ac.30s.200w.f10.He	239 ± 4	90.4	7.7	1.9	ND	13.4 ± 1.65	1940 ± 240

A curious finding was that the lower flow rate resulted in a thicker PP acetylene film and showed greater SLS strength. The trend that was previously followed was that a greater flow rate allowed for greater deposition for a given amount of time, and a thicker film led to weaker SLS strengths. The pressure during the deposition may have played a role here. The pressure during the preparation of Ac.30s.200w.f20.He was 25 mTorr, while the pressure during the preparation of Ac.30s.200w.f10.He was only 3.5 mTorr. This may account for the difference in the deposition rate for the two experiments. As mentioned earlier in Section 6.6.2, pressure influences on plasma polymerization include an effect on residence time (which increases with increasing pressure).[11, 12] An explanation that could account for the lower thickness of He.Ac.005 involves the residence time of activated species. At higher flow rates, the residence time of the feed gases decreases and thus the activated species may be pumped away before they can interact with the substrate.[11] If this is not offset by the increase in residence time due to increased pressure, then this would result in a thinner film.

6.7 No Carrier Gas

The effect of the thickness and input power on the composition of PP acetylene thin films (no carrier gas) and the performance of SLS joints was evaluated by comparing samples Ac.120s.200w.f10, Ac.30s.200w.f10, and Ac.130s.10w.f10. Samples Ac.120s.200w.f10 and Ac.30s.200w.f10 were pretreated with an oxygen plasma (20 sccm, 200W, 10 minutes), and then subjected to an acetylene plasma (no carrier gas, 10 sccm, 200 W). Ac.120s.200w.f10 was exposed to the acetylene plasma for 2 minutes, while Ac.30s.200w.f10 was exposed for 30 seconds. Sample Ac.130s.10w.f10 was treated in a different plasma reactor that was horizontal rather than vertical (see Chapter 3 for reactor descriptions). It was pretreated with an oxygen plasma (20 sccm, 50W, 2 minutes), then subjected to an acetylene plasma at much lower power (no carrier gas, 10 sccm, 10 W, 2 minutes). Ac.120s.200w.f10, Ac.30s.200w.f10, and Ac.130s.10w.f10 had PP acetylene film thicknesses of 583 ± 13Å and 73 ± 22 Å, and 545 ± 15 Å, respectively. Their SLS strengths were 8.55 ± 0.97 MPa (1240 ± 140 psi), 14.3 ± 2.41 (2080 ± 350 psi), and 12.0 ± 0.55 MPa (1739 ± 80 psi), respectively. Surprisingly, the two sample sets treated for approximately 2 minutes (Ac.120s.200w.f10 and Ac.130s.10w.f10) showed no thickness variation with input power, which was probably due to the different reactor geometries.[12] Also, the samples prepared at lower input power exhibited a higher average SLS strength than films of the same thickness prepared at higher input power. Because this also could have been a reactor geometry effect (PP films prepared in different geometry reactors often differ), no conclusions were drawn from these experiments.

The results of these three experiments support the notion that thinner PP acetylene films provide stronger joints; the thinnest film (73 ± 22 Å) yielded the strongest SLS strength 14.3 ± 2.41 MPa (2080 ± 350). Table 6.11 lists the elemental surface compositions of the samples, which were very similar. Generally, when no carrier was used, PP film compositions exhibited increased carbon content and more C-H/C-C dominated C 1s photopeaks. Comparing Figure 6.14, Figure 6.5 (from Section 6.4), and Figure 6.15, the C 1s photopeaks for these samples were very similar. Interestingly, without a carrier gas, the composition of the PP acetylene films did not vary with PP film thickness.

Table 6.11: XPS results for Ac.120s.200w.f10, Ac.30s.200w.f10, and Ac.130s.10w.f10.

Sample	Thickness (Å)	% C	% O	% N	% Ti	SLS (MPa)	SLS (psi)
Ac.120s.200w.f10	583 ± 13	91.8	8.0	Trace	ND	8.55 ± 0.97	1240 ± 140
Ac.30s.200w.f10	73 ± 22	91.5	8.1	Trace	ND	14.3 ± 2.41	2080 ± 350
Ac.130s.10w.f10	545 ± 15	93.2	6.8	ND	ND	12.0 ± 0.55	1739 ± 80

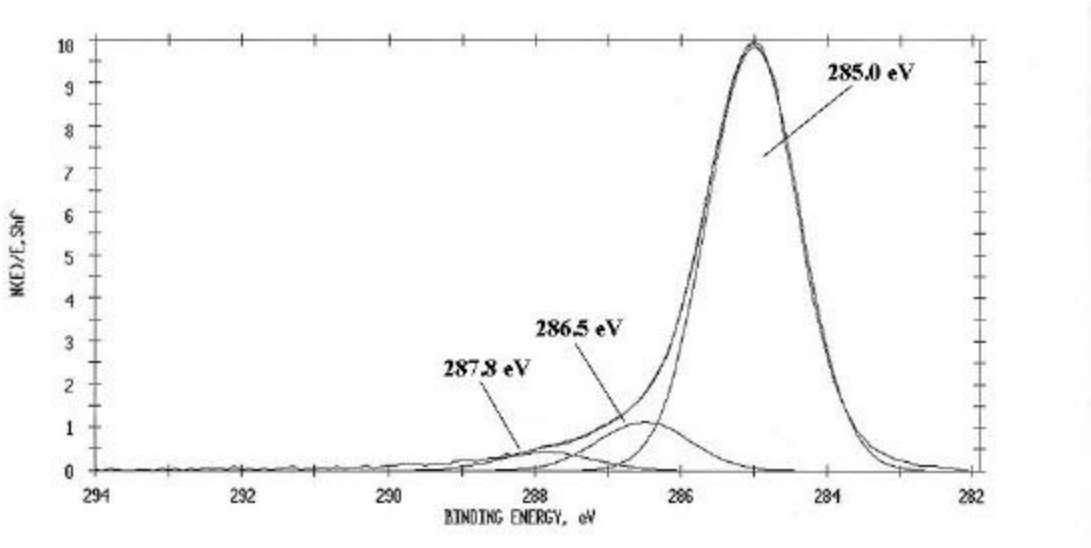

Figure 6.14: Curve-fit C 1s photopeak for non-bonded Ac.30s.200w.f10.

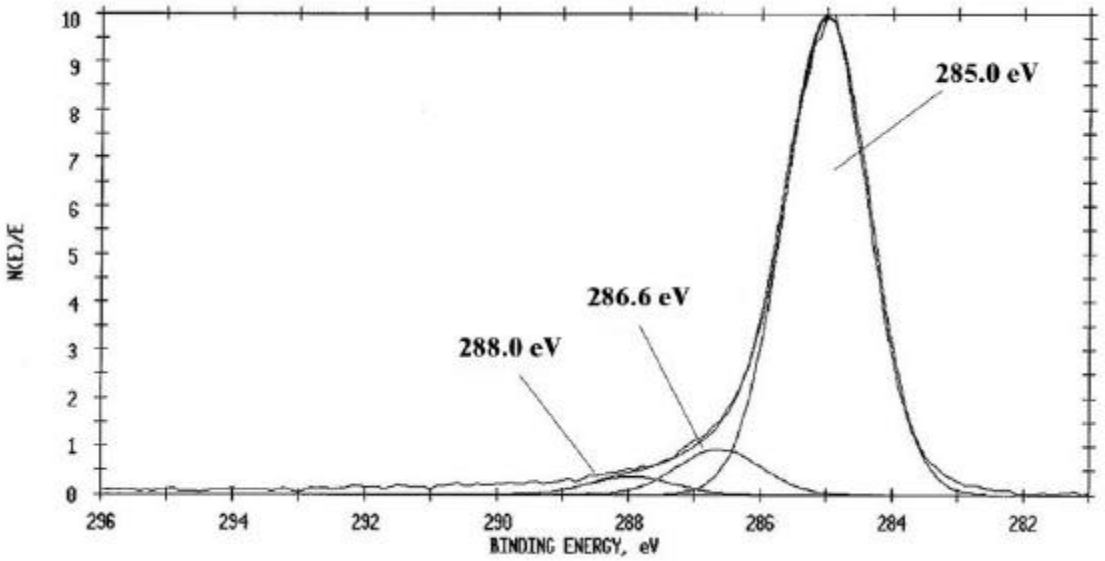

Figure 6.15: Curve-fit C 1s photopeak for non-bonded Ac.130s.10w.f10.

6.8 Surface Roughness Effects

Samples Ac.120s.100w.f10.Ar and Ac.120s.100w.f10.Ar (polished) were pretreated with an oxygen plasma (20 sccm, 200 watts, 10 minutes), then treated with an argon/acetylene plasma (Ar/acetylene - 20 sccm/10 sccm, 100 watts, 2 minutes). The only difference between the samples was that the substrates for Ac.120s.100w.f10.Ar (polished) were polished to a smooth finish before treatment using 0.3 micron grit alumina. Samples of Ac.120s.100w.f10.Ar were acetone cleaned, but were considerably rougher, as described in Chapter 4. An SEM photomicrograph of sample Ac.120s.100w.f10.Ar (polished) (Figure 6.16) was featureless at very high magnification (5.0 kx), while the SEM photomicrograph of the PP film on Ti-6Al-4V (not polished) was relatively rough (Figure 6.17), even at lower magnification (1.0 kx). XPS analysis of the two samples revealed that their compositions were almost identical (Table 6.12). The thicknesses of the films were 127 ± 30 Å and 223 ± 13Å for samples Ac.120s.100w.f10.Ar and Ac.120s.100w.f10.Ar (polished), respectively. Surprisingly, the deposition rate was higher on the polished Ti-6Al-4V than on the rougher substrate. The pressures during deposition were 1 and 2 mTorr for Ac.120s.100w.f10.Ar and Ac.120s.100w.f10.Ar (polished), respectively. The thickness variation might be due to the increased residence time of the acetylene during treatment of samples Ac.120s.100w.f10.Ar (polished), or PP acetylene may have a higher affinity for the polished Ti-6Al-4V surface. Recall that the surface composition of acetone cleaned Ti-6Al-4V differed from the surface composition of polished Ti-6Al-4V (see Chapter 4), and this may have affected nucleation and subsequent growth of PP films.

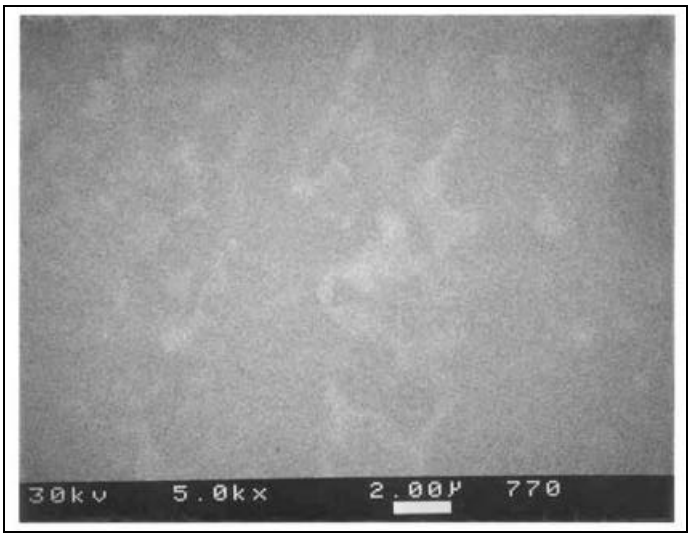

Figure 6.16: SEM photomicrograph of Ac.120s.100w.f10.Ar (polished) (5.0 kx).

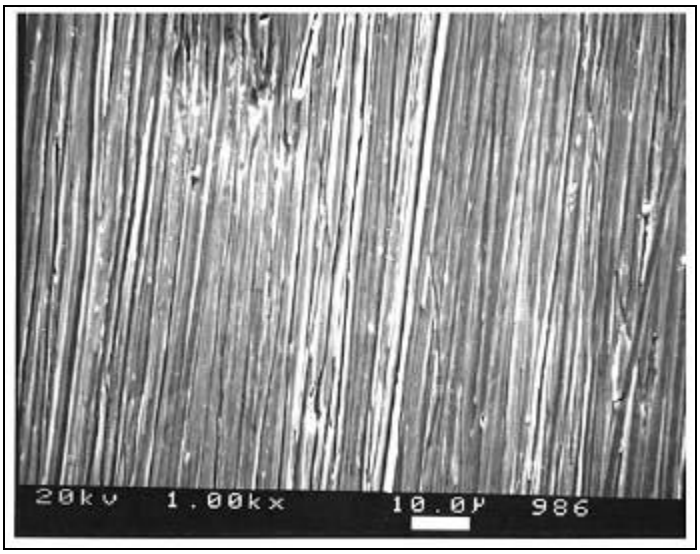

Figure 6.17: SEM photomicrograph of Ac.120s.100w.f10.Ar (unpolished) (1.0 kx).

Table 6.12: XPS results for Ac.120s.100w.f10.Ar and Ac.120s.100w.f10.Ar (polished).

Sample	Thickness (Å)	% C	% O	% N	% Ti	SLS (MPa)	SLS (psi)
Ac.120s.100w.f10.Ar	127 ± 30	89.8	10.2	ND	ND	11.4 ± 0.15	1656 ± 22
Ac.120s.100w.f10.Ar (polished)	223 ± 13	86.8	11.6	1.5	ND	9.31 ± 2.21	1350 ± 320

Ac.120s.100w.f10.Ar and Ac.120s.100w.f10.Ar (polished) gave average SLS strengths of 11.4 ± 0.15 MPa (1656 ± 22 psi) and 9.31 ± 2.21 (1350 ± 320 psi), respectively. Failure was at

the PP film/Ti-6Al-4V interface for both sets of samples. The surface roughness was not a large SLS strength-determining factor. It was thought that decreased mechanical interlocking for polished Ti-6Al-4V would decrease its SLS strength. However, this effect was not observed, and the two average SLS strengths were essentially equal, within the standard deviations.

6.9 Grounding Effects

It was speculated that by grounding the samples during plasma treatment, the positive ions of the plasma would be accelerated toward the substrates because of increased charge attractions. It was hoped that these plasma species would have a greater kinetic energy and collide with the samples with greater force, thus increasing ablation of the substrate and enhancing substrate-plasma interactions. This is the premise behind applying a substrate bias during plasma processes, which many researchers have investigated.[13, 14, 15, 16]

Specimens prepared in Ac.30s.100w.f10.N and Ac.30s.100w.f10.N (grounded) were both pretreated with a nitrogen plasma (20 mTorr, 100 W, 5 minutes), then treated with a nitrogen/acetylene plasma (10 sccm/10 sccm, 100 W, 30 seconds). The samples for experiment Ac.30s.100w.f10.N (grounded) were grounded with a silver-coated copper wire that ran from the sample holder to ground. The surface compositions of the PP films are given in Table 6.13; they were essentially identical. The C 1s curve-fit photopeak for sample Ac.30s.100w.f10.N (Figure 6.18) showed contributions from C-H/C-C (285.0 eV), C-N (286.1 eV), C-O (286.6 eV), and C=O (288.1 eV) groups. The C 1s photopeak of Ac.30s.100w.f10.N (grounded) (not shown) was identical to that of Ac.30s.100w.f10.N. The O 1s curve-fit photopeaks (not shown) were identical for the two samples and showed the typical contributions from C-O and C=O.

Ac.30s.100w.f10.N and Ac.30s.100w.f10.N (grounded) had PP film thicknesses of 31 ± 2 Å and 23 ± 3 Å, respectively, and SLS strengths of 19.2 ± 3.31 MPa (2780 ± 480 psi) and 15.0 ± 0.90 MPa (2170 ± 130 psi) respectively. Considering the very similar surface compositions and the similar thicknesses of theses samples, grounding the samples during treatment actually had very little effect on the deposition of PP acetylene. These two sample sets yielded essentially the same SLS results within statistical limits.

Table 6.13: XPS results for Ac.30s.100w.f10.N and Ac.30s.100w.f10.N (grounded).

Sample	Thickness (Å)	% C	% O	% N	% Ti	SLS (MPa)	SLS (psi)
Ac.30s.100w.f10.N	31 ± 2	76.4	7.3	16.2	ND	19.2 ± 3.31	2780 ± 480
Ac.30s.100w.f10.N (grounded)	23 ± 3	77.2	9.1	13.7	ND	15.0 ± 0.90	2170 ± 130

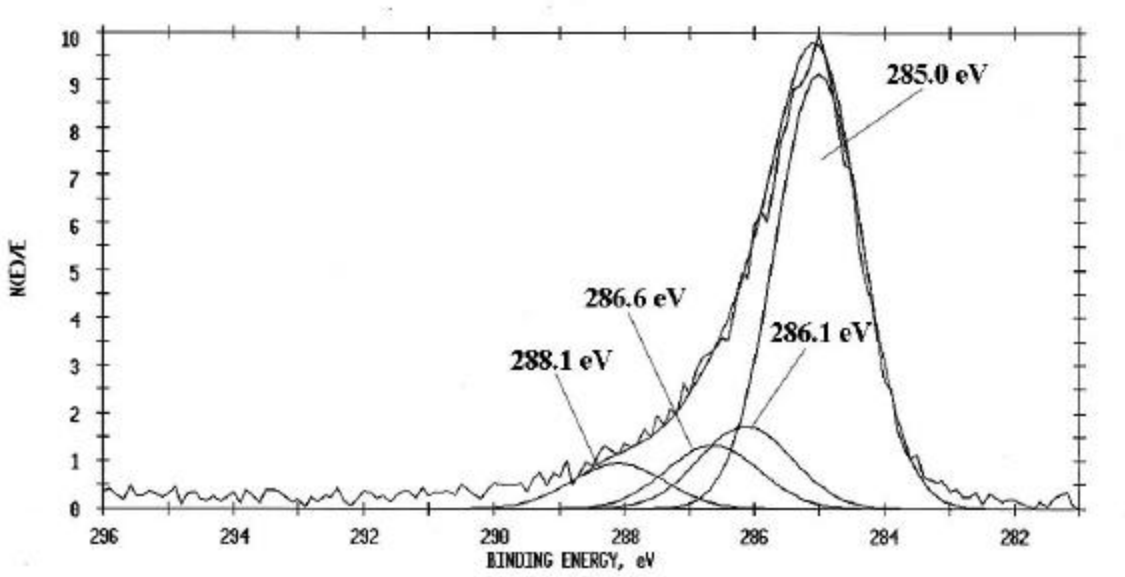

Figure 6.18: Curve-fit C 1s photopeak for non-bonded Ac.30s.100w.f10.N (grounded).

6.10 Overall Thickness Effect

Because PP film thickness appeared to influence adhesive strength, the SLS strength was considered as a function of thickness. Other researchers have reported this effect.[4] For example, Dynes and Kaelble[9] reported that SLS strength decreased as PP acetylene film thickness increased for SLS specimens prepared using an epoxy. As the PP film thickness was increased up to 1500 Å, the amount cohesive failure (within the epoxy), as determined visually, decreased to almost zero.

A plot of SLS strength vs. thickness is shown in Figure 6.19 for all of the samples in the current study (the polynomial-fit line serves only to guide the eye). The plot shows that, regardless of carrier gas, power input, flow rate, pretreatment, and grounding effects, the SLS strength decreased with increasing thickness. Figure 6.19 emphasizes that PP film thickness may

be the dominant factor among all others in dictating or influencing PP film adhesion and SLS strength. The effect is most pronounced up to a thickness of 400 Å, then it levels off. For all but one of the SLS strengths plotted in Figure 6.19, the failure mode was interfacial at the PP film/Ti-6Al-4V interface. The point in Figure 6.19 with the small arrow next to it represents the SLS joints that failed within the PP film (Ac.120s.200w.f10.He).

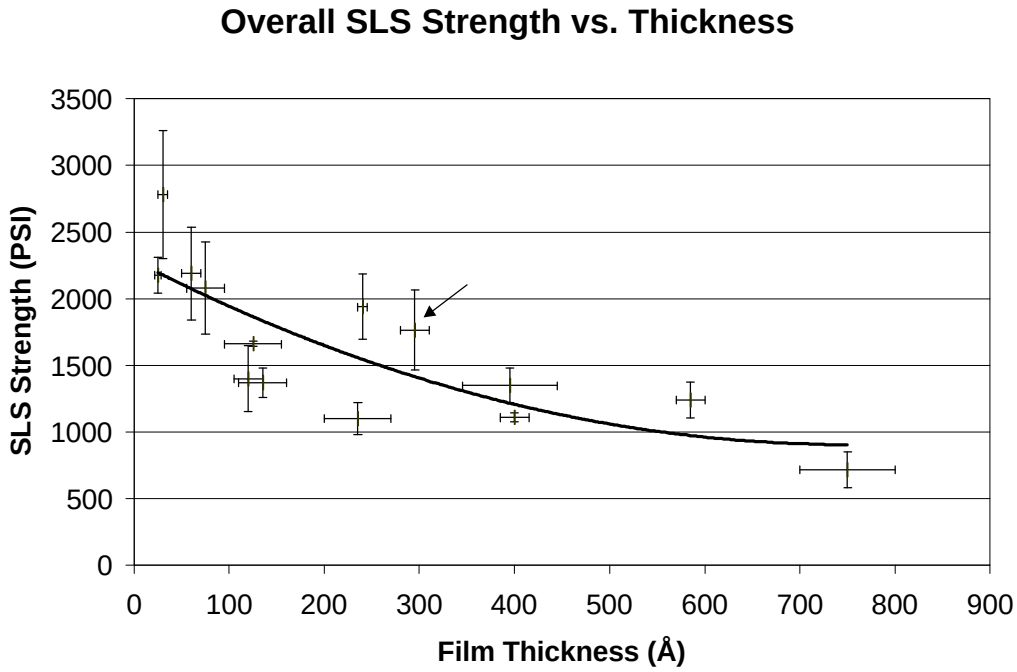

Figure 6.19: Overall SLS strength vs. thickness.

Another trend was observed when the XPS data were thickness normalized. Figure 6.20 shows the SLS strength as a function of the surface carbon content divided by the film thickness. As the percent carbon/thickness value increased, so did the SLS lap shear strength. This suggests that films that are more carbon-like are desirable for improving the SLS shear strength, and that PP films with high nitrogen and oxygen content were not efficient adhesion promoters.

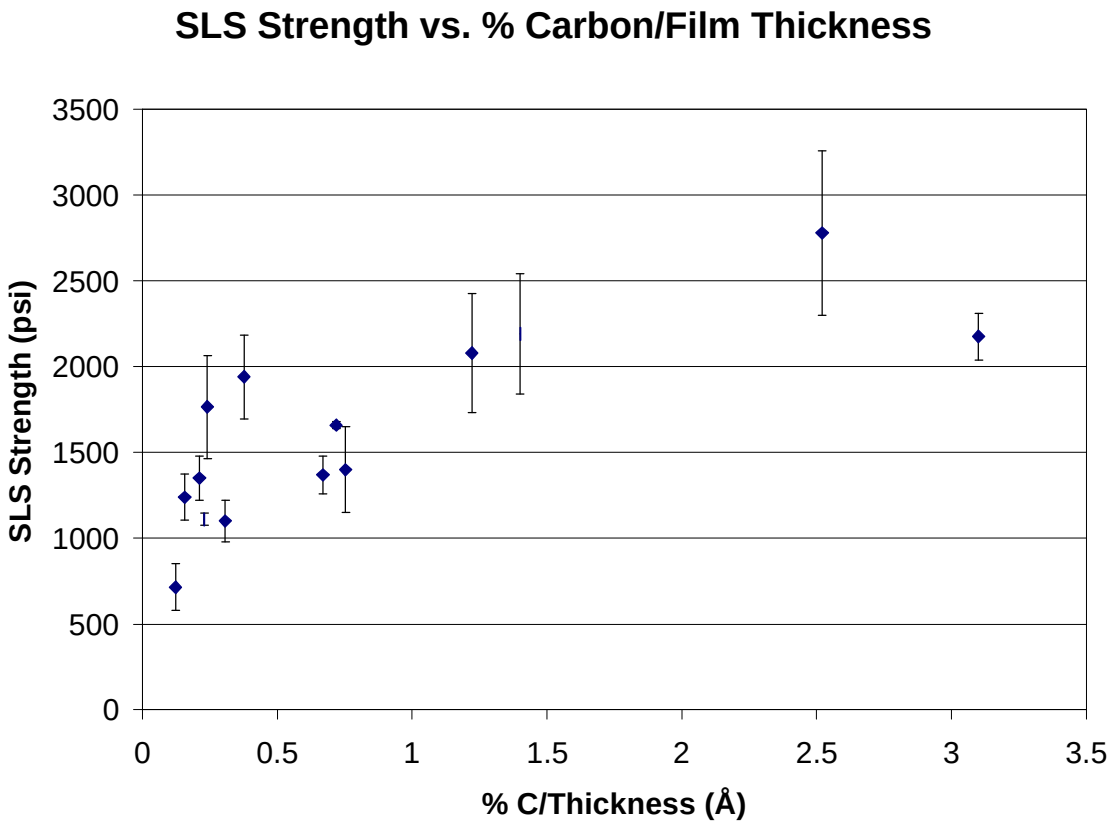

Figure 6.20: SLS strength vs. thickness-normalized % carbon content.

6.11 Investigation of Unsaturation

In an early study using an inductively coupled reactor (13.56 MHz), Kaplan and Dilks[6] ranked PP films formed from ethane, ethylene, and acetylene according to their unsaturated character, as determined by ^{13}C NMR. Acetylene had the highest percentage of unsaturation (38 %), followed by ethylene (24 %) and ethane (19 %). ^{13}C NMR results further indicated that over 50 % of the unsaturated carbons and over 20 % of the saturated carbons had no directly bonded hydrogen, suggesting a high degree of branching or cross-linking in the films. The NMR results provided direct evidence of the highly complex, three-dimensional networks of PP films.

The degree of unsaturation of the PP acetylene films was investigated in this study by exposing PP films to the vapor above 2M bromine in CCl_4 for 24 hours. An example of the classic bromination reaction with 1-hexene is shown in Figure 6.21.[17] Sample

Ac.120s.200w.f10.Ar was first pretreated with an oxygen plasma (20 sccm, 200 W, 10 minutes), then treated with an argon/acetylene plasma (20 sccm/10sccm, 200 W, 2 minutes). The thickness of the film was 400 ± 15 Å. The sample was placed in a tube furnace at 65° C for 1 hour following bromine exposure to remove any physisorbed bromine (the boiling point of bromine is 59° C). There was no significant color change of the film due to bromine exposure. XPS revealed that PP acetylene contained only 2.4 % bromine after physisorbed bromine was removed (see Table 6.14). The low amount of unsaturation could be a result of the small sampling depth of the XPS (50 Å). Alternatively, it may indicate that the film is more highly cross-linked and saturated than expected.

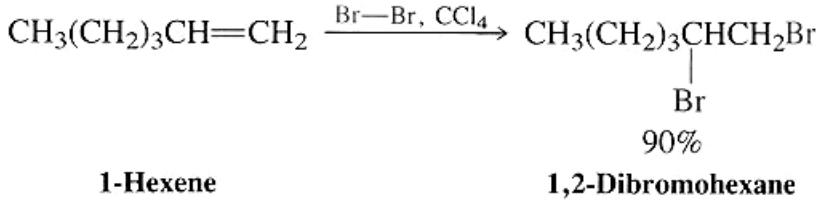

Figure 6.21: An example of bromination.

Table 6.14: XPS results from bromination experiments.

Sample	% C	% O	% Br
Ac.120s.200w.f10.Ar	91.4	8.6	ND
after exposure to bromine, prior to heating	81.7	14.5	3.4
after exposure to bromine, after heating	81.6	15.7	2.4

6.12 Oxidation

Most PP films contain trapped free radicals that readily react with atmospheric oxygen and H_2O after deposition.[3, 7, 18] As discussed by Yasuda and coworkers,[19, 20] films with a large density of free radicals are often produced in plasma polymerization. These free radicals can be long lived, surviving for many days and even months after deposition. Consequently, oxygen incorporation into the film most likely arises from post-deposition chemical reactions between the radicals and oxygen and water vapor molecules from ambient air.[18] PP films of acetylene oxidize readily, and Tsai et al[1] found that after several days of atmospheric exposure, the FTIR

spectrum of PP acetylene was dominated by bands related to carbonyl and hydroxyl groups. Figure 6.22 shows a possible oxidation process for organic PP films. The scheme shown is representative; the reactions are not balanced and the figure does not show all of the possible reactants and products.

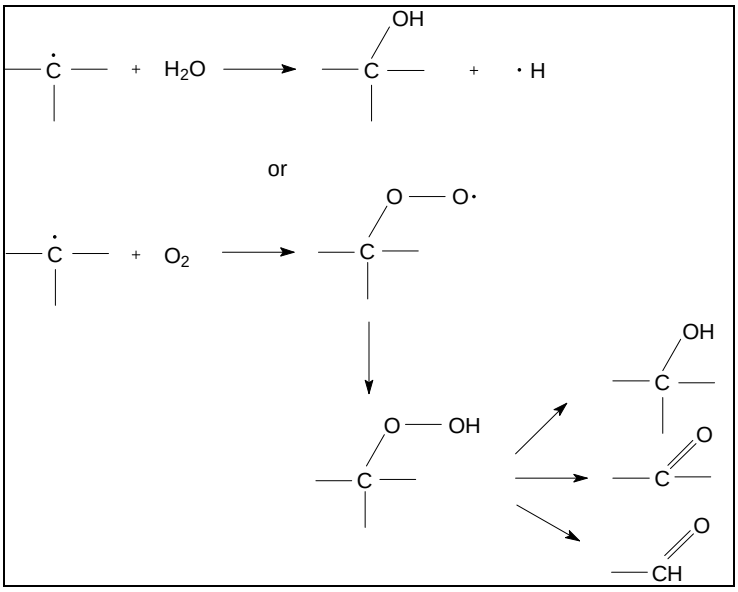

Figure 6.22: Proposed oxidation of free radicals (adapted from ref. 18).

Gerenser[21] reported the oxidation of PP polyethylene before and after removal from a vacuum chamber. XPS of the PP polyethylene still under vacuum showed no indication of oxidation (no O 1s signal and no broadening on the C 1s photopeak). When the sample was briefly exposed to the atmosphere (RT), 2 % oxygen was detected. Kim et al[22] also reported a substantial increase in bonded oxygen and a shift in the O 1s peak when oxygen plasma treated polyethylene was exposed to the atmosphere. In a study by Durrent et al,[23] amorphous hydrogenated and oxygenated carbon films were deposited from C_6H_6/O_2/He/Ar mixtures in an RF plasma deposition system. The presence of C=O absorption bands in the FT-IR spectrum of a PP film was interesting in films deposited when the oxygen flow rate was zero, because no O_2 was deliberately introduced into the chamber. The results of Kim et al and Durrent et al indicated that, unless oxygen is present in the reaction chamber during a plasma process, the incorporation of oxygen PP films does not occur until it is exposed to the atmosphere.

The XPS C 1s photopeaks of PP acetylene shown throughout this chapter are very similar to those reported by Tsai et al.[1] These films closely resemble PP acetylene films that had been exposed to the atmosphere for 2 days.

6.13 FTIR Measurements

FTIR spectra of samples Ac.120s.200w.f10.Ar and Ac.120s.200w.f10 were taken using the parameters discussed in Chapter 3. Both samples were pretreated with an oxygen plasma (250 W, 20 sccm, 10 minutes). PP acetylene (with argon as the carrier gas) was deposited onto samples of Ac.120s.200w.f10.Ar using an input power of 200 W, flow rates of 10/10 sccm (Ar/acetylene), and a treatment time of 2 minutes. The power, flow rate, and deposition time for Ac.120s.200w.f10 (no carrier gas) were 200 W, 10 sccm, and 2 minutes, respectively. The XPS analysis results are given in Table 6.15. The high nitrogen content of Ac.120s.200w.f10.Ar could be due to a reactor leak during the PP film deposition. The pressure during deposition for Ac.120s.200w.f10.Ar and Ac.120s.200w.f10 was 18.5 and 8 mTorr, respectively. The C 1s photopeak for Ac.120s.200w.f10 (not shown) was narrow and showed mostly C-H/C-C, but was also curve-fit with C-O and C=O contributions. The O 1s photopeak of Ac.120s.200w.f10 (not shown) was resolved into C=O and C-O components. The C 1s photopeak of Ac.120s.200w.f10.Ar was much broader, and was curve-fit with contributions from C-H/C-C, C-N, C-O, C=O, and CO_2. The O 1s photopeak for Ac.120s.200w.f10.Ar was similarly more broad than that of Ac.120s.200w.f10, and it was curve-fit with contributions from C-O, C=O, and CO_2.

Table 6.15: XPS results for Ac.120s.200w.f10.Ar and Ac.120s.200w.f10.

Sample	Thickness (Å)	% C	% O	% N	% Ti	SLS (psi)
Ac.120s.200w.f10.Ar	89 ± 18	61.5	18.6	19.9	ND	3942 ± 539
Ac.120s.200w.f10	382 ± 36	87.4	11.5	1.1	ND	1567 ± 28

The FTIR spectra were consistent with spectra obtained of PP acetylene films deposited from an inductively coupled reactor by other researchers.[18] The spectra are shown in Figure 6.23 and the peak assignments are given in Table 6.16. In the table of peak assignments, the

references refer to FTIR measurements of PP acetylene films by Yasuda et al,[18] Colthup,[24] and Tsai et al.[1]

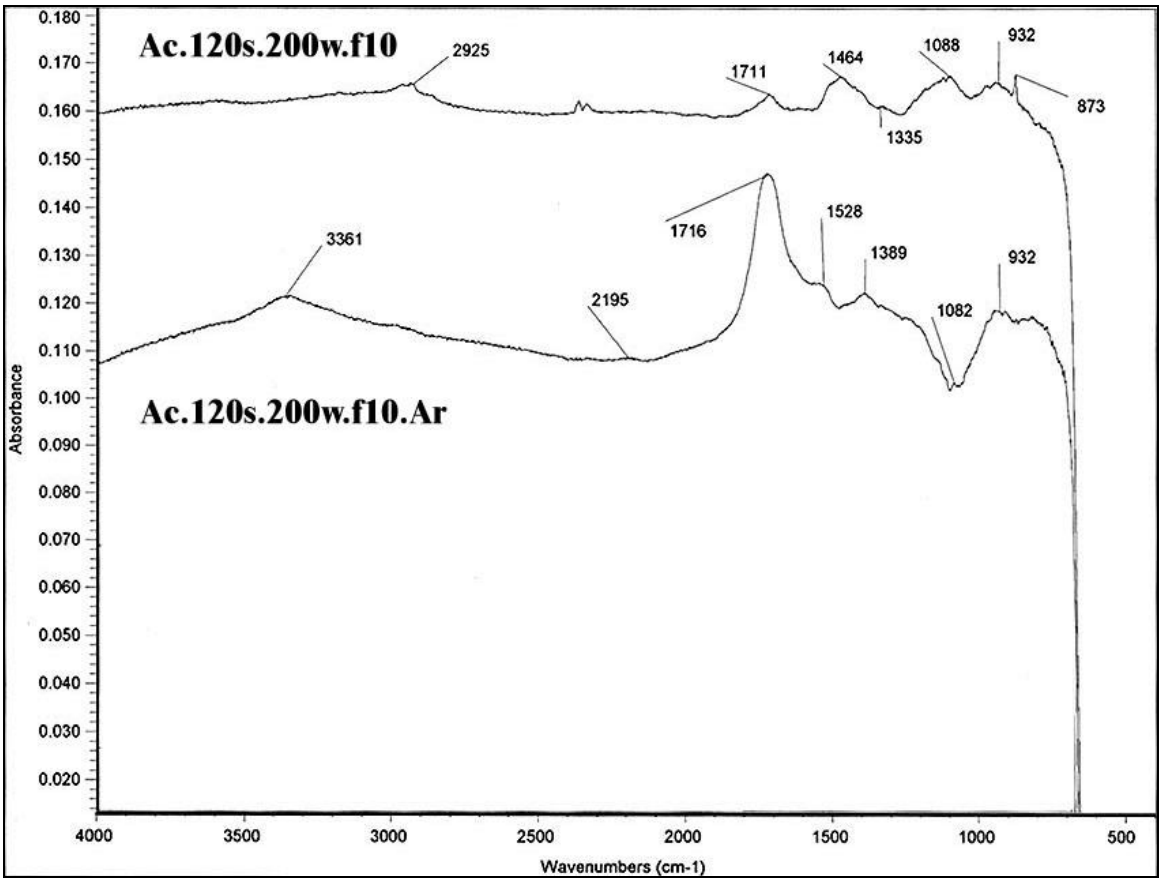

Figure 6.23: FTIR results from samples Ac.120s.200w.f10.Ar and Ac.120s.200w.f10.

Table 6.16: FTIR peak assignments.

Wave # (cm^{-1})	Assignment	Reference
873	C=CH- stretch	Colthup
932	CH_2 out of plane wag in R-CH=CH_2	Tsai and Boerio
1082	Aromatic activity/alkane	Colthup
1088	Aromatic activity/alkane	Colthup
1335	C-H wag in CH_2	Tsai and Boerio
1389	C-H deformation in CH_3	Tsai and Boerio
1464	C-H deformation in CH_2	Tsai and Boerio
1528	C-H aromatic bend or N-H deformation	Tsai et al/Yasuda et al
1711	C=O stretch of saturated ketone or aldehyde	Yasuda et al/Tsai and Boerio
1716	C=O stretch of saturated ketone or aldehyde	Yasuda et al/Tsai and Boerio
2195	C≡C stretch in RC≡CR	Tsai et al
2925	C-H out of phase stretch (CH_2)	Tsai and Boerio
3361	≡C-H stretch or O-H stretch/N-H stretch	Tsai and Boerio/Yasuda et al

Both PP films contained contributions from CH_2 out of plane wag in R-CH=CH_2 (932 cm^{-1}), aromatic activity/alkane stretches (≈ 1085 cm^{-1}), C-H deformation in CH_3 (1389 cm^{-1}), and C=O stretches of saturated ketones or aldehydes (≈ 1713 cm^{-1}). The aromatic character of PP acetylene films suggested by the peaks around 1085 cm^{-1} has been confirmed by Tsai et al[3] using ToF-SIMS.

Sample Ac.120s.200w.f10 yielded peaks characteristic of hydrocarbons near 2925 cm^{-1} (CH_2 stretching), 1460 cm^{-1} (C-H deformation in CH_2), and 1340 cm^{-1} (C-H deformation in CH_3). The doublet at around 2340 cm^{-1} (not labeled) was due to CO_2. Sample Ac.120s.200w.f10.Ar, which contained a large amount of nitrogen (19.9 %), had a broad peak at 3361 cm^{-1} that might be due to N-H stretching. It also contained bands that indicated the presence of alkyne groups (C≡C stretch in RC≡CR at 2195 cm^{-1} and possibly a ≡C-H stretch at 3361 cm^{-1}). The spectrum of Ac.120s.200w.f10.Ar also had a much larger peak at 1716 cm^{-1}, indicating that it had more C=O groups than Ac.120s.200w.f10. The highly branched nature of the films was evident by the lack of strong absorption near 730 cm^{-1}, which is characteristic of straight chains of four or more methylene groups.[3]

Ac.120s.200w.f10.Ar had an abnormally large carbonyl peak compared to Ac.120s.200w.f10, even when considering that the XPS-determined oxygen content of the two PP films was 18.6 and 11.5 %, respectively. This could be explained by a reactor leak during the deposition of Ac.120s.200w.f10.Ar. While the oxygen from Ac.120s.200w.f10 was due to surface oxidation, oxygen was probably incorporated into the PP film of Ac.120s.200w.f10.Ar.

Since RAIR-FTIR measures the absorbance throughout the whole film and not just on the surface (XPS), carbonyl groups present throughout the film would lead to a large absorbance around 1720 cm^{-1}.

6.14 Contact Angle Measurements

To gain further insight into the surface properties of the non-bonded PP films, water contact angle measurements were taken of selected PP films that were discussed in detail earlier in the thesis. Table 6.17 lists the H_2O contact angle, the XPS-determined oxygen content, the SLS strength, and the thickness of several PP films. Notice that the PP films demonstrate a wide range of water contact angles, from 42.3 ± 1.8 (Ac.30s.200w.f20.He) to 18.8 ± 1.7 degrees (Ac.120s.200w.f10.He). Higher energy surfaces cause lower water contact angle values and high-energy surfaces are desirable for improved adhesive wetting.

Table 6.17: Water contact angles and other properties of selected PP films.[25]

Sample	H_2O contact angle (°)	% O	SLS (MPa)	SLS (psi)	Thickness (Å)
Ac.30s.100w.f10.N	29.6 ± 1.8	7.3	19.2 ± 3.31	2780 ± 480	31 ± 2
Ac.30s.100w.f10.N (grounded)	20.7 ± 2.3	9.1	15.0 ± 0.90	2170 ± 130	23 ± 3
Ac.120s.200w.f10.He	18.8 ± 1.7	10.4	12.1 ± 2.07	1760 ± 300	293 ± 15
Ac.120s.100w.f10.He	24.9 ± 2.4	12.5	7.58 ± 0.83	1100 ± 120	234 ± 37
Ac.30s.200w.f20.He	42.3 ± 1.8	9.0	9.65 ± 1.72	1400 ± 250	119 ± 15
Ac.120s.200w.f10.Ar	32.2 ± 1.8	9.0	7.65 ± 0.21	1110 ± 30	400 ± 15

The oxygen content was examined because it was expected that PP films with higher oxygen content would have lower contact angles. Polar oxygen groups attract and can hydrogen bond with water, and this will generally lower the water contact angle. Surprisingly, this trend was not seen, as shown in Figure 6.24. Instead, the figure shows that the PP film oxygen content does not correlate with water contact angle (the lines connecting the data points only serve to guide the eye). Additionally, no correlation was found between water contact angle and SLS strength or film thickness. The differences in contact angle measurements may be a result of the various amounts and types of C-H incorporated into the PP films. CH_3, CH_2, and CH groups

each possess a different affinity for water and will cause differences in the spreading of liquids on the PP film surface. Water molecules can more closely approach carbon atoms when fewer hydrogen atoms are present because hydrogen atoms partially screen the major attractive forces.[26]

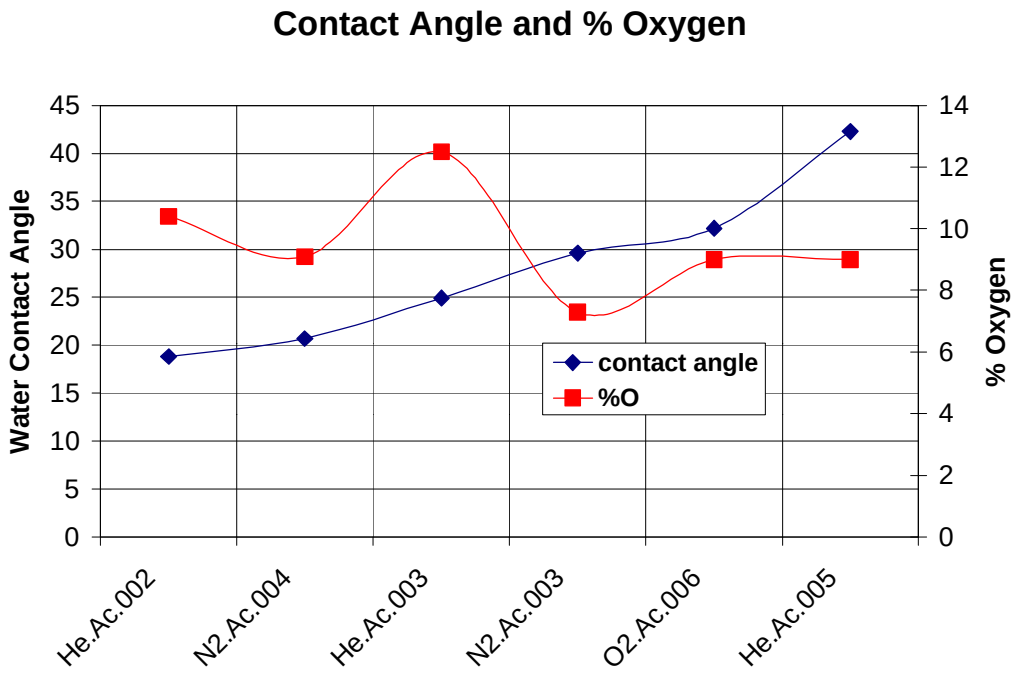

Figure 6.24: Water contact angle measurements and % oxygen content for selected PP acetylene films.

For most untreated hydrocarbon polymers, the surface energy is 25 to 50 dynes/cm, with water contact angles ranging from 95 to 60 degrees (see Table 6.18).[27] The water contact angles for the PP acetylene films given in Table 6.17 were much lower than for the conventional polymers listed in Table 6.18. This indicates that PP films of acetylene are more easily wetted than conventional polymers. However, there is not always a good correlation between wetting and bonding.[27]

PP acetylene films studied by Inagaki and Yasuda[28] had γ^d and γ^p values of 45.4 and 12.2 dynes/cm, respectively for a total surface energy of 57.2 dynes/cm using a goniometer drop-on plate method. This is a higher surface energy than any of the conventional polymers listed in Table 6.18, and the PP films of acetylene in this study were expected to have similar surface energies. Inagaki and Yasuda[28] used a capacitively coupled, magnetically enhanced reactor to

deposit 2060 Å films. The surface energies were determined according to Kaelble's method[29] using water, glycerol, formamide, methylene iodide, and tricresyl phosphate. Unfortunately, the researchers did not provide any other information regarding the chemistry of the films, such as FTIR or XPS results, and thus they did not correlate surface energy with film chemistry.

The surface energy of sample Ac.120s.200w.f10.Ar was measured by the harmonic mean method.[30] Ac.120s.200w.f10.Ar, which was discussed in section 6.3, was pretreated with an oxygen plasma (200 W, 20 sccm, 20 minutes), then coated with PP acetylene (200 W, 10 sccm, 2 minutes) using argon as the carrier gas (20 sccm). The PP film thickness was 400 ± 15Å, and the surface composition was 91.0 % C and 9.0 % O. The bonded sample had an average SLS strength of 7.58 ± 0.21 MPa (1110 ± 30 psi). The water contact angle for this sample was quite high at 59.7 ± 2.2 degrees. The dispersive (γ^d) and polar (γ^p) components of the surface energy were 36.5 dynes/cm and 18.7 dynes/cm, respectively. This yielded a total surface energy of 55.2 + 3.1 dynes/cm, which was similar to the surface energy of PP acetylene measured by Inagaki and Yasuda[28] discussed previously.

Generally, lower water contact angles translate into higher surface energies, so for the samples in Table 6.17, it was expected that they would have higher surface energies than Ac.120s.200w.f10.Ar. Recall from Chapter 4 that the surface energy of acetone cleaned Ti-6Al-4V was 59.6 ±5.2 dynes/cm, and the surface energy of an oxygen plasma treated substrate was 60.7 ± 4.9 dynes/cm. These are slightly higher than the surface energy of the selected PP acetylene film discussed here. Because there is less spreading on a surface with a lower surface energy, the adhesive is likely to better interact with the higher surface energy substrates. However, as discussed previously, the SLS specimens never failed at the PP film/adhesive interface, so the surface energies of all of the PP films seemed sufficiently high for adequate interaction with the adhesive.

Table 6.18: Water contact angles and surface energies of some common polymers.[25]

Conventional polymer	H_2O contact angles (°)	Surface energy (dynes/cm)
Polypropylene	87	29
Polyethylene	87	31
Polystyrene	72.5	38
Polyethylene terephthalate	76.5	41
Polyimide	79	40

6.15 Nanomechanical Study

Nanoindentation and nanoscratch tests were performed using a Hysitron TriboScope® by Hysitron, Inc using the parameters specified in the experimental section (Chapter 3). The tip was driven into the samples using forces varying from 15 - 300 μN, then withdrawn by decreasing the applied force. The loads used for indentation were selected to minimize the possible effects of the substrate on the mechanical properties of the thin films. The indentation depth of penetration was kept at approximately 25 % of the total film thickness.

Multiple scratches (3-5) were made on each sample using the parameters discussed in the experimental section (Chapter 3), and the adhesion of the PP film to its substrate was evaluated by comparing force-displacement curves recorded during the scratches. A characteristic critical load at debond was obtained by noting the discontinuity that occurred in the force-displacement curve when a film debonded from a surface. This critical load at debond is a reliable empirical measure of the adhesive strength of the film,[31] but there was no way to confirm the mechanism of the failure mode.

6.15.1 High vs. Low Power Input

6.15.1.1 Experimental

A horizontal reaction chamber (see Chapter 3) was used for film deposition and was purged with oxygen for 10 minutes prior to plasma treatment of Ac.130s.10w.f10 and Ac.110s.200w.f10. The oxygen pretreatment was used to remove loosely bound contaminants on the substrates prior to depositing PP acetylene films. The samples were treated with an oxygen plasma (50 W) for 2 minutes, using an O_2 flow rate of 20 sccm. Chamber pressure was approximately 20 mTorr. For PP film deposition, acetylene gas was introduced directly into the reaction chamber. No carrier gas was used. Samples Ac.130s.10w.f10 were treated for 130 seconds with acetylene (10 sccm) at a power of 10 W and a pressure of 17 mTorr. Samples

Ac.110s.200w.f10 were treated for 110 seconds with acetylene (10 sccm) at a power of 200 W and a pressure of 17 mTorr. These treatment times were selected to produce films of similar thickness (approximately 500 Å). All samples were subjected to a 5-minute O_2 purge immediately following deposition. After film deposition, all samples were removed from the reactor and stored in a desiccator. The XPS results represent the average of two measurements on the same sample; because the data were very similar, curve-fitting was performed on only one set of XPS data. A maximum load of 1000 μN was used during the scratch testing of these samples.

6.15.1.2 Nanoindentation Results

The composition of the films was predominantly carbon (see Table 6.19), with oxygen as the other main constituent. Less than 1 % of nitrogen was also present on some of the samples. The elemental compositions of the surfaces were independent of the treatment power and substrate. Curve-fit C 1s photopeaks revealed very similar distributions of C-H/C-C (285.0 eV), C-O (286.5 eV), and C=O (288.0 eV) species within the films (see Table 6.20). Figure 6.25 shows the curve-fit C 1s photopeak for Ac.130s.10w.f10.Ti, which is representative of the C 1s photopeaks for all of the samples. Figure 6.26 shows the curve-fit O 1s for Ac.130s.10w.f10.Ti, which is representative of the O 1s photopeaks. The findings confirm that oxygen was incorporated into the film as carbonyl or ether. The photopeaks at 532.3 eV and 533.5 eV are typical of C=O and R-O-R/R-OH species, respectively.[10] The large shoulder on the O 1s photopeak in Figure 6.26 at high binding energy could be caused by adsorbed H_2O, which typically appears higher than 533.9 eV.[32]

Table 6.19: XPS atomic concentrations and film thicknesses of the PP films (average of 2 measurements for the XPS data).

Sample	Thickness (Å)	Std. Dev. (Å)	% C	Std. Dev.	% O	Std. Dev.	% N
Ac.130s.10w.f10.Ti	545	15	93.2	0.07	6.8	0.07	< 0.5
Ac.110s.200w.f10.Ti	755	25	92.3	0.07	7.0	0.07	< 1.0
Ac.130s.10w.f10.Si	430	35	93.3	0.07	6.7	0.07	< 0.5
Ac.110s.200w.f10.Si	605	40	92.3	0.00	7.1	0.14	< 1.0

Table 6.20: Curve-fit C 1s data for as-prepared PP films.

Sample	% C-H/C-C	% C-O	% C=O
Ac.130s.10w.f10.Ti	88.8	8.1	3.1
Ac.110s.200w.f10.Ti	89.4	7.6	3.0
Ac.130s.10w.f10.Si	88.8	8.1	3.1
Ac.110s.200w.f10.Si	89.4	7.6	3.0

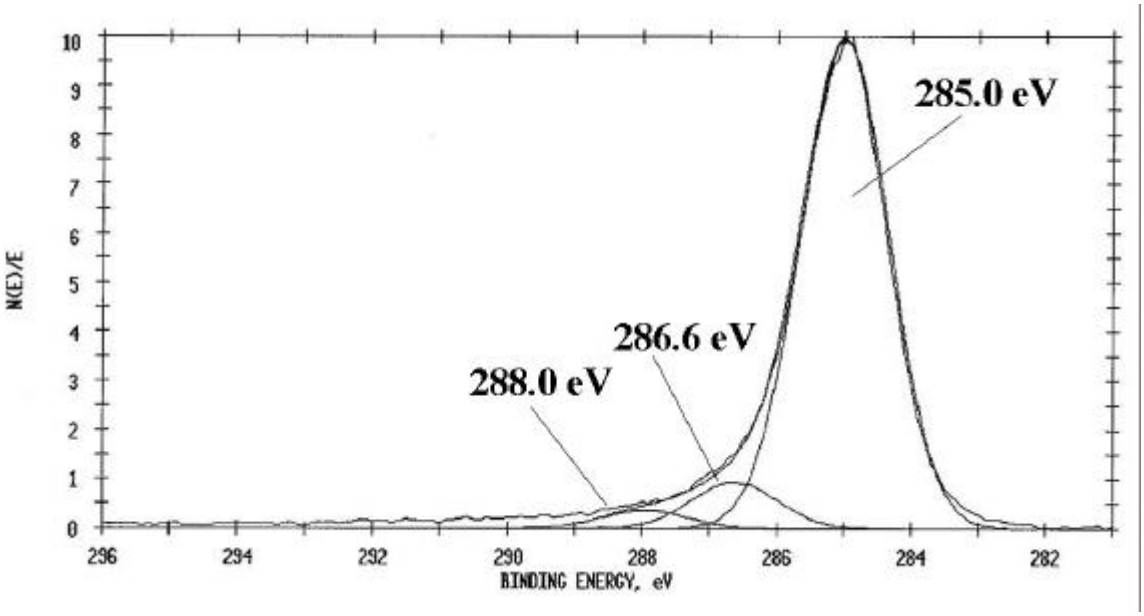

Figure 6.25: Curve-fit C 1s photopeak for Ac.130s.10w.f10.Ti.

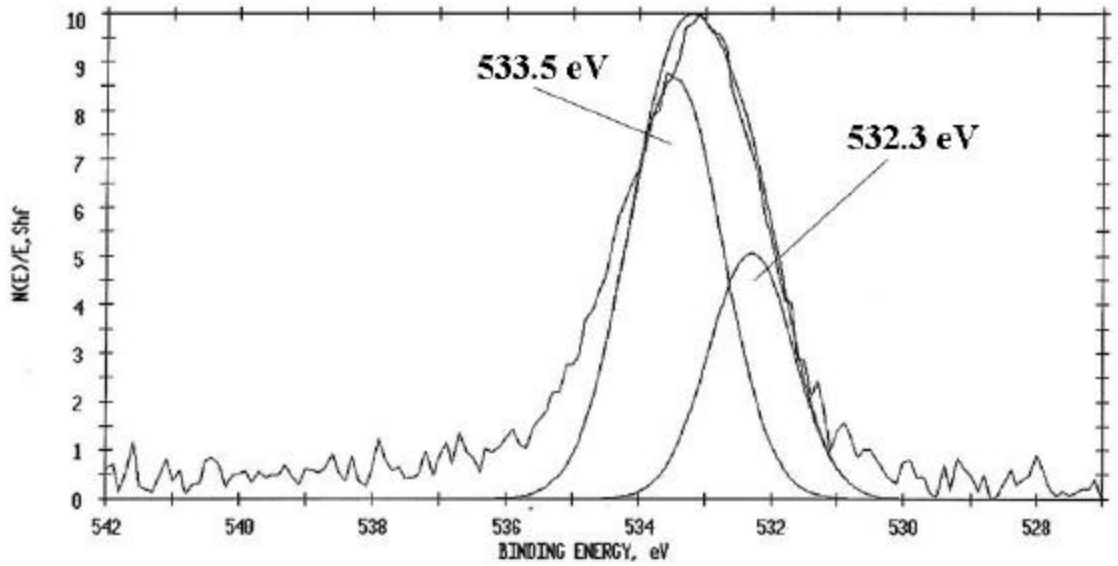

Figure 6.26: Curve-fit O 1s photopeak for Ac.130s.10w.f10.Ti.

The thicknesses of the films (Table 6.19) ranged from 430 Å (Ac.130s.10w.f10.Si) to 755 Å (Ac.110s.200w.f10.Ti). Recall that Ac.130s.10w.f10.Ti and Ac.130s.10w.f10.Si were treated in the same reactor during the same plasma polymerization. Samples Ac.110s.200w.f10.Ti and Ac.110s.200w.f10.Si were treated simultaneously during a separate experiment. The fact that the thicknesses differed by over 100 Å for samples treated during the same plasma polymerization experiment might be attributed to the different surface roughnesses of the polished Ti-6Al-4V and silicon wafer substrates (see AFM micrographs in Chapter 4). Polished Ti-6Al-4V was rougher than the silicon wafer, and a rougher surface may aid nucleation at the beginning of and throughout film formation.[33] The differences in thickness might also be a result of PP films depositing at different rates on different substrates. This has been reported by other researchers.[34, 35] In a morphological assessment of sub-50 nm thick hydrogenated amorphous carbon (a-C:H) films produced from rf plasma enhanced chemical vapor deposition (PECVD) using Ar/C_2H_2 gas mixture onto heterogeneous Al_2O_3–TiC ceramic substrates, Lemoine et al[34] found that the substrate affects the rate of growth and the surface microstructure of the amorphous carbon film. Furthermore, using transmission electron microscopy, ToF-SIMS, and angle resolved XPS to analyze film thickness, Xu et al[35] found that the growth mechanisms of plasma-deposited diamond-like coatings (DLC) depended on substrate surfaces. They saw variations of the DLC overcoat thickness ranging from 154 to 169 Å even with the exact same deposition conditions.

The thickness difference on different substrates is believed to be determined at an early stage of deposition due to differences in initial nucleation.[35] Current theories regarding amorphous carbon growth suggest that high quality film formation proceeds via densification of a surface layer due to ion subplantation,[36, 37] so the thickness variations observed for the PP films being studied are most likely initiated early in the deposition process. This may also affect the density of the PP film.

Despite the compositional similarities of the PP films, differences in the hardness and modulus values were evident from the nanoindentation tests, as shown in Table 6.21. The values in Table 6.21 are somewhat counter intuitive. With increasing power, the increased energy of the film-forming ions that impinge on a substrate's surface should result in a film that is harder and more diamond-like in nature.[38] It was expected that the film deposited at high power would be

harder and have a higher reduced modulus because of the greater amount of fragmentation and crosslinking expected within those films.[39] Films prepared using higher input power should be more disordered and crosslinked, while films prepared at lower power should retain more of the molecular structure of the monomer and resemble a more conventional polymer.[40] This was not found; the Ac.130s.10w.f10 samples were significantly harder than the Ac.110s.200w.f10 samples. For example, Ac.130s.10w.f10.Ti and Ac.110s.200w.f10.Ti had hardnesses of 4.70 and 3.35 GPA, respectively. Ac.130s.10w.f10.Si and Ac.110s.200w.f10.Si had hardnesses of 5.87 and 3.72 GPa, respectively.

Table 6.21: Hardness and reduced modulus values from nanoindentation tests.

Sample	H (GPa)	Std. Dev. (GPa)	E_r (GPa)	Std. Dev. (GPa)	h_c (Å)	Std. Dev. (Å)	h_c/ thickness
Ac.130s.10w.f10.Ti	4.70	0.34	72.9	5.1	134	8	0.246
Ac.110s.200w.f10.Ti	3.35	0.32	51.9	2.9	180	14	0.238
Ac.130s.10w.f10.Si	5.87	0.31	91.7	1.6	110	5	0.256
Ac.110s.200w.f10.Si	3.72	0.18	62.1	1.7	164	7	0.271

The fact that lower input power results in a higher hardness might be due to different growth mechanisms at the different power inputs. Yasuda[4] reported that there are two major trends regarding internal stresses. Slower depositions of PP film result in larger internal stresses and forces acting at the PP film/substrate interfaces are proportional to film thickness. The PP film deposited at lower input power had a lower deposition rate, thus it would be expected to be in a higher stress state than the film deposited at higher input power. These higher stresses could be the source of the differences in hardness. Lu and Komvopoulos[41] saw a decrease in hardness with increasing input power and offered a similar explanation. They studied the nanomechanical properties of thin films of rf sputtered amorphous carbon (60 - 950 Å thick) deposited on silicon(100) substrates using the method of Oliver and Pharr[42]. Pure argon was sputtered onto a graphite target to deposit the films, and they reported lower film hardness (19.4 GPa vs. 25.4 GPa) with increasing rf power (250 vs. 200 watts). They proposed that increasing the flux of incoming carbon atoms decreased the mobility of adsorbed carbon atoms. This reduced the likelihood of newly adsorbed carbon atoms migrating to lower-potential energy sites, and resulted in lower film density and lower nanohardness. They also reported that higher growth rates resulted in films with a lower nanohardness.

Overall, these hardness values are consistent with or lower than literature values for similar films. Table 6.22 summarizes literature values discussed below.

DLC films (≈2000Å thick) deposited from methane gas on silicon(100) using an asymmetric capacitively coupled RF PECVD system were studied by Sun.[38] Using the continuous stiffness option of the Nanoindenter II (Nano Instruments) and a maximum load of 10 mN, Sun found hardnesses ranging from 15 to 20 GPa, depending on the pressure and the bias used during deposition. Unfortunately, Sun gives no details about the method used to calculate hardness.

Chan et al[43] studied the hardness of amorphous nitrogenated carbon films deposited on silicon(100) from a standard magnetron sputter deposition system (with a graphite target and a bias applied to target and substrates). They used a Hysitron nanoindenter/triboscope equipped with a Berkovich indenter and the approach of Pharr and Oliver[44] to determine hardness. For films of approximately 5000Å, they reported hardnesses of between 14 and 22 GPa, depending on the film preparation parameters.

Using a Berkovich diamond indenter attached to a Hysitron nanoindenter, Kulkarni and Bhushan[45] measured the average hardness of amorphous carbon coatings deposited by various methods. Thin films (1000 Å) deposited from DC magnetron sputtering, direct ion beam, and cathodic arc had hardnesses of 17.0, 15.1, and 24.2 GPa, respectively.

Christiansen et al[46] studied PECVD (rf electrode reactor) DLC on alumina/aluminosilicate glass composites for biomedical applications. Thin coatings (500 to 4000 Å) were deposited on self-biased, polished substrates using acetylene as the feed gas. Measurements of a 3000 Å film using a Nanotest 500 (5 nN max load) yielded a hardness value of 14.2 ± 0.09 GPa.

Ong et al[47] studied amorphous carbon films (1000 - 1500 Å thick) that were deposited on polycarbonate using a laser ablation technique and pyrolytic graphite target. Using a Nanoindenter II, the hardness of each film was approximately 5 GPa, as determined by the geometrical dimensions of the diamond indentations.

Lacerda et al[48] studied amorphous carbon-nitrogen films (≈ 3500 Å thick) on silicon (100) deposited by rf magnetron sputtering. They reported a hardness of approximately 2 GPa. A Berkovich diamond tip and a Nanoindenter II were used to make measurements and the method of Pharr and Oliver[42] was used to calculate hardness.

Li and Bhushan[49] characterized the nanomechanical properties of thin amorphous carbon coatings (50 - 4000 Å) deposited on Al_2O_3-TiC by an ion beam deposition technique. They used a commercially available nanoindenter, a 200 μN force, and a Berkovich diamond to perform the tests. The hardness and elastic modulus of a 4000 Å film were 19 and 150 GPa, respectively, and did not change with increasing indentation depth up to 900 Å (22.5 % of film thickness).

Film type	Deposition method	Substrate(s)	Thickness (Å)	Hardness (GPa)	Reference
DLC	RF PECVD	Silicon(100)	≈ 2000	15 - 20	Sun[38]
Amorphous C/N	Magnetron sputtering	Silicon(100)	≈ 5000	14 - 22	Chan et al[43]
Amorphous C	Various	Silicon(100)	≈ 1000	15.1 - 24.2	Kulkarni and Bhushan[45]
DLC	RF PECVD	Glass composites	500 - 4000	14.2	Christiansen et al[46]
Amorphous C	Laser ablation	Poly(carbonate)	1000 - 1500	≈ 5	Ong et al[47]
Amorphous C/N	Magnetron sputtering	Silicon(100)	≈ 3500	≈ 2	Lacerda et al[48]
Amorphous C	Ion beam	Al_2O_3-TiC	50 - 4000	≈ 19	Li and Bhushan[49]

Table 6.22: Comparison of hardness values from literature.

The differences in hardness and reduced modulus of the films on different substrates in this work have two possible explanations. The values could reflect a substrate effect. Results reported in Chapter 5 showed that oxygen plasma treated silicon (10.21 GPa) was significantly harder than oxygen plasma treated Ti-6Al-4V (5.75 GPa), and the samples discussed here were treated with an oxygen plasma prior to film deposition. Furthermore, at both power input levels, the PP film deposited on silicon was thinner than the PP film deposited on polished Ti-6Al-4V. If a substrate effect were present, thinner films would show more of a substrate influence than thicker films, and this could explain the differences in hardness.

A substrate effect is unlikely, however, because the indents penetrated into the film an average of 25 % of the total film thickness (see the last column of Table 6.21). Most researchers maintain that the effect of the substrate on the nanoindentation measurement should be considered only when the indentation depth exceeds 25 % of the thickness of the film.[44, 50] Additionally, finite element modeling of indentations of thin films by a conical indenter showed

that indentation depths of 10 to 33 % of the film thickness results in accurate measurements of film properties.[51]

Another possible explanation for the differences in hardness and reduced modulus could be that there is a fundamental difference in the film composition within the bulk of the materials. Although the XPS results show that these films are very similar, XPS is only able to characterize the top 50 Å of a film. Additionally, changes in density of the films would not necessarily yield different XPS spectra. Similar to the effect that a substrate can have on film thickness due to differences in nucleation, substrates can also have a large impact on bulk film characteristics.[34] A different morphology induced by the different substrates could very well lead to different mechanical properties.

A plot of hardness and reduced modulus vs. thickness (Figure 6.27) shows that hardness and reduced modulus decrease with film thickness, regardless of input power or substrate. The linear trend lines show high confidence for the correlations; R^2 was 0.8902 for hardness vs. thickness and 0.9454 for reduced modulus vs. thickness. Figure 6.28 is a plot of depth of penetration vs. thickness and it shows how the depth of penetration increases with increasing film thickness. This relationship was an extension of the fact that the thicker films had a lower hardness, thus an indenter under the same load (100 μN) penetrated more deeply into the softer film.

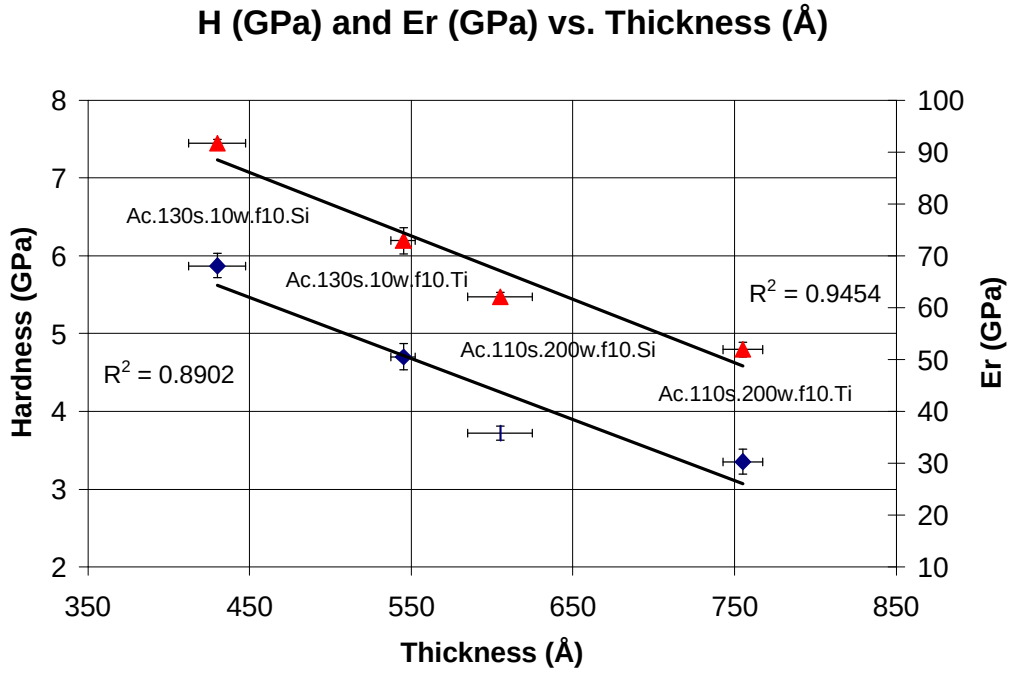

Figure 6.27: Hardness and reduced modulus vs. thickness for the nanoindentation tests on Ac.130s.10w.f10 and Ac.110s.200w.f10. The triangular data points are the reduced moduli and the diamond data points are the hardness values.

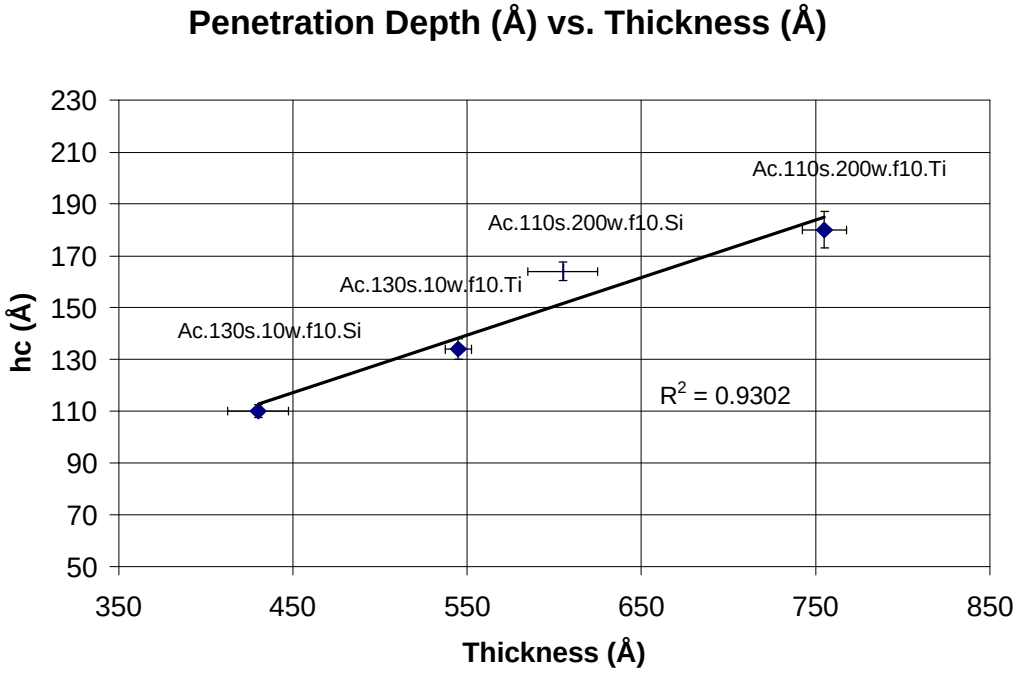

Figure 6.28: Depth of penetration vs. thickness for the nanoindentation tests on Ac.130s.10w.f10 and Ac.110s.200w.f10.

A plot of hardness and reduced modulus vs. depth of penetration (Figure 6.29) shows that softer films (thicker) result in deeper indents, as would be expected.

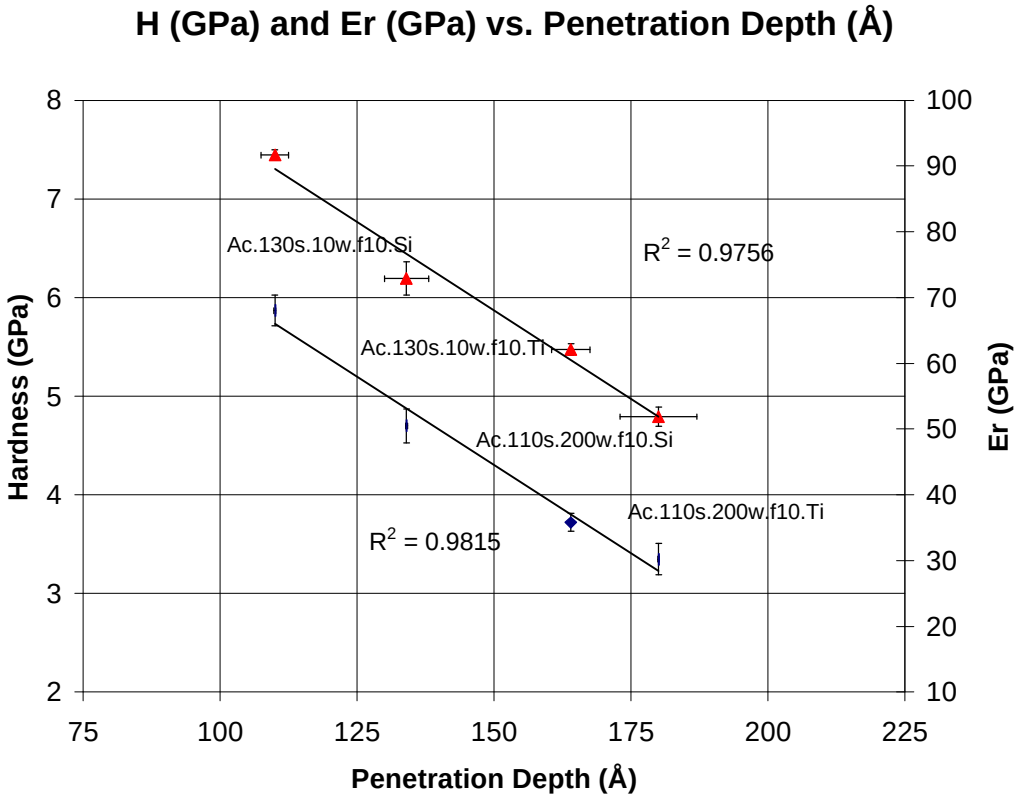

Figure 6.29: Hardness and reduced modulus vs. depth of penetration for Ac.130s.10w.f10 and Ac.110s.200w.f10. The triangular data points are the reduced moduli and the diamond data points are the hardness values.

Figure 6.30 is an in situ AFM topographic micrograph of one of the indents in Ac.110s.200w.f10.Si. The edges of the indent are approximately 120 nm in length. The poor quality of the AFM micrograph limits the amount of information that it provides. However, there does not seem to be a build up of material around the edges of the indent, which would have been indicative of excess plastic deformation.

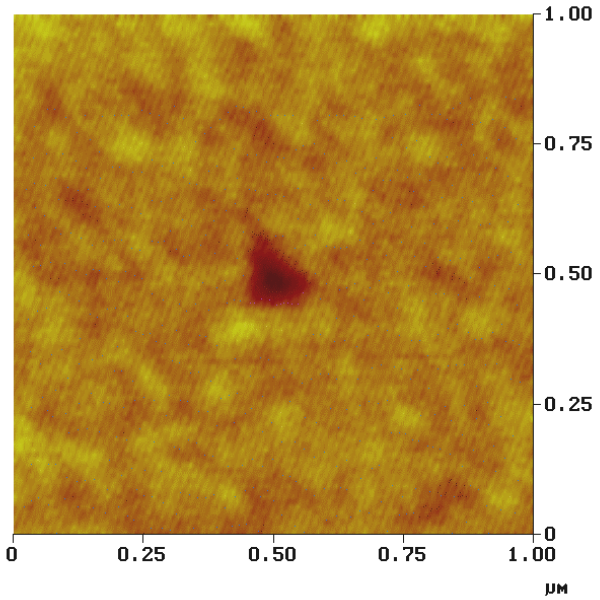

Figure 6.30: In situ topographic image of indentation in Ac.110s.200w.f10.Si under 100 µN load.

6.15.1.3 Nanoscratch Results

Figure 6.31 shows the result of the 8 µm ramp force scratch test for Ac.130s.10w.f10.Si. The left graph in the figure shows the ramping of the normal force (µN) with time (seconds), and the right side plot shows normal displacement (nm) vs. time (seconds). The first heavy red lines running vertically in the plots show the debond event (also marked with arrows). On the right side graph of Figure 6.31, the debond event is characterized by a huge drop in the normal displacement. This rapid decrease in the normal displacement occurs because the diamond tip of the scratch tester has broken through the film. Recall that the film thickness for Ac.130s.10w.f10.Si was 430 ± 35 Å. As shown in Figure 6.31, the normal displacement when debond occurred for Ac.130s.10w.f10.Si was approximately 445 Å, which was consistent with the AES results and indicated that failure occurred at the PP film/substrate interface.

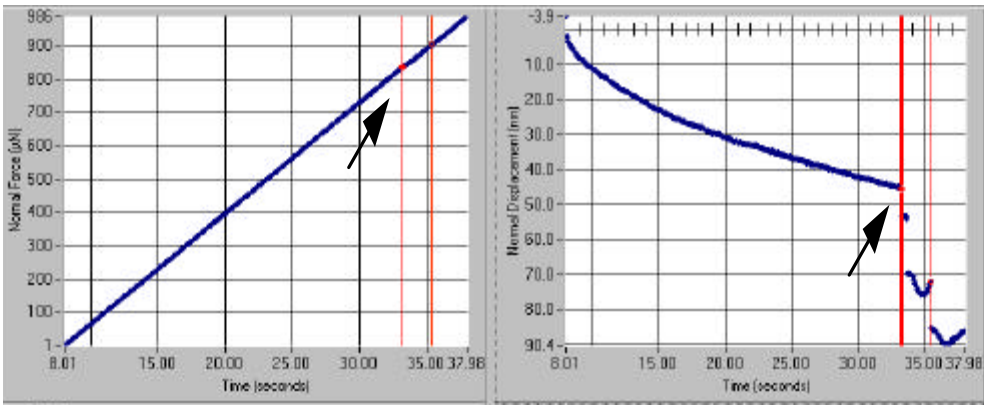

Figure 6.31: Results of an 8µm ramp force scratch test (max force 1000 µN) on Ac.130s.10w.f10.Si.

Table 6.23 summarizes all of the scratch test data, including the thickness of the PP films, the normal displacement at debond, the critical load at debond, and the critical load divided by the film thickness. The normal displacement at debond refers to the depth that the AFM diamond tip traveled into the sample when debonding occurred. Note that the normal displacement values at debond meet or exceed the AES-determined thickness of the films for all samples. This implies that in all cases, failure did not occur cohesively within the films. Instead, failure occurred at the PP film/substrate oxide interface or within the substrate oxide layer. Failure may have occurred at the PP film/substrate oxide interface for every sample, but plastic deformation of the film during the scratch test may have artificially inflated the normal displacement values at debond.[44]

Table 6.23: Film thickness (AES) and critical load at debond values (AFM scratch test).

Sample	AES thickness (Å)	Normal displacement at debond (Å)	Critical load (µN)	Load/ thickness (µN/Å)
Ac.130s.10w.f10.Ti	545 ± 15	600	692 ± 159	1.27 ± 0.29
Ac.110s.200w.f10.Ti	755 ± 25	980	808 ± 173	1.07 ± 0.23
Ac.130s.10w.f10.Si	430 ± 35	445	782 ± 44	1.82 ± 0.10
Ac.110s.200w.f10.Si	605 ± 40	680	751 ± 135	1.24 ± 0.22

As evident from the data in Table 6.23, there was no correlation of the critical load with hardness, modulus, or chemical composition, and it is unclear at this point what film properties

influence the critical load at debond. The high standard deviations for the scratch test results make it challenging to identify trends.

It was expected that the higher power depositions would result in higher critical loads at debond due to the increased atomic interfacial mixing during deposition. This was noted for PP films deposited on polished Ti-6Al-4V; Ac.130s.10w.f10.Ti had a critical load at debond of 692 μN, while Ac.110s.200w.f10.Ti had a critical load at debond of 808 μN. Unfortunately, the trend did not repeat for PP acetylene films deposited on SiO_2 (782 μN for Ac.130s.10w.f10.Si and 751 μN for Ac.110s.200w.f10.Si). The differences in behavior of the films on the two substrates might be due to substrate surface roughness differences or differences in bulk film compositions. The rougher surface of the polished Ti-6Al-4V increases the possibility that the scratch tip could suddenly strike the substrate, which could increase the stress concentration in front of the scratch tip and cause brittle fracture of the substrate.[49]

The critical load at debond may be affected by PP film thickness, so the critical load at debond data were normalized by dividing the critical load by the film thickness. Regardless of the substrate or the film preparation, this ratio increased with increasing hardness and modulus, as shown in Figure 6.32. This indicates that the harder films adhere to the substrates better than the softer films. The confidence of the linear trend lines was high for the relationship shown in Figure 6.32; R^2 was 0.8847 and 0.9161 for hardness vs. critical load/thickness and reduced modulus vs. critical load/thickness, respectively. These results indicate that it may be possible to predict the adhesion of a thin film to its substrate based on the hardness and modulus values from nanoindents. Nanoscratch testing would therefore not be required to assess adhesion.

Based on the critical load/thickness ratio, PP acetylene adheres better to the silicon wafer substrates within both sets of samples. This is probably due to plasma-state species having a higher affinity for SiO_2 vs. Ti-6Al-4V. The fact that the silicon wafer is smoother than the polished Ti-6Al-4V may play a role, as well. The increased roughness of the polished Ti-6Al-4V may induce debond at a lower critical load because of non-uniformities and stress concentrations that could exist within the Ti-6Al-4V/PP film interphase.[49]

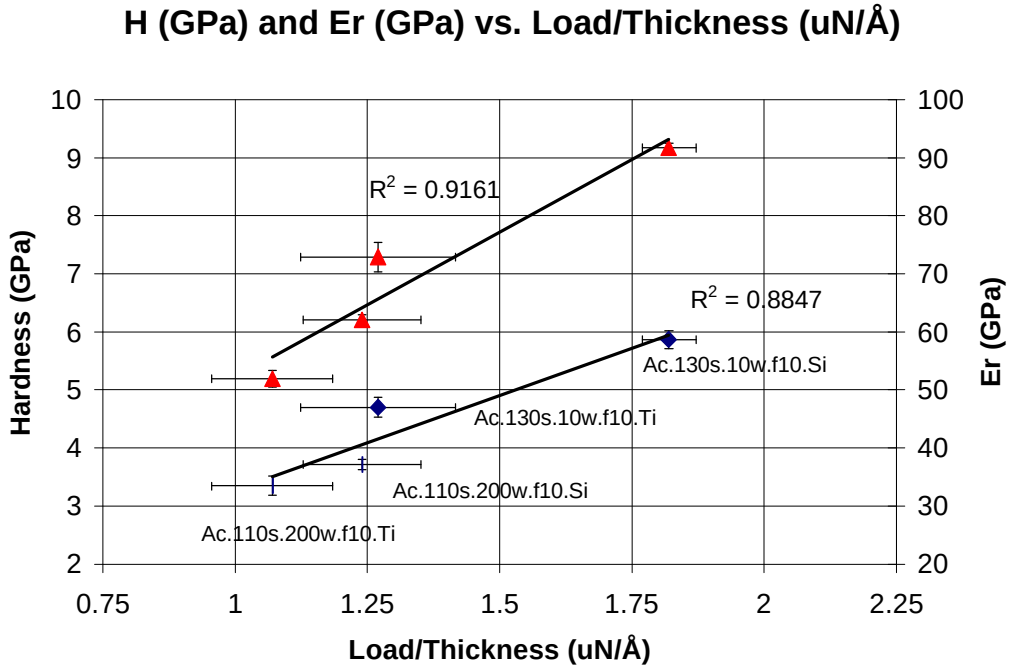

Figure 6.32: Hardness and reduced modulus vs. load/thickness.

The in situ AFM topographical images for samples Ac.130s.10w.f10.Ti and Ac.130s.10w.f10.Si are shown in Figure 6.33 and Figure 6.34, respectively. These micrographs are representative of the scratch images for this set of samples. The scratch begins at the top of the micrograph and digs into the film until debond occurs toward the bottom of the micrograph. The lighter areas in the micrographs represent raised features. Note how clean the scratches are; very little ploughing is evident during the scratches until debond occurs at the end of the scratch. The difference in surface roughness of the samples has not visibly influenced the scratches. Comparing the figures, the scratch of Ac.130s.10w.f10.Ti seems to have generated more debris, probably because the PP film was thicker on this substrate than on the silicon wafer. Overall, the scratches were very similar in terms of uniformity until the debonding event; the critical load at debond results do not appear to be due to any anomalies that occurred during the scratch test.

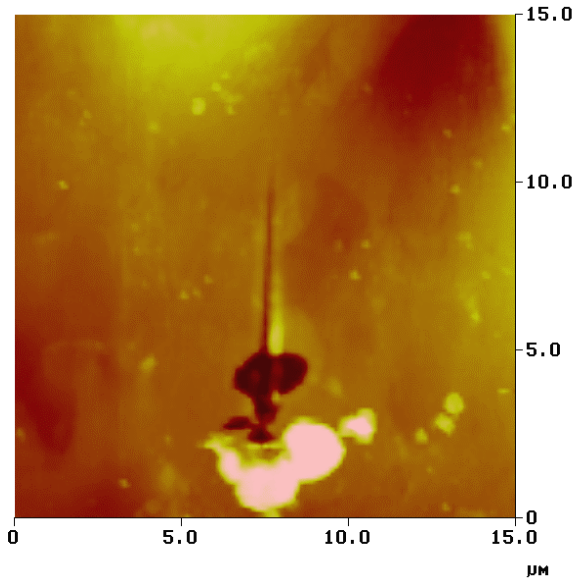

Figure 6.33: In situ topographic image of an 8 µm ramp force scratch in Ac.130s.10w.f10.Ti under 1000 µN peak load with a <1 µm conical tip.

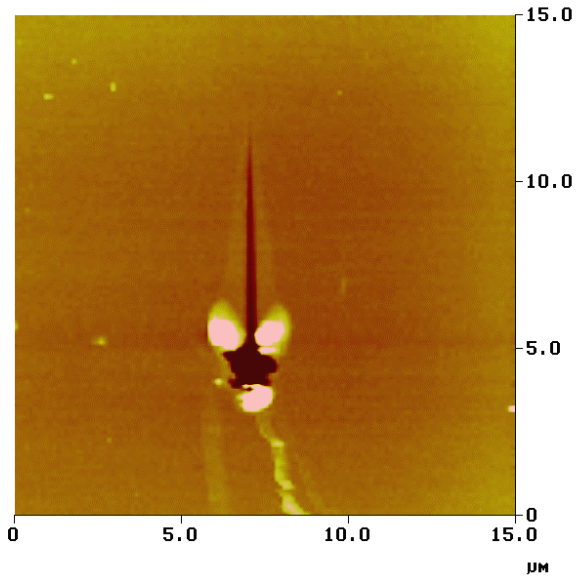

Figure 6.34: In situ topographic image of an 8 µm ramp force scratch in Ac.130s.10w.f10.Si under 1000 µN peak load with a <1 µm conical tip.

The critical loads at debond reported here are consistent with values reported in the literature. Deng et al[52] evaluated silicon carbide, carbon, and carbon nitride ultrathin overcoats on pure silicon (111) using a Nanoindenter II with a Berkovich indenter. The 200 Å films were deposited by dc magnetron sputtering (100 - 150 watts) in a pure Ar or Ar + N_2 mixed

atmosphere. A 100 μm scratching track at a constant velocity of 1 μm/s was applied to all test samples, and four normal ramping load ranges were used (0.01 to 1, 0.02 to 2, 0.03 to 3, and 0.04 to 4 mN). The critical load at debond was lowest for SiC (500 - 600 μN), slightly higher for the carbon film (600 - 700 μN), and the highest for the carbon nitride film (800 μN). The SiC film was more brittle than the others and the overcoat was damaged more severely than the others during scratch testing, as evidenced by SEM micrographs of the tested areas.

Li and Bhushan[49] characterized the adhesion properties of three thin amorphous carbon coatings (thicknesses of 50, 100, and 200 Å) deposited on Al_2O_3-TiC by an ion beam deposition technique. Using a conical diamond indenter (1 μm tip radius) and loads ramped from 0.2 to 25 mN (sample dependent), the critical load at debond was independent of film thickness. The critical load at debond was 800, 850, and 900 μN for the 50, 100, and 200 Å films, respectively. AFM and SEM images of the scratches showed ploughing of the film during the scratch, and debris and buckling of the film at debond. These researchers noted a feature of the scratch test that was reported here; the debris from thicker coatings was larger than the debris from thinner coatings. However, they also suggested that the debris could be affected by the residual stresses in the films.

6.15.1.4 Correlation with SLS Strength

For almost every sample tested, SLS joints primed with PP acetylene films failed at the PP acetylene/Ti-6Al-4V interface. One of the motivating factors for studying the nanomechanical properties of thin PP acetylene films was to discover whether PP film/substrate adhesion and other nanomechanical properties could be correlated with SLS strength. It was hypothesized that, because the mode of failure was consistently interfacial for the SLS tests, this should be possible. Table 6.24 compares the nanomechanical properties of Ac.130s.10w.f10.Ti and Ac.110s.200w.f10.Ti with their SLS strengths.

Table 6.24: SLS strength and PP film properties for Ac.130s.10w.f10.Ti and Ac.110s.200w.f10.Ti.

Sample	Thick-ness (Å)	Hardness (GPa)	Critical Load (μN)	critical load/ thick (μN/Å)	SLS strength (psi)
Ac.130s.10w.f10.Ti	545 ± 15	4.70 ± 0.34	692 ± 159	1.27 ± 0.29	1740 ± 80
Ac.110s.200w.f10.Ti	755 ± 25	3.35 ± 0.32	808 ± 173	1.07 ± 0.23	990 ± 210

The SLS specimens tested were prepared from acetone cleaned Ti-6Al-4V substrates that were not polished, so the SLS specimens were significantly rougher than the nanomechanical samples. However, the films were of identical composition and were prepared in exactly the same way. It was expected that the samples that had the higher SLS strength (Ac.130s.10w.f10.Ti) would also have the higher critical load at debond. However, this was not the case; Ac.110s.200w.f10.Ti had critical load at debond of 808 μN, which was higher than the critical load at debond of Ac.130s.10w.f10.Ti (692 μN). The differences in thickness may have played a role here. When the critical load at debond was normalized by dividing it by PP film thickness, the sample with the higher SLS strength (Ac.130s.10w.f10.Ti) also had the higher critical load at debond/thickness value (1.27 μN/Å). Because there are only two data points and the standard deviations of the critical load at debond/thickness are so high, it is difficult to ascertain if this is a real trend. Another possible trend is that increased hardness of the PP film seems to correlate with increased SLS strength. As shown in Table 6.24, Ac.130s.10w.f10.Ti was over 40 % harder than Ac.110s.200w.f10.Ti, and its SLS strength was over 75 % greater. This is not a PP film thickness effect because when the hardness and SLS were normalized with respect to film thickness, this relationship was even more pronounced.

6.15.2 Curing Effects

6.15.2.1 Experimental

Ac.110s.200w.f10.N2cure.Ti, Ac.110s.200w.f10.N2.Si, Ac.110s.200w.f10.Air.Ti, and Ac.110s.200w.f10.Air.Si were prepared exactly as described above for Ac.110s.200w.f10, but were subject to a high temperature treatment following film deposition. The peak annealing

temperature, 350° C, was chosen to simulate the curing conditions of the adhesive. The samples were placed in a tube furnace purged with either air or N_2 and heated to 350° C at a rate of 98° C/minute. After 1 hour at 350 °C, the oven was turned off, and the samples remained in the furnace for 10 minutes before the furnace was opened and allowed to cool to room temperature. Scratch testing was carried out exactly as described previously, except that maximum loads of 3000 μN instead of 1000 μN were used.

6.15.2.2 Nanoindentation Tests

Table 6.25 shows the film thickness (AES) and XPS data for the annealed PP films. The two PP films heated in air had similar surface compositions, as did the two PP films heated in nitrogen. Compared to the original film compositions (see Table 6.19 from Section 6.15.1.2), the annealing process increased the atomic concentration of oxygen within the samples at the expense of carbon. For samples heated in air, the atomic concentration of carbon decreased from 92.3 to ≈ 78.9 % and the atomic concentration of oxygen increased from ≈ 7.0 to ≈ 20.5 %. For samples heated in nitrogen, the atomic concentration of carbon decreased from 92.3 to ≈ 88.9 % and the atomic concentration of oxygen increased from ≈ 7.0 to ≈ 10.7 %. The incorporation of more oxygen into the films annealed in air was a result of the film being exposed to oxygen during heating. Films annealed in nitrogen were exposed to atmospheric oxygen after heating.

Table 6.25: Film thickness and XPS data for thermally treated samples.

Sample	Thickness (Å)	Std. Dev. (Å)	% C	Std. Dev.	% O	Std. Dev.	% N
Ac.110s.200w.f10.Ti	755	25	92.3	0.07	7.0	0.07	trace
Ac.110s.200w.f10.Ti.Air	560	15	78.9	0.49	20.5	0.57	trace
Ac.110s.200w.f10.Ti.N2	725	80	88.9	0.21	10.4	0.35	trace
Ac.110s.200w.f10.Si	605	40	92.3	0.00	7.1	0.14	trace
Ac.110s.200w.f10.Si.Air	435	45	78.2	0.57	21.0	0.57	trace
Ac.110s.200w.f10.Si.N2	680	25	88.2	0.28	11.1	0.14	trace

From Table 6.19 (Section 6.15.1.2), the thicknesses of the PP films on Ac.110s.200w.f10.Ti and Ac.110s.200w.f10.Si prior to thermal treatment were 755 ± 25 Å and

605 ± 25Å, respectively. The thickness of Ac.110s.200w.f10.Ti.Air decreased almost 26 % to 560 ± 15 Å due to the cure, while the thickness of Ac.110s.200w.f10.Ti.N2 remained essentially unchanged (within standard deviations). For the PP films deposited on the silicon wafer, the thickness of Ac.110s.200w.f10.Si.Air decreased over 28 % to 435 ± 45 Å, while the thickness of Ac.110s.200w.f10.Si.N2 actually increased over 12 % to 680 ± 25Å. This post-nitrogen treatment increase in thickness cannot be readily explained; it may be a result of a discrepancy that occurred during film deposition that was sample-placement induced. A decrease in the thickness of all of the films was expected due to thermally induced rearrangements and densification of the films. This was noted in a study of amorphous carbon-nitrogen films (≈ 3500 Å thick) deposited by rf magnetron sputtering.[48] Lacerda et al[48] reported the main result of annealing (in a vacuum, between 300 and 700° C) was an increase of 20 % in the film density. The thickness of the films, as measured by an alpha-step stylus profilometer, decreased as a function of annealing temperature from 3350 Å to 1600 Å (a decrease of over 52 %). Additionally, Kulisch et al[53] reported a similar result; the thickness of PP amorphous carbon nitride films (PECVD) decreased over 50 % after annealing at 400 °C in argon for 30 minutes. Ellipsometry was used to determine the thickness of the films, which initially ranged from 2900 to 8700 Å in thickness.

Table 6.26 shows the XPS C 1s curve-fit data for the annealed samples. Figure 6.35 and Figure 6.36 show the curve-fit C 1s photopeaks for samples Ac.110s.200w.f10.Ti.Air and Ac.110s.200w.f10.Si.N2, respectively. The principal change in the C 1s photopeak for the heated PP films compared to the films that were not heated (see Figure 6.25 of Section 6.15.1.2) was the emergence of a photopeak at high binding energy (≈ 289.2 eV). This peak was attributed to carboxyl groups within the films.[10] The other major difference was the increase in C-O and C=O contributions to the overall C 1s photopeak. This coincided with the increased oxygen content, which became incorporated into the films as ether and carbonyl groups. For example, The % C-O and % C=O measured for Ac.110s.200w.f10.Ti was 7.6 % and 3.0 %, respectively, prior to annealing. The % C-O and % C=O increased to 15.6 % and 8.4 %, respectively, after the air annealing and to 9.3 % and 5.1 %, respectively, after the nitrogen annealing. These increases in oxygen content were significant and corresponded with changes in the mechanical properties of the cured PP films.

Table 6.26: Curve-fit C 1s data for annealed PP films.

Sample	% C-H/C-C	% C-O	% C=O	% O=C-OH
Ac.110s.200w.f10.Ti.Air	70.2	15.6	8.4	5.8
Ac.110s.200w.f10.Ti.N_2	83.8	9.3	5.1	1.8
Ac.110s.200w.f10.Si.Air	68.6	14.4	9.5	7.5
Ac.110s.200w.f10.Si.N_2	82.0	9.8	5.7	2.5

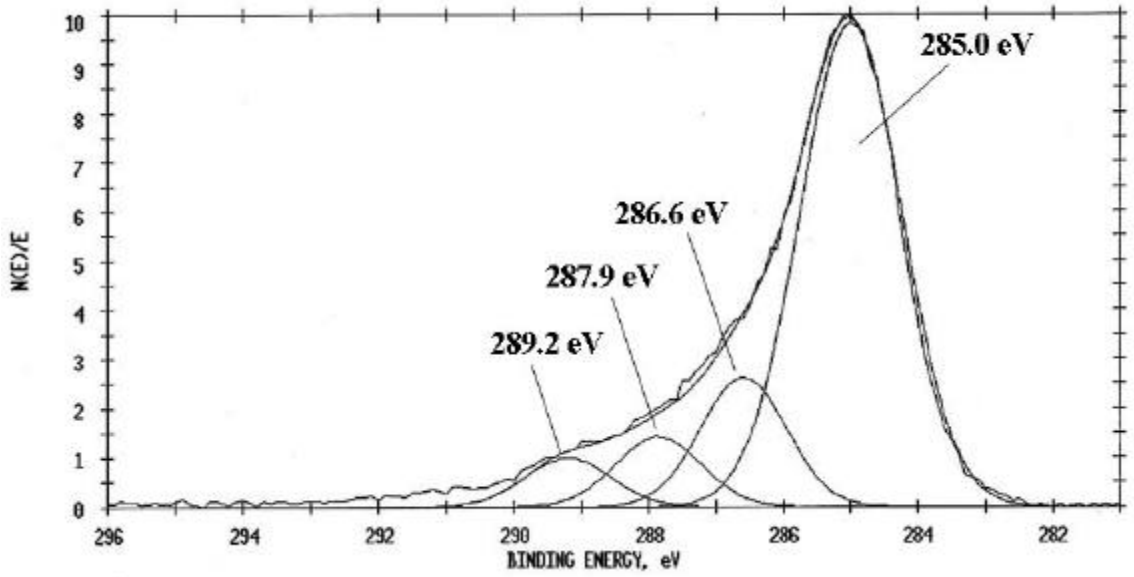

Figure 6.35: Curve-fit C 1s photopeak for Ac.110s.200w.f10.Ti.Air.

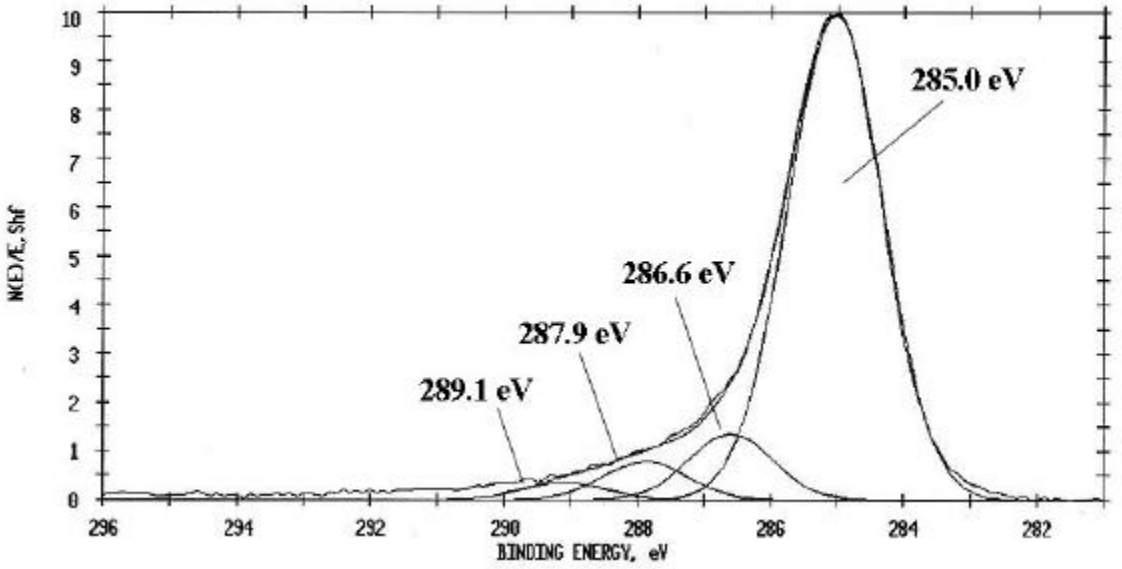

Figure 6.36: Curve-fit C 1s photopeak for Ac.110s.200w.f10.Si.N2.

Figure 6.37 and Figure 6.38 show the curve-fit O 1s peak for samples Ac.110s.200w.f10.Ti.Air and Ac.110s.200w.f10.Si.N2, respectively. The curve-resolved photopeaks are almost identical and represent the C=O (531.9 eV) and C-O-C (533.1 eV) components of the overall O 1s photopeak. Note that these binding energies are lower than those for the O 1s photopeaks prior to thermal treatment (532.3 eV and 533.5 eV), probably due to slight changes in the valence state of oxygen.[54]

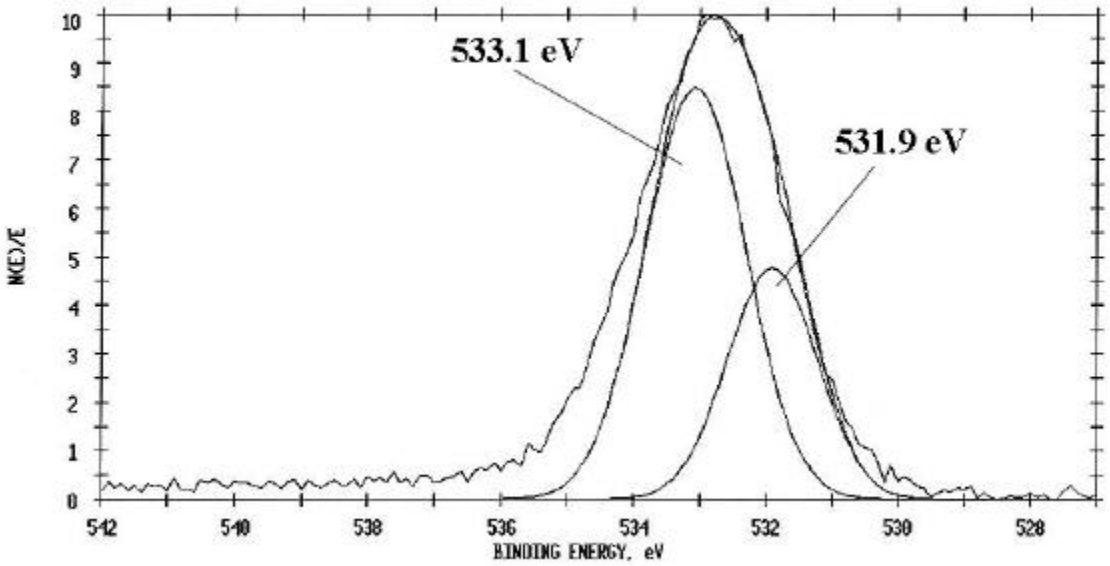

Figure 6.37: Curve-fit O 1s photopeak for Ac.110s.200w.f10.Ti.Air.

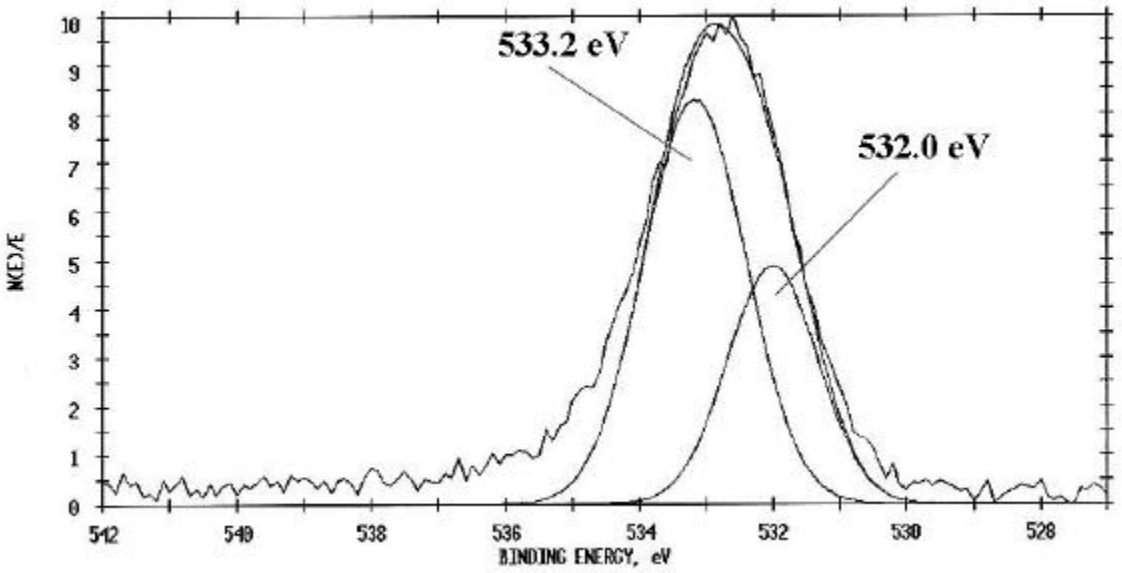

Figure 6.38: Curve-fit O 1s photopeak for Ac.110s.200w.f10.Si.N2.

Table 6.27 shows the nanoindentation results for the thermally treated films. The relative depth of penetration of the indents was high for Ac.110s.200w.f10.Ti and Ac.110s.200w.f10.Si, as shown by the h_c/thickness value. However, any substrate influence on these measurements seems unlikely, because these two samples had the lowest hardness values of the eight tested. If the substrate influenced these values, it would be expected that the hardness and modulus values would be inflated, yet the opposite is true. Recall that the hardness and modulus of the oxygen plasma treated substrates were substantially higher than for the PP films (5.75 GPa for polished Ti-6Al-4V and 10.21 GPa for a silicon wafer), as reported in Chapter 5.

Table 6.27: Hardness, reduced modulus, and depth of penetration values for annealed PP films from nanoindentation tests.

Sample	Thickness (Å)	H (GPa) before	H (GPa) after	E_r (GPa)	hc (Å)	hc/ thickness
Ac.110s.200w. f10.Ti.Air	560 ± 15	3.35 ± 0.32	2.71 ± 0.11	43.90 ± 1.28	212 ± 7	3.8
Ac.110s.200w. f10.Si.Air	435 ± 45	3.72 ± 0.18	1.89 ± 0.08	42.86 ± 1.86	280 ± 8	6.5
Ac.110s.200w. f10.Ti.N_2	725 ± 80	3.35 ± 0.32	3.47 ± 0.41	52.26 ± 3.19	175 ± 16	2.4
Ac.110s.200w. f10.Si.N_2	680 ± 25	3.72 ± 0.18	3.20 ± 0.16	51.46 ± 0.59	186 ± 8	2.7

From Table 6.21 (6.15.1.2), the hardness values of the PP films on samples Ac.110s.200w.f10.Ti and Ac.110s.200w.f10.Si were 3.35 GPa and 3.72 GPa, respectively. The hardness of every PP film decreased after the thermal treatment, except for the hardness of Ac.110s.200w.f10.Ti.N2, which showed essentially no change in hardness within standard deviations. A decrease in hardness of thin PP films upon annealing has been reported by other researchers. [55, 56, 57] It is believed that for the PP films of acetylene discussed here, the overall hardness and reduced modulus values decreased because of annealing-induced relaxation of the stresses in the films.

Bai et al[56] studied thin amorphous carbon nitride films (600 Å) deposited on silicon(111) by an ion beam assisted deposition method. The films were annealed under vacuum (1×10^{-6} Torr) at temperatures up to 380° C, and nanomechanical properties were determined using a Berkovich diamond tip (20 nm radius) and the method of Oliver and Pharr[42]. They measured the internal stresses of the films using a conventional beam-bending method, and Raman spectral analysis was used to study the evolution of microstructure due to annealing. They found that the stress-state of the films played a much larger role than the microstructure in nanomechanical properties after annealing. The hardness and scratch wear resistance of the amorphous films with large compressive internal stresses decreased after annealing due to the relaxation of the stresses induced by annealing. Conversely, the hardness and scratch resistance of the thin films with predominantly tensile internal stresses increased or remained unchanged due to annealing-induced relaxation of these stresses.

Lu et al[57] investigated the mechanical stability of amorphous carbon films (100 - 700 Å thick) deposited on Si(100) substrates by radio-frequency sputtering. They used a scanning force microscope (20 nm radius pyramidal diamond tip) and a maximum load of 20 μN to evaluate the films. The carbon was deposited at 750 watts onto a biased substrate (-200 V) then annealed at 495 °C for 70 minutes in the high vacuum chamber of an XPS system with a base pressure of 10^{-8} Torr. The hardness of the film decreased after annealing by over 50 %, from 39.2 ± 3.5 to 17.9 ± 2.8 GPa. They attributed this softening to the relaxation of films during annealing, which led to rearrangement of the carbon atoms and the loss of residual stresses within the films.

Table 6.28 shows the percent change in thickness, hardness, and modulus of the PP films following the thermal treatment. There was no correlation between change in thickness and

decrease in hardness. Ac.110s.200w.f10.Ti.N_2 lost 4.0 % of its thickness, yet the hardness and reduced modulus values for the film increased slightly. Conversely, the two films annealed in air lost over 25 % of their thickness, which corresponded to a significant lowering of their hardness and reduced modulus values. It is worth noting that the PP film of Ac.110s.200w.f10.Si.Air shrunk the most during the cure (-28.1 %) and also had the largest decrease in hardness (-49.2 %) and reduced modulus (-31.0 %). Also, the PP films cured in nitrogen showed the smallest changes in thickness and hardness.

Table 6.28: Changes in film thickness and mechanical properties due to annealing.

Sample	% change in thickness	% change in hardness	% change in modulus
Ac.110s.200w.f10.Ti.Air	-25.8	-19.1	-15.4
Ac.110s.200w.f10.Ti.N_2	-4.0	+3.6	+0.7
Ac.110s.200w.f10.Si.Air	-28.1	-49.2	-31.0
Ac.110s.200w.f10.Si.N_2	+12.4	-14.0	-17.1

Figure 6.39 shows a plot of hardness and reduced modulus vs. film thickness. Notice that the trend observed for uncured PP films (Figure 6.27 of Section 6.15.1.2 showed thinner films were harder) has reversed for the thermally treated samples. Likewise, the plot of penetration depth vs. thickness shown in Figure 6.40 shows the opposite trend compared to results for the untreated films. Because the thicker films were harder, the depth of penetration was smaller for these measurements. The thicker films show a higher hardness and reduced modulus than the thinner films. This change is believed to be due to a thermally induced crosslinking effect. During annealing of the thin PP films, extended crosslinking is believed to occur as mobility within the films increases and unstable species are able to react and form a stable network. The mobility in a thinner film is more restricted than the mobility in a thicker film because thinner films are more constrained by the boundaries of the substrate and the film surface. It is hypothesized that thinner PP films are crosslinked to a lesser degree than thicker PP films during annealing because of this decreased mobility. Therefore, the thicker PP films were more highly crosslinked, and this resulted in higher hardness values for these thicker PP films.

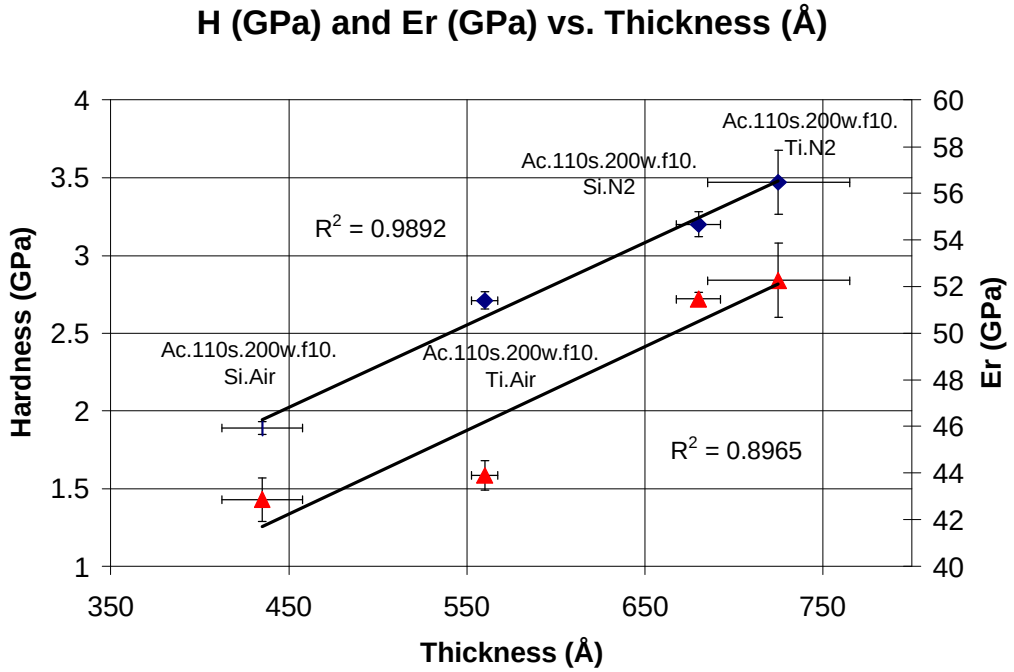

Figure 6.39: Hardness and reduced modulus vs. thickness for the nanoindentation tests on cured Ac.110s.200w.f10 samples. The triangular data points are the reduced moduli and the diamond data points are the hardness values.

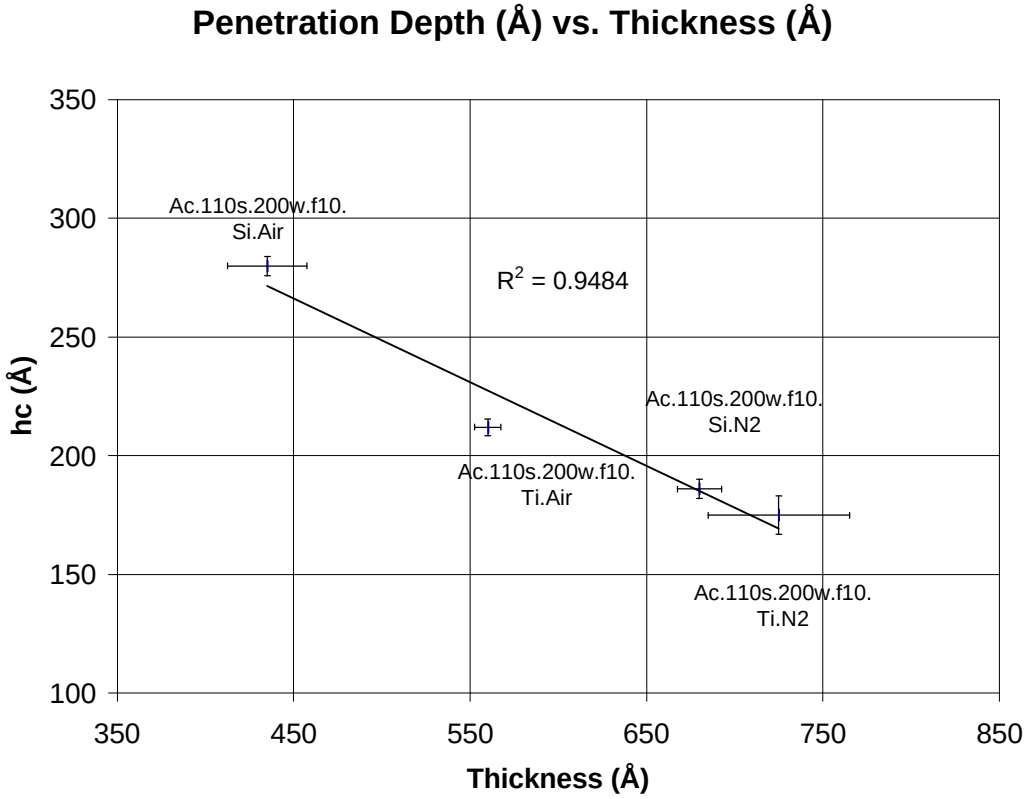

Figure 6.40: Depth of penetration vs. thickness for the nanoindentation tests of thermally treated samples.

From Figure 6.39, notice that the cured PP films on Ti-6Al-4V were harder and had a higher reduced Young's modulus than the PP films deposited on silicon wafers. This is in direct contrast to the behavior exhibited by the untreated films. It is believed that this trend change was a direct result of the thickness effect discussed above. Because the PP films on polished Ti-6Al-4V were thicker than the PP films on silicon, their hardness and reduced modulus values were higher due to the increased crosslinking that occurred in the thicker films.

6.15.2.3 Nanoscratch Tests

Table 6.29 lists the film thicknesses, the normal displacement and critical loads at debond, and the thickness-normalized critical loads at debond. The values for the original samples (before heating) are listed at the bottom of the table. The critical loads at debond are higher for the heated samples and the thickness-normalized critical loads at debond increased by

over twofold for the cured PP films. This suggests that the heated films adhere to the substrates better after annealing, probably due to stress-relaxations that occur at the PP film/substrate interface.

For the two samples that were annealed in air, notice that the normal displacement at debond was almost twice the thickness of the PP films. Plastic deformation of the film during the scratch test may have caused this discrepancy. Alternatively, failure may not have occurred at the PP film/substrate interface for these samples. Instead, failure could have occurred somewhere within the substrate. However, any differences in the failure mode did not significantly affect the critical load at debond/thickness value.

Figure 6.41 shows how the critical load values at debond varied with PP film thickness. The thicker films had higher critical load values at debond, regardless of substrate or annealing atmosphere. This trend was not observed for the non-heated samples, so it was probably induced by the annealing process. Consistent with the arguments presented regarding the effect of thermal treatment of the PP films, the thicker films exhibited a higher hardness due to increased crosslinking, and thus they were more difficult to remove from the substrate surfaces than thinner films. The films heated in nitrogen yielded higher critical load at debond than the films heated in air, but this was most likely due to a thickness effect rather than a substrate effect.

Table 6.29: Film thicknesses (AES) and critical loads at debond.

Sample	Film thickness (Å)	Normal displacement at debond (Å)	Critical load (μN)	Critical load/ thickness (μN/Å)
Ac.110s.200w.f10.Ti (not heated)	755 ± 25	980	808 ± 173	1.07 ± 0.23
Ac.110s.200w.f10.Ti.Air	560 ± 15	1130	1310 ± 380	2.34 ± 0.68
Ac.110s.200w.f10.Ti.N2	725 ± 80	870	1845 ± 305	2.54 ± 0.42
Ac.110s.200w.f10.Si (not heated)	605 ± 40	680	751 ± 135	1.24 ± 0.22
Ac.110s.200w.f10.Si.Air	435 ± 45	810	895 ± 290	2.06 ± 0.67
Ac.110s.200w.f10.Si.N2	680 ± 25	880	1770 ± 235	2.60 ± 0.35

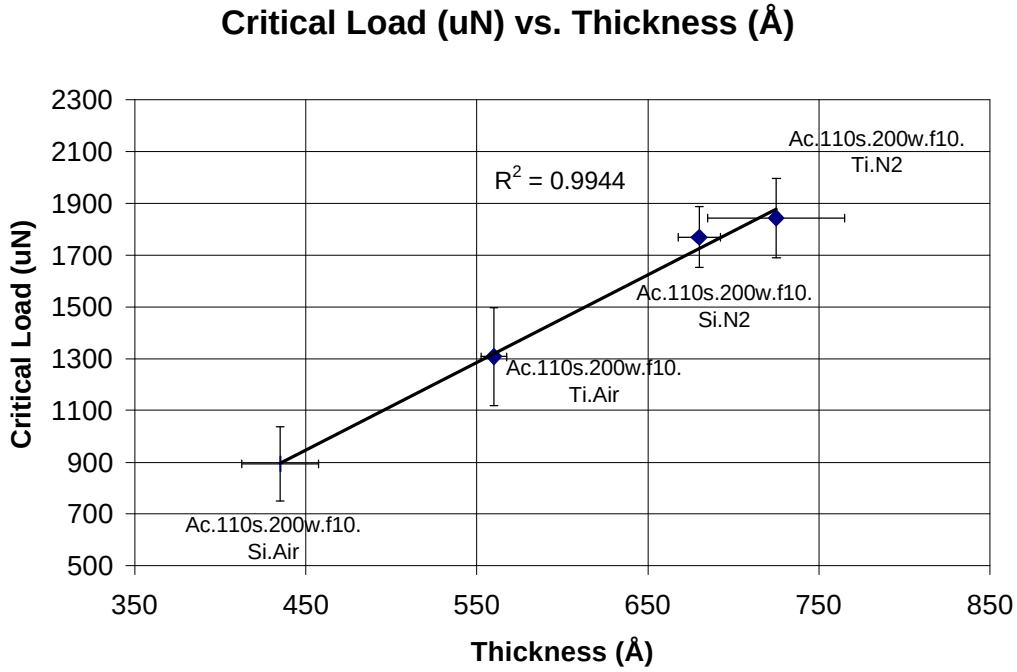

Figure 6.41: Critical load at debond vs. thickness for the annealed samples.

Figure 6.42 shows the correlation between hardness, reduced Young's modulus, and critical load at debond. This trend was absent from the data for the non-heated films. The graph shows that the higher hardness PP films yielded the highest critical load at debond. PP films heated in nitrogen were the hardest and therefore exhibited the highest critical load at debond. Figure 6.43 shows hardness and reduced Young's modulus vs. critical load at debond/thickness. This was a confirmation of the trend for the uncured PP films. Films of higher hardness and reduced Young's modulus displayed higher critical load at debond when the critical loads were thickness-normalized.

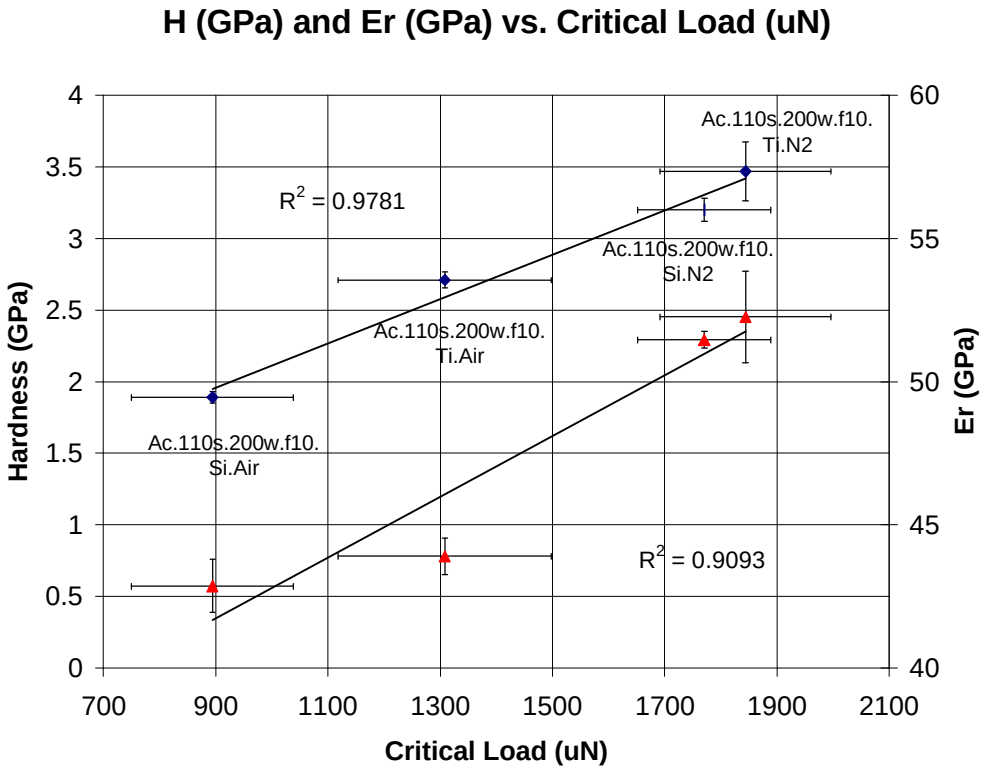

Figure 6.42: Hardness and reduced modulus vs. critical load for annealed samples.

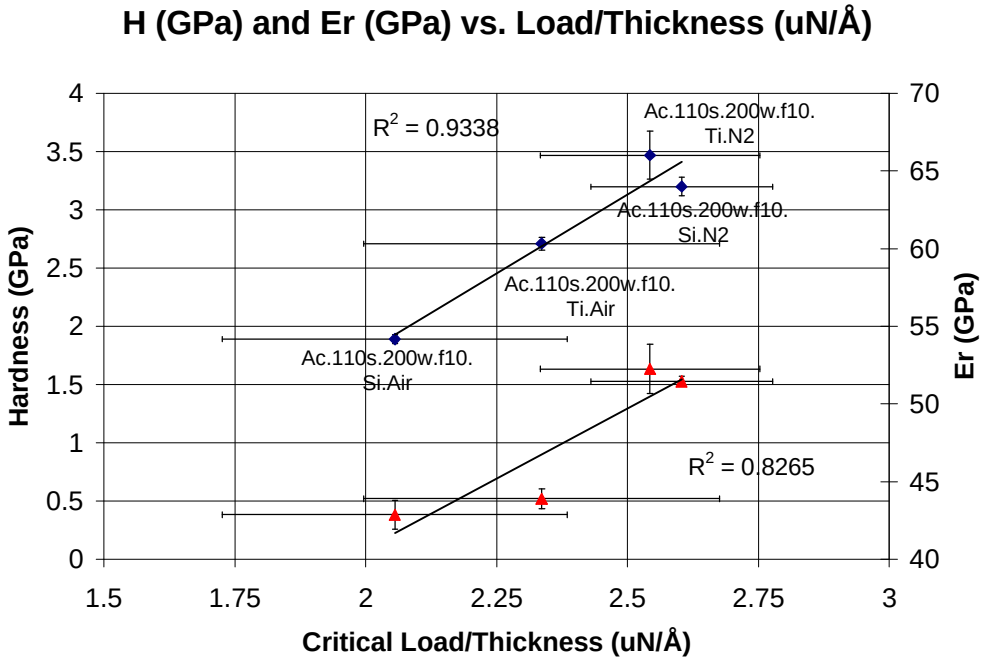

Figure 6.43: Hardness and reduced modulus vs. critical load/thickness for annealed samples.

6.16 Conclusions

Plasma polymerized acetylene films were investigated as adhesion-promoters for the bonding of Ti-6Al-4V with FM-5. It was determined that the strength of SLS joints was limited by the adhesion of the PP acetylene to the Ti-6Al-4V substrate. For all SLS specimens tested, the adhesion between PP acetylene and FM-5 adhesive was quite adequate. The effects of a large number of plasma parameters, such as substrate pretreatment, carrier gas, input power, flow rate and film thickness were investigated, but none succeeded in producing the strong PP acetylene/TiO_2 interactions needed for improved SLS strength. All samples failed at the PP film/Ti-6Al-4V interface or within the PP acetylene film.

XPS and FTIR spectra of the PP films were consistent with literature reports. The films were predominantly carbon, with varying degrees of oxygen and nitrogen incorporated into the films. There was also evidence of some unsaturation within the films. Oxygen and nitrogen were incorporated into the films due to post-deposition reactions with purge gases or with the atmosphere. Oxygen was incorporated as carbonyl and ether groups.

From the analysis of miniature SLS joints, thicker PP films yielded lower SLS strengths. Although a limit was not quantitatively determined, it appeared that PP film thickness should not exceed 400 Å. In addition, when there was a large difference in thickness, the surface composition of the films differed. This was due to that fact that certain functional groups do not form at the beginning of a deposition process, but rather form later in the process through the recombination of free radicals. Increasing the power input had the effect of increasing overall bond strength for plasmas using helium as a carrier gas, but power input had no obvious effects for systems utilizing argon as the carrier gas. In all cases, an increase in power input led to an increase in deposition rate. However, the surface composition of the PP acetylene was not influenced by power input. Flow rate did not influence SLS strength when argon was the carrier gas, and it was unclear whether it affected systems incorporating helium. Varying the length of the oxygen plasma pretreatment had little affect on the overall SLS strength, and the location of acetylene introduction (above or below the induction coil) was a non-factor, as well. Grounding

the samples during deposition had a negligible effect on the composition of the PP film and the SLS strength.

The best SLS performance obtained from a PP acetylene-primed SLS set of samples was 2780 ± 480 psi, which was produced from a nitrogen/acetylene plasma pretreated sample with a PP film thickness of approximately 30 Å. When compared with the strength of an acetone cleaned sample of titanium (5461 ± 168 psi, see Chapter 4), PP films of acetylene did not offer any strength benefits as a surface preparation treatment for this type of high performance application.

The nanomechanical properties of PP films were studied using AFM nanoindentation and nanoscratch techniques. PP acetylene films were deposited onto polished Ti-6Al-4V and silicon wafers. Film deposition occurred at a faster rate on Ti-6Al-4V, probably due to a roughness effect. For both substrates, PP films deposited at lower power exhibited higher hardness and reduced modulus than films deposited at higher power. At both power levels, PP films deposited on silicon exhibited higher hardness and reduced modulus values than PP films deposited on polished Ti-6Al-4V. This finding could have been a thickness effect. Overall, thinner films exhibited higher hardness and reduced Young's modulus than thicker films. For the samples tested, the PP films of higher hardness yielded higher critical loads at debond (thickness normalized) during the nanoscratch test.

The PP films deposited at high input power were annealed for 1 hour in air and nitrogen environments at 350° C. For both substrates, the hardness and reduced modulus values of the PP films decreased due to annealing because of the relaxation of stresses within the films. Interestingly, the thicker films yielded a higher hardness and reduced modulus after annealing, in contrast to the trend that was noted for non-annealed PP films. This was hypothesized to be a result of the higher degree of crosslinking that the thicker films underwent compared to thinner films. For annealed PP films, films of higher hardness yielded higher critical load at debond (thickness normalized), a result that was consistent with the behavior of the non-annealed PP films.

6.17 References

[1] Y.M. Tsai; F.J. Boerio; R. Aggarwal; D.B. Zeik; S.J. Clarson; W.J. van Ooij; A. Sabata *J. Appl. Polym. Sci.: Appl. Polym. Symp.* **1994,** *54*, 3.
[2] Y.M. Tsai; F.J. Boerio; W.J. Van Ooij; D.K. Kim *J. Adhes.* **1997**, *62*, 127.
[3] Y.M. Tsai; F.J. Boerio; W.J. van Ooij; D.K. Kim; T. Rau *Surf. Interface Anal.*, **1995**, *5*, 261.
[4] H. Yasuda *Plasma Polymerization*; Academic Press: Orlando, FL, 1985, Chapter 10.
[5] D. C. Nonhebel; J. C. Walton *Free Radical Chemistry*; Cambridge University Press: Cambridge, 1974.
[6] S. Kaplan; A. Dilks *J. Appl. Polym. Sci.: Appl. Polym. Symp.* **1984**, 38, 105.
[7] Y.M. Tsai; F.J. Boerio *J. Appl. Polym. Sci.* **1998**, *70*, 1283.
[8] H. Yasuda; T. Hirotsu *J. Polym. Sci., Polym. Chem. Ed.* **1978**, *16*, 313.
[9] P.J. Dynes; D.H. Kaelble *J. Macromol. Sci., Chem.* **1976**, *A10*, 535.
[10] C.D. Wagner; W.M. Riggs; L.E. Davis; J.F. Moulder; G.E. Muilenburg *Handbook of X-Ray Photoelectron Spectroscopy*; Perkin-Elmer: Eden Prarie, MN, 1979; Appendix 3.
[11] F. Shi *Surf. Coat. Technol.* **1996**, *82*, 1.
[12] H. Yasuda *Plasma Polymerization*; Academic Press: Orlando, FL, 1985, Chapter 8.
[13] M.K. Fung; W.C. Chan; K.H. Lai; I. Bello; C.S. Lee; N.B. Wong; S.T. Lee *J. of Non-Cryst. Solids* **1999**, *254*, 167.
[14] D.L. Pappas, J. Hopwood *J. Vac. Sci. Technol. A* **1994**, *12*, 1576.
[15] J. Hopwood *Plasma Sources Sci. Technol.* **1992**, *1*, 109.
[16] W.C. Chan; M.K. Fung; I. Bello; C.S. Lee; S.T. Lee *Diamond Relat. Mater.* **1999**, *8*, 1732.
[17] K.P.C. Vollhardt *Organic Chemistry*; Freeman and Company: New York, NY, 1987, Chapter 12.
[18] H. Yasuda, H.C. Marsh; M.O. Bumgarner; N. Morosoff *J. Appl. Polym. Sci.* **1975**, *19*, 2845.
[19] N. Morosoff; B. Crist; M. Bumgarner; T. Hsu; H. Yasuda *J. Macromol. Sci. Chem.* **1976**, *A10*, 451.
[20] H. Yasuda; T.S. Hsu *J. Polym.Sci. Polym. Chem. Ed.* **1977**, *15*, 81.
[21] L. Gerenser *J. Adhes. Sci. Tech.* **1987**, *1*, 303.
[22] C. Kim; D. Goring; G. Suranyi *J. Poly Sci., Part C* **1970**, *30*, 533.
[23] S.F. Durrent; R.T Oliveira; S.G.C. Castro; L.E. Bolivar-Marinez; D.S. Galvao; M.A.B. Moraes *J. Vac. Sci. Technol.* **1997**, *A 15*, 1334.
[24] N.B. Colthup, *J. Opt. Soc. Am.* **1950**, *40*, 397.
[25] P.W. Rose; E.M. Liston *Plastics Eng.* **1985**, *41*, 1.
[26] N.K. Adam In *Contact Angle, Wettability, and Adhesion*; R.F. Gould, Ed.; ACS: Washington, DC, 1964, Chapter 2.
[27] E.M. Liston *J. Adhes.* **1989**, *30*, 199.
[28] N. Inagaki; H. Yasuda *J. Appl. Polym. Sci.* **1981**, *26*, 3333.
[29] D.H. Kaelble *Physical Chemistry of Adhesion*; Wiley-Interscience: New York, NY, 1971.
[30] S. Wu *Polymer Interface and Adhesion*; Marcel Dekker, Inc.: New York, NY, 1982; Chapter 5.
[31] C. C. Schmitt; J. R. Elings *Digital Instruments Brochure*, 1997.
[32] M.R. Alexander; S. Payan; T.M. Duc *Surf. Interface Anal.* **1998**, *26*, 961.
[33] N.R. Moody; D. Medlin; D. Boehme; D.P. Norwood *Engineering Fracture Mechanics* **1998**, *61*, 107.

[34] P. Lemoine; R.W. Lamberton; A.A. Ogwu; J.F. Zhao; P. Maguire; J. Mclaughlin *J. of Appl. Phys.***1999**, *86*, 6564.
[35] W. Xu; L.J. Huang; Y.Z. Shih; T. Kim; Y. Hung; G. Li *Thin Solid Films* **1999**, *355-356*, 353.
[36] J. Robertson *Pure Appl. Chem.* **1994**, *66*, 1789.
[37] R.G. Lacerda; F.C. Marques; F.L. Freire *Diamond Relat. Mater.* **1999**, *8*, 495.
[38] Z. Sun *J. Non-Crystal. Solids* **2000**, *261*, 211.
[39] H. Yasuda *Plasma Polymerization*; Academic Press: Orlando, FL, 1985, p. 190.
[40] H. Biederman; D. Slavinska *Surf. Coat. Technol.* **2000**, 125, 371.
[41] W. Lu; K. Komvopoulos *J. Appl. Phys.* **1999**, *86*, 2268.
[42] W.C. Oliver; G.M. Pharr *J. Mater. Res.* **1992**, *10*, 1564.
[43] W-C. Chan; B. Zhou; Y-W. Chung; C.S. Lee; S.T. Lee *J. Vac. Sci. Technol. A* **1998**, *16*, 1907.
[44] G.M. Pharr; W.C. Oliver *MRD Bull.* **1992**, *17*, 28.
[45] A.V. Kulkarni; B. Bhushan *J. Mater. Res.* **1997**, *12*, 2707.
[46] S. Christiansen; M. Albrecht; H.P. Strunk; H. Hornberger; P.M. Marquis; J. Franks *J. Mater. Res.* **1996**, *11*, 1934.
[47] H.C. Ong; R.P.H. Chang; N. Baker; W.C. Oliver *Surf. Coat. Technol.* **1997**, *89*, 38.
[48] M.M. Lacerda; F.L. Freire; R. Prioli; C.M. Lepinski; G. Mariotto *J. Vac. Sci. Technol. A* **1999**, *17*, 2811.
[49] X. Li; B. Bhushan *Wear* **1998**, *220*, 51.
[50] X.H. Yun; R.C. Hsiao; D.B. Bogy; C.S. Bhatia *IEEE Transactions on Magnetics* **1997**, *33*, 938.
[51] B. Bhushan In *Handbook of Micro/Nanotribology*; B. Bhushan, Ed.; CRC Press: Boca Raton, FL, 1995, 321.
[52] H. Deng; T.W. Scharf; J.A. Barnard *J. Appl. Phys.* **1997**, *81*, 5396.
[53] W. Kulisch; C. Popov; L. Zambov; J. Bulir; M.P. Delplancke-Ogletree; J. Lancok; M. Jelinek *Thin Solid Films* **2000**, *377*, 148
[54] W. Possart; W. Unger in *Adhesion 15*, K.W. Allen, Ed.: Elsevier Applied Science, New York, NY; 1991, 148.
[55] L.G. Jacobsohn; R. Prioli; F.L. Freire Jr.; G. Mariotto; M.M. Lacerda; Y.M. Chung *Diamond Relat. Mater.* **2000**, *9*, 680.
[56] M. Bai; K. Kato; N. Umehara; Y. Miyake; J. Xu; H. Tokisue *Thin Solid Films* **2000**, *376*, 170.
[57] W. Lu; K. Komvopoulos; S.W. Yeh *J. Appl. Phys.* **2001**, *89*, 2422.

7.0 Plasma Polymerized Titanium Isobutoxide

7.1 Introduction

Polymer composites containing metal and metal oxide particles have received increased interest because of their electrical, magnetic, optical, and corrosion-resistant properties. There are many techniques for the preparation of these types of composites, and some of the techniques are already used commercially.[1] Traditional sol/gel processes that utilize metal alkoxides allow the low temperature synthesis of high purity ceramic-type materials.[2] These sol/gel pretreatments create hybrid inorganic/organic coatings that provide a gradient between the metal adherend and a polymeric adhesive.[3, 4] Specifically, the polycondensation of metal alkoxides with H_2O results in three-dimensional mixed metal oxide/hydroxide/alkoxide clusters.[5] These films are effective as corrosion-protective coatings on metal substrates because of their ability to act as a barrier coating by covalently interacting with the oxide layer at the metal surface.[6, 7] While some of these treatments have out-performed chromic acid anodized (CAA) pretreatments under certain conditions, the sol/gel process is tedious and reproducibility is limited.[2] For example, in some cases a minimum of 24 hours is needed to promote tackiness before a sol/gel film can be cured.[2] In an effort to improve the strength of the Ti-6Al-4V/FM-5 bond using an environmentally friendly, more efficient process, novel PP thin films with "sol/gel-like" properties were sought via the vapor plasma polymerization of titanium(IV) isobutoxide (TiiB). There is no evidence in the literature that PP sol/gel like films have ever been investigated for use as adhesion promoters.

When a titanium substrate is heated above 300 °C, carbon-free TiO_2 layers are typically deposited from the plasma polymerization of titanium(IV) isopropoxide (TiiP).[8, 9] Titanium species incorporated into an organic polymer matrix can also be generated during plasma enhanced chemical vapor deposition (PECVD) of TiiP or TiiB precursors using an unheated substrate. The resultant films consist of TiO_x ($0 < x < 2$) clusters dispersed throughout a host polymeric medium. These TiO_x/polymeric films are potentially attractive for electrical, optical, thermal, chemical, and magnetic applications.[1, 8, 10]

PP films from organo-metallic starting materials may be able to take advantage of the reactive phenyl acetylene end-groups of FM-5 and form covalent linkages across the interphase. Unsaturation in the PP film would allow crosslinking with FM-5, providing strong covalent linkages for better joint performance. Inagaki et al[1] used a capacitively coupled (13.56 MHz) bell jar reactor to plasma polymerize sublimated titanium acetylacetonate [$TiO(C_5H_7O_2)_2$] at low pressures for use as CO gas sensor devices. They presented FTIR evidence that indicating non-complexing C=C and C=O groups within the film, with fewer absorption peaks due to organo-metallic bonds. This evidence of unsaturation suggests that interactions between the FM-5 and the PP film could be significant. Even if a sufficient amount of unsaturation cannot be generated, PP organo-metallics should enhance adhesive performance by creating a gradient from the titanium alloy to the polyimide adhesive.

In a study of PP TiiP on low density poly(ethylene) and glass slides by Ratcliffe et al,[8] domains of TiO_2 dispersed in an organic matrix were also detected. They characterized the PP films by XPS and FT-IR. Using an IC RF plasma, they found that more TiO_2-rich layers were formed at lower input power (5 W) and more organic-rich layers were formed at higher input power (30 W). Based on these findings, low input powers were investigated in this study.

7.2 Experimental

Titanium(IV) isobutoxide ($Ti[(CH_3)_2CHCH_2O]_4$), a liquid at room temperature, was chosen as the starting material because it has adequate vapor pressure at room temperature and it has been used as a starting material for traditional sol/gel pretreatments. Early experiments revealed that there was no deposition unless the TiiB was heated, and it was found that the optimum temperature was 70° C. There was no advantage to heating the TiiB above this temperature. A carrier gas was bubbled through the heated TiiB and then introduced through a side inlet into the reactor. When the flow rate is mentioned in the discussion, it pertains to the flow rate of the carrier gas. Reactor profile studies revealed that the most uniform films were deposited when the samples were placed along the bottom of the reactor, from 8 to 20 cm (3.15 - 7.87 inches) from the end of the induction coil.

After PP TiiB film deposition, the surface of the Ti-6Al-4V was visibly coated. The PP films ranged in color from metallic blue to a dull gold, depending on plasma deposition conditions. Although a thorough study of solvent resistance was not performed, PP films from TiiB did not visually dissolve in acetone, tetrahydrofuran, N-methyl-2-pyrrolidinone, or n-hexane. This confirmed that the PP films of TiiB behaved like typical plasma polymers, with respect to their highly branched and/or crosslinked structure.

7.3 Initial PP Films

7.3.1 Carrier Gas

No film deposition occurred unless a carrier gas was used and was bubbled through the TiiB. Simply introducing TiiB vapor to the reactor chamber did not result in any deposition, probably because the vapor pressure of the TiiB at room temperature was too low. This was reported by other researchers during an attempt to deposit thin PP films of TiiP onto silicon wafers.[9] Nitrogen and argon were the most suitable carrier gases. Using oxygen as the carrier gas did not result in any deposition, a result that has also been reported in the literature.[9] The thicknesses of the PP films deposited using nitrogen and argon as the carrier gases were very similar, measuring 158 ± 21 and 182 ± 19 Å, respectively.

Figure 7.1 shows the XPS surface analysis results from using various carrier gases in the deposition of PP TiiB on titanium alloy. Each experiment was performed using a treatment time of 20 minutes, an input power of 40 watts, and a flow rate of 2.5 sccm. Nitrogen and argon yielded films with similar characteristics. The films were composed of ≈ 65 % carbon, ≈ 17 % oxygen, and ≈ 4 % titanium. With nitrogen as the carrier gas, the PP film contained a larger percentage of nitrogen (17 %) because the carrier gas was incorporated into the organic matrix of the film during deposition. The nitrogen from films deposited with argon as the carrier gas was probably due to nitrogen from the atmosphere that was incorporated through a small leak in the reactor.

The films were similar in composition to those of PP titanium acetylacetonate (TiAcAc) discussed by Inagaki et al.[1] Using a capacitively coupled, parallel electrode reactor and an input power of 60 watts, they obtained PP films composed of ≈ 69 % carbon, 28 % oxygen, and 2.5 % titanium. FTIR analysis revealed that films of PP TiAcAc showed few absorption peaks due to titanium/ligand bonds, but strong absorption peaks due to free C=O and C=C groups. They reasoned that the complexing bonds were cleaved during the plasma polymerization to give TiO_2 in an organic matrix.

When oxygen was used as the carrier gas, visually no PP film was evident on the Ti-6Al-4V surface. The effect of the plasma process was essentially the same as that of an oxygen plasma treatment, and the atomic concentrations were similar to those presented in Chapter 5 (≈ 26 % carbon, 52 % oxygen, and 17 % titanium). Aluminum (2.6 %) was also noted in the XPS results when oxygen was used as the carrier gas, confirming that no film deposition occurred. Therefore, with oxygen as the carrier gas, ablative processes dominated and this resulted in a cleaned Ti-6Al-4V surface.

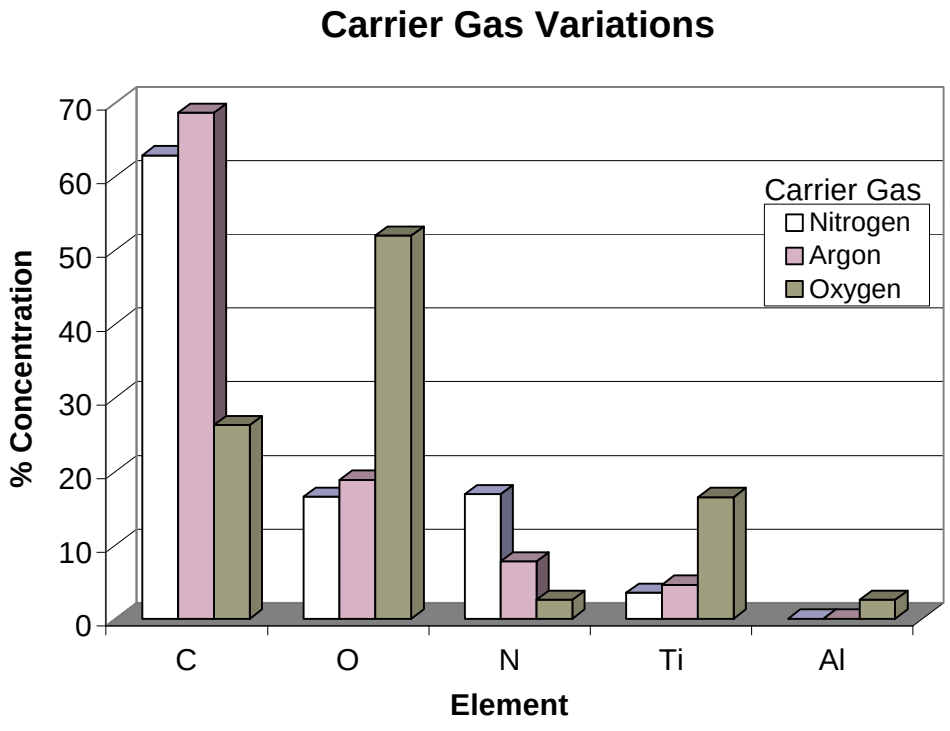

Figure 7.1: Carrier gas effects on film deposition.

7.3.2 XPS Characterization

Figure 7.2 shows the curve-fit C 1s photopeak of the PP film deposited using nitrogen as the carrier gas. The C 1s photopeak was not very different from some of the C 1s photopeaks of PP acetylene shown in Chapter 6. The photopeak was also consistent with literature reports of PP titanium(IV) isopropoxide which showed a carbon matrix consisting of C-H/C-C groups, C-O groups, and C=O groups.[8] Contributions from C-H/C-C (285.0 eV), C-N (286.0 eV), C-O (286.8 eV), and C=O (288.1 eV) were prevalent in the spectrum shown. Note the absence of any photopeak around 283 eV. This would be the location of a titanium carbide photopeak.[11, 12] The absence of this photopeak suggested that the titanium within the PP films was not covalently linked with any organic species. This was confirmed by the O 1s (Figure 7.3) and Ti 2p photopeaks (Figure 7.4), which revealed that the ≈ 4 % titanium was incorporated into the film as TiO_2. The O 1s photopeak showed contributions from TiO_2 (530.1 eV), C=O (531.5 eV), and C-O (532.5 eV). It was typical of all O 1s photopeaks for PP TiiB. The curve-fit O 1s photopeak at 530.1 eV represented 41.2 % of the oxygen peak, which accounted for 6.9 % (41.2 % x 16.6 %) of the total oxygen in the PP film. This was approximately twice the titanium content (3.5 %), and was a confirmation of the presence of TiO_2.

The titanium $2p_{3/2}$ and $2p_{1/2}$ photopeaks were separated by 5.7 eV, which is characteristic of TiO_2.[13] The Ti $2p_{3/2}$ and Ti $2p_{1/2}$ peak positions of 458.6 and 464.3 eV, respectively, were in close agreement with literature values for bulk TiO_2.[8, 13, 14, 15] If any titanium carbide were present, the Ti $2p_{3/2}$ photopeak for Ti-C should appear at a lower binding energy (≈ 454.7 eV).[13] The fact that the Ti $2p_{3/2}$ photopeak shown in Figure 7.4 was so narrow was another indication that it was not very likely that titanium was incorporated as Ti-C or Ti-O-C. Wagner et al[16] reported the XPS position of the Ti-O-C photopeak from titanium acetylacetonate at 457.9 eV. Additionally, in a study of sputtered titania coatings on PET, Ben Amor et al[17] proposed that the broadening of the Ti $2p_{3/2}$ photopeak was due to the appearance of a Ti-O-C band at 457.8 eV. No such broadening of the Ti $2p_{3/2}$ photopeak was seen for the PP films prepared in this study.

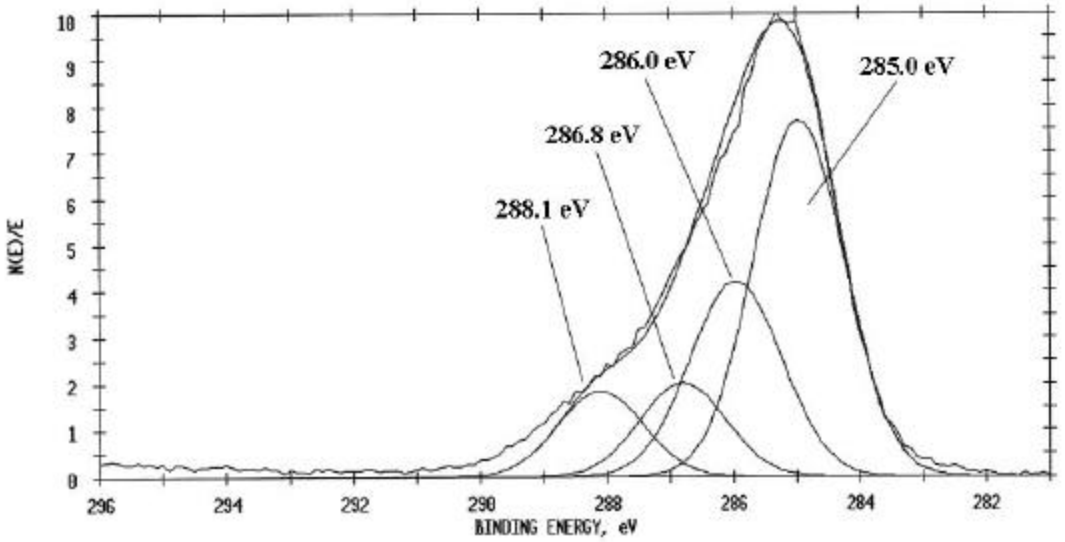

Figure 7.2: Curve-fit C 1s photopeak for PP TiiB with argon as the carrier gas.

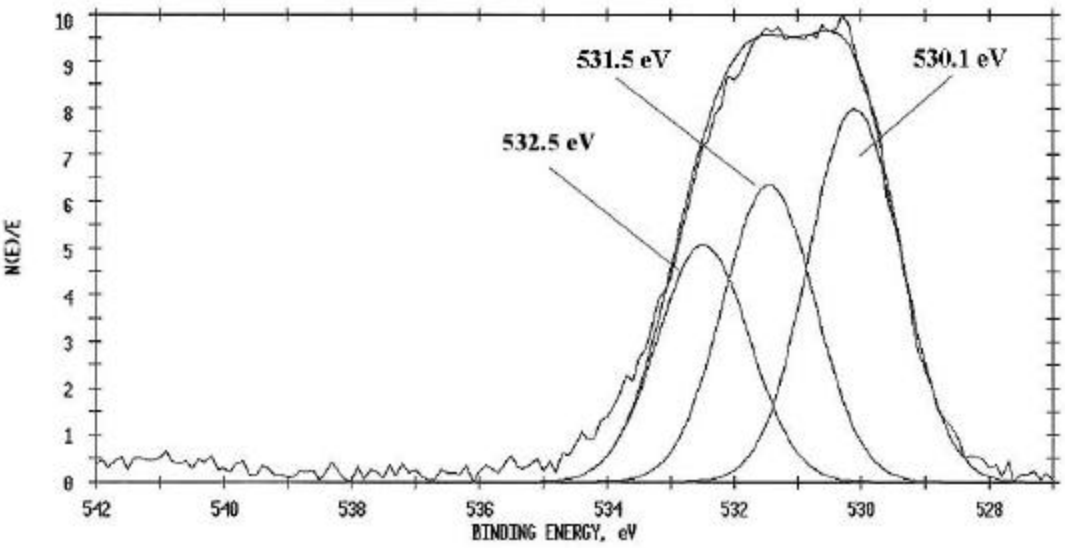

Figure 7.3: Curve-fit O 1s photopeak for PP TiiB with argon as the carrier gas.

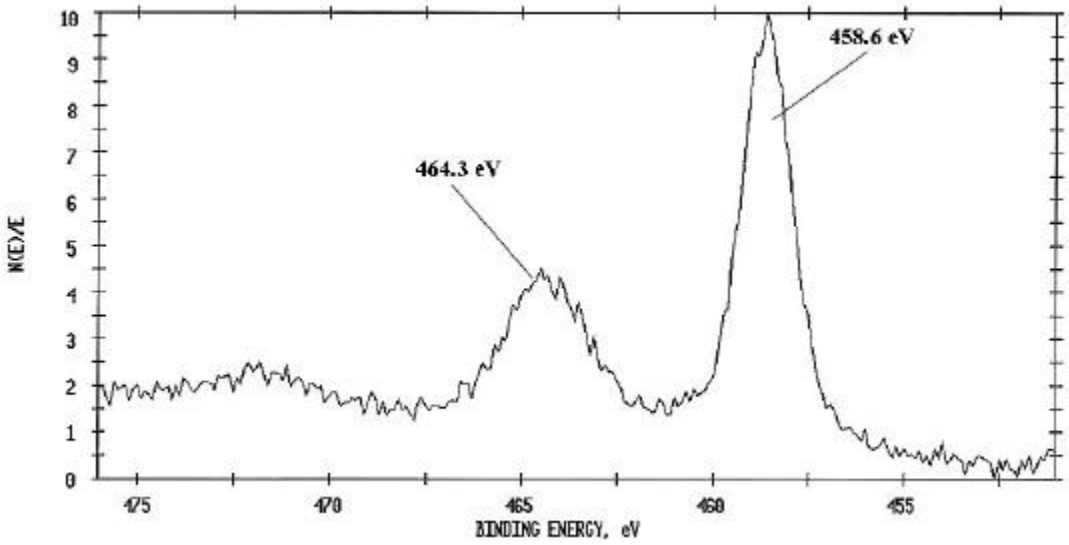

Figure 7.4: Ti 2p photopeaks for PP TiiB with argon as the carrier gas.

The stoichiometries of the PP films deposited using nitrogen and argon as carrier gases were $TiO_{4.7}C_{18.0}N_{4.8}$ and $TiO_{4.1}C_{14.9}N_{1.7}$, respectively. If the titanium were in the form of TiO_2, then there must have been substantial organic oxygen incorporated into the PP films. This was observed, as described above in the discussion of the C 1s photopeaks.

7.3.3 Mechanism of Deposition

Overall, the mechanism of plasma polymerization and deposition for organo-metallics is not well understood and these films were difficult to characterize. Thermal decomposition of TiiP at a surface results in a number of stable by-products from eliminations:[18, 19]

$$Ti[(CH_3)_2CHO]_4 \rightarrow \quad TiO_2(s) + H_2(g) + (CH_3)_2C{=}O(g) + CH_2{=}CHCH_3(g) + (CH_3)_2CH(OH)(g)$$

Plasma-induced free radicals formed from these types of species are believed to be present during the plasma polymerization of TiiB.[8] The PP film can also be formed by the direct reduction of oxidized metal atoms by the energetic electrons in the gaseous plasma, as described for the plasma polymerization of copper acetylacetonate.[20] The activation of the starting material

then leads to the formation of microscopic metal oxide clusters in the initial state, which gradually enlarge to macroscopic islands. The metal clusters are isolated from each other in the polymer matrix that forms from the polymerization of the ligands of the organo-metallic. This type of mechanism was also proposed for the plasma polymerization of TiiP on glass substrates.[14] In that study by Kagami et al,[14] they produced PP films of metallic and organic layers corresponding to TiO_x ($0 < x < 2$) and $(CH_2)_n$, respectively. Their PP films exhibited surface and bulk stoichiometries of $TiC_{1.21}O_{1.72}$ and $TiC_{0.56}O_{1.55}$, respectively.

It has been proposed that titanium-containing moieties and carbon containing moieties deposit independently after the initial fragmentation of the starting material in the plasma, and it seems likely that this occurs for the plasma polymerization of TiiB.[21] This situation was described by Yasuda and Yasuda[21] after studying the plasma polymerization of tetramethyl silane (TMS). They found the deposition rates of silicon species to be much different from the deposition rate of organic species in a TMS plasma. In the system studied here, the mass difference between titanium (47.88 g/mole) vs. carbon (12.01 g/mole) and oxygen (16.00 g/mol) results in the activated titanium species being less mobile than others in the plasma state. Therefore, fewer activated titanium species are able to interact with the substrate or the PP film developing on the substrate. Additionally, the stability of the TiO_2 moiety makes it more likely that activated titanium will have a short lifetime in the plasma. Stable TiO_2 species can then be pumped out of the reactor after very little interaction with the organic species. This could explain why very little titanium was incorporated into the PP films.

7.4 PP Film Profile

Initial studies indicated that freshly deposited PP TiiB films readily adsorbed titanium(IV) isobutoxide vapor after the plasma was terminated. This was not surprising due to the reactive nature of PP film surfaces following deposition. Additionally, adsorption of the monomer on substrates in the absence of a glow discharge has been reported elsewhere.[8] In this study, the amount of TiiB adsorbed consistently increased up to 30 minutes after film deposition, as shown by the increasing titanium content in Figure 7.5. The data plotted in Figure 7.5 are from individual experiments, where the PP film deposition conditions were identical and only the

purge time after treatment was varied. The titanium content increased from an initial value of ≈ 1 % to a limiting value of over 10 % after 30 minutes. The oxygen content increased from 12.4 % to 29.5 %, and the carbon content decreased from 77.7 % to 54.7 %. These changes in surface composition represented a changing of the film surfaces to more TiiB-like character. The stoichiometrically calculated weight percent of TiiB is 56.5 % C, 14.1 % Ti, 18.8 % O, and 10.6 % H. After the 30 minute purge, the surface composition was 58.5 % C, 10.2 % Ti, 29.5 % O, and 1.7 % N. The Ti 2p photopeaks, however, remained consistent and indicated the presence of TiO_2.

To determine if the XPS-measured titanium was a result of adsorption, and to investigate the bulk chemistry of the film, an etching experiment was carried out using XPS. Sputtering was accomplished by argon sputtering the sample at 3 keV and 25 mAmps (spot size of 1 cm x 1 cm). XPS spectra were obtained after each etch into the film. The film investigated was deposited on an oxygen plasma cleaned substrate using the following parameters: a treatment time of 11 minutes, an input power of 10 watts, and an argon flow rate of 50 sccm. The PP film was purged with pure argon for 10 minutes following deposition. The thickness of the film was 281 ± 73 Å, as determined by AES.

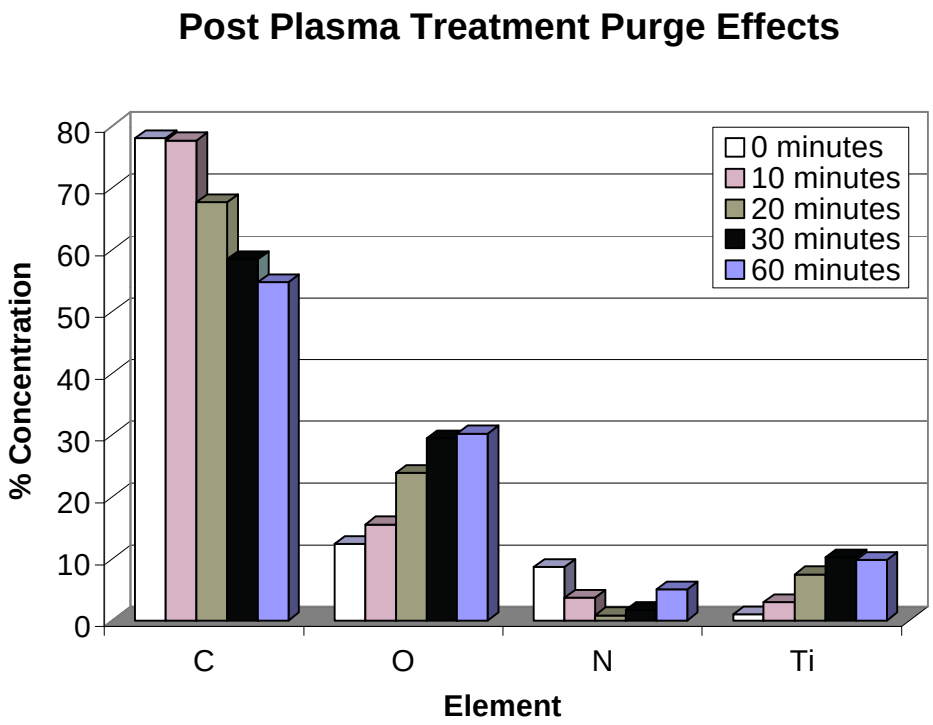

Figure 7.5: Post PP film deposition purge effects.

Figure 7.6 shows the XPS results after etches of 25, 50, 75, 150, and 225 Å into the PP TiiB film. The results should be evaluated discreetly, because ion induced chemical changes from sputtering may have altered the film chemistry. Unfortunately, there was no way to account for this possibility, because even the lowest feasible sputtering energy (1 keV) would be enough to break organic bonds. Therefore, this experiment mostly served to get an idea about the approximate relative elemental concentrations throughout the PP film.

The upper diamond-shaped points represent the percent carbon detected, and they correspond to the right-hand side axis. All of the other data points correspond to the left-hand side axis, and they are appropriately identified in the legend. Along the x-axis is the sputter depth. The surface of the original film is represented by a depth of zero, and as the sputter depth increases, the Ti-6Al-4V substrate is being approached. The lines serve only to guide the eye. As a check of the reproducibility, Figure 7.7 shows the XPS results after etches of 25, 50, 75, 150, 225, and 300 Å into the PP film of a separate sample that was treated simultaneously with the sample discussed above. The observed compositional trends were very similar for the two PP films.

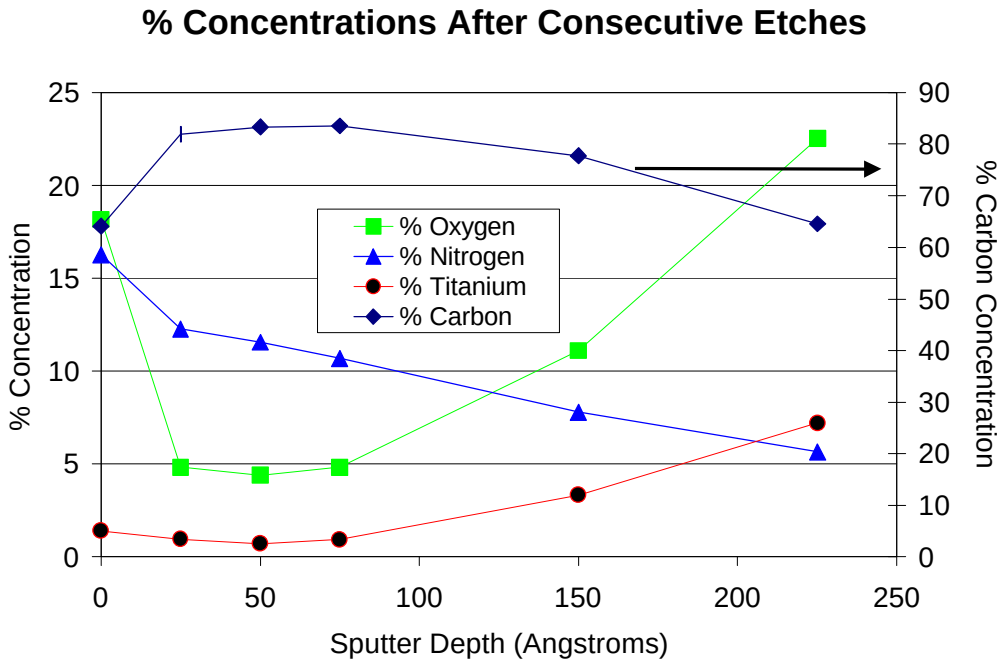

Figure 7.6: Atomic concentrations after consecutive etches, sample 1.

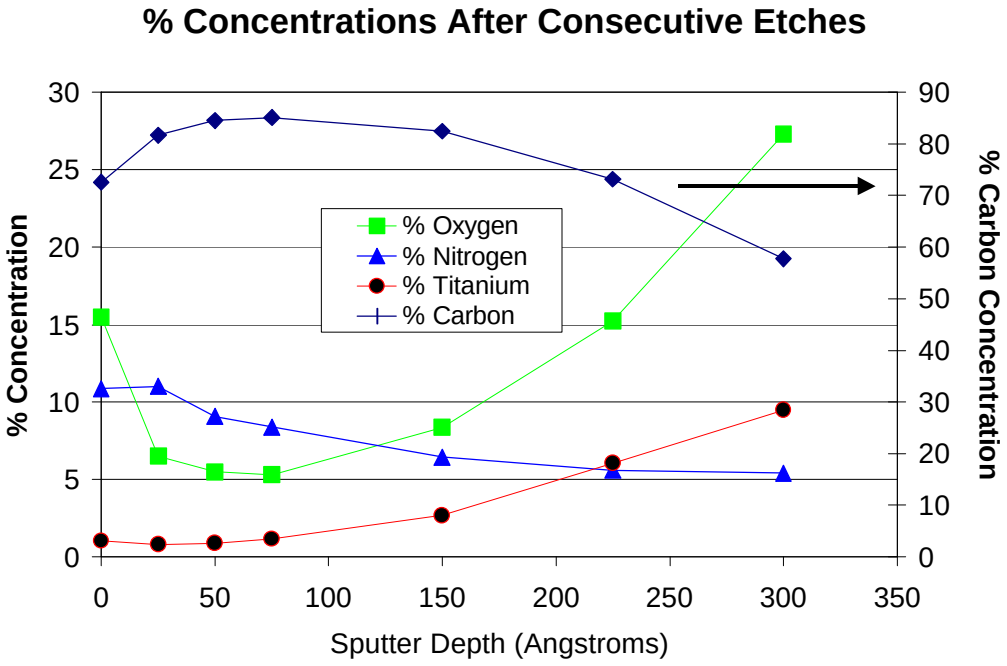

Figure 7.7: Atomic concentrations after consecutive etches, sample 2.

From Figure 7.6, the titanium content decreased from its initial value of ≈ 1.4 % to a low of ≈ 0.8 % after the 50 Å etch. This indicated that, although at a very low level, there was some incorporation of titanium into the bulk of the PP TiiB film. The Ti content increased dramatically after the 150 and 225 Å etches because Ti from the Ti-6Al-4V substrate was being measured as the substrate's surface was being approached. The oxygen content decreased dramatically after the 25 Å etch (from ≈ 18 % to ≈ 5 %), which indicated that the initial oxygen detected was mostly due to the oxidation of organic species at the surface of the PP film. The oxygen content increased after the 75 Å etch because the surface oxide layer on Ti-6Al-4V was being approached.

The nitrogen content also decreased significantly after the 25 Å etch, indicating that some of it was due to reaction with the atmosphere after deposition. However, there was a significant amount of nitrogen throughout the bulk of the film (from ≈ 8 to ≈ 11 %). The pressure during deposition was 30 mTorr, and a small leak in the reactor could have allowed nitrogen from the atmosphere to enter the reactor and incorporate into the organic matrix of the PP film.

Approximately 225 Å into the film, about 7 % titanium was detected, indicating that the PP film/substrate interface was approached. This corresponded well with the AES-determined film thickness (281 ± 73 Å). Figure 7.8 shows the C 1s photopeaks for the etched PP TiiB sample. The electron counts (N(E)/E on the y-axis) of the initial photopeak and the photopeak after the 225 Å etch were shifted for clarity. The initial C 1s photopeak was the broadest due to the high level of contributions from nitrogen (16.3 %) and oxygen (18.2 %). After the 25 Å etch, the C 1s peak narrowed due to decreased nitrogen and oxygen concentrations (see Figure 7.6). The XPS measurements taken after the 25, 50, 75, and 150 Å etches were essentially identical, which implied a consistent composition throughout the bulk. After the 225 Å etch, the intensity of the C 1s peak decreased, as the carbon content dropped approximately 15 % upon approaching the substrate surface.

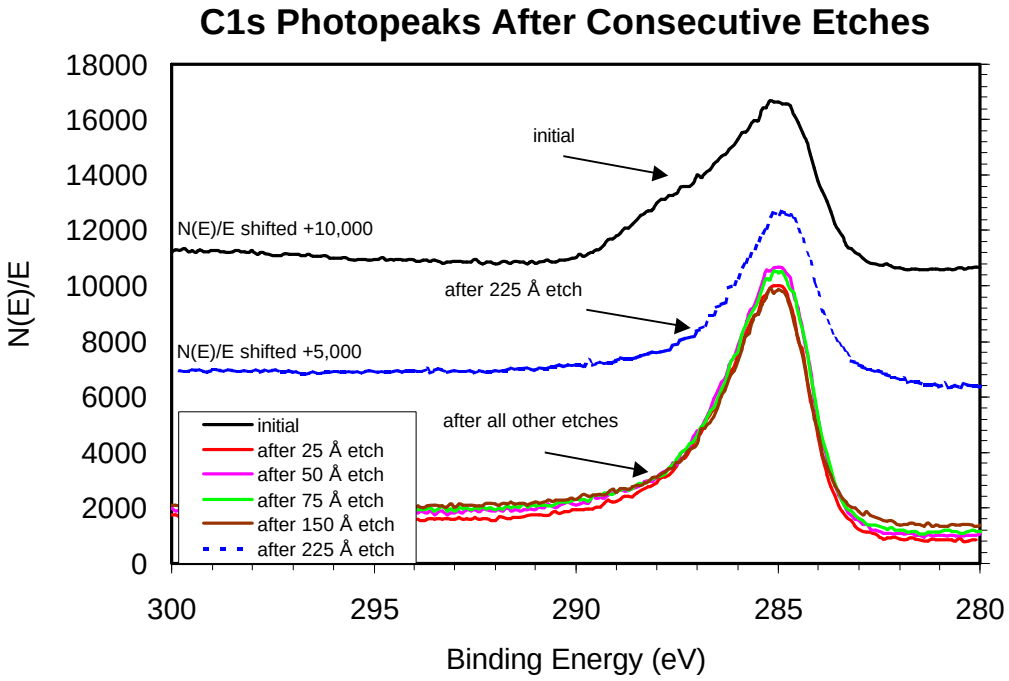

Figure 7.8: C 1s photopeaks after consecutive etches.

Figure 7.9 shows the O 1s photopeaks for the etched PP TiiB sample. The electron counts (N(E)/E) of the initial photopeak were shifted for better clarity. The surface of the PP film was resolved into mostly C=O and C-O components because of the low Ti content. Figure 7.9 differs from the O 1s photopeak of PP TiiB previously discussed (Figure 7.3) primarily because of the differences in titanium incorporated within the two samples (≈ 1.4 % vs. ≈ 4.0 %). After the initial etch, the O 1s photopeak decreased substantially due to the overall decrease in oxygen incorporated into the bulk of the film (see Figure 7.6). The oxygen content after the 25, 50, and 75 Å etches was relatively constant at ≈ 5 %. After the 150 and 225 Å etches, the O 1s photopeak increased in intensity and was shifted to lower binding energy, due to the increasing contributions from TiO_2 (≈ 530.2 eV) as the surface was approached.

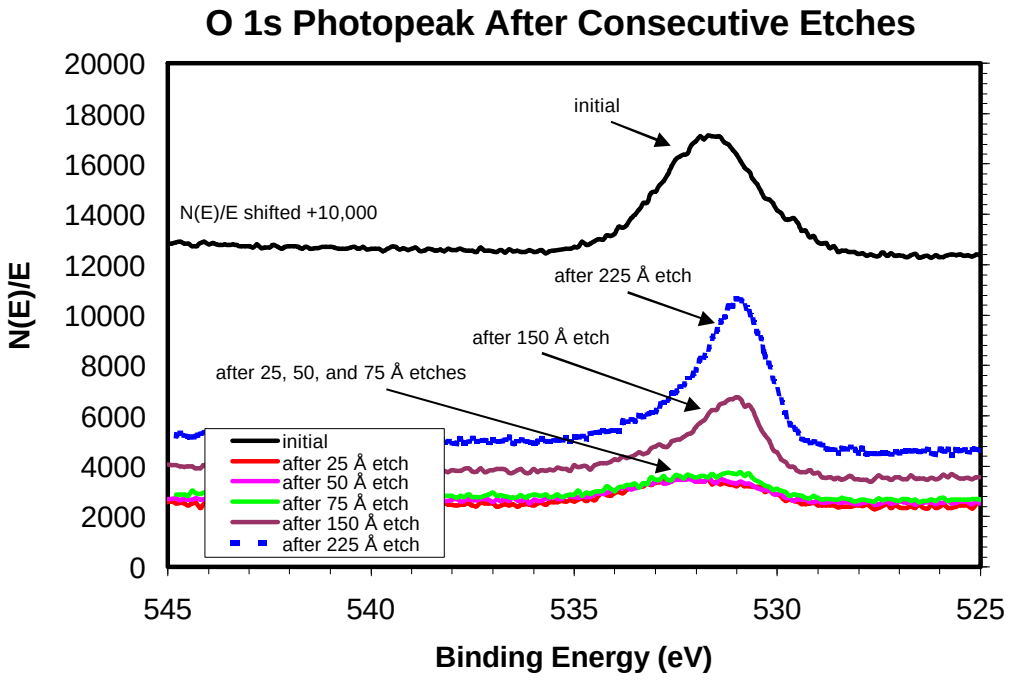

Figure 7.9: O 1s photopeaks after consecutive etches.

The Ti 2p photopeaks after consecutive etches are shown in Figure 7.10. The electron counts of the initial photopeak were shifted for clarity. Initially, the Ti 2p photopeaks were well resolved. However, after the first 25 Å etch, the intensity of the Ti 2p photopeaks was low due to the low Ti content in the bulk of the film. Toward the surface of the Ti-6Al-4V substrate, the Ti 2p photopeaks began to grow and broaden (after the 150 and 225 Å etches). Although the photopeaks could not be resolved exactly, the lower binding energy contributions to the Ti $2p_{3/2}$ photopeak close to the substrate could be due to titanium bonded to oxygen from various titanium suboxides, or titanium carbide (≈ 454.7 - 455 eV).[10, 13, 22] However, the absence of a low binding energy peak in the C 1s spectrum after etching suggests that the existence of Ti-C is unlikely. Reduction of the titanium due to the argon sputtering was probably the cause of broadening of the Ti $2p_{3/2}$ photopeaks. Additionally, TiO_2 is favored thermodynamically over titanium carbide,[22] and because there was 4 times more oxygen than titanium in the starting material, there was ample opportunity for the formation of the more stable TiO_2. However, titanium carbide may play a role as an intermediate.

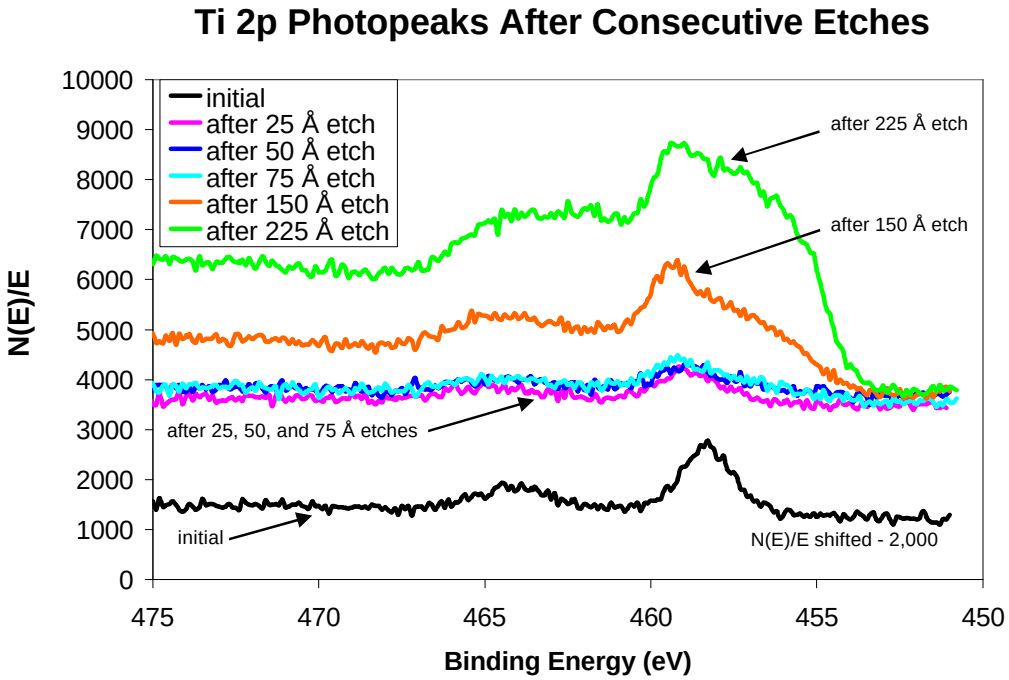

Figure 7.10: Ti 2p photopeaks after consecutive etches.

These experiments served to give a better understanding of the bulk composition of PP TiiB. Titanium was present throughout the PP film and was not simply due to adsorbed titanium species. Additionally, the majority of oxygen detected on the surface was attributed to the oxidation of organic species, and nitrogen was incorporated in the organic matrix throughout the bulk of the film. No decisive evidence was found supporting the presence of titanium carbide.

The literature on the nature of PP film/metal interactions is limited, especially for PP organo-metallics. A study by Grundmeier and Stratmann[23] gave insight into the interfacial processes at the iron oxide/plasma polymer interface. The interpretation of grazing incidence FTIR results and quartz crystal micro balance data suggested that PP hexamethyldisiloxane (HMDS) covalently bonded with the iron oxide substrate during the initial stages of film formation. FTIR peaks such as Si-O-Fe were specific to the plasma zone and indicated covalent bonding. It was hypothesized that these bonds resulted from dangling bonds on the oxide surface. Dangling bonds were caused by the ablation of hydroxyls and their subsequent interaction with silyl radicals that impinged on the surface.[23] Voltage-potential measurements of the plasma

modified surface showed that Fe^{3+} states were partly reduced to Fe^{2+} states during the formation of the initial plasma polymer layers.

Alexander et al[24] investigated the interfacial interactions of PP acrylic acid and an oxidized aluminum surface using XPS and FTIR. They reported FTIR evidence of a monodentate carboxylate complex (-C(=O)-O-Al) at the interface between AlOOH and a monolayer of strongly bonded PP acrylic acid that remained after solvent washing.

Van Ooij et al[25] deposited PP thin films of HMDS and ethylene on cold-rolled steel, electro-galvanized steel, and on polished pure zinc substrates. The film compositions, structures, and the metal-polymer interfacial composition were investigated using FTIR, XPS, and time of flight secondary ion mass spectrometry (TOF-SIMS). The investigators were unable to draw any conclusions regarding the exact nature of the substrate-PP film interactions, but no evidence of any covalent linkages was reported.

Based on the results presented in this study, no clear evidence of any covalent linkages between the metal substrate and the PP film was observed, which suggests that there are independent clusters of TiO_2 dispersed within an organic matrix. The absence of evidence of Ti-C linkages in this study does not entirely preclude the existence of covalent bonding between Ti-6Al-4V and the PP film. For example, Ti-O-C bonds could exist within the film or at the substrate/PP film, and these types of linkages would be much more difficult to discern using XPS. The difficulty arises because C-O photopeaks from the PP film are already present, and the Ti $2p_{3/2}$ photopeak for Ti-O-C ($\approx$ 457.8 eV) would overlap the Ti $2p_{3/2}$ photopeak for TiO_2. Any shoulder due to small amounts of Ti-O-C would therefore be difficult to see.

7.5 SLS Results

The SLS strength results of selected PP TiiB films are discussed as representative samples. The deposition conditions for the PP films are given in Table 7.1. Every sample, except for TiiB.11m.10w.50f.Ar, was pretreated with an oxygen plasma (20 sccm, 50 watts for 1 or 2 minutes) prior to film deposition. Argon was the carrier gas for each deposition, and the treatment time, input power, flow rate, and sample placement varied slightly in each experiment. The XPS, AES, and SLS strength results are given in Table 7.2.

Table 7.1: Film deposition conditions for selected experiments.

Parameter	TiiB.11m. 10w.50f.Ar	TiiB.11m. 10w.50f.Ar (no pretreatment)	TiiB.25m. 25w.25f.Ar (12 cm)	TiiB.25m. 25w.25f.Ar (7 cm)	TiiB.60m. 10w.25f.Ar
TiiB temp. (°C)	70	70	70	70	70
Carrier gas	Argon	Argon	Argon	Argon	Argon
Time (minutes)	11	11	25	25	60
Power (watts)	10	10	25	25	10
Flow rate (sccm)	50	50	25	25	25
Pressure (mTorr)	30	30	82	85	17
Sample distance from coil (cm)	20	20	12	7	7

The XPS results for PP films deposited using the conditions listed in Table 7.1 are given in graphical form in Figure 7.11. The carbon content varied from a low of 54.1 % (TiiB.11m.10w.50f.Ar) to a high of 70.8 % (TiiB.60m.10w.25f.Ar), but the percentage of oxygen stayed relatively constant among the PP films (≈ 19 %). The Ti content ranged from a low of 1.3 % (TiiB.11m.10w.50f.Ar (no pretreatment)) to a high of 4.7 % (TiB.062). The amount of nitrogen incorporated into the films was surprising, and it was believed that atmospheric nitrogen entered the chamber during deposition and was the source of the nitrogen for each film. The shapes for the C 1s photopeaks of the PP films were all similar. The C 1s photopeak of TiiB.60m.10w.25f.Ar was the narrowest because it had the smallest nitrogen content of the five films. TiiB.25m.25w.25f.Ar (12 cm) and TiiB.25m.25w.25f.Ar (7 cm) were identical and a little broader than TiiB.60m.10w.25f.Ar, and they showed typical contributions from C-C/C-H, C-N, C-O, and C=O. The C 1s photopeaks of TiiB.11m.10w.50f.Ar (no pretreatment) and TiiB.11m.10w.50f.Ar were identical and were the broadest of the C 1s photopeaks because they contained the highest nitrogen content of all of the films. The O 1s photopeaks were all fairly similar, and they showed respective contributions related to their TiO_2, C=O and C-O content. The O 1s photopeaks of TiiB.25m.25w.25f.Ar (12 cm), TiiB.25m.25w.25f.Ar (7 cm), and TiiB.60m.10w.25f.Ar were all shifted to lower binding energy as the TiO_2 component (at ≈ 530.2 eV) became more prevalent.

Table 7.2: XPS, AES, and SLS results for selected TiiB experiments.

Sample	% C	% O	% N	% Ti	SLS (MPa)	SLS (psi)	Thickness (Å)
TiiB.11m.10w.50f.Ar	63.0	18.2	17.5	1.3	30.3 ± 3.5	4388 ± 508	281 ± 73
TiiB.11m.10w.50f.Ar (no pretreatment)	54.1	18.6	25.5	1.8	22.4 ± 4.1	3254 ± 589	274 ± 17
TiiB.25m.25w.25f.Ar (12 cm)	64.7	18.9	13.2	3.2	9.03 ± 0.21	1309 ± 31	846 ± 209
TiiB.25m.25w.25f.Ar (7 cm)	63.5	20.0	12.9	3.6	9.39 ± 0.40	1362 ± 58	638 ± 158
TiiB.60m.10w.25f.Ar	70.8	21.0	3.5	4.7	9.51 ± 1.43	1379 ± 208	504 ± 49

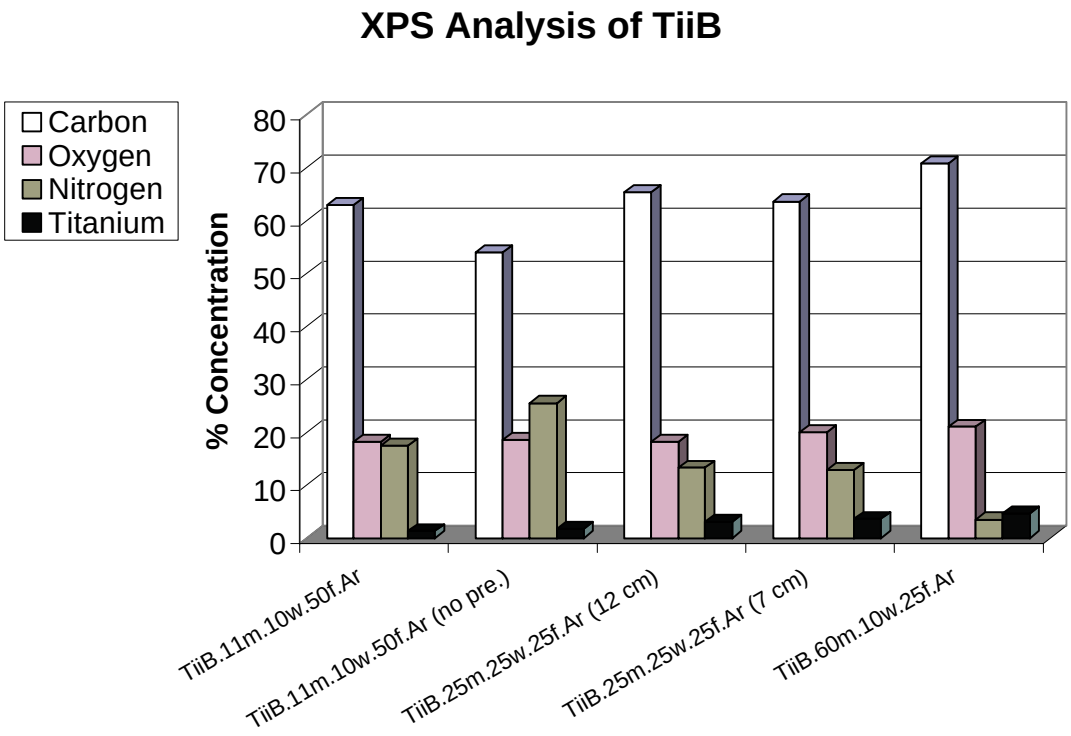

Figure 7.11: XPS analysis for selected PP TiiB films.

Samples TiiB.11m.10w.50f.Ar (no pretreatment) and TiiB.11m.10w.50f.Ar were deposited under identical conditions, except that TiiB.11m.10w.50f.Ar (no pretreatment) was not pretreated with an oxygen plasma prior to film deposition. There was some variation in their surface compositions due to different nitrogen content (17.5 and 25.5 %), and this was reflected

in their respective C 1s photopeaks (not shown). The oxygen plasma pretreatment also affected the SLS strength, as shown in Figure 7.12. The oxygen plasma pretreated samples yielded a SLS strength of 4388 ± 508 psi, while the samples that were not oxygen plasma pretreated yielded SLS strength values of 3254 ± 589 psi. This confirmed results presented in Chapter 6 which showed that an oxygen plasma pretreatment was beneficial to the SLS strength for specimens primed with PP acetylene thin films.

Samples TiiB.25m.25w.25f.Ar (12 cm) and TiiB.25m.25w.25f.Ar (7 cm) were identical, except that the sample positions were varied. As shown in Figure 7.11 and Figure 7.12, the change in sample position from 7 to 12 cm had no effect on the PP film composition or SLS strength. The SLS strengths for TiiB.25m.25w.25f.Ar (12 cm) and TiiB.25m.25w.25f.Ar (7 cm) were 1309 ± 31 and 1362 ± 58 psi, respectively. The C 1s and O 1s photopeaks (not shown) were identical, showing appropriate contributions from C-H/C-C, C-N, C-O, and C=O, and TiO_2 groups.

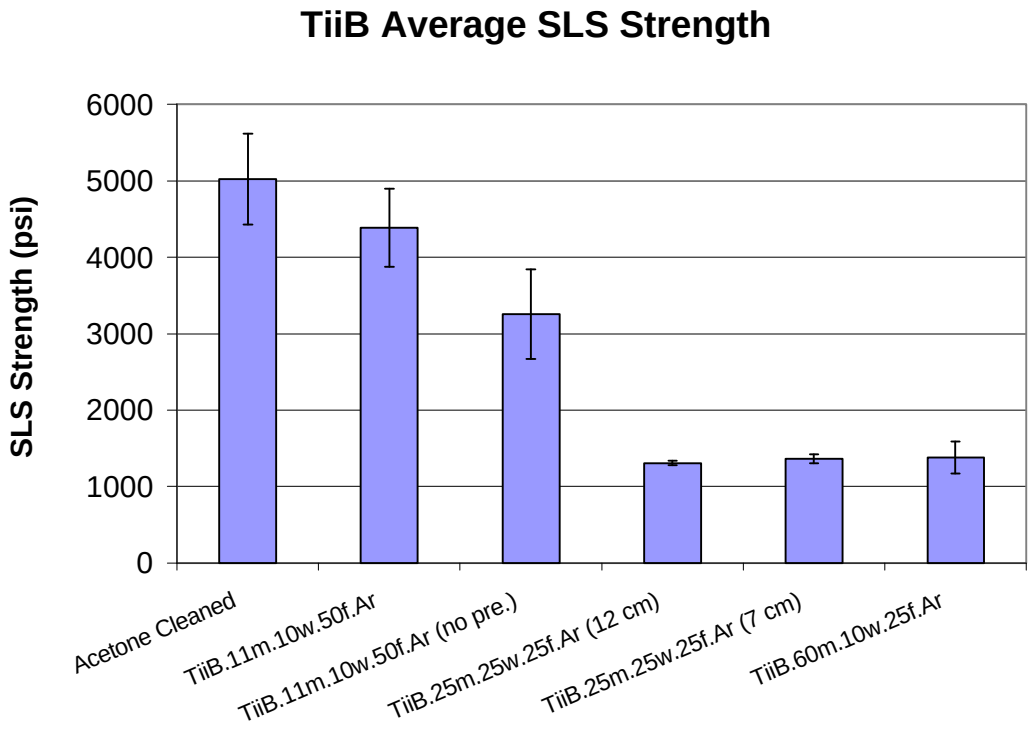

Figure 7.12: Average SLS strength for selected TiiB samples.

There was no correlation among the data of thickness-normalized Ti content with SLS strength. There was a correlation between the thickness-normalized carbon content and SLS strength, as shown in Figure 7.13. As the amount of carbon increased, the SLS strength increased, indicating that more carbon-like films were better adhesion promoters. This trend correlated well with results discussed in Chapter 6, where the SLS strength of PP acetylene-primed specimens also increased with % carbon content/thickness.

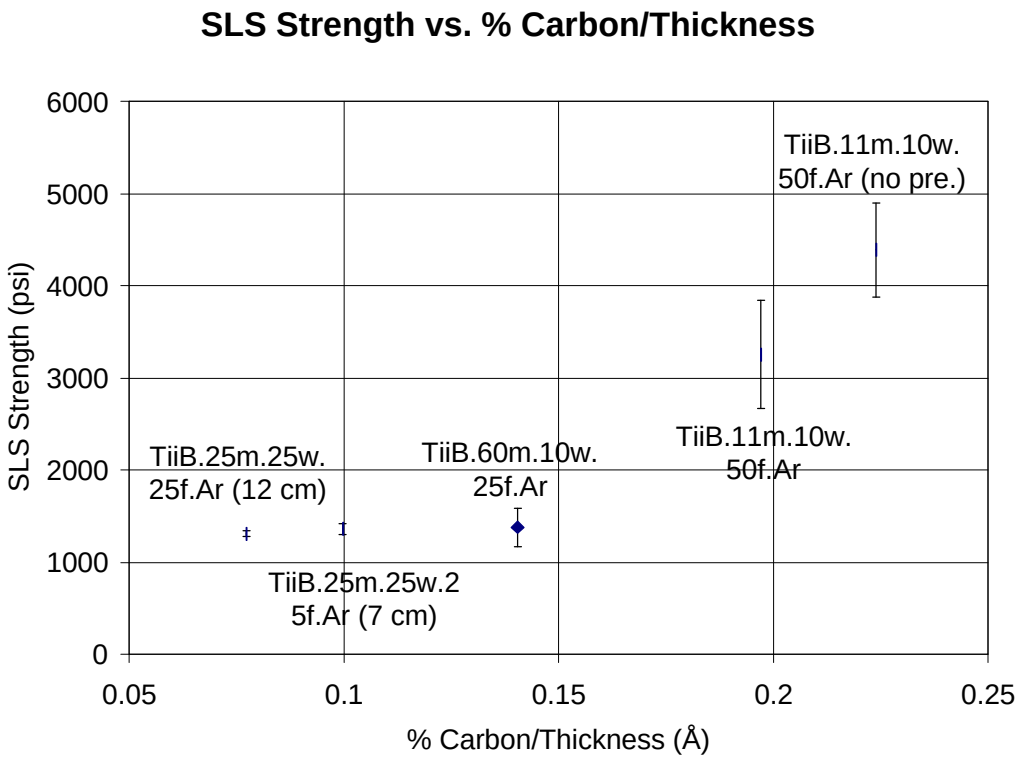

Figure 7.13: SLS strength vs. thickness-normalized carbon content.

The failure mode of each of the SLS joints discussed above was determined using XPS as described in Chapter 4. In every case, failure occurred at the PP film/substrate interface. As was the case for PP acetylene, the adhesion of PP TiiB to the adhesive was adequate, but the interactions between the substrate and the PP film limited the SLS strength.

7.6 Nanomechanical Properties

7.6.1 Experimental

Hardness and modulus values were obtained for PP TiiB deposited on polished Ti-6Al-4V (TiiB.60m.10w.25f.Ar.Ti) and silicon (TiiB.60m.10w.25f.Ar.Si) substrates using the method described in Chapter 3. The PP films were deposited simultaneously on the two substrates in the same reaction chamber. The films were deposited on oxygen plasma pretreated substrates using argon as the carrier gas (25 sccm), a treatment time of 60 minutes, and an input power of 10 watts. The samples were placed on the bottom of the reactor approximately 12 cm from the induction coil. The pressure during deposition was 17 mTorr, and the reactor chamber was purged with oxygen for 5 minutes following deposition. The maximum indentation loads were 35 and 15 μN for PP TiiB on polished Ti-6Al-4V and PP TiiB on silicon, respectively. Ramp force scratches with a maximum load of 200μN were performed using a <1 μm conical diamond tip.

7.6.2 Nanoindentation

The XPS and AES data for the two samples are presented in Table 7.3. Notice that the film compositions were very similar. The nitrogen content was lower for these samples compared to those previously discussed because the pressure during deposition was considerably lower (≈ 17 mTorr vs. >30 mTorr). The major difference between the PP films deposited on the different substrates here was that the carbon content was lower and the oxygen content was higher for the PP film on polished Ti-6Al-4V. The higher titanium content, as TiO_2, translated into a higher amount of oxygen and a lower amount of carbon. This was confirmed by the C 1s curve-fit photopeaks, which are shown in Figure 7.14 and Figure 7.15. The curve-fit C 1s photopeak for TiiB.60m.10w.25f.Ar.Ti (Figure 7.14) was resolved into contributions from C-C/C-H (285.0 eV), C-N (286.0 eV), C-O (286.6 eV), and C=O (288.1 eV). The curve-fit C 1s photopeak for TiiB.60m.10w.25f.Ar.Si (Figure 7.15) was similar to that of

TiiB.60m.10w.25f.Ar.Ti, except for slight differences that arose from oxygen assignments. Table 7.4 lists the C 1s curve fit assignments and photopeak percentages. They agree well with the curve-fit O 1s photopeaks (Table 7.5).

Table 7.3: XPS comparison of surface compositions.

Sample	Film thickness (Å)	% C	% O	% N	% Ti
TiiB.60m.10w.25f.Ar on polished Ti-6Al-4V	500 ± 50	70.8	21.0	3.5	4.7
TiiB.60m.10w.25f.Ar on silicon wafer	380 ± 40	76.1	16.6	4.4	2.9

Table 7.4: Peak assignments for curve-fit C 1s photopeaks for TiiB.60m.10w.25f.Ar.Ti and TiiB.60m.10w.25f.Ar.Si.

Sample	% C-H/C-C	% C-N	% C-O	% C=O
TiiB.60m.10w.25f.Ar.Ti	83.8	4.2	5.9	6.1
TiiB.60m.10w.25f.Ar.Si	79.4	5.6	9.4	5.6

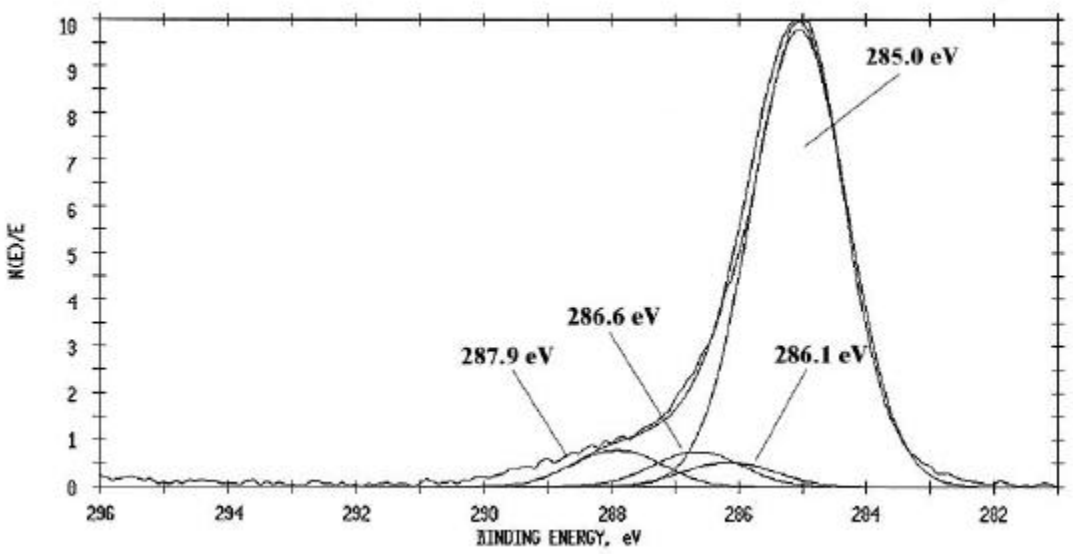

Figure 7.14: Curve-fit C 1s photopeak for TiiB.60m.10w.25f.Ar.Ti.

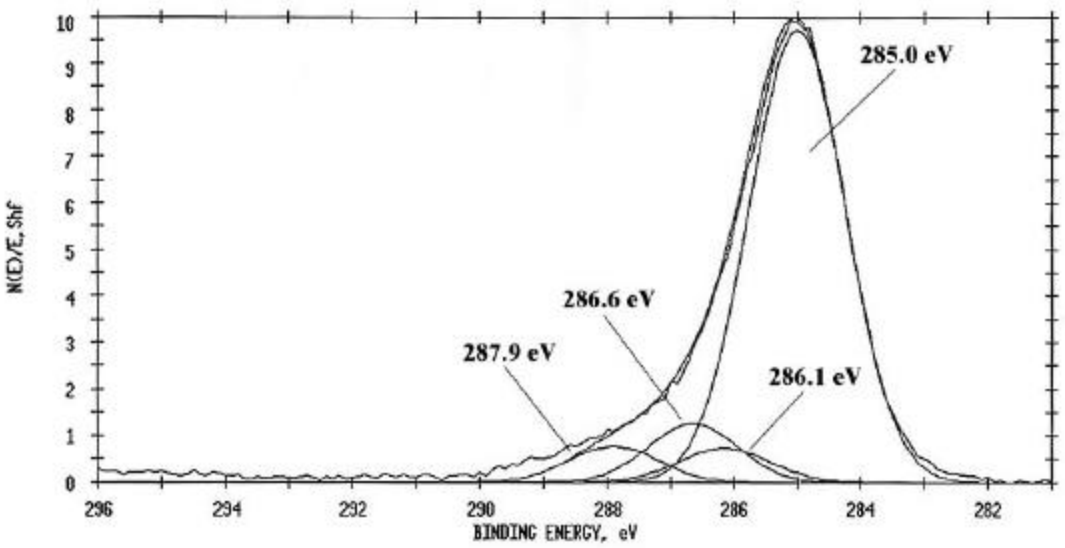

Figure 7.15: Curve-fit C 1s photopeak for TiiB.60m.10w.25f.Ar.Si.

Table 7.5: Peak assignments for curve-fit O 1s photopeaks for TiiB.60m.10w.25f.Ar.Ti and TiiB.60m.10w.25f.Ar.Si.

Sample	% Ti-O	% C=O	% C-O
TiiB.60m.10w.25f.Ar.Ti	49.7	22.9	27.4
TiiB.60m.10w.25f.Ar.Si	32.1	22.0	45.9

The O 1s photopeaks are shown in Figure 7.16 and Figure 7.17. The low binding energy photopeak at 530.4 eV in Figure 7.16 is typical of oxygen bonded to titanium,[26] and it was the major contributor (49.7 %) to the total O 1s photopeak. The photopeaks at 531.8 eV (22.9 %) and 532.9 eV (27.4 %) were due to the carbonyl and ether contributions, respectively. The O 1s photopeak of TiiB.60m.10w.25f.Ar.Si showed contributions from the same types of oxygen species as TiiB.60m.10w.25f.Ar.Ti, with only very slight shifts in the photopeak positions. However, the intensity of the photopeaks from the various species was substantially different. Compared to Figure 7.16, the oxygen photopeak due to TiO_2 at 530.4 eV decreased to 32.1 % of the total area, and the C-O photopeak at 532.7 eV increased to 45.9 % of the total area. This was consistent with the lower TiO_2 content of TiiB.60m.10w.25f.Ar.Si (2.9 % compared to 4.7 %), and the larger C-O contribution resolved from the C 1s photopeak of TiiB.60m.10w.25f.Ar.Si (12.4 % compared to 9.7 %).

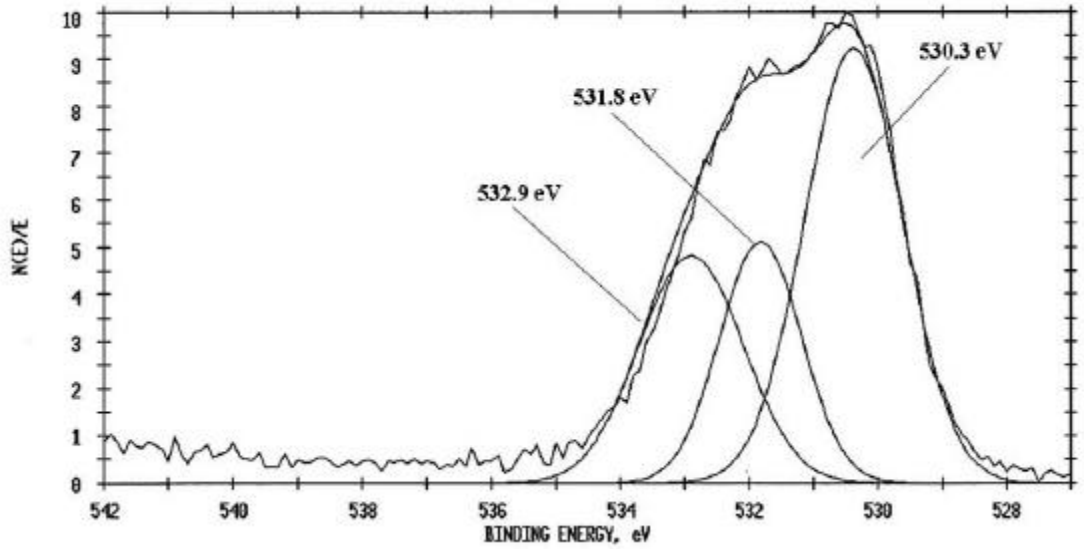

Figure 7.16: Curve-fit O 1s photopeak for TiiB.60m.10w.25f.Ar.Ti.

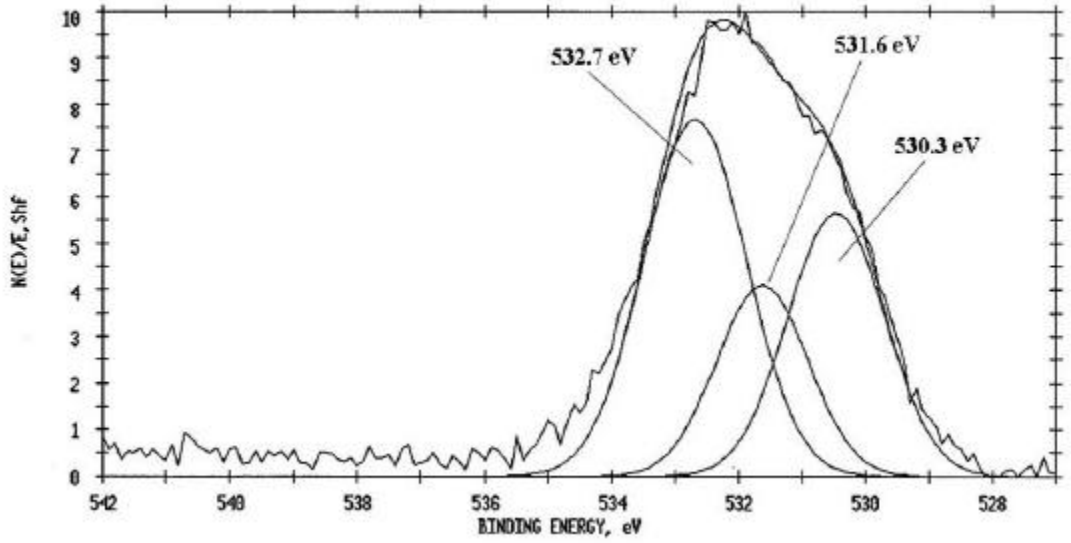

Figure 7.17: Curve-fit O 1s photopeak for TiiB.60m.10w.25f.Ar.Si.

An XPS comparison of the Ti 2p photopeaks of the PP TiiB films is shown in Figure 7.18. The characteristic photopeaks at 458.7 eV and 464.4 eV are from the $2p_{3/2}$ and $2p_{1/2}$ contributions, respectively. The separation of 5.7 eV between the $2p_{3/2}$ and $2p_{1/2}$ peaks is

characteristic of titanium in the +4 oxidation state, as in TiO_2.[26] This was consistent with information from the C 1s and O 1s curve-fit photopeaks, and suggested that independent clusters of TiO_2 were dispersed throughout a carbon matrix. Although TiiB.60m.10w.25f.Ar.Ti contained a slightly higher amount of titanium (4.7 %) than TiiB.60m.10w.25f.Ar.Si (2.9 %), neither sample showed any evidence of elemental titanium metal, which typically appears between 454 and 455.0 eV.[1, 13]

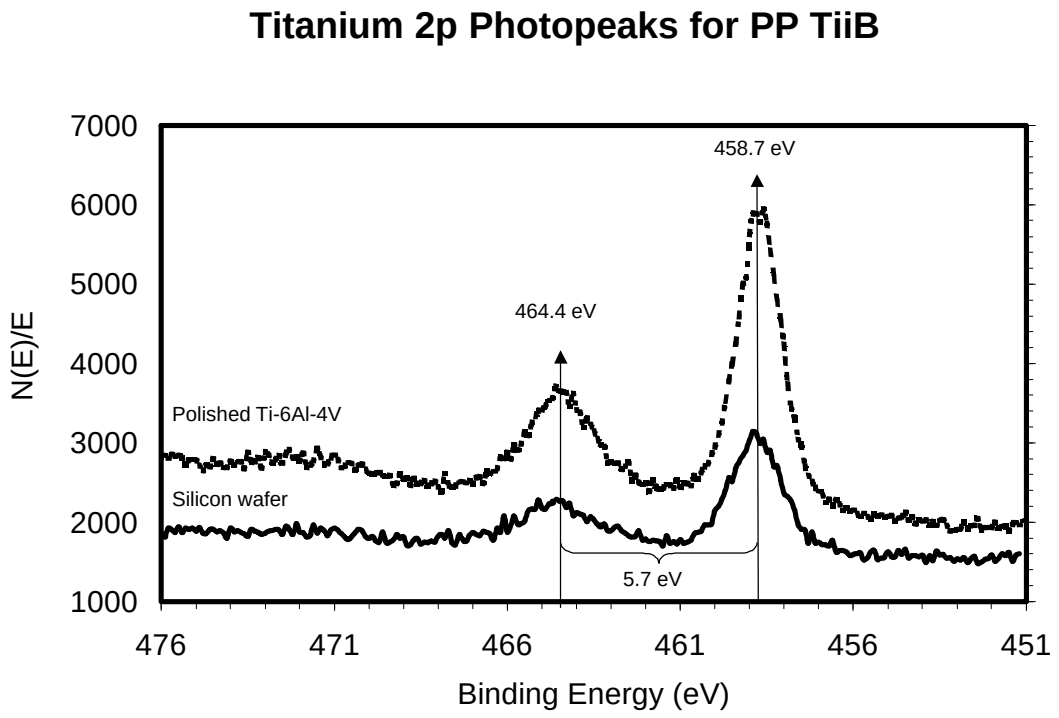

Figure 7.18: Titanium 2p photopeaks for TiiB.60m.10w.25f.Ar on polished Ti-6Al-4V and silicon.

The Auger depth profile of TiiB.60m.10w.25f.Ar.Ti is shown in Figure 7.19. The AES-determined film thickness was 500 Å for TiiB.60m.10w.25f.Ar.Ti and 380 Å for TiiB.60m.10w.25f.Ar.Si. The substrate affected the deposition rate of PP TiiB similarly to the way it affected PP acetylene; the PP film grew at a faster rate on the polished Ti-6Al-4V. This was probably a roughness effect or due to the differences in surface chemistry of the two bare substrates. The polished titanium alloy was rougher than the silicon wafer, and this may aid nucleation at the beginning of and throughout film formation.[27]

Note in Figure 7.19 the large oxygen peak that appeared at the PP film/substrate interface (≈ 510 Å). The thickness of the oxide layer on this sample, which was approximately 70 Å, was consistent with AES results reported in Chapter 4 for oxygen plasma treated polished Ti-6Al-4V. These substrates were pretreated with an oxygen plasma prior to film deposition, and this depth profile confirmed that the PP TiiB film was deposited on TiO_2, rather than on bare titanium metal. The AES of the PP film deposited onto silicon (not shown) showed a much smaller oxygen peak at the film/substrate interface, because the oxide layer on the silicon wafer was much thinner (≈ 6 Å from Chapter 4).

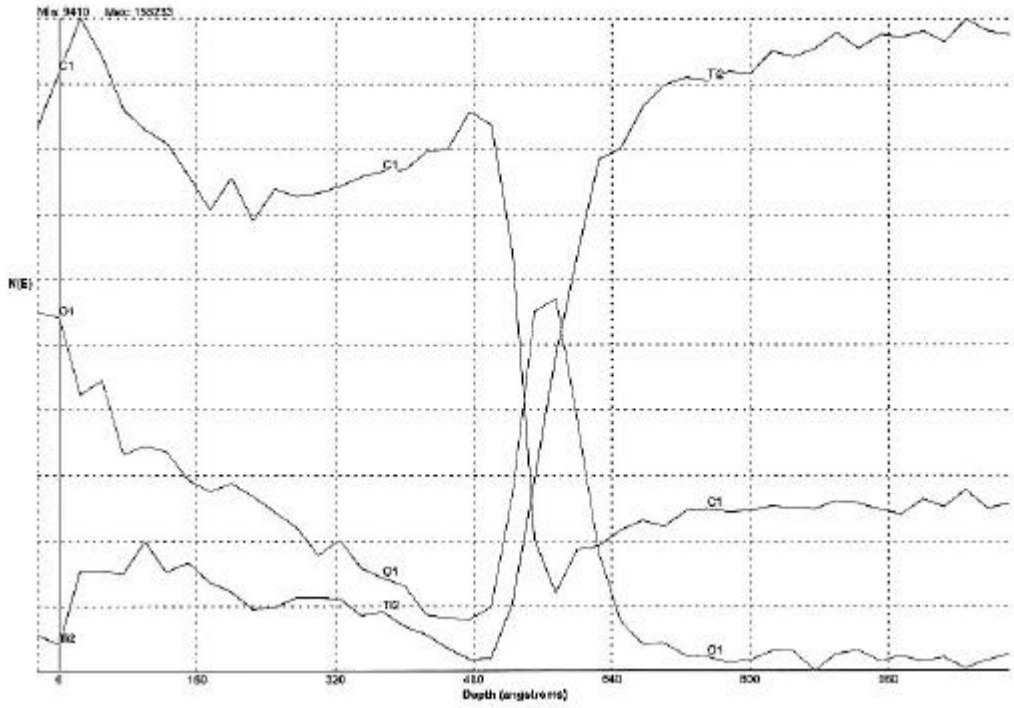

Figure 7.19: AES depth profile for TiiB.60m.10w.25f.Ar on polished Ti-6Al-4V.

The mechanical properties of the PP films from the nanoindentation tests are presented in Table 7.6. The hardness values of the films were 3.35 and 1.16 GPa for TiiB.60m.10w.25f.Ar.Ti and TiiB.60m.10w.25f.Ar.Si, respectively. These films were softer than the PP acetylene films prepared at 10 watts that were reported in Chapter 6 (Ac.130s.10w.f10.Ti and Ac.130s.10w.f10.Si). Recall that PP acetylene on polished Ti-6Al-4V had a hardness and reduced Young's modulus of 4.7 and 72.9 GPa, respectively, while PP acetylene on silicon had a hardness and reduced Young's modulus of 5.87 and 91.7 GPa, respectively. These values are also

given in Table 7.6 for comparison. Unlike the PP films of acetylene, the two PP films of TiiB had compositional differences (% C, % O, and % Ti) that probably influenced their mechanical properties.

The PP film with the higher TiO_2 content (TiiB.60m.10w.25f.Ar.Ti) was the harder material and also had the higher reduced Young's modulus. The reduced Young's modulus values for the two films were 75 and 32 GPa for TiiB.60m.10w.25f.Ar.Ti and TiiB.60m.10w.25f.Ar.Si, respectively. The other significant difference between the PP TiiB films was the C-O content, as resolved from the curve-fit O 1s photopeaks. TiiB.60m.10w.25f.Ar.Ti and TiiB.60m.10w.25f.Ar.Si had C-O contributions to their O 1s photopeaks of 27.4 and 45.9 %, respectively. This difference may have contributed to the differences in mechanical properties of the films in ways not fully understood.

Table 7.6: Hardness and reduced modulus values from nanoindentation tests.

Sample	H (GPa)	Std. Dev. (GPa)	E_r (GPa)	Std. Dev. (GPa)	h_c (Å)	Std. Dev. (Å)	h_c/ thickness
TiiB.60m.10w.25f.Ar.Ti	3.35	0.70	75.09	11.84	82.4	15	0.165
TiiB.60m.10w.25f.Ar.Si	1.16	0.21	32.26	6.17	96.3	13	0.253
Ac.130s.10w.f10.Ti*	4.70	0.34	72.9	5.1	134	8	0.246
Ac.130s.10w.f10.Si*	5.87	0.31	91.7	1.6	110	5	0.256

*Values from Chapter 6.

7.6.3 Nanoscratch Tests

Scratch tests performed on both PP TiiB films were unsuccessful because the films were too soft to produce a clear debonding event. Therefore, scratch testing was unable to determine critical loads at debond.

Figure 7.20 shows the results of the 8 μm ramp force scratch test on TiiB.60m.10w.25f.Ar.Si. A change in normal displacement was observed as the indenter tip moved through the PP film to the substrate surface at approximately 400 Å. This was marked with the vertical red line on the right-hand side plot of Figure 7.20. This event corresponded well

with the AES-determined thickness for TiiB.60m.10w.25f.Ar.Si (380 ± 40 Å). Unfortunately, the change was too gradual to cause a true debonding event. The change was caused because the substrates were significantly harder than the films. The surprising complaince of these films is thought to be due to the low input power (10 watts) of deposition and the large molecular weight of the starting material. In order to achieve comparable conditions, according to Yasuda,[28] the discharge power (W) must be increased as the flow rate of monomer increases and/or as the molecular weight of the monomer increases. Compared to acetylene, the molecular weight of the starting material (TiiB) was approximately 13 times larger. Because of the high molecular weight, the input power was insufficient to thoroughly fragment the TiiB, and this probably led to a film that was not very highly crosslinked. This also resulted in PP films that more closely resembled the starting material. Neat, hydrolyzed TiiB in its hydrated solid state is quite soft and compliant.

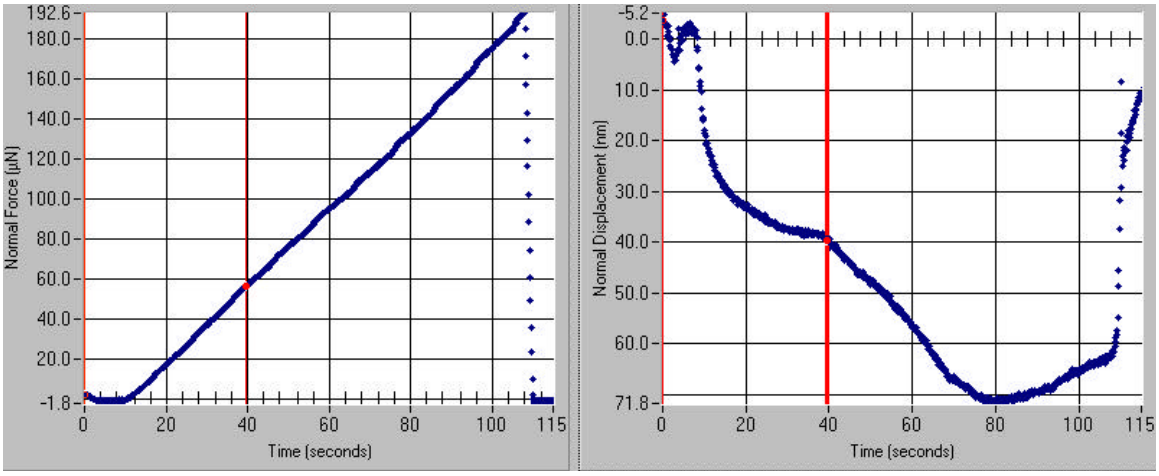

Figure 7.20: Results of an 8 µm ramp force scratch test, peak force 200 µN, on TiiB.60m.10w.25f.Ar.Si.

Figure 7.21 and Figure 7.22 show the in situ topographic images of scratches in TiiB.60m.10w.25f.Ar.Ti and TiiB.60m.10w.25f.Ar.Si, respectively. The lighter regions in the AFM micrographs represent raised features, and ploughing was evident as the tip was driven into the film (moving from the top to the bottom of the micrograph). TiiB.60m.10w.25f.Ar.Si, which was the softer of the two samples, showed ploughing from almost the beginning of the scratch, and overall, TiiB.60m.10w.25f.Ar.Si showed much more ploughing than TiiB.60m.10w.25f.Ar.Ti. This corresponded to the hardness data, which showed that TiiB.60m.10w.25f.Ar.Si was softer than TiiB.60m.10w.25f.Ar.Ti.

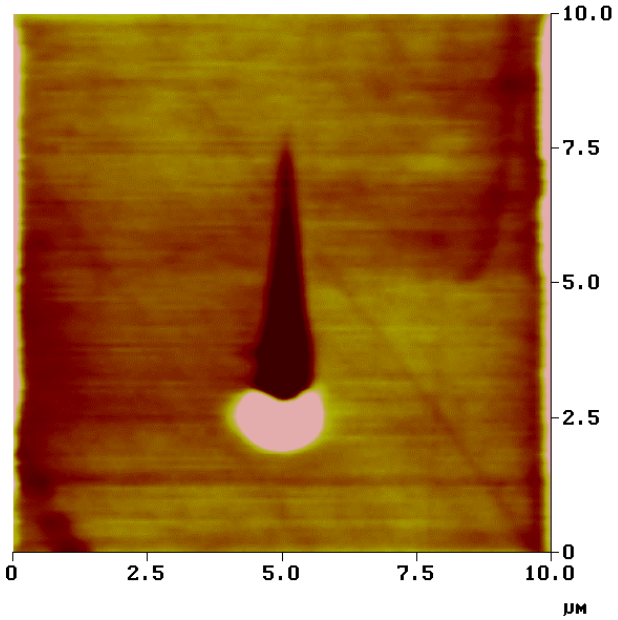

Figure 7.21: In situ topographic image of a scratch in TiiB.60m.10w.25f.Ar.Ti.

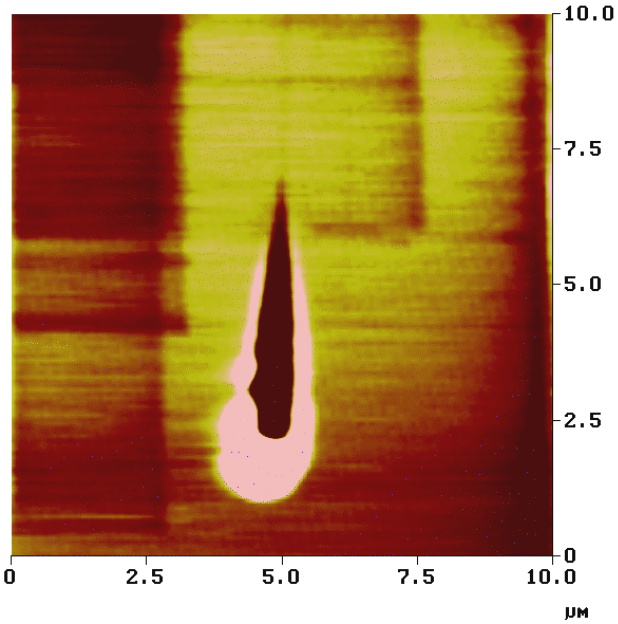

Figure 7.22: In situ topographic image of a scratch in TiiB.60m.10w.25f.Ar.Si

7.7 Conclusions

Novel films exhibiting the benefits of traditional sol/gel thin films were sought in a rapid, efficient plasma polymerization process. Thin films were developed via the vapor plasma polymerization of titanium(IV) isobutoxide, and their chemical, mechanical, and adhesion-promoting properties were investigated.

Heating the organo-metallic starting material (70 °C) was needed for PP film deposition, and argon was an adequate carrier gas. XPS analysis revealed that deposited films were mostly organic in nature; typical films were composed of ≈ 65 % carbon, ≈ 17 % oxygen, ≈ 12 % nitrogen, and ≈ 4 % titanium. The source of the nitrogen was unknown, but was thought to be due to atmospheric nitrogen that entered the plasma through a leak in the reactor. XPS C 1s, O 1s, and Ti 2p photopeaks suggested that titanium was incorporated into the film as TiO_2 dispersed in an organic matrix, and there was no collaborating evidence among the photopeaks for any Ti-C linkages.

An XPS profile of an 300 Å thick film showed that most of the oxygen detected from the initial XPS results was due to surface oxidation of the film; the bulk of the film contained approximately 5 % oxygen. Conversely, a significant amount of nitrogen was present throughout the film. The titanium content decreased in the bulk of the film, but approximately 1 % was still detectable in the bulk. As the surface of the Ti-6Al-4V substrate was approached, the carbon content decreased drastically, while the oxygen and titanium content increased. The Ti 2p photopeaks near the substrate surface broadened and shifted to lower binding energy, but there was insufficient evidence to assert the existence of Ti-C linkages at the Ti-6Al-4V/PP TiiB interface. Because a Ti-C low binding energy C 1s photopeak did not emerge simultaneous to the broadening of the Ti $2p_{3/2}$ photopeak, this change was probably due to argon ion-induced reduction of the titanium.

The SLS strength results of selected experiments illustrated that PP TiiB - primed specimens did not perform as well as acetone cleaned specimens. The best SLS strength was obtained from specimens primed with a PP TiiB film deposited using an input power of 10 watts, an argon flow rate of 50 sccm, and a deposition time of 11 minutes. The film thickness was 281 ± 73 Å, and the SLS strength was 4388 ± 508 psi. An additional finding was that films with a

higher carbon content were better adhesion promoters, as discussed in Chapter 6. The failure mode of all samples pretreated with PP TiiB was interfacial at the PP film/substrate interface.

The nanomechanical properties of PP TiiB films deposited on polished Ti-6Al-4V and silicon were measured. The hardness and reduced Young's modulus of PP TiiB on polished Ti-6Al-4V was 3.4 and 75.1 GPa, respectively. The hardness and reduced Young's modulus of PP TiiB on the silicon oxide wafer was 1.2 GPa and 32.3 GPa, respectively. The PP TiiB film on polished Ti-6Al-4V was harder and had a higher modulus than the same film prepared on silicon wafers, confirming that substrate had an effect on the film composition, which affected PP film properties. PP TiiB on polished Ti-6Al-4V contained a higher content of TiO_2, and this appeared to be the reason for its higher modulus and hardness. The PP films of TiiB were much more compliant than PP acetylene films, and this was hypothesized to be due to the decreased fragmentation and thus crosslinking that occurred during PP TiiB film deposition. Scratch tests were performed on both of the PP TiiB samples, but the films were too soft to obtain a critical load at debond.

Based on the characterization of these PP thin films, they do not seem to exhibit sol-gel like qualities as was expected. Because of the way that titanium is suspected of incorporating itself into the films, a more appropriate name for these films might be "titanium dioxide-doped plasma polymerized films."

7.8 References

[1] N. Inagaki; S. Tasaka; Y. Nozue *J. Appl. Polym. Sci.* **1992**, *45*, 1041.
[2] C.R. Wold; M.D. Soucek *J. Coat. Technol.* **1998**, *70*, 43.
[3] K.Y. Blohowiak *Proc. Int. SAMPE Tech. Conf.* **1996**, *28*, 440.
[4] H. Zheng *Proc. Int. SAMPE Tech. Conf.* **1996**, *28*, 447.
[5] P.P. Tzaskomapaulette; A. Naseri *J. Electrochem. Soc.* **1997**, *144*, 1307.
[6] T. Sugama; L.E. Kukacka; N. Carciello *Prog. Org. Coat.* **1990**, *18*, 173.
[7] T. Sugama; C. Taylor *J. Mater. Sci.* **1992**, *27*, 1723.
[8] P.J. Ratcliffe; J. Hopkins; A.D. Fitzpatrick; C.P. Barker; J.P.S. Badyal *J. Mater. Chem.* **1994**, *4*, 1055.
[9] H.J. Frenck; W. Kulish; M. Kuhr; R. Kassing *Thin Solid Films* **1991**, *201*, 327.
[10] Y. Kagami; T. Amauchi; Y. Osada *J. Appl. Phys.* **1990**, *68*, 610.
[11] F.S. Ohuchi; S.C. Freilich *J. Vac. Sci. Technol. A* **1986**, *4*, 1039.
[12] F.S. Ohuchi; S.C. Freilich *Polymer* **1987**, *28*, 1908.

[13] C.D. Wagner; W.M. Riggs; L.E. Davis; J.F. Moulder; G.E. Muilenburg *Handbook of X-Ray Photoelectron Spectroscopy*; Perkin-Elmer: Eden Prairie, MN, 1979, p. 69.
[14] Y. Kagami; T. Amauchi; Y. Osada *J. Appl. Phys.* **1990**, *68*, 610.
[15] M. Murata; K. Wakino; S. Ikeda *J. Electron. Scpectrosc. Relat. Phenom.* **1975**, *6*, 459.
[16] C.D. Wagner; L.H. Gale; R.H. Raymond *Anal. Chem.* **1979**, *51*, 466.
[17] S. Ben Amor; G. Baud; M. Benmalek; H. Dunlo; R. Frier; M. Jacquet *J. Adhes.* **1998**, *65*, 307.
[18] K.L. Siefering; G.L. Griffin *J. Electrochem. Soc.* **1990**, *137*, 814.
[19] Y-M. Wu; D.C. Bradley; R.M. Nix *Appl. Surf. Sci.* **1993**, *64*, 21.
[20] Y. Osada; K. Yamada; I. Yoshizawa *Thin Solid Films* **1987**, *151*, 71.
[21] H. Yasuda; T. Yasuda *J. Polym. Sci.: Part A: Polym. Chem.* **2000**, *38*, 943.
[22] K. Konstadinidis; R.L. Opila; J.A. Taylor; A.C. Miller *J. Adhes.* **1994**, *46*, 197.
[23] G. Grundmeier; M. Stratmann *Thin Solid Films* **1999**, *352*, 119.
[24] M.R. Alexander; S. Payan; T.M. Duc *Surf. Interfac. Anal.* **1998**, *26*, 961.
[25] W.J. van Ooij; F.J. Boerio; A. Sabata; D.B. Zeik; C.E. Taylor; S.J. Clarson *J. Test. Eval.* **1995**, *23*, 33.
[26] S.B. Amor; G. Baud; M. Benmalek; H. Dunlop; R. Frier; M. Jacquet *J. Adhes.* **1998**, *65*, 307.
[27] N.R. Moody; D. Medlin; D. Boehme; D.P. Norwood *Eng. Fracture Mech.* **1998**, *61*, 107.
[28] H. Yasuda *Plasma Polymerization*; Academic Press: Orlando, FL, 1985, Chapter 9.

8.0 Overall Summary

An examination of the feasibility of utilizing plasma processes to enhance the performance of the Ti-6Al-4V/FM-5 adhesive joint has been carried out. The effects of plasma pretreatments on surface chemistry were studied using x-ray photoelectron spectroscopy (XPS), Auger electron spectroscopy (AES), Fourier Transform Infrared analysis (FTIR), and contact angle measurements. The nanomechanical properties (modulus, hardness and adhesion) were studied using atomic force microscopy (AFM) nanoindentation and nanoscratch testing. Relationships between composition, mechanical properties, and adhesion of plasma polymerized (PP) films were investigated and discussed.

A design of experiments (DOE) three factorial model was used to optimize the parameters for oxygen plasma pretreatments. The effects of varying treatment time, input power, and oxygen flow rate were studied. One-step oxygen plasma pretreatments enhanced joint strength by cleaning the titanium surface and creating an extended oxide layer. Interaction graphs showed that interactions between the treatment time and flow rate, and interactions between flow rate and input power were significant, so the effects of these parameters should not be considered individually. The model suggested that at low flow rates, SLS strength was optimized using low input power and short treatment times. At high flow rates, the SLS strength was optimized by using high input power and high treatment times. Visual analysis and XPS results confirmed that the failure mode was partially cohesive for oxygen plasma treated-bonded specimens. For the portion of the failure mode that was interfacial, the crack propagated along the adhesive/TiO_2 interface. AFM nanoindentation of oxygen plasma treated substrates showed essentially no change in the surface mechanical properties due to the oxygen plasma treatment. This suggested that the improved SLS strength of the oxygen plasma pretreated substrates was due to the cleaning of the substrate and the removal of carbonaceous contaminants, rather than any changes in the morphology of the oxide layer.

The compositions of thin films prepared from PP acetylene were predominantly carbon. Oxygen (incorporated mostly as C-O and C=O) and nitrogen were also present within the films. XPS and FTIR spectra of the PP films were consistent with literature reports. For all SLS specimens tested, the adhesion between PP acetylene and FM-5 adhesive was never a problem.

However, the strength of SLS joints was limited by the adhesion of the PP acetylene to the Ti-6Al-4V substrate. The effects of a large number of plasma parameters, such as substrate pretreatment, carrier gas, input power, flow rate and film thickness were investigated. All samples failed at the PP film/Ti-6Al-4V interface or within the PP acetylene film, and thicker PP films yielded lower SLS strengths.

On both polished Ti-6Al-4V and silicon wafers, PP films deposited at lower power exhibited higher hardness and reduced modulus than films deposited at higher power. At both power levels, PP films deposited on silicon exhibited higher hardness and reduced modulus values than PP films deposited on polished Ti-6Al-4V. Overall, thinner films exhibited higher hardness and reduced Young's modulus than thicker films. The PP films of higher hardness yielded higher critical loads at debond (thickness normalized) during the nanoscratch test. For both substrates, the hardness and reduced modulus values for the PP films decreased due to annealing because of the relaxation of stresses within the films. Thicker films yielded a higher hardness and reduced modulus after annealing, in contrast to the trend that was noted for non-annealed PP films. This was thought to be a result of the higher degree of crosslinking that the thicker films underwent compared to thinner films. For annealed PP films, films of higher hardness yielded higher critical loads at debond (thickness normalized).

Films exhibiting the benefits of traditional sol/gel thin films were sought in a rapid, efficient plasma polymerization process. Thin films were developed via the vapor plasma polymerization of titanium(IV) isobutoxide (TiiB), and their chemical, mechanical, and adhesion-promoting properties were investigated. The deposited films were mostly organic in nature; typical films were composed of ≈ 65 % carbon, ≈ 17 % oxygen, ≈ 12 % nitrogen, and ≈ 4 % titanium. XPS C 1s, O 1s, and Ti 2p photopeaks suggested that titanium was incorporated into the film as TiO_2 clusters dispersed in an organic matrix, and there was no evidence among the photopeaks for any Ti-C or Ti-O-C linkages. Films with a higher carbon content were better adhesion promoters. The failure mode for all samples pretreated with PP TiiB was interfacial at the PP film/substrate interface. Based on the characterization of these PP thin films, they did not seem to exhibit sol-gel like qualities. Because of the way titanium was incorporated into the films, a more appropriate name for these films might be "titanium dioxide-doped plasma polymerized films."

The PP TiiB film on polished Ti-6Al-4V was harder and had a higher modulus than a film prepared simultaneously on silicon, confirming that substrate had an effect on the film composition, which affected PP film properties. PP TiiB on polished Ti-6Al-4V contained a higher content of TiO_2, and this resulted in a higher modulus and hardness. The PP films of TiiB were much more compliant than PP acetylene films, and this was attributed to the decreased fragmentation and lower crosslinking that occurred during PP TiiB film deposition. The PP TiiB films on both substrates were too soft to obtain a critical load at debond.

This work has shown that plasma processes are effective at altering the surface chemistry of Ti-6Al-4V for adhesive bonding. However, when compared with simple acetone cleaning, the PP films studied did not offer any strength benefits as a surface preparation treatment for this type of high performance application. Relationships were found between PP film thickness, PP film chemistry, PP mechanical properties, and adhesion. These relationships may be applicable to other adhesively bonded systems and should guide further studies into plasma processes as adhesion-promoting alternatives.

Vita

The author, Ronald Attilio DiFelice, was born in Rochester, NY in 1972, as the third and final child of Attilio and Anne DiFelice. He graduated from Webster High School in 1990 and enrolled at the Rochester Institute of Technology (RIT) in the fall of that same year. He earned a Bachelor of Science degree in chemistry from RIT in 1994 and a Master of Science degree in polymer chemistry in 1995 under the direction of Dr. Andreas Langner. After working in the Polymer Research Laboratories of Eastman Kodak for almost a year, he enrolled in graduate school at Virginia Tech in the fall of 1996 to pursue his Ph.D. in polymer/physical chemistry. Under the guidance of Dr. John G. Dillard, he became interested in adhesion and surface science, and was funded by the Adhesive and Sealant Education Foundation through the Center for Adhesive and Sealant Science. Additional funding was provided through a Virginia Space Grant Consortium Fellowship. The author defended his Ph.D. dissertation on April 18th, 2001. At publication time, his post-graduation plans are uncertain. He has applied to several MBA schools, including Fuqua (Duke), Darden (UVA), Kenan-Flagler (UNC - Chapel Hill), and Simon (University of Rochester). He has also been interviewing for industrial research and development chemist positions, but may opt to follow his dream of becoming a balloon artist.

"Let me tell you the secret that has led me to my goal. My strength lies solely in my tenacity." -Louis Pasteur, chemist and bacteriologist (1822-1895)